From low dimensions to full configuration space: Generalising models for nonadiabatic molecular dynamics

LEA-MARIA IBELE

From low dimensions to full configuration space: Generalising models for nonadiabatic molecular dynamics

A thesis submitted in partial fulfilment for the degree of Doctor of Philosophy in Chemistry

Lea-Maria Ibele

Durham University

Department of Chemistry

Internal reviewer David J. Tozer

Department of Chemistry

Durham University

External reviewer Dmitry Shalashilin

School of Chemistry

University of Leeds

Supervisor Basile F. E. Curchod

2021

Abstract

This thesis aims to bridge the development of nonadiabatic dynamics methods and their application for studies of real molecular systems.

First, this work explores fundamental concepts of photochemistry by investigating two different pictures, arising from the Born-Oppenheimer and the exact factorisation representation. Based on a simplistic model, a photochemical experiment from the excitation up to the formation of photoproducts is simulated. This study then compares the Born-Oppenheimer and exact factorisation representations of the processes. Subsequently, the influence of the Born-Oppenheimer picture for approximate nonadiabatic dynamics is investigated on two-dimensional model systems around conical intersections. The effects of neglected couplings and geometric phase are evaluated for ab initio multiple spawning (AIMS), a method for nonadiabatic molecular dynamics based on classically moving Gaussians.

Afterwards, this work introduces a standardised test set of molecules to connect between tests of newly developed nonadiabatic dynamics methods on one-dimensional model systems and their intended application to full-dimensional molecules. Inspired by the widely used one-dimensional Tully models, three molecules are selected to form the *molecular Tully models*, which undergo similar photophysical processes, but in a high-dimensional space. In addition, the recently proposed stochastic-selection AIMS framework is also tested on two molecules undergoing ring-opening reactions to explore the strengths and limitations of the method.

Finally, a direct comparison between experimental and computational results is presented. The photochemistry of 2(5H)-thiophenone is probed during and after the initial ring opening using time-resolved photoelectron spectroscopy. Static and dynamic calculations unravel the photoprocesses and identify a variety of photoproducts. Using the computational results, the experimental signal can be translated to insights into the ongoing photochemistry.

Overall, this thesis aims to bring models in nonadiabatic dynamics in a real-world context. This work contributes to facilitating the transfer of new nonadiabatic dynamics methods towards the study of molecules in their full dimensionality.

Acknowledgement

This thesis has been far from being a one-person project and therefore, there are numerous people that I want to thank for their various contributions at this point.

First and foremost, I want to express my deepest gratitude to my supervisor Basile Curchod. You have truly been the best supervisor for this thesis I could have imagined. Thank you for letting me have the honour of becoming your academic firstborn. Thank you for all the things you have taught me throughout the past three years — not only for all the theoretical knowledge but also for guiding me throughout various parts of academia and helping me find my way. Thank you for letting me explore the projects I was interested in, for helping me navigate through situations when I was stuck and for sharing all the fun and excitement of science. Thank you for your patience with me and for listening to my opinions and respecting my views. Thank you for all the cheese and cheese dishes shared. Thank you for not only having been a great scientific advisor but also for becoming a friend.

Next, I want to thank all the people I have collaborated with on projects in these past 3 years. First, Federica Agostini, thank you for hosting me for some weeks in Paris, despite all hindering circumstances, for giving me great insight into the exact factorisation, for all your patient explanations and all the fun we had (and will have) doing science together.
Furthermore to Neepa Maitra and Patricia Vindel-Zandbergen. Thank you for letting me take part in your project, for all the very exciting scientific discussions and for the nice conversations during the regular zoom calls.
Lastly, to Mike Ashfold, Daniel Rolles, Shashank Pathak and João Pedro Figueira Nunes, for the amazing collaborations on thiophenone. Thank you for giving me all the insight into experimental analysis, for introducing me to your scientific views and for all the very stimulating discussions.

I also want to thank all the past and present members of the In-Silico-Photochemistry group, Angus, Antonio, Jack, Maru, Emanuele, Lewis, Joe, Yorick, Oscar, Alex, Luke, Jiři, Zoe, Joshua and Daniel. Thank you all for the amazing, entertaining scientific and not so scientific discussions, all the beers and food and cakes shared over the last years. Additionally, also I want to thank Valentina for being the aunt and most honorary member of the group, thank you for all your support and also for all the animal pictures, videos and adventures, as well as to Matteo (and PomPom) for providing a great place to write this thesis.

Additionally, I want to thank all the people that have supported me in various ways over the past three years. First, to Sandra, Clemens and Mateo, thank you for being my family on this island, for the celebrations of three kings, for all the Spaß and broken noses. Especially thank you, Sandra, for sharing not only all the fun memories but also for collaborating, sharing science together, teaching me to use Quantics, listening to my random ideas and also being one of my best friends.
To Elena, thank you for making Durham a much more enjoyable place, listening to all my rantings, sharing insane amounts of food, and for being my favourite peach person.
Felix, danke für deine unerschütterliche Unterstützung, für die unzähligen Wein-Videotelefonate, für dein immer offenes Ohr, das meinen endlosen Erzählungen über Quantenmechanik gelauscht hat, und natürlich für all die Funfacts über Lehmmauern. Und, oh Gott, Felix, wir werden erwachsen.
Danke Anna-Lena, dass ich immer auf dich zählen kann, egal wie lang die Funkstille war.
An Ralph, danke dass jedes Wiedersehen so ist, als wäre es gestern gewesen; du musst mich nie fragen warum.

Am meisten möchte ich aber meiner Familie, Angelika, Rainer und Tabea danken. Ohne euch wäre ich nicht, wo ich bin. Danke für eure unendliche Unterstützung, Geduld und Wertschätzung. Danke, dass ihr bei jedem meiner Probleme für mich da seid und ich auf euch zählen kann. Ebenso geht mein Dank an Oma. Danke, dass ihr alle mich die letzen Jahre bei alldem unterstützt habt, ohne zu wissen, wobei genau eigentlich.

Finalemente, a Davide. Grazie. Non so, come esprimerti la mia gratitudine. Grazie per avermi motivato, sostenuto e per avermi dato una ragione, prospettiva e contestualizzazione del mio lavoro scientifico. Grazie per ispirarmi, senza di te non sarei qui oggi. Si parte, si torna insieme!

Declaration and statement of copyright

The material contained within this thesis has not previously been submitted for a degree at Durham University or any other university. The research reported within this thesis has been conducted by the author unless indicated otherwise.

The copyright of this thesis rests with the author. No quotation from it should be published in any format, including electronic and the internet, without the author's prior written consent. All information derived from this thesis must be acknowledged appropriately.

Contents

Glossar

Acronyms

Acronym	Description
A-FSSH	augmented fewest switches surface hopping
ADC(2)	algebraic diagrammatic construction of second order
AIMD	*ab initio* molecular dynamics
AIMS	*ab initio* multiple spawning
BAT	bra-ket averaged Taylor expansion
BE	binding energy
BH	Born-Huang
BMA	bis(methylene)adamantyl
BO	Born-Oppenheimer
CCSD(T)	coupled cluster single-double and perturbative triple
CI	conical intersection
CT-MQC	coupled-trajectories mixed quantum-classical
DBOC	diagonal Born-Oppenheimer correction
DFT	density functional theory
DISH-XF	decoherence-induced surface hopping based on exact factorisation
DMABN	4-*N,N'*-dimethylaminobenzonitrile
dTSH	decoherence corrected trajectory surface hopping
EDC	energy-based decoherence correction
EF	exact factorisation
ESSAIMS	stochastic-selection *ab initio* multiple spawning based on an energy criterion
FC	Franck-Condon
FEL	free-electron laser
FMS	full multiple spawning
FSSH	fewest switches surface hopping
GD	gauge-dependent
GI	gauge-invariant
GP	geometric (Berry) phase
IFGA	independent first generation approximation

Acronym	Description
IP	ionisation potential
IP_{vert}	vertical ionisation potential
ITA	independent trajectory approximation
LIIC	linear interpolation in internal coordinates
LR-TDDFT	linear-response time-dependent density functional theory
LVC	linear vibronic coupling
MCE	multiconfigurational Ehrenfest
MCTDH	multiconfigurational time-dependent Hartree
MECI	minimum energy conical intersection
MP2	Møller-Plesset perturbation theory to second order
MS-CASPT2	multistate complete active space perturbation of second order
NACs	second-order nonadiabatic couplings
NACV	first-order nonadiabatic coupling vector
OSSAIMS	stochastic-selection *ab initio* multiple spawning based on the overlap
PES	potential energy surface
pITA	pseudo-independent trajectory approximation
QD	quantum dynamics
SA-CASSCF	state-averaged complete active space self-consistent field
SHAIMS	surface hopping approach to *ab initio* multiple spawning
SPA0	saddle point approximation of order zero
SPA1	saddle point approximation of first order
SSAIMS	stochastic-selection *ab initio* multiple spawning
TBF	trajectory basis function
TDPES	time-dependent potential energy surface
TDSE	time-dependent Schrödinger equation
TDVP	time-dependent vector potential
TISE	time-independent Schrödinger equation
TRPES	time-resolved photoelectron spectroscopy
TSH	trajectory surface hopping
UDFT	unrestricted density functional theory
UED	ultrafast electron diffraction
vMCG	variational multiconfigurational gaussians
ZPE	zero-point energy

Symbols

Symbol	Description
$\boldsymbol{A}$	time-dependent vector potential
$\boldsymbol{\alpha}$	width of the Gaussian
B_0	amplitude of the electric field
C	complex, time-dependent expansion coefficient
$\boldsymbol{C}$	decoherence parameter for the energy-based decoherence correction
χ	nuclear wavefunction
$\tilde{\chi}$	trajectory basis function
c_{Ji}^{dia}	expansion coefficients for the diabatic electronic wavefunctions
D_{IJ}	second-order nonadiabatic couplings between states I and J
$\boldsymbol{d}_{IJ}$	first-order nonadiabatic coupling vector between states I and J
D_{JJ}	diagonal Born-Oppenheimer correction for state J
$\boldsymbol{E}$	electric field
e	elementary charge
ϵ_0	vacuum permittivity
$\epsilon_{\text{BO}}^{(J)}$	electronic energy of state J
$\mathcal{F}$	time-dependent pulse shape of the electric field
ϵ	time-dependent scalar potential
$\boldsymbol{F}$	classical nuclear force
ω	carrier frequency of the electric field
ζ	gauge function
$\boldsymbol{g}_{IJ}$	energy difference gradient; branching space coordinate
γ	geometric phase
H	Hamiltonian matrix (element) between two Gaussians
$\mathbf{H}_{\text{BO}}^{\text{adi}}$	adiabatic Hamiltonian
$\hbar$	reduced Planck's constant
$\hat{H}_{\text{BO}}$	Born-Oppenheimer Hamiltonian
$\mathbf{H}_{\text{BO}}^{\text{dia}}$	diabatic Hamiltonian
$\boldsymbol{h}_{IJ}$	coupling gradient; branching space coordinate
$\hat{H}_{\text{m}}$	molecular Hamiltonian
$\hat{H}_{\text{m}}^{\text{GP}}$	adiabatic molecular Hamiltonian including geometric phase effect
H_{n}	nuclear Hamiltonian
$\mathcal{P}$	hopping probability
$\mathbf{J}_{\boldsymbol{d}_{IJ}}$	Jacobian of the nonadiabatic coupling vector
m_{e}	mass of an electron
θ	mixing, or adiabatic-to-diabatic transformation angle

Symbol	Description
M_ρ	mass of the ρth nucleus
$\boldsymbol{\mu}$	transition dipole moment
N_β^J	number of trajectory basis functions in state J associated with branch β
N_{dof}	number of degrees of freedom
N_{el}	number of electrons
N_{ini}	initial number parent trajectory basis functions
N_{n}	number of nuclei
$N_{\text{TBF}}^{(J)}$	time-dependent number of trajectory basis functions in state J
N_{traj}	number of trajectories
S	overlap matrix (element) between two Gaussians
$\boldsymbol{P}$	nuclear momenta
$\bar{\boldsymbol{P}}$	nuclear momentum at the center of the Gaussian
$\bar{\gamma}$	phase of the Gaussian
Φ	electronic wavefunction
$\boldsymbol{\epsilon}^\lambda$	polarisation vector of the electric field
p	coherent population
Ψ	molecular wavefunction
Q_{pot}	quantum potential
$\boldsymbol{R}$	nuclear coordinates
$\boldsymbol{r}$	electronic coordinates
$\bar{\boldsymbol{R}}$	nuclear position at the center of the Gaussian
$\mathcal{S}$	phase of the nuclear wavefunction
T_{IJ}^{eff}	effective coupling between states J and I
ε	threshold for the stochastic selection
$\hat{T}_{\text{n}}$	nuclear kinetic energy operator
$\hat{U}_{\text{en}}$	electron-nuclear coupling operator
$\hat{V}_{\text{ext}}$	external potential
v_{int}	interaction scalar potential
W	Wigner transform
Z_ρ	atomic number of the ρth nucleus

1 Introduction

"When I think of the wave-particle dilemma, which is the cornerstone of the universe, I would without hesitation emphasize that energy is freedom. I believe that the material particle is a packet of imprisoned energy. Light is a state of energy. Can one deny the free flow of light? We must take into consideration that quanta are defined as energy's smallest particle state and are today almost seen as the factor that explains all diversity. Yes, quantum motion is the creative power of all diversity. I cannot resist asking whether this is the God that humanity has been searching for all along." — Abdullah Öcalan[1]

At the beginning of the 20th century, the field of photochemistry, where light absorption processes activate chemical reaction pathways inaccessible by other means, started to emerge on the way towards its modern form. From 1899 onward, Armenian descendent Giacomo Ciamician had regularly exposed his various reaction tubes and flasks to the sun on the roof of his laboratory at the Università di Bologna. Together with Paul Silber, he was the first person to investigate the chemical effects of light, making the first systematic study of the behaviour of organic compounds toward light, pioneering the field of photochemistry. They discovered a multitude of photochemical reactions and set a path for the subsequent developments of modern photochemistry.[2,3]

The subsequent developments have recently cumulated in a multitude of applications of photochemical processes that fundamentally assist our life: photodynamic therapy exploits light for less aggressive treatment of cancer, solar and photovoltaic cells make the energy of the sun accessible for our use. More recent developments in photoorganic and photoinorganic chemistry include photocatalysis and photoredox catalysis,[4,5] that have emerged since the discovery of the photocatalytic water splitting on TiO_2 electrodes.[6] It has found various other applications from carbon dioxide reduction, to the development of new solar cell materials and in a multitude of organic syntheses.[7–9]

Due to the undeniable rise of photochemistry in various applications, following the processes of a molecule after light absorption has become increasingly important for a fundamental understanding of its capabilities. In 1988, Ahmed Zewail presented the

first experiment that followed the photoinduced dissociation of ICN.[10] This experiment marked the beginning of the rise of femtochemistry, where photoinduced reactions are spectroscopically probed in femtosecond time scale. Ultrafast dynamics based on diffraction techniques (ultrafast electron and X-ray diffraction) are directly sensitive to the spatial distribution of atoms. Through ultrafast electron diffraction, it was achieved to measure the nuclear motion in photoexcited molecular crystals with femtosecond resolution.[11,12]

These advances in experimental techniques have necessitated equal advancements in computational methods to describe the processes following photoexcitations: molecular quantum dynamics. Many parts of our way to picture chemistry have been heavily influenced by the Born-Oppenheimer approximation,[13] the assumption that the motion of nuclei and electrons can be treated separately in a molecule. Chemical structures, properties, and reactivity are often discussed mostly in terms of the evolution of nuclear degrees of freedom in a single electronic eigenstate —- a direct result of the Born-Oppenheimer approximation, which, by decoupling the motion of electrons and nuclei, introduces the concept of potential energy surfaces.[14,15] This picture is often sufficient for an accurate description of how molecules absorb light, i.e. which wavelength of the light is mainly absorbed and which excited states are accessed through the absorption. The photochemical processes following photoexcitation, in contrast, go beyond the Born-Oppenheimer approximation; upon photoexcitation, the ground state wavefunction is projected into a higher excited state where it is likely to become a nuclear wavepacket. Such a nuclear wavepacket will subsequently evolve on the excited electronic state and can eventually encounter regions where two (or more) electronic states come close in energy and therefore are coupled. In these regions of high *nonadiabaticity*, nuclear motion can induce a change of electronic eigenstate and the Born-Oppenheimer approximation will break down (cf. Fig. 1.1).

An exact description of this process requires the solution of the time-dependent Schrödinger equation, which is only possible for the smallest systems. For a quantum mechanical description of the photoprocesses of molecules, it is, therefore, necessary to rely on approximations. In the past 40 years, a very large number of so-called *nonadiabatic dynamics* methods have been proposed that describe electron and nuclear motion in very different ways. Upon development, the largest part of these methods has been tested on one-dimensional, exactly-solvable model systems that are, models with predefined one-dimensional potential energy curves and couplings between the states. These tests

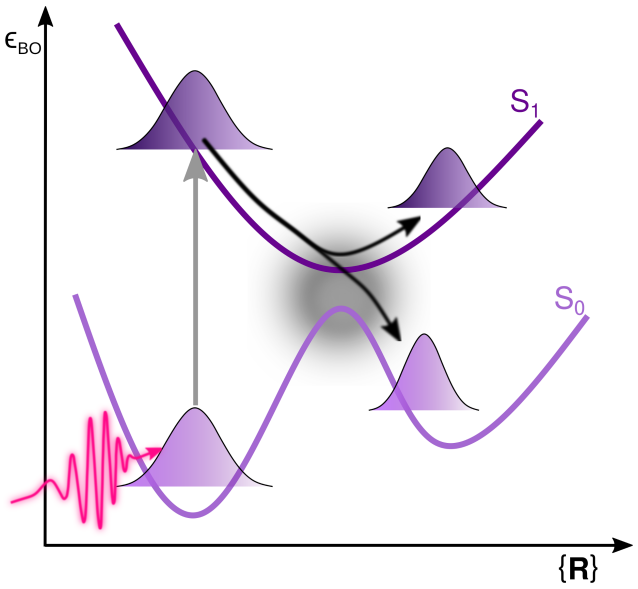

Fig. 1.1.: Schematic representation of the evolution of a wavepacket upon photoexcitation. The nuclear wavefunction is initially fully prepared in the S_0 ground state. It is hit by a laser pulse, excited to the S_1 state where it forms a nuclear wavepacket. This evolves on the S_1 state until it encounters a coupling region, where a splitting on the wavepacket occurs.

are of fundamental importance since the approximations underlying each method need to be carefully assessed in order to understand the limitations that such approximations impose on the use of the technique.

One very famous set of one-dimensional model systems are the so-called *Tully Models*, proposed by John C. Tully in 1990.[16] Since their publication, these simple model systems have been extensively used to assess the quality of newly-developed methods or test new approximations or corrections proposed for existing ones. The diversity of strategies tested with some or all of Tully models is astonishing.[17] It includes, among others, full multiple spawning,[18] semiclassical initial value representation,[19] symmetrical quasi-classical windowing combined with Meyer-Miller mapping Hamiltonian,[20] extended classical mapping model with commutator variables,[21] surface hopping Herman-Kluk semiclassical initial value representation method,[22] semiclassical Monte-Carlo,[23] dephasing representation of quantum fidelity,[24] counter-propagating wave methods trajectories,[25] Ehrenfest-Plus,[26] coupled-trajectory mixed quantum/classical dynamics,[27,28] quantum trajectory mean-field approach,[29] iterative linearised approach to nonadiabatic dynamics,[30] mean-field dynamics with stochastic decoherence,[31] nonadiabatic Bohmian dynamics,[32,33], bohmion method,[34] mean-field molecular dynamics with surface hopping,[35] non-Hermitian surface hopping,[36] multi-state trajectory approach to nonadiabatic dynamics,[37] partial linearised density ma-

trix dynamics,[38] ring polymer surface hopping,[39] quantum trajectory surface hopping,[40] consensus surface hopping,[41] or quasiclassical mapping Hamiltonian methods,[42]. This list is intended to illustrate the great variety of nonadiabatic dynamics methods that have been developed in the past 30 years and that have proven their strengths on one-dimensional model systems.

In contrast, only a drastically smaller number of methods is commonly employed for the investigation of the photochemistry of molecular systems. The most commonly employed methods are for example multiconfigurational time-dependent Hartree, variational multiconfigurational Gaussians, multiconfigurational Ehrenfest, ab initio multiple spawning, and the most widely used trajectory surface hopping.

The questions arising at this point are: Why only a few theoretical methods are used to simulate the photochemistry of molecules among the immense variety of strategies proposed in the literature? What would be required to bridge the development of new methods for nonadiabatic dynamics and their application for molecular systems?

One possible cause leading to the issues highlighted by these questions is the potential lack of connections between simple, one-dimensional models and the reality of photochemical processes for molecular systems. This concern is legitimate already from an electronic structure perspective, as moving from one to two nuclear degrees of freedom forces us to account for conical intersections (in the adiabatic representation).[43–46] Conical intersections are points in configuration space where two adiabatic electronic states become degenerate and are known to be ubiquitous in the photodynamics of molecular systems and responsible for ultrafast funnelling processes between electronic states.

Before elaborating on how to bridge this gap between nonadiabatic dynamics methods shown to succeed on one-dimensional model systems and their applicability to real molecules, I want to consider what one usually means when using the term *model*. For the often used one-dimensional models, this question appears trivial: They consist of (analytically) defined potential energy surfaces and their couplings as well as the state, position and momentum of the initial wavefunction. The potentials are constructed such that they reproduce particular situations in excited-state dynamics that would challenge the tested methods, such as decoherence and recoherences, dephasing, etc. The problem of defining a model becomes more difficult if one wants to move to the dynamics of molecules in their full configuration space. These dynamics are usually desired to be carried out on the fly, meaning without the need of precomputed potential energy surfaces but obtaining

the necessary electronic structure quantities (energies, gradients and couplings of the electronic states) at each step of the dynamics. Defining a controlled set of parameters and models based on molecules immediately becomes more challenging. In addition, while analytical models can be tuned to pose specific challenges for nonadiabatic dynamics methods, finding a set of molecules that probe the limitations of these methods is less straightforward. There is a consensus in the community that such unified *hard* benchmark tests,[47] using models in higher dimensions, would be highly beneficial for benchmarking the different methods available and dissecting their approximations. The Libra library is a project going in this direction.[48]

Another component of what is meant by *models* is the representation it uses to picture a photochemical process. All the previous discussion is based on a (post) Born-Oppenheimer picture: A molecule evolves in different, separated static electronic states that can become coupled in certain regions of configuration space. However, this picture, based on the Born-Huang expansion of the molecular wavefunction, is only one possible representation. This *model* of photochemistry has been challenged by the so-called *exact factorisation*, where the wavefunction is represented as a product of a time-dependent electronic and nuclear part, giving rise to a picture a single, moving electronic state. While we have relied largely on the Born-Oppenheimer based model of photochemistry in the past, challenging this picture has the potential of increasing our fundamental understanding of photophysical and photochemical processes.

In this thesis, I focus on the various uses of models for bridging the basic understanding of photochemical processes and the development of new methodologies to their applications for theoretical studies of molecular systems, and more generally to a synergy between experiment and theory. The thesis is structured as follows. In chapter 2, I give an introduction to the different representations of the molecular wavefunction – the Born-Oppenheimer and exact factorisation pictures – and their implications for photochemistry. A brief overview of the key ingredients of an in-silico photochemical experiment is given before focusing on two main approaches for nuclear dynamics and their derived methodologies that are most widely used throughout this thesis.

Chapter 3 introduces different fundamental ways of picturing photochemistry by comparing a complete simulated photochemical experiment within the Born-Oppenheimer and the exact factorisation picture from the explicit excitation up until the formation of

photoproducts in a two-dimensional model. In addition, a framework to propagate classical and quantum trajectories based on the exact factorisation potentials is introduced.

In chapter 4, the implications of the Born-Oppenheimer picture on the approximations of the ab initio multiple spawning method are investigated. For a series of two-dimensional model systems, the approximated dynamics in the vicinity of a conical intersection are probed and the effects of the approximations are dissected with a specific focus on the influence of the neglected quantities – second-order nonadiabatic couplings and geometric phase effects.

Having investigated nonadiabatic dynamics methods on low dimensional systems, this work then proposes a bridge towards models for molecules in their full configuration space. In chapter 5, a set of molecules is defined that probes similar photoprocesses as the original one-dimensional Tully models. The molecular models are introduced and it is exemplified which typically observed photophysical processes they probe; their dynamics are dissected, specifically the evolution of the electronic populations, obtained with different nonadiabatic dynamics methods. In addition, this study shows how some of these models can be used to test the performance of new versions of nonadiabatic dynamics methods.

Following the use of molecules to probe dynamics methods, in chapter 6, two molecules that undergo ring-opening processes are chosen as model systems in order to specifically probe the strengths and limitations of a newly developed strategy, stochastic selection ab initio multiple spawning, for the prediction of the electronic population decay.

The final chapter of this thesis proposes perhaps the strongest reference model for any nonadiabatic dynamics methods: a direct comparison between theory and experiment. In the final results chapter 7, complementary time-resolved photoelectron spectroscopy and computational studies are carried out on a prototypical molecule for heterological ring-opening. It is exemplified on this molecule, how the experimental studies can follow the ring-opening and subsequent product formation, the interplay with computational studies is fundamental for a complete understanding of the electron and nuclear dynamics processes. It is shown how experimental observables can be obtained from simulations in an efficient way that allows for a maximal insight into the ongoing molecular processes. The findings have been further interpreted and validated by ultrafast electron diffraction experiments and the corresponding simulated quantities.

Finally, I summarise the work of this thesis and draw conclusions towards the still open questions of the use and developments of models in various contexts of nonadiabatic dynamics.

Theory

2

Parts of this chapter are based on the following publications:
L. M. Ibele, A. Nicolson, and B. F. E. Curchod, “Excited-state dynamics of molecules with classically driven trajectories and Gaussians”, Mol. Phys. 118, e1665199 (2020)
L. M. Ibele and B. F. E. Curchod, "Dynamics near a conical intersection – a diabolical compromise for the approximations of ab initio multiple spawning", J. Chem. Phys. 155, 174119 (2021)

This chapter provides an overview of the various ingredients necessary for an *in-silico* photochemical experiment, i.e. the simulation of a photochemical experiment on the computer. Starting from a general overview of the key problem — solving the time-dependent Schrödinger equation — the central quantity, the molecular wavefunction, will be introduced. It will be explored how the representation of the molecular wavefunction shapes our understanding of (photo)chemistry. Subsequently, all the elements that constitute an *in-silico* photochemical experiment will be dissected, before focusing on strategies to solve at various levels of accuracy the nuclear dynamics of molecular systems upon photoexcitation.

2.1 Time-dependent Schrödinger equation

The quantum mechanical description of any system implies the treatment of its wavefunction. The wavefunction is an element of the Hilbert space of square-integrable functions and encodes the complete information on all properties of a pure system. The state of a molecular system is described by its time-dependent molecular wavefunction $[\Psi(\boldsymbol{r}, \boldsymbol{R}, t)]$ depending on all $3N_{\text{el}}$ electronic $[\boldsymbol{r}]$ and $3N_{\text{n}}$ nuclear coordinates $[\boldsymbol{R}]$. The time-evolution of the molecular wavefunction is characterised, in a non-relativistic framework, by the time-dependent Schrödinger equation, TDSE:[49]

$$i\hbar\frac{\partial}{\partial t}\Psi(\boldsymbol{r}, \boldsymbol{R}, t) = \hat{H}_{\text{m}}(\boldsymbol{r}, \boldsymbol{R}, t)\Psi(\boldsymbol{r}, \boldsymbol{R}, t)\,. \tag{2.1}$$

The full, molecular Hamiltonian [$\hat{H}_\mathrm{m}(\boldsymbol{r}, \boldsymbol{R}, t)$] consists of the nuclear kinetic energy [$\hat{T}_\mathrm{n}(\boldsymbol{R})$], the electronic potential energy through the Born-Oppenheimer Hamiltonian [$\hat{H}_\mathrm{BO}(\boldsymbol{r}, \boldsymbol{R})$], and can include an external potential [$\hat{V}_\mathrm{ext}(\boldsymbol{r}, \boldsymbol{R}, t)$]:

$$\begin{aligned}\hat{H}_\mathrm{m}(\boldsymbol{r}, \boldsymbol{R}, t) =& \hat{T}_\mathrm{n}(\boldsymbol{R}) + \hat{H}_\mathrm{BO}(\boldsymbol{r}, \boldsymbol{R}) + \hat{V}_\mathrm{ext}(\boldsymbol{r}, \boldsymbol{R}, t) \\ =& \sum_{\rho}^{N_\mathrm{n}} \frac{-\hbar^2}{2M_\rho} \nabla^2_{\boldsymbol{R}_\rho} - \sum_{i}^{N_\mathrm{el}} \frac{\hbar^2}{2m_\mathrm{e}} \nabla^2_{\boldsymbol{r}_i} + \sum_{i}^{N_\mathrm{el}} \sum_{j>i}^{N_\mathrm{el}} \frac{e^2}{4\pi\epsilon_0 |\boldsymbol{r}_i - \boldsymbol{r}_j|} \\ &+ \sum_{\rho}^{N_\mathrm{n}} \sum_{\mu>\rho}^{N_\mathrm{n}} \frac{Z_\rho Z_\mu e^2}{4\pi\epsilon_0 |\boldsymbol{R}_\mu - \boldsymbol{R}_\rho|} - \sum_{\rho}^{N_\mathrm{n}} \sum_{i}^{N_\mathrm{el}} \frac{Z_\rho e^2}{4\pi\epsilon_0 |\boldsymbol{R}_\rho - \boldsymbol{r}_i|} + \hat{V}_\mathrm{ext}(\boldsymbol{r}, \boldsymbol{R}, t) \,.\end{aligned} \tag{2.2}$$

The Born-Oppenheimer Hamiltonian consists of the electronic kinetic energy, the electron-electron interaction, the nucleus-nucleus interaction and the electron-nucleus interaction.

2.2 Born-Oppenheimer picture

Under the assumption of an infinite mass of the nuclei (and neglecting the external potential), the full Hamiltonian becomes the Born-Oppenheimer Hamiltonian. The eigenvalues and eigenvectors of $\hat{H}_\mathrm{BO}(\boldsymbol{r}, \boldsymbol{R})$ can be determined for a fixed nuclear configuration [$\boldsymbol{R}$] by the time-independent Schrödinger equation (TISE):

$$\hat{H}_\mathrm{BO}(\boldsymbol{r}, \boldsymbol{R}) \Phi_J(\boldsymbol{r}; \boldsymbol{R}) = \epsilon^{(J)}_\mathrm{BO}(\boldsymbol{R}) \Phi_J(\boldsymbol{r}; \boldsymbol{R}) \,. \tag{2.3}$$

This yields a set of othornormal electronic basis function [$\{\Phi_J(\boldsymbol{r}; \boldsymbol{R})\}_{J\in\mathbb{R}}$], the electronic (adiabatic) wavefunctions, where J labels the electronic state associated with electronic energy [$\epsilon^{(J)}_\mathrm{BO}$]. The electronic energies for a state J for all fixed $\boldsymbol{R}$ create a so-called adiabatic potential energy surface (PES). Within the famous Born-Oppenheimer (BO) approximation,[13] the molecular wavefunction is then approximated to be a product of one of these electronic, time-independent wavefunctions and a corresponding nuclear time-dependent wavefunction [$\chi(\boldsymbol{R}, t)$]:

$$\Psi_\mathrm{BO}(\boldsymbol{r}, \boldsymbol{R}, t) = \Phi_J(\boldsymbol{r}; \boldsymbol{R}) \chi_J(\boldsymbol{R}, t) \,. \tag{2.4}$$

The BO approximation assumes that the nuclear and electronic motion can be decoupled, restricting the dynamics of the nuclear wavefunction to a single adiabatic electronic state J. Thus, within this approximation, the propagation of the molecular wavefunction through

the time-dependent Schrödinger equation results in evolution on one adiabatic PES, where the wavefunction remains at all times in this single electronic state; this propagation is called adiabatic dynamics. This means that at no time throughout the dynamics the electronic state of the nuclear wavefunction can change. While this might be accurate for ground-state processes where no other states are energetically accessible, for photochemical processes, i.e. for the dynamics following photoexcitation, the molecule probably encounters regions of configuration space where multiple electronic states become close in energy. In these regions, the coupling between the electronic states becomes very large and the nuclear dynamics lead to a change of electronic state. In this situation, the nuclear and electronic motion cannot be considered uncoupled anymore; the BO approximation breaks down necessitating the inclusion of *nonadiabatic* effects.

This problem can be overcome through the so-called Born-Huang (BH) expansion[50]. Instead of considering the molecular wavefunction as a single product of an adiabatic electronic and nuclear wavefunction, it is expanded in the full basis of adiabatic electronic wavefunctions $[\{\Phi_J(\boldsymbol{r};\boldsymbol{R})\}_{J\in\mathbb{R}}]$, where the nuclear wavefunctions act as time-dependent expansion coefficients:

$$\Psi(\boldsymbol{r},\boldsymbol{R},t) = \sum_{J}^{\infty} \Phi_J(\boldsymbol{r};\boldsymbol{R})\chi_J(\boldsymbol{R},t)\,. \tag{2.5}$$

Within this representation, the time-dependence of the molecular wavefunction is solely grouped in the nuclear wavefunctions for each state J. Therefore, in order to characterise the time-dependence of the molecular wavefunction — to carry out quantum molecular dynamics — one can look at the time-evolution of the nuclear amplitudes. To this end, the BH expansion (Eq. (2.5)) is inserted in the TDSE (Eq. (2.1)); after left multiplication with $\Phi_I^*(\boldsymbol{r};\boldsymbol{R})$ and integration over all electronic coordinates $[\boldsymbol{r}]$, this yields a set of coupled equations of motion for the nuclear amplitudes:

$$\begin{aligned} i\hbar\frac{\partial}{\partial t}\chi_I(\boldsymbol{R},t) = &\left(\sum_{\rho}^{N_\mathrm{n}} \frac{-\hbar^2}{2M_\rho}\nabla^2_{\boldsymbol{R}_\rho} + \epsilon^{(I)}_{\mathrm{BO}}(\boldsymbol{R})\right)\chi_I(\boldsymbol{R},t) \\ &- \sum_{J}^{\infty}\left[\sum_{\rho}^{N_\mathrm{n}}\left[\frac{\hbar^2}{M_\rho}\left\langle\Phi_I\right|\nabla_{\boldsymbol{R}_\rho}\left|\Phi_J\right\rangle_{\boldsymbol{r}}\nabla_{\boldsymbol{R}_\rho} + \frac{\hbar^2}{2M_\rho}\left\langle\Phi_I\right|\nabla^2_{\boldsymbol{R}_\rho}\left|\Phi_J\right\rangle_{\boldsymbol{r}}\right]\right]\chi_J(\boldsymbol{R},t) \\ &+ \left\langle\Phi_I\right|\hat{V}_{\mathrm{ext}}(\boldsymbol{R},t)\left|\Phi_J\right\rangle_{\boldsymbol{r}}\chi_J(\boldsymbol{R},t)\,. \end{aligned} \tag{2.6}$$

The notation $\langle \cdots \rangle_{\boldsymbol{r}}$ implies integration over all coordinates $\boldsymbol{r}$. The first two terms on the left-hand side of Eq. (2.6) are the nuclear kinetic energy and electronic potential energy. They give rise to the adiabatic evolution of the nuclear wavefunction $[\chi_I(\boldsymbol{R}, t)]$ on state I, following the corresponding static PES given by $\epsilon_{\mathrm{BO}}^{(I)}(\boldsymbol{R})$. The last two terms are the so-called *nonadiabatic couplings*, which are the terms that are neglected by the BO approximation, and couple the different adiabatic states to each other. For real electronic wavefunctions, the first order nonadiabatic coupling vectors (NACVs) $[\boldsymbol{d}_{IJ}(\boldsymbol{R}) = \langle \Phi_I | \nabla_{\boldsymbol{R}} | \Phi_J \rangle_{\boldsymbol{r}}]$ are only non-zero for $I \neq J$. The second order couplings have a not null contribution for $I = J$, $[D_{JJ}(\boldsymbol{R}) = \langle \Phi_J | \nabla^2_{\boldsymbol{R}} | \Phi_J \rangle_{\boldsymbol{r}}]$, called the diagonal Born-Oppenheimer correction (DBOC), and a contribution for $I \neq J$, $[D_{IJ}(\boldsymbol{R}) = \langle \Phi_I | \nabla^2_{\boldsymbol{R}} | \Phi_J \rangle_{\boldsymbol{r}}]$, called second order nonadiabatic couplings (NACs). The first-order nonadiabatic couplings measure the variation of the electronic wavefunction with the nuclear coordinates, and can be rewritten to explicitly highlight their dependence on the energy difference between two states I and J as[51]

$$\boldsymbol{d}_{IJ}(\boldsymbol{R}) = \langle \Phi_I | \nabla_{\boldsymbol{R}} | \Phi_J \rangle_{\boldsymbol{r}} = \frac{\langle \Phi_I | \nabla_{\boldsymbol{R}} \hat{H}_{\mathrm{BO}}(\boldsymbol{R}) | \Phi_J \rangle_{\boldsymbol{r}}}{\epsilon_{\mathrm{BO}}^{(J)}(\boldsymbol{R}) - \epsilon_{\mathrm{BO}}^{(I)}(\boldsymbol{R})} \,. \tag{2.7}$$

The BH expansion still considers the evolution of the nuclear wavefunction on individual, time-independent, adiabatic electronic states, but allows population transfer between nuclear wavefunctions associated with different electronic states through the nonadiabatic couplings. It can, thus, be viewed as a post-Born-Oppenheimer picture: keeping the same spirit of static, adiabatic states, but simply coupling them with each other through the nonadiabatic couplings.

2.2.1 Photochemistry in a (post) Born-Oppenheimer picture

The most common understanding of photochemical and photophysical processes is inseparably connected with the BO picture: usually, the excited-state molecular dynamics of a molecule is pictured throughout as radiative or nonradiative transfers between different electronic states.[14] An example for a typical photochemical experiment in the BO picture is schematically shown in Fig. 2.1. Initially, the molecule is in its ground electronic and vibrational state (*Initialisation*), when it is hit by an ultrashort light pulse which triggers a transition to a higher-lying electronic state, S_n, (*Excitation*). Through the light-matter interaction, a portion of the original nuclear wavefunction is projected onto the excited state, forming a nuclear wavepacket. This means that part of the original nuclear wavefunction

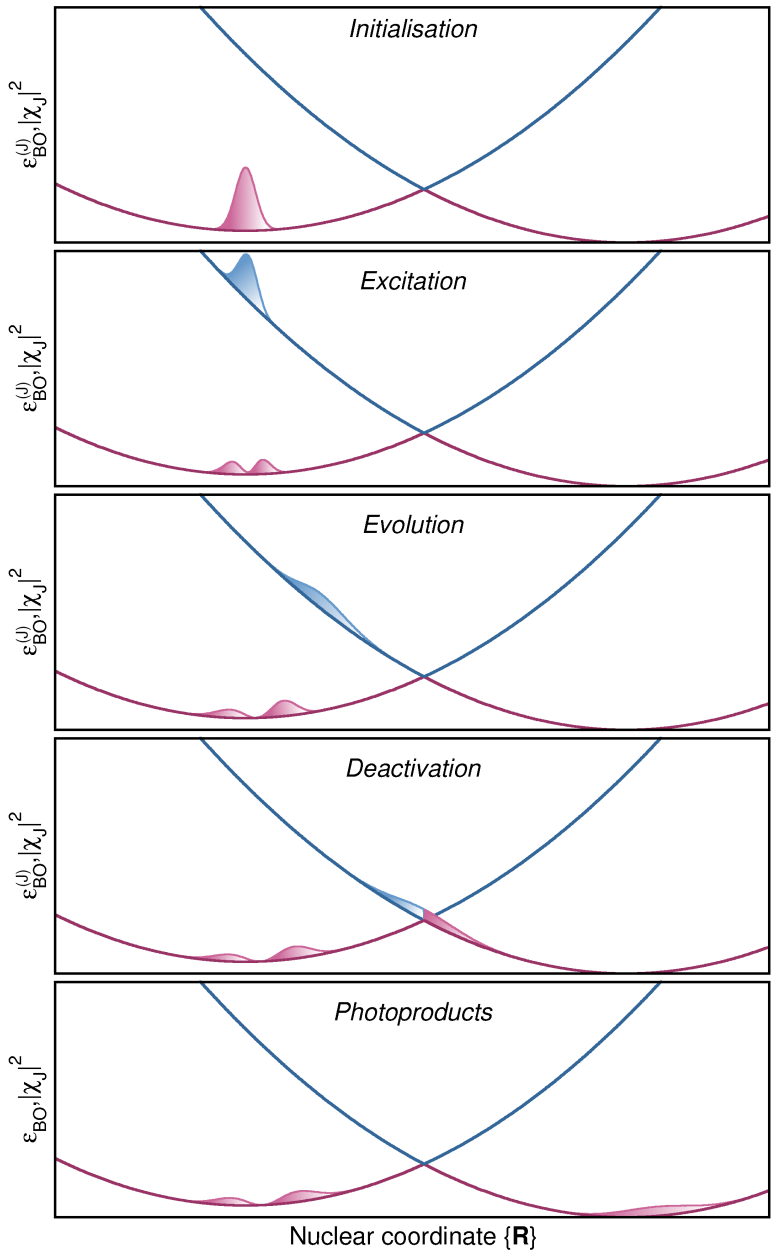

Fig. 2.1.: Schematic overview of the steps of an *in-silico* photochemical experiment within the (post) Born-Oppenheimer picture.

is represented as a linear combination of the nuclear eigenstates for the new electronic state S_n. Additionally, part of the ground-state wavefunction can be also excited to a higher vibrational eigenstate of the electronic ground state (as depicted in the example in Fig. 2.1). The excited-state nuclear wavepacket subsequently evolves on the S_n state (*Evolution*). The nuclear wavepacket encounters a region of configuration space, where the electronic state it evolves on comes close in energy to another electronic state and nonadiabatic effects become strong, leading to decay back to the ground state (*Deactivation*). This means, in these regions, the nuclear wavepacket transfers amplitude to the coupled electronic state, which leads to a branching of the resulting wavepackets on the different electronic states. This particular nonradiative decay is called internal conversion and it is usually the most efficient relaxation process for a molecule. After the system has decayed to the ground state, it can very often access regions of configuration space, that were not accessible from the equilibrium and through that form *Photoproducts*.

This very general picture of common photochemical processes is intrinsically based on the BH expansion of the molecular wavefunction: every process consists of static electronic states where the nuclear wavepacket evolves in and occasionally, these states exhibit strong coupling between each other.

2.2.2 Representation of the electronic basis

In the BH expansion, the molecular wavefunction is expressed in a basis of electronic functions; thus, one has to choose a representation for this electronic basis.[52,53] As done in Eq. (2.5), the most common choice is to use the eigenfunctions of the electronic Hamiltonian (Eq. (2.4)), giving rise to the widely used *adiabatic* representation of the molecular wavefunction. An alternative is provided by choosing electronic wavefunctions that do not (parametrically) depend on the nuclear coordinates, meaning that they keep their electronic character. This basis of electronic wavefunctions is called *diabatic* and can be related to the adiabatic wavefunctions as:

$$\Phi_J(\boldsymbol{r};\boldsymbol{R}) = \sum_i c_{Ji}^{\mathrm{dia}}(\boldsymbol{R})\Phi_J^{\mathrm{dia}}(\boldsymbol{r};\boldsymbol{R}_0)\,. \tag{2.8}$$

These diabatic states $[\Phi_J^{\mathrm{dia}}(\boldsymbol{r};\boldsymbol{R}_0)]$ are defined at a particular geometry $\boldsymbol{R}_0$, at which they are eigenstates of the electronic Hamiltonian, but they maintain their electronic *character* and do not diagonalise the electronic Hamiltonian at any geometries different from $\boldsymbol{R}_0$.

Within this representation, all the couplings between electronic states are absorbed in the off-diagonal elements of the Hamiltonian matrix and therefore, the nonadiabatic coupling terms from Eq. (2.6) become redundant as the nuclear kinetic energy operator becomes diagonal in the diabatic representation.

The relation between the diabatic and adiabatic basis can be illustrated through the diabatic-adiabatic transformation. This can be exemplified with a simple two-state system, where the potential energy matrix of a diabatic Hamiltonian is defined as[52,54,55]

$$\mathbf{H}_{\mathrm{BO}}^{\mathrm{dia}}(\boldsymbol{R}) = \begin{pmatrix} V_{11}(\boldsymbol{R}) & V_{12}(\boldsymbol{R}) \\ V_{12}(\boldsymbol{R}) & V_{22}(\boldsymbol{R}) \end{pmatrix}, \tag{2.9}$$

where $V_{IJ} = \langle \Phi_I^{\mathrm{dia}}(\boldsymbol{R}_0) | \, \hat{H}_{\mathrm{BO}}(\boldsymbol{R}) \, | \Phi_J^{\mathrm{dia}}(\boldsymbol{R}_0) \rangle_{\boldsymbol{r}}$. Diagonalising the potential energy matrix, results in the adiabatic electronic states as the eigenfunctions of $\hat{H}_{\mathrm{BO}}(\boldsymbol{r}, \boldsymbol{R})$. The diagonalisation can be done through the unitary transformation matrix [U]

$$\mathbf{U}(\boldsymbol{R}) = \begin{pmatrix} \cos\theta(\boldsymbol{R}) & \sin\theta(\boldsymbol{R}) \\ -\sin\theta(\boldsymbol{R}) & \cos\theta(\boldsymbol{R}) \end{pmatrix}, \tag{2.10}$$

resulting in the relation between adiabatic states $[\Phi_{1,2}(\boldsymbol{r}; \boldsymbol{R})]$ and diabatic states $[\Phi_{1,2}^{\mathrm{dia}}(\boldsymbol{r}; \boldsymbol{R}_0)]$:

$$\begin{pmatrix} \Phi_1(\boldsymbol{r}; \boldsymbol{R}) \\ \Phi_2(\boldsymbol{r}; \boldsymbol{R}) \end{pmatrix} = \begin{pmatrix} \cos\theta(\boldsymbol{R}) & \sin\theta(\boldsymbol{R}) \\ -\sin\theta(\boldsymbol{R}) & \cos\theta(\boldsymbol{R}) \end{pmatrix} \begin{pmatrix} \Phi_1^{\mathrm{dia}}(\boldsymbol{r}; \boldsymbol{R}_0) \\ \Phi_2^{\mathrm{dia}}(\boldsymbol{r}; \boldsymbol{R}_0) \end{pmatrix}, \tag{2.11}$$

where $\theta(\boldsymbol{R})$ is the mixing angle (or adiabatic-to-diabatic transformation angle) between the diabatic electronic states $V_{11}(\boldsymbol{R})$ and $V_{22}(\boldsymbol{R})$ and can be defined as

$$\theta(\boldsymbol{R}) = \frac{1}{2} \arctan \frac{2V_{12}(\boldsymbol{R})}{V_{11}(\boldsymbol{R}) - V_{22}(\boldsymbol{R})} \, . \tag{2.12}$$

An interesting thing to note at this point is that this mixing angle can be related to the nonadiabatic coupling vector $[\boldsymbol{d}_{IJ}(\boldsymbol{R})]$ by inserting the expressions for the adiabatic states from Eq. (2.11) as follows:[52]

$$\boldsymbol{d}_{12}(\boldsymbol{R}) = \langle \Phi_I | \, \nabla_{\boldsymbol{R}} \, | \Phi_J \rangle_{\boldsymbol{r}} = -\nabla_{\boldsymbol{R}} \theta(\boldsymbol{R}) \, . \tag{2.13}$$

The ground and excited adiabatic electronic energies, $\epsilon_{\mathrm{BO}}^{(-)}$ and $\epsilon_{\mathrm{BO}}^{(+)}$, respectively, can be obtained from the diabatic energies as

$$\epsilon_{\mathrm{BO}}^{(\pm)} = \frac{V_{11}(\boldsymbol{R}) + V_{22}(\boldsymbol{R})}{2} \pm \frac{1}{2}\sqrt{(V_{22}(\boldsymbol{R}) - V_{11}(\boldsymbol{R}))^2 + 4V_{12}^2(\boldsymbol{R})}\,. \tag{2.14}$$

In the general case, for systems including more than two electronic states, it is not possible to find a basis of strictly diabatic states.[53] In applications to larger systems, quasi-diabatic states can be found as a set of electronic states that minimise the NACVs terms. This is, however, not straightforward and therefore, often the photochemistry of molecules is treated in the adiabatic picture.

2.2.3 Conical intersections

One feature of particular importance of adiabatic PESs are so-called *conical intersections* (CI), points of degeneracy between two adiabatic surfaces.[44,51,52,56] Consequently, the nonadiabatic coupling becomes singular exactly at these points, and very strong in their vicinity. Therefore, CIs are points in configuration space, in whose vicinity the BO approximation breaks down completely and they often act as funnels for nonradiative decay processes.

But how can one characterise and identify these diabolical features of the PESs? To simplify the problem, the previously introduced two-state diabatic Hamiltonian defined in Eq. (2.9) is considered. For the eigenvalues of this matrix to be degenerate, two conditions must be satisfied:[51]

$$V_{11}(\boldsymbol{R}) - V_{22}(\boldsymbol{R}) = 0 \tag{2.15}$$

$$V_{12}(\boldsymbol{R}) = 0\,. \tag{2.16}$$

Considering a molecule with $N_{\mathrm{dof}} = 3N_{\mathrm{n}} - 6$ degrees of freedom, these two conditions are satisfied spanning a subspace of dimension $N_{\mathrm{dof}} - 2$. Neumann and Wigner first introduced these conditions for degeneracy for a diatomic molecule as the noncrossing rule — in the case of only one degree of freedom, two electronic states cannot become degenerate.[57] However, polyatomic molecules include many degrees of freedom and therefore their electronic states can indeed become degenerate. These degeneracies, giving rise to CIs, occur indeed in a majority of polyatomic molecules and act as funnels for nonadiabatic events. As a consequence of the noncrossing rule, in systems of more than two dimensions,

CIs do not occur as isolated points but rather span a so-called *seam*, a connected $(N_{\mathrm{dof}}-2)$-dimensional subspace, with the space orthogonal to it called the *branching* space.[51,56]

For characterising conical intersections, determining the branching space is a crucial step. For a CI between electronic states I and J, the branching space is spanned by the energy difference gradient $[\boldsymbol{g}_{IJ}(\boldsymbol{R})]$ and the coupling gradient $[\boldsymbol{h}_{IJ}(\boldsymbol{R}) = \langle\Phi_I|\,\nabla_{\boldsymbol{R}}\hat{H}_{\mathrm{BO}}(\boldsymbol{R})\,|\Phi_J\rangle_{\boldsymbol{r}}]$.[58] The potential energy matrix of Eq. (2.9) transforms in the branching plane of the CI to[51]

$$\mathbf{H}_{bs}(X_1, X_2) = (s_1 X_1 + s_2 X_2)\mathbf{1} + \begin{pmatrix} gX_1 & hX_2 \\ hX_2 & -gX_1 \end{pmatrix}, \tag{2.17}$$

where X_1 and X_2 are displacements along the $\boldsymbol{g}_{IJ}$ and $\boldsymbol{h}_{IJ}$ directions, respectively, g and h are the norm of the respective vectors and s_1 and s_2 are the projections of $(\boldsymbol{g}_I + \boldsymbol{g}_J)/2$ onto the branching plane. The eigenvalues of $\mathbf{H}_{bs}$ then become

$$\epsilon_{\mathrm{BO}}^{(\pm)}(X_1, X_2) = s_1 X_1 + s_2 X_2 \pm \sqrt{(gX_1)^2 + (hX_2)^2}\,. \tag{2.18}$$

Plotting the energy of the two electronic states around the CI along these two coordinates, the potential forms the characteristic double cone — leading to the notion of CIs as *diabolical* points. The topography of the CI is determined by the parameters g and h, which give the slope of the cone in the respective directions, and s_1 and s_2, which give the tilt of the cone. A symmetric cone has equal slopes in g and h, while they differ for an asymmetric cone. Another important classification is between peaked or sloped CIs. For a peaked CI, both s_1 and s_2 are zero, while if one or two of the parameters s_1 and s_2 are nonzero, it gives rise to a sloped conical intersection.[51,56,58] As will be shown in later parts of this thesis, the topography of a CI can have a crucial influence on the nonadiabatic dynamics observed in the system.

2.2.4 Geometric phase

CIs give rise to one crucial feature: the geometric phase (GP) or Berry phase.[59,60] In 1958, Longuet-Higgins[60] found for a Jahn-Teller model that when a real-valued, adiabatic wavefunction forms a closed loop in nuclear coordinate space encircling a CI, the wavefunction must change its sign. In 1984, Berry[59] showed that a system in a given eigenstate transported along a contour acquires a time-dependent phase factor $[\exp(i\gamma_J(t))]$. This phase $[\gamma_J(t)]$ becomes independent of the time, for a closed contour and a long enough time

needed for the excursion along this contour. In analogy to Longuet-Higgins findings, Berry showed that if the closed contour [Γ] lies in a plane containing a CI, the phase $[\gamma_J(\Gamma)]$ is π and the overall wavefunction changes sign.[52] This phase factor was defined by Berry as

$$\gamma_J(\Gamma) = i \oint_\Gamma \langle \Phi_J | \nabla_{\boldsymbol{R}} \Phi_J \rangle_{\boldsymbol{r}} \, \mathrm{d}\boldsymbol{R} \,. \tag{2.19}$$

A correct inclusion of the GP is quite challenging as the exact functional form of the phase is not known for more complex and real systems.[61] However, it was shown in previous works that the inclusion of the GP can be vital for an accurate description of the evolution of molecules upon photoexcitation in an adiabatic picture, where a lack of GP effects predicts drastically slower population decay.[54,61]

It is convenient to return to the two-state model system as defined in Eq. (2.9) for a simplified, exemplary case of accounting for the GP. Based on the seminal work by Mead and Truhlar[43], it is known that the GP is the same for both states considered in a two-state system, i.e. $\gamma_1 = \gamma_2 = \gamma$. Furthermore, Mead and Truhlar showed how the GP can be related to the mixing angle between diabatic and adiabatic states as defined in Eq. (2.12).[55] Close investigation of $\theta(\boldsymbol{R})$ shows that upon encircling, the phase of the adiabatic electronic wavefunction, as defined by Eq. (2.11), changes by a factor of π.[61–63] This factor of π means that the (real) adiabatic wavefunctions, given by Eq. (2.11), changes their sign by circling around a conical intersection. This phase shift and subsequent flip of sign is a manifestation of the GP.[59,60] However, the GP leads to a double-valuedness of the electronic wavefunctions. For a proper description of the molecular wavefunction (which is overall needs to remain single-valued), one would need to use doubled-valued boundary conditions for the nuclear wavefunctions as well.[55,61,63] However, as suggested by Mead and Truhlar[43] this can be avoided by instead transforming the adiabatic Hamiltonian $[\mathbf{H}_{\mathrm{BO}}^{\mathrm{adi}}]$ as

$$\mathbf{H}_{\mathrm{BO}}^{\mathrm{adi(GP)}}(\boldsymbol{r}, \boldsymbol{R}) = e^{i\theta(\boldsymbol{R})} \mathbf{H}_{\mathrm{BO}}^{\mathrm{adi}}(\boldsymbol{r}, \boldsymbol{R}) e^{-i\theta(\boldsymbol{R})} \,. \tag{2.20}$$

However, the choice of the GP is not universal, and while the above choice as the mixing angle is valid for many two-state linear-vibronic coupling models, the GP still depends on the system studied.[44]

It is important to keep in mind, that this quantised GP $[\gamma(\Gamma)]$ arises as an artefact of the BO approximation and is a direct consequence of the presence of CIs in the adiabatic representation. At the point of the conical intersection, the nuclear BO wavefunction

becomes multivalued as a consequence of the nonanalyticity of the potential. Therefore, to preserve the single-valuedness of the overall wavefunction, the electronic contribution to the BO wavefunction must be multivalued as well and if encircling the closed path around the conical intersection, changes its sign.[64] Contrary to populist beliefs, the molecular GP (a quantised, topological phase) is not an observable; indeed, in a diabatic picture (and in the exact factorisation picture, see Sec. 2.3), such a GP does not occur.[65]

2.3 Exact factorisation

A contrasting picture to the previously described (post)BO picture is given by the exact factorisation (EF). Instead of expressing the molecular wavefunction as an infinite sum over time-independent electronic eigenfunctions and time-dependent nuclear amplitudes, the EF[66,67] proposes a subtle alternative:

$$\Psi(\boldsymbol{r}, \boldsymbol{R}, t) = \Phi(\boldsymbol{r}, t; \boldsymbol{R})\chi(\boldsymbol{R}, t)\,. \tag{2.21}$$

This exact representation of the molecular wavefunction consists now of a single product between a nuclear wavefunction $[\chi(\boldsymbol{R}, t)]$ and an electronic wavefunction $[\Phi(\boldsymbol{r}, t; \boldsymbol{R})]$ — parametrically dependent on the nuclear coordinates $[\boldsymbol{R}]$. Note that now both nuclear and electronic wavefunction are time-dependent. By imposing the partial normalisation conditions

$$\langle \Phi(t; \boldsymbol{R}) | \Phi(t; \boldsymbol{R}) \rangle_{\boldsymbol{r}} = 1 \;\forall \boldsymbol{R}, t\,, \tag{2.22}$$

the existence and uniqueness — up to a gauge transformation — of the single product as given by Eq. (2.21) can be proven.[66,68] Consequently, it is ensured that $|\chi(\boldsymbol{R}, t)|^2$ reproduces the nuclear density as obtained from $\Psi(\boldsymbol{r}, \boldsymbol{R}, t)$ at all times. Therefore the nuclear wavefunction can also be expressed as

$$\chi(\boldsymbol{R}, t) = \exp\left(\frac{i}{\hbar}\mathcal{S}(\boldsymbol{R}, t)\right)\sqrt{\langle \Phi(t; \boldsymbol{R}) | \Phi(t; \boldsymbol{R}) \rangle_{\boldsymbol{r}}}\,, \tag{2.23}$$

where the phase of the nuclear wavefunction $[\mathcal{S}(\boldsymbol{R}, t)]$ is a real function of nuclear positions and time.

This expansion of the molecular wavefunction is invariant under a gauge transformation of nuclear and electronic wavefunctions.[68] Multiplication of $\chi(\boldsymbol{R}, t)$ by a phase factor $[g(\boldsymbol{R}, t)]$ and $\Phi(\boldsymbol{r}, t; \boldsymbol{R})$ by its complex conjugate $[g^*(\boldsymbol{R}, t)]$, does not change the product

of the two wavefunctions. As a consequence of the partial normalisation condition, the absolute value squared of this phase factor needs to equal one $[|g(\boldsymbol{R},t)|^2 = 1]$, so it can be defined as $g(\boldsymbol{R},t) = e^{i/\hbar\zeta(\boldsymbol{R},t)}$, for a real gauge function $[\zeta(\boldsymbol{R},t)]$. For uniqueness of the wavefunction it is necessary to fix the gauge by choosing a suitable $\zeta(\boldsymbol{R},t)$. The gauge function $[\zeta(\boldsymbol{R},t)]$ can also be absorbed into the phase of the nuclear wavefunction $[\mathcal{S}(\boldsymbol{R},t)]$ as choosing the phase of the nuclear wavefunction implies fixing the gauge. The topic of the gauge freedom will be discussed in more detail below.

In order to investigate the time-evolution of the molecular wavefunction, inserting the factored form (Eq. (2.21)) into the TDSE (Eq. (2.3)) and by using the partial normalisation condition (Eq. (2.22)), coupled equations of motion for the nuclear and electronic wavefunctions can be derived.

$$i\hbar\frac{\partial}{\partial t}\chi(\boldsymbol{R},t) = \left[\sum_{\rho}^{N_\mathrm{n}}\frac{\left[-i\hbar\nabla_{\boldsymbol{R}_\rho} + \boldsymbol{A}_\rho(\boldsymbol{R},t)\right]^2}{2M_\rho} + \epsilon(\boldsymbol{R},t) + v_\mathrm{int}(\boldsymbol{R},t)\right]\chi(\boldsymbol{R},t) \tag{2.24}$$

$$i\hbar\frac{\partial}{\partial t}\Phi(\boldsymbol{r},t;\boldsymbol{R}) = \left[\hat{H}_\mathrm{BO}(\boldsymbol{r},\boldsymbol{R}) + \hat{V}_\mathrm{ext}(\boldsymbol{r},\boldsymbol{R},t) + \hat{U}_\mathrm{en}[\Phi,\chi](\boldsymbol{R},t) - \epsilon(\boldsymbol{R},t) - v_\mathrm{int}(\boldsymbol{R},t)\right]\Phi(\boldsymbol{r},t;\boldsymbol{R}) \tag{2.25}$$

The electron-nuclear coupling operator $[\hat{U}_\mathrm{en}[\Phi,\chi](\boldsymbol{R},t)]$ depends explicitly on the nuclear wavefunction $[\chi(\boldsymbol{R},t)]$ and also implicitly contains the electronic wavefunction $[\Phi(\boldsymbol{r},t;\boldsymbol{R})]$ through the time-dependent vector potential $[\boldsymbol{A}_\rho(\boldsymbol{R},t)]$

$$\hat{U}_\mathrm{en}[\Phi,\chi](\boldsymbol{R},t) = \sum_{\rho}^{N_\mathrm{n}}\frac{\hbar^2}{M_\rho}\left(\frac{[-i\hbar\nabla_{\boldsymbol{R}_\rho} - \boldsymbol{A}_\rho(\boldsymbol{R},t)]^2}{2} + \left(\frac{-i\hbar\nabla_{\boldsymbol{R}_\rho}\chi(\boldsymbol{R},t)}{\chi(\boldsymbol{R},t)} + \boldsymbol{A}_\rho(\boldsymbol{R},t)\right)\left(-i\hbar\nabla_{\boldsymbol{R}_\rho} - \boldsymbol{A}_\rho(\boldsymbol{R},t)\right)\right). \tag{2.26}$$

With these two equations of motion, the two new potentials within the framework of the EF are introduced: the time-dependent vector potential (TDVP),

$$\boldsymbol{A}_\rho(\boldsymbol{R},t) = \left\langle\Phi(t;\boldsymbol{R})\right| - i\hbar\nabla_{\boldsymbol{R}_\rho}\Phi(t;\boldsymbol{R})\big\rangle_{\boldsymbol{r}}\,, \tag{2.27}$$

and the time-dependent potential energy surface (TDPES), consisting of the two scalar potentials,

$$\epsilon(\boldsymbol{R},t) = \langle\Phi(t;\boldsymbol{R})|\,\hat{H}_{\mathrm{BO}}(\boldsymbol{R}) + \hat{U}_{\mathrm{en}}[\Phi,\chi](\boldsymbol{R},t) - i\hbar\frac{\partial}{\partial t}\,|\Phi(t;\boldsymbol{R})\rangle_{\boldsymbol{r}} \tag{2.28}$$

$$v_{\mathrm{int}}(\boldsymbol{R},t) = \langle\Phi(t;\boldsymbol{R})|\,\hat{V}_{\mathrm{ext}}(\boldsymbol{R},t)\,|\Phi(t;\boldsymbol{R})\rangle_{\boldsymbol{r}} \tag{2.29}$$

that mediate the electron nuclei coupling beyond the adiabatic picture.[69,70]

Since the scalar potential $[\epsilon(\boldsymbol{R},t)]$ is obtained as the sum of expectation values on $\Phi(\boldsymbol{r},t;\boldsymbol{R})$ of the three operators $\hat{H}_{\mathrm{BO}}$, $\hat{U}_{\mathrm{en}}$ and $-i\hbar\frac{\partial}{\partial t}$, it seems to depend explicitly on the nuclear wavefunction $[\chi(\boldsymbol{R},t)]$ as the electron-nuclear coupling operator $[\hat{U}_{\mathrm{en}}[\Phi,\chi](\boldsymbol{R},t)]$ depends explicitly on it.[68] Subsequently, also the "nuclear Hamiltonian" from Eq. (2.24) would depend on $\chi(\boldsymbol{R},t)$ as well. However, from the definition of the TDVP and the partial normalisation condition it follows that

$$\langle\Phi(t;\boldsymbol{R})| - i\hbar\nabla_{\boldsymbol{R}_\rho} - \boldsymbol{A}_\rho(\boldsymbol{R},t)\,|\Phi(t;\boldsymbol{R})\rangle_{\boldsymbol{r}} = \langle\Phi(t;\boldsymbol{R})| - i\hbar\nabla_{\boldsymbol{R}_\rho}\,|\Phi(t;\boldsymbol{R})\rangle_{\boldsymbol{r}} - \boldsymbol{A}_\rho(\boldsymbol{R},t) = 0\,, \tag{2.30}$$

and thus, neither $\epsilon(\boldsymbol{R},t)$ nor the nuclear Hamiltonian depend on $\chi(\boldsymbol{R},t)$.

While the equations of motion (Eqs. (2.24) and (2.25)) are form-invariant under a gauge transformation, the scalar and vector potential transform as

$$\tilde{\epsilon}(\boldsymbol{R},t) = \epsilon(\boldsymbol{R},t) + \frac{\partial}{\partial t}\zeta(\boldsymbol{R},t) \tag{2.31}$$

$$\tilde{\boldsymbol{A}}_\rho(\boldsymbol{R},t) = \boldsymbol{A}_\rho(\boldsymbol{R},t) + \nabla_{\boldsymbol{R}_\rho}\zeta(\boldsymbol{R},t)\,. \tag{2.32}$$

The TDVP is inherently gauge dependent, while the TDPES can be decomposed in gauge-invariant, (GI), and gauge-dependent (GD) contributions $[\epsilon(\boldsymbol{R},t) = \epsilon_{\mathrm{GI}}(\boldsymbol{R},t) + \epsilon_{\mathrm{GD}}(\boldsymbol{R},t)]$.*

$$\begin{aligned}\tilde{\epsilon}_{\mathrm{GI}}(\boldsymbol{R},t) = \epsilon_{\mathrm{GI}}(\boldsymbol{R},t) &= \langle\Phi(t;\boldsymbol{R})|\,\hat{H}_{\mathrm{BO}}(\boldsymbol{R})\,|\Phi(t;\boldsymbol{R})\rangle_{\boldsymbol{r}} \\ &\quad + \sum_{\rho}^{N_{\mathrm{n}}}\frac{\hbar^2}{2M_\rho}\langle\nabla_{\boldsymbol{R}_\rho}\Phi(t;\boldsymbol{R})|\nabla_{\boldsymbol{R}_\rho}\Phi(t;\boldsymbol{R})\rangle_{\boldsymbol{r}} - \sum_{\rho}^{N_{\mathrm{n}}}\frac{\boldsymbol{A}_\rho^2(\boldsymbol{R},t)}{2M_\rho}\end{aligned} \tag{2.33}$$

$$\tilde{\epsilon}_{\mathrm{GD}}(\boldsymbol{R},t) = \epsilon_{\mathrm{GD}}(\boldsymbol{R},t) + \frac{\partial}{\partial t}\zeta(\boldsymbol{R},t) = \langle\Phi(t;\boldsymbol{R})| - i\hbar\frac{\partial}{\partial t}\,|\Phi(t;\boldsymbol{R})\rangle_{\boldsymbol{r}} + \frac{\partial}{\partial t}\zeta(\boldsymbol{R},t) \tag{2.34}$$

*The external scalar potential $[v_{\mathrm{int}}(\boldsymbol{R},t)]$ that contributes to the TDPES, is also invariant under gauge transformation

For any meaningful conclusions to be drawn from EF quantities, it is necessary to fix the gauge. While there exists a freedom, some choices might facilitate expressions more than others. A common choice for one-dimensional systems is to fix the gauge such that the TDVP is always zero. However, for higher dimensional systems, this is not a valid choice and therefore, it is often chosen that the phase of the nuclear wavefunction $[\mathcal{S}(\boldsymbol{R}, t)]$ is zero, which enforces a real, positive nuclear wavefunction at all time.

2.3.1 Photochemistry in an exact-factorisation picture

The EF provides a very different picture of photochemistry than the (post) BO picture does. The main difference is that now our electronic wavefunction is explicitly time-dependent. The concept of a nuclear wavefunction evolving on a set of static adiabatic electronic states, which are coupled only in regions of space where they are close in energy, can no longer be applied. Concepts such as conical intersections or the geometric phase do not exist in the EF framework.

In the EF, a *single* potential energy surface drives the dynamics. At this point, only a qualitive introduction will be provided on how the picture of photochemistry changes in the EF picture, but this will be discussed and analysed in greater detail in chapter 3 of this thesis. First, the focus will be generally on the concept of a single, time-dependent potential energy surface that drives the dynamics. In Fig. 2.2, the same steps of the same photochemical experiment are shown as in Fig. 2.1. The left column of the plots shows the $\epsilon_{\mathrm{BO}}(\boldsymbol{R}) = \langle \Phi(t;\boldsymbol{R})|\, \hat{H}_{\mathrm{BO}}(\boldsymbol{R})\, |\Phi(t;\boldsymbol{R})\rangle_{\boldsymbol{r}}$ contribution to the TDPES, in order to clarify the connection with the BO picture. The right column of the plots shows the full TDPES that guides the time-evolution of the nuclear wavefunction. Looking at the ϵ_{BO} contribution it becomes visible that throughout the parts of the photochemical process, where nonadiabatic effects play a minor role (*Initialisation, Photoproducts*), it takes the form of either of the adiabatic states, while during nonadiabatic processes (*Excitation, Evolution, Deactivation*), it provides a mean-field like potential. Looking at the full TDPES, it is revealed how the dynamics of the nuclear wavepacket are already encoded in the TDPES.[71–73] Initially, the wavepacket is fully in a harmonic like potential. During the *Excitation*, the TDPES develops a structure where a second, lower well is produced. During the *Evolution*, the wavepacket starts to split into two parts with one developing a node. The TDPES shows the reason: at the position of the node it shows a strong, nodal-like feature that separates the wavepacket. The splitting is caused by a significant step created

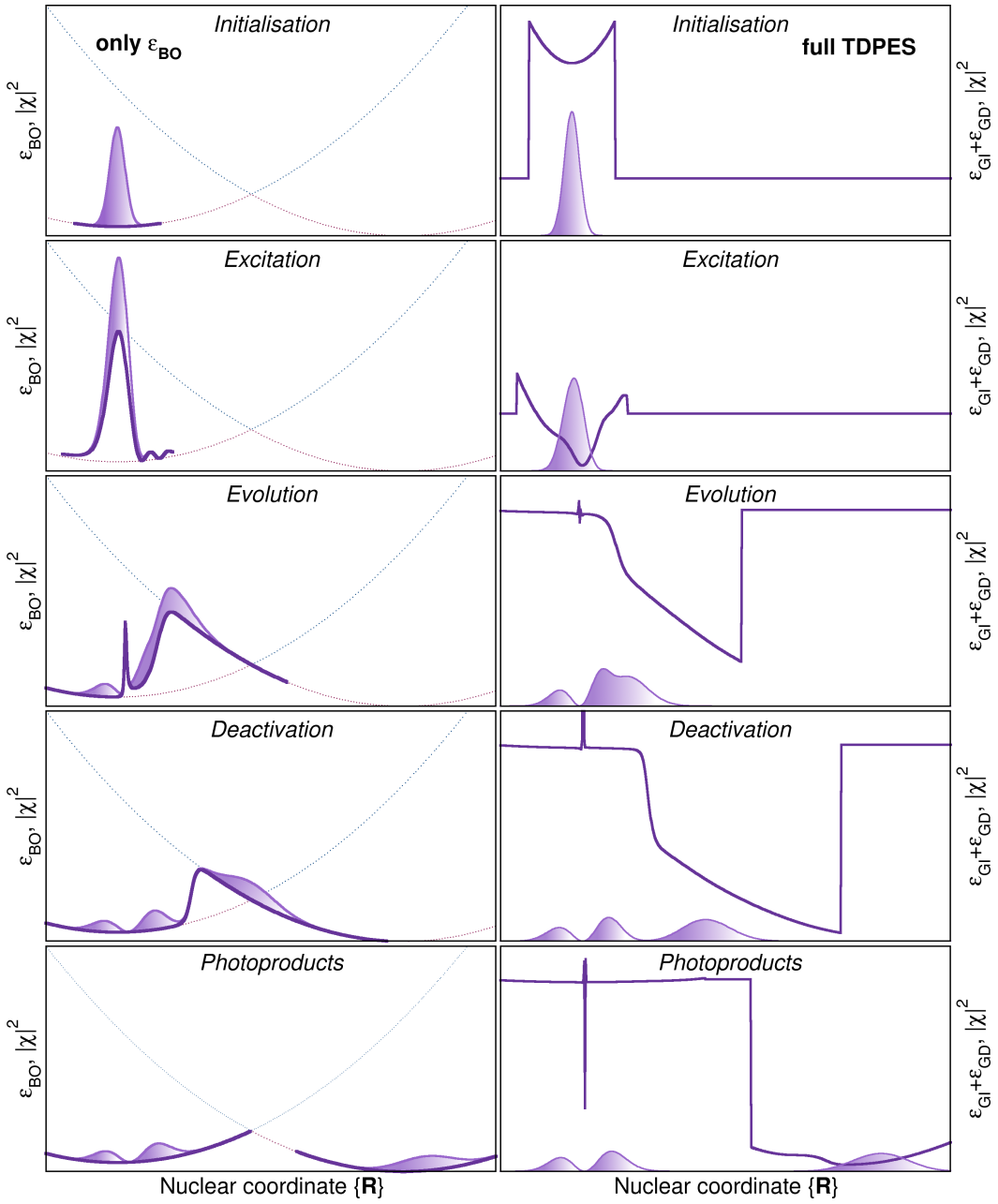

Fig. 2.2.: Schematic overview of the steps of an *in-silico* photochemical experiment within the EF picture. The BO term of the time-dependent potential energy surface is depicted in the left column of plots, while the right column shows the full TDPES.

in the TDPES. These same features continue to develop during the *Deactivation*. It can be seen that the change of adiabatic state, as observed in the BO picture, is in no way reflected in the TDPES. Finally, the *Photoproducts* have formed distinguished through a well-separated step in the potential.

The other driving potential is the time-dependent vector potential. It can be connected to the momentum in the nuclear TDSE and can be related to a nuclear velocity field.[74,75] This relation and the behaviour of the TDVP around conical intersections will be introduced in chapter 3 of this thesis.

2.4 Ingredients to simulate photochemistry

As this thesis focuses on the theory, methods and applications of *in-silico* photochemistry, the "ingredients" that are necessary to perform a photochemical experiment on the computer will be briefly introduced.

2.4.1 Initial conditions

A photochemical experiment usually starts with the system in the electronic ground state, either in its ground vibrational state or equilibrated at a specific temperature. Thus, for our nuclear dynamics method of choice, it is crucial that at time $t = 0$ the position and momentum distribution of the desired initial quantum state is well represented. The method of choice of initialising dynamics depends fully on the system studied and its size, and also in which way the nuclear dynamics will be described.

When using dynamics methods based on classically moving trajectories or trajectory basis functions (see sections 2.6.2 and 2.5.3 for details), the goal is to represent the initial wavefunction through individual trajectories. Therefore, it is necessary to map the ground-state wavefunction onto a phase-space.[76] For this quantum approach of phase-space sampling, one technique is the Wigner transform of the initial wavefunction in position (nuclear coordinates $\boldsymbol{R}$) and momentum (nuclear momenta $\boldsymbol{P}$) space.[77,78]

$$W(\boldsymbol{R},\boldsymbol{P}) = \frac{1}{(2\pi)^{3N_\mathrm{n}}}\int_{-\infty}^{\infty} \mathrm{d}\boldsymbol{s}\, \exp(i\boldsymbol{P}\boldsymbol{s})\left[\chi_{S_0,v_0}(\boldsymbol{R}-\boldsymbol{s}/2)\chi^*_{S_0,v_0}(\boldsymbol{R}+\boldsymbol{s}/2)\right] \tag{2.35}$$

χ_{S_0,v_0} is the (electronic and vibrational) ground-state nuclear wavefunction, and $\boldsymbol{s}$ is a displacement vector. However, for most molecular systems consisting of more than a few

degrees of freedom, calculating χ_{S_0,v_0} is not feasible and the initial conditions must be sampled from an approximate distribution.

A possible approximation, while conserving the quantum nature of the distribution, consists in approximating the Wigner distribution by expressing χ_{S_0,v_0} approximately as a product of the eigenstates of uncoupled harmonic oscillators.[78–80] This means that the ground-state nuclear wavefunction is approximated through uncoupled harmonic oscillators, where each frequency corresponds to the normal modes of the molecule. Then, the approximated Wigner distribution becomes a Husimi distribution:

$$W(\boldsymbol{R},\boldsymbol{P}) \approx \tilde{W}_{\mathrm{UHO}}(\boldsymbol{R},\boldsymbol{P}) = \frac{1}{(2\pi)^{3N_\mathrm{n}}} \prod_{\rho}^{3N_\mathrm{n}-6} \exp\left(-\boldsymbol{R}_\rho^2 \cdot 4\mu_\rho\omega_\rho\right) \exp\left(-\frac{\boldsymbol{P}_\rho^2}{\mu_\rho\omega_\rho}\right), \qquad (2.36)$$

where now positions and momenta are sampled independently from each normal mode $[\rho]$, with frequency $[\omega_\rho]$, and reduced mass, $[\mu_\rho]$. While this offers an easily accessible and widely used method to sample initial conditions, it is also connected to several approximations that need to be treated with care in some situations. The assumption of harmonic oscillators for all modes ignores any anharmonicities, which can create issues for low-frequency modes.[81] A second problem arises from the fact that a distribution of classical degrees of freedom is created with average classical energy approaching the $v = 0$ energy of the system. The classical modes can freely distribute energy between each other leading to a zero-point energy (ZPE) leakage, because quantum mechanically, each normal mode should contain at least the ZPE.[82]

Additionally, Wigner sampling is not always practical for very large systems as it requires a frequency calculation of all normal modes, especially when treating systems in an embedding scheme, where for example solvent molecules are explicitly included. In this case, an often-used approach is the classical sampling of positions and momenta from a thermal distribution.[79] This is usually done by running a long time *ab initio* molecular dynamics (or classical molecular dynamics for very large systems) at a chosen temperature in the ground electronic state and sampling the positions and momenta from this dynamics. However, this approach faces the drawback that the classical treatment at 300 K yields a distribution with average internal energy significantly lower than the ZPE of a molecule.[76,80]

These sampling methods show ways to generate initial conditions — positions and momenta — for classically moving trajectories (or trajectory basis functions). In contrast,

methods that directly simulate a quantum wavepacket, such as multiconfigurational time-dependent Hartree (MCTDH, see below), can directly express the ground-state wavepacket. Approximate methods, such as variational multiconfigurational Gaussians (vMCG, see below) also manage to directly express the ground-state wavepacket but dress it with unpopulated Gaussians. Due to their quantum propagation based on the Dirac-Frenkel variational principle, an appropriate initialisation is not trivial. However, when using quantum trajectories, the above approaches are all destined to fail. While for classical trajectories, nuclear positions and momenta can be regarded as independent variables, this is no more the case for quantum trajectories. Their nuclear position and momentum at each time step are related. Thus, while the initial positions can still be sampled randomly from the distribution of the initial wavefunction, the corresponding momentum at time $t = 0$ for quantum trajectories needs to be determined. One possible way is presented in the results of chapter 3.

2.4.2 Photoexcitation

Having found a good representation of the initial wavefunction, the next step to consider is the light absorption process. Light absorption can induce a transition between states with the energy difference corresponding to the wavelength of the light. For transitions between electronic states, this process happens at several orders of magnitude faster than nuclear motion, so the excitation is expected to happen "vertically" at the same nuclear configuration. Assuming an infinitely short laser pulse, the transition probability of the system from electronic state $|\Phi_I\rangle$ to electronic state $|\Phi_J\rangle$ is given by the oscillator strength $[f_{I\to J}]$. The oscillator strength indicates the number of electrons oscillating per spatial dimension during an electronic transition.[83,84] For a vertical excitation, i.e. assuming static nuclei during the excitation, the oscillator strength is related to the energy gap between the two states and the squared electronic transition dipole moment,

$$f_{I\to J}(\boldsymbol{R}) = \frac{2m_\mathrm{e}}{3\hbar^2}(\epsilon^{(J)}_\mathrm{BO}(\boldsymbol{R}) - \epsilon^{(I)}_{BO}(\boldsymbol{R}))\left|\langle\Phi_I|\,\hat{\boldsymbol{\mu}}^\mathrm{el}\,|\Phi_J\rangle_{\boldsymbol{r}}\right|^2 , \tag{2.37}$$

with the electronic transition dipole moment operator $[\hat{\boldsymbol{\mu}}^\mathrm{el}(\boldsymbol{r})]$. A commonly used approach to initialise nonadiabatic dynamics consists of sampling the ground-state wavefunction as described above, but then projecting this wavepacket directly on the excited states, meaning to assume vertical excitations, and begin the dynamics from there. A possible

way of choosing which initial conditions are excited to which state, is done stochastically based on a transition probability calculated as $f_{0\to J}/(\epsilon_{BO}^{(0)}(\boldsymbol{R}) - \epsilon_{\mathrm{BO}}^{(J)}(\boldsymbol{R}))^2$.[85]

Since this approach assumes an infinitely short laser pulse, it is an approximation that might not always well reflect the reality of a photochemical experiment, where lasers of finite length are used. Thus, one might choose to include explicitly the excitation process in the dynamics. This can be done by including the external field as an external, time-dependent potential term in the Hamiltonian (Eq. (2.2)). Within the dipole approximation, this term then is defined as

$$\hat{V}_{\mathrm{ext}}(\boldsymbol{r}, \boldsymbol{R}, t) = \hat{\boldsymbol{\mu}}(\boldsymbol{r}, \boldsymbol{R}) \cdot \boldsymbol{E}(t)\,. \tag{2.38}$$

Generally, an electric field is defined by its amplitude B_0, polarisation vector $\boldsymbol{\epsilon}^{\lambda}$, the envelope, determining the time-dependent pulse shape $\mathcal{F}(t)$ and the carrier frequency ω

$$\boldsymbol{E}(t) = \boldsymbol{\epsilon}^{\lambda} B_0 \mathcal{F}(t) \cos(\omega t)\,. \tag{2.39}$$

It should be noted that very often the excitation of interest, however, is not an ultrashort laser pulse, but natural sunlight, since many photochemical processes of interest occur in nature through the absorption of sunlight. A very recent work[86] proposed a framework for simulations of nonadiabatic dynamics (within a mixed-quantum classical approach, see Sec. 2.6) initiated by solar radiation. The schematic approach is to sample initial conditions from a broad blackbody spectrum, running the dynamics with conventional methods and considering the field and the realisation time in the ensemble averaging. As many photochemical processes naturally occurring on earth are initiated by sunlight, this approach presents an interesting starting point for future methodological developments.

2.4.3 Electronic structure

The previously derived set of equations of motion for nuclear amplitudes (Eq. (2.6)) makes it clear that a solution of the time-dependent Schrödinger equation in the adiabatic representation requires knowledge of the following information: electronic energies $[\epsilon_{\mathrm{BO}}^{(J)}(\boldsymbol{R})]$, nonadiabatic coupling vectors $[\boldsymbol{d}_{IJ}(\boldsymbol{R})]$, and, potentially, the gradients of the electronic energies and second-order nonadiabatic couplings $[D_{IJ}(\boldsymbol{R})]$, for and between all electronic states considered. These quantities can be obtained from a vast range of methods that aim

at approximating the time-independent electronic Schrödinger equation (Eq. (2.3)) with critical *caveats* and limitations existing for any of these electronic structure methods.[14]

Many electronic structure methods are based on recovering the deficiency of Hartree-Fock — used as a starting point — in the description of electronic correlations, the interaction among electrons in a quantum picture. In particular, this can be distinguished in dynamical correlation, given by instantaneous interaction among electrons, and static correlation, given by the contribution or more possible electronic configurations, missing in a single-reference method as Hartree-Fock.

Ideally, an electronic-structure method would (*i*) provide all the quantities needed for the nuclear dynamics, (*ii*) describe equally well the different electronic states of interest, (*iii*) be able to describe accurately the couplings between electronic states, (*iv*) be efficient if used in combination with on-the-fly (direct) dynamics (see below), (*v*) be robust enough when visiting different regions of the configuration space, (*vi*) be capable of describing (or at least detecting) multiconfigurational character of the electronic wavefunction(s).

Since the main focus of this thesis is on the nuclear dynamics aspect, only a brief list of the most commonly employed electronic-structure methods will be provided. The density functional theory approach (DFT) approach uses the three dimensional density as a replacement of the high dimensional electronic wavefunction, and is usually a very reliable method for ground-state energies. Its most commonly used extension to excited states, is linear-response time-dependent density functional theory (LR-TDDFT).[87] While LR-TDDFT usually offers a very good compromise with regard to computational efficiency, it has several, well known limitations:[†] It can fail to describe electronic states with a charge-transfer character[88–94], conical intersections between the ground and first excited state,[95] electronic states with double-excitation character,[95–99] and can formally only be used to describe ground-to-excited-state quantities like nonadiabatic coupling vectors[100–107] even if linear-response theory already offers a good approximation.[108] Different benchmarks of LR-TDDFT and exchange/correlation functionals for the description of electronic energies have been proposed in the literature[109], and with more specific benchmarks related to, for example, oscillator strengths[110] or nonadiabatic dynamics[111].

The algebraic diagrammatic construction of second-order (ADC(2)) can be seen as an extension of Møller-Plesset perturbation theory up to second-order to excited states. ADC(2), in its standard formulation, cannot be used to describe the coupling between the

[†]Note, that the crucial approximation leading to issues with a practical use of LR-TDDFT lies within the adiabatic approximation for the exchange-correlation kernel.

ground and first excited state but a spin-flip variant has recently been proposed.[112] The single configurational nature of the method is also its main deficiency, as it cannot recover static correlation. In addition, it has recently been shown that ADC(2) leads to artificial S_1/S_0 crossings for carbonyl-containing molecules upon C=O elongation.[113]

One very widely used method for various levels of nonadiabatic dynamics is state-averaged complete active space self-consistent field (SA-CASSCF). It allows a selection of an active space — a selection of occupied and unoccupied orbitals that are dominating the excited states of interest of the molecule — and constructs a full-configuration interaction wavefunction from the possible excitations within this active space. One of SA-CASSCF central issues is its neglect of dynamic correlation for practically accessible active spaces, leading to a potentially imbalanced description of electronic states.[114] In addition, in many cases a choice of active space might not be able to describe the potential equally well after the nuclear dynamics have been driven far from equilibrium. For example, if the molecule acquires high kinetic energy after deactivation, it might potentially form photoproducts with vastly different nuclear geometries which the initially chosen orbitals do not manage to describe.[115,116]

Multistate complete active space perturbation of second-order (MS-CASPT2) includes dynamic correlation effects through perturbation theory in a multistate approach. It is a highly accurate multiconfigurational method, but its computational cost might be the most limiting factor of its use for dynamics. The other problems, MS-CASPT2 might suffer from during dynamics are the appearance of intruder states and instabilities near conical intersections.[114,117] However, the latter has been partially overcome by the extended MS-CASPT2.[117] This list is far from complete but just highlights some of the common electronic structure methods for nonadiabatic dynamics used throughout the thesis.

An important distinction exists between different nonadiabatic dynamics techniques, depending on *when* the electronic-structure quantities are calculated. Some nuclear dynamics strategies require a *global* knowledge of the PESs and couplings over the entire nuclear configuration space considered. Therefore, such methods necessitate the precalculation of all electronic structure quantities *prior* to the actual nuclear propagation. They also often rely on the fitting of the electronic structure quantities to certain functional forms, or the use of a model Hamiltonian.[118,119] Contrarily, other nonadiabatic methods only require the electronic structure information to be known *locally*, allowing for *on-the-fly nonadiabatic dynamics* (also called "direct" or "*ab initio*" dynamics). In this case, the electronic quanti-

ties are computed at each nuclear propagation time step, or when required. The cost of electronic-structure calculations can become a serious bottleneck when performing on-the-fly excited-state dynamics of molecular systems. Recent developments could achieve a dramatic reduction of this computational cost, for instance by combining nonadiabatic dynamics with quantum chemical calculations accelerated on graphics processing units (GPUs)[120–123], or by employing machine (or deep-) learning strategies.[124,125]

2.4.4 Nuclear dynamics

Different strategies have been proposed to describe the nuclear dynamics of an electronically-excited molecule. A numerically exact solution of the TDSE is possible, but only in the framework of a subspace of the original infinite-dimensional Hilbert space. Hence, our problem is projected onto the space spanned by the N basis functions. The wavefunction, however, is usually not expressed in an orthogonal basis but rather represented as a discrete set of time-dependent complex amplitudes on a *grid*. These grid points can be understood as the coefficients of spatially localised basis functions, which in turn are related by a unitary transformation to a conventional basis of orthogonal functions and consequently, they span the same subspace and have analogous properties of orthogonality and completeness. This means, that in the so-called *standard method* the nuclear amplitudes, as well as the different operators, are evaluated on a numerical grid prior to the propagation of the nuclear wavefunction. The nuclear amplitudes are discretised by expressing each nuclear degree of freedom $(1, \ldots, N_{\text{dof}})$ in a basis of $(\mathcal{N}_1, \ldots, \mathcal{N}_{N_{\text{dof}}})$ time-independent functions. As mentioned, these time-independent functions are spatially localised and hence, close to δ-functions. The choice of the time-independent primitive basis functions depends usually on the problem on hand. However, assuming $\mathcal{N}$ basis functions in each of the N_{dof} degrees of freedom, the computational cost scales as $\mathcal{N}^{N_{\text{dof}}}$ limiting the application of the standard method to systems with usually no more than 10 degrees of freedom.

With the aim to allow the description of more degrees of freedom or larger molecules, the multiconfigurational time-dependent Hartree (MCTDH)[126–129] was proposed, which constitutes one of the most accurate methods. It uses time-dependent single-particle basis functions, which are in turn expanded in time-independent basis functions. Coupled equations of motion for the complex amplitudes and the single-particle functions are obtained through the Dirac-Frenkel variational principle. These basis functions constitute the grid on which the TDSE are solved. The basis functions can move and variationally

sample the space, which allows the treatment of more nuclear degrees of freedom as the number of basis functions is reduced. Consequently, in the limit of the single-particle functions covering the full space, there is no more time evolution of the basis and it converges towards the standard method.

Two very widely used strategies of nuclear dynamics will be discussed in great detail in sections 2.5 and 2.6. The first strategy consists in expressing the nuclear wavefunctions using a moving grid of basis functions (see Sec. 2.5), which can be derived from first principles and can be converged to the standard method. The other strategy, mixed quantum/classical dynamics (see Sec. 2.6), enforces a classical approximation for the nuclei, resulting in classical trajectories.

While all these methods mentioned are based on the BH representation of the wavefunction (cf. Eq. (2.5)), employing the classical nuclei approximation within the EF framework (cf. Eq. (2.21)) gives rise to the coupled-trajectory mixed quantum-classical (CT-MQC) algorithm.[27,130,131] The strategy of CT-MQC is to propagate classical trajectories simultaneously on a time-dependent vector potential.

Note that apart from these strategies, a variety of other formalisms has been developed to describe non-BO dynamics, such as semiclassical approaches,[19,132,133] including e.g. the mapping approach,[134,135] symmetrical quasi-classical windowing models,[136,137] quantum-classical Liouville approaches[138–140] and Bohmian dynamics.[32,141–143]

2.5 Nonadiabatic dynamics with Gaussian functions

In the following, strategies to perform nonadiabatic quantum dynamics in practice for molecular systems will be introduced. Starting from the exact expansion of the nuclear wavefunction in a Gaussian basis, various exact approaches will be introduced. The main focus will be on the framework of classically moving Gaussians and approximations to it that makes it feasible for full dimensional molecular systems.

2.5.1 Time-dependent Schrödinger equation in a Gaussian basis

Coming back to the BH expansion of the molecular wavefunction (Eq. (2.5)), the time-dependence can be fully grouped into the time-dependent nuclear expansion coefficients, i.e. the nuclear wavefunctions. Nonadiabatic dynamics, within the (post) BO picture, is centred around solving the nuclear equations of motion (Eq. (2.6)), but an exact solution

is not possible for molecules with more than a few degrees of freedom. Therefore, more practical strategies and carefully considered approximations become necessary.

One starting point for such frameworks is to expand the nuclear wavefunction $[\chi_J(\boldsymbol{R},t)]$, in a basis of $N_{\mathrm{TBF}}^{(J)}$ *trajectory basis functions* (TBFs) $[\{\tilde{\chi}_m^{(J)}\}_{m=1}^{N_{\mathrm{TBF}}^{(J)}}]$. These TBFs $[\tilde{\chi}_m^{(J)} = \tilde{\chi}_m^{(J)}\left(\boldsymbol{R}; a_{m,1}^{(J)}(t), ..., a_{m,N_p}^{(J)}(t)\right)]$, each depend on a set of N_p time-dependent parameters $[a_{m,N_p}^{(J)}(t)]$. This expansion can be inserted into the BH representation of the molecular wavefunction to express it within a multi-set formalism as

$$\Psi(\boldsymbol{r},\boldsymbol{R},t) = \sum_{J}^{\infty}\sum_{m}^{N_{\mathrm{TBF}}^{(J)}} C_m^{(J)}(t)\tilde{\chi}_m^{(J)}\left(\boldsymbol{R}; a_{m,1}^{(J)}(t), ..., a_{m,N_p}^{(J)}(t)\right)\Phi_J(\boldsymbol{r};\boldsymbol{R})\,. \tag{2.40}$$

Here, $C_m^{(J)}(t)$ are the complex, time-dependent (nuclear) expansion coefficients for state J. A common and practical choice of TBFs is to use moving, multidimensional, Gaussian functions,

$$\chi_J(\boldsymbol{R},t) = \sum_{m}^{N_{\mathrm{TBF}}^{(J)}} C_m^{(J)}(t)\tilde{\chi}_m^{(J)}\left(\boldsymbol{R}; \bar{\boldsymbol{R}}_m^{(J)}(t), \bar{\boldsymbol{P}}_m^{(J)}(t), \bar{\gamma}_m^{(J)}(t), \boldsymbol{\alpha}(t)\right), \tag{2.41}$$

where the (moving) Gaussians are defined by their (time-dependent) position $[\bar{\boldsymbol{R}}_m^{(J)}(t)]$ and momentum $[\bar{\boldsymbol{P}}_m^{(J)}(t)]$ at the centre, width $[\boldsymbol{\alpha}(t)]$ and a phase $[\bar{\gamma}_m^{(J)}(t)]$. Alternatively, a single-set formalism can be used. Then, the molecular wavefunction is expressed as

$$\Psi(\boldsymbol{r},\boldsymbol{R},t) = \sum_{m}^{N_{\mathrm{TBF}}^{(J)}}\left(\sum_{J}^{\infty} C_J^m(t)\Phi_J(\boldsymbol{r};\boldsymbol{R})\right)\tilde{\chi}_m\left(\boldsymbol{R}; a_{m,1}(t), ..., a_{m,N_p}(t)\right). \tag{2.42}$$

It is noted that the single-set formalism can also use a sum of normalised linear combination of electronic states (Ehrenfest configurations), and introduce an amplitude to weight the nuclear contributions. In both, multi- and single-set formalism[‡], each $3N_{\mathrm{n}}$-dimensional TBF is defined as a product of $3N_{\mathrm{n}}$ one-dimensional Gaussians as

$$\tilde{\chi}_m^{(J)} = e^{\frac{i}{\hbar}\bar{\gamma}_m^{(J)}(t)}\prod_{\rho}^{3N_{\mathrm{n}}}\tilde{\chi}_{m\rho}^{(J)}\left(R_\rho; \bar{R}_{m\rho}^{(J)}(t), \bar{P}_{m\rho}^{(J)}(t), \bar{\gamma}_m^{(J)}(t), \alpha_\rho(t)\right) \tag{2.43}$$

$$\tilde{\chi}_{m\rho}^{(J)} = \left(\frac{2\alpha_\rho}{\pi}\right)^{1/4}\exp\left[-\alpha_\rho(t)\left(R_\rho - \bar{R}_{m\rho}^{(J)}(t)\right)^2 + \frac{i}{\hbar}\bar{P}_{m\rho}^{(J)}(t)\left(R_\rho - \bar{R}_{m\rho}^{(J)}(t)\right)\right]. \tag{2.44}$$

[‡]It should however be noted that in the single-set formalism, there is not state dependence on the definition of the TBFs.

If this Gaussian expansion of the BH representation is inserted into the TDSE (Eq. (2.1)), (after left multiplication by $\left(\tilde{\chi}_k^{(I)}\left(\boldsymbol{R};\bar{\boldsymbol{R}}_k^{(I)}(t),\bar{\boldsymbol{P}}_k^{(I)}(t),\bar{\gamma}_k^{(I)}(t),\boldsymbol{\alpha}(t)\right)\Phi_I(\boldsymbol{r};\boldsymbol{R})\right)^*$ and integration over all electronic [$\boldsymbol{r}$] and nuclear [$\boldsymbol{R}$] coordinates) one obtains a set of equations of motions for the complex expansion coefficients

$$\frac{\mathrm{d}\mathbf{C}^I}{\mathrm{d}t} = -\frac{i}{\hbar}\mathbf{S}_{II}^{-1}\left[(\mathbf{H}_{II} - i\hbar\dot{\mathbf{S}}_{II})\mathbf{C}^I + \sum_{J\neq I}^{\infty}\mathbf{H}_{IJ}\mathbf{C}^J\right] . \tag{2.45}$$

Here, $\mathbf{S}_{II}$ is the overlap matrix between two TBFs with elements

$$S_{km}^{II} = \langle\tilde{\chi}_k^{(I)}|\tilde{\chi}_m^{(J)}\rangle_{\boldsymbol{R}} . \tag{2.46}$$

$\mathbf{H}_{II}$ and $\mathbf{H}_{IJ}$ are intra- and interstate Hamiltonian matrices:

$$H_{km}^{IJ} = \langle\tilde{\chi}_k^{(I)}\Phi_I|\,\hat{H}_{\mathrm{m}}\,|\Phi_J\tilde{\chi}_m^{(J)}\rangle_{\boldsymbol{r},\boldsymbol{R}} . \tag{2.47}$$

These intra- and interstate Hamiltonian matrix elements are the crucial elements that couple the TBFs with each other, on the same and different electronic states.

The definition of the TBFs, the description of the time evolution of their parameters as well as the computation (and possible approximation) of the Hamiltonian matrix elements, establish various approaches for Gaussian based nonadiabatic quantum molecular dynamics.[§]

Under the condition that the TBFs closely follow the evolution of the nuclear wave packet, the number of TBFs used can be greatly reduced. Hence, it is necessary to find equations of motion for the TBFs which provide proper support for the nuclear wavefunctions at a reasonable computational cost. Following the idea of MCTDH, the equations of motion for the basis functions can be determined from the Dirac-Frenkel variational principle defining the framework of variational Multiconfigurational Gaussians (vMCG).[144–146] Through the quantum propagation of the Gaussian functions, a good representation of the nuclear wavefunction is ensured and the necessary number of Gaussian functions is reduced. In principle, the time-dependent variational principle also allows propagation of the width of the Gaussians however this usually introduces instabilities in the dynamics and usually

[§]One should note, however, that up to this point no approximations were introduced, so independent of the way to treat the time evolution of the Gaussians, in the limit of enough Gaussian functions and an exact evaluation of the Hamiltonian matrix elements, all Gaussian based methods converge to the exact solution of the TDSE.

frozen Gaussians are used in vMCG.[144] The better description offered by the quantum propagation comes at the cost of highly coupled equations of motion that increase the complexity (and hence computational cost) of the dynamics of the TBFs.

In multiconfigurational Ehrenfest (MCE), the Gaussian functions with frozen width are propagated classically in the single-set formalism, following Ehrenfest trajectories.[147–149] As a result, the TBFs are propagated on an averaged potential energy surface in regions of strong nonadiabaticity, composed of a linear combination of the adiabatic surfaces weighted by electronic coefficients.

Alternatively, the method called full multiple spawning (FMS) proposes to propagate the Gaussian functions classically on adiabatic PESs in the multi-set formalism.[150–152] However, the number of basis functions can be expanded when nonadiabatic regions are encountered during the dynamics by using a spawning algorithm. While all these TBF based methods are *in principle* exact within the limit of the basis set, approximations have been introduced for all of them in order to be able to simulate the nonadiabatic dynamics of molecules on the fly, resulting in direct-dynamics vMCG, *ab initio* MCE and *ab initio* multiple spawning (AIMS). In an effort to take the best of both ansätzen, MCE and multiple spawning have been combined yielding the multiple cloning method,[153] where an Ehrenfest configuration is cloned into two, of which one is guided by a single PES and the other follows the mean-field potential of the remaining states.

The on-the-fly formulation of FMS, *ab initio* multiple spawning (AIMS) and its derivations makes the dynamics of medium and larger sized molecules accessible. This framework has been extensively tested and used throughout the work of this thesis. Therefore, in this section, the working equations starting from the in-principle exact FMS and showing the stepwise approximations to reach AIMS and further approximations to make it an even more practical method, will be introduced.

2.5.2 Full multiple spawning

Full multiple spawning expresses the nuclear wavefunction in a basis of Gaussian functions in the form of Eqs. (2.43) and (2.44), with the difference that it employs Heller's ansatz of *frozen* Gaussians,[154–157] i.e. the width of the Gaussian $[\boldsymbol{\alpha}(t) = \boldsymbol{\alpha}]$ is fixed and no more time-dependent. The most characteristic feature of the method is however that the size of the Gaussian basis is time-dependent $[N_{\mathrm{TBF}}^{(J)}(t)]$, since it can be extended through the

so-called *spawning* algorithm, whenever necessary (as will be detailed below).[150,158] The nuclear wavefunction is expanded as

$$\chi_J(\boldsymbol{R},t) = \sum_{m}^{N_{\mathrm{TBF}}^{(J)}(t)} C_m^{(J)}(t)\,\tilde{\chi}_m^{(J)}\left(\boldsymbol{R};\bar{\boldsymbol{R}}_m^{(J)}(t),\bar{\boldsymbol{P}}_m^{(J)}(t),\bar{\gamma}_m^{(J)}(t),\boldsymbol{\alpha}\right). \tag{2.48}$$

As mentioned above, the TBFs in FMS follow classical trajectories. The TBF $[\tilde{\chi}_m^{(J)}]$ on electronic state J evolves adiabatically on the PES given by $\epsilon_{\mathrm{BO}}^{(J)}(\boldsymbol{R})$, and its positions and momenta are propagated using Hamilton's equations of motion.

$$\frac{\mathrm{d}\bar{R}_{m\rho}^{(J)}(t)}{\mathrm{d}t} = \frac{\bar{P}_{m\rho}^{(J)}(t)}{M_\rho} \tag{2.49}$$

$$\frac{\mathrm{d}\bar{P}_{m\rho}^{(J)}(t)}{\mathrm{d}t} = -\left.\frac{\partial\epsilon_{\mathrm{BO}}^{(J)}(\boldsymbol{R})}{\partial R_{m\rho}}\right|_{R_{m\rho}=\bar{R}_{m\rho}^{(J)}(t)} \tag{2.50}$$

The time evolution of the phase $[\bar{\gamma}_m^{(J)}(t)]$ is obtained, based on semiclassical arguments, by integrating the classical Lagrangian.[79]

$$\frac{\mathrm{d}\bar{\gamma}_m^{(J)}(t)}{\mathrm{d}t} = \sum_{\rho}^{3N_{\mathrm{n}}} \frac{\left(\bar{P}_{m\rho}^{(J)}(t)\right)^2}{2M_\rho} - \epsilon_{\mathrm{BO}}^{(J)}\left(\bar{\boldsymbol{R}}_m^{(J)}(t)\right) \tag{2.51}$$

For the evaluation of the complex expansion coefficients, the same set of equations of motions is obtained as shown above in Eq. (2.45).

Spawning algorithm

An important aspect of FMS is the time-dependence of the size of the basis set. At time $t = 0$, the initial wavefunction is represented by a linear combination of N_{ini} coupled TBFs, the *parent* TBFs. Each of these parent TBFs has the possibility of creating new, *child* TBFs over time. To express this explicitly, one can rewrite the wavefunction in the BH representation as[79,159]

$$\begin{aligned}\Psi(\boldsymbol{r},\boldsymbol{R},t) &= \sum_{\beta}^{N_{\mathrm{ini}}} \tilde{\Psi}_\beta(\boldsymbol{r},\boldsymbol{R},t) \\ &= \sum_{\beta}^{N_{\mathrm{ini}}}\sum_{J}^{\infty}\sum_{m}^{N_\beta^J(t)} C_{m\beta}^{(J)}(t)\,\tilde{\chi}_{m\beta}^{(J)}\left(\boldsymbol{R};\bar{\boldsymbol{R}}_{m\beta}^{(J)}(t),\bar{\boldsymbol{P}}_{m\beta}^{(J)}(t),\bar{\gamma}_{m\beta}^{(J)}(t),\boldsymbol{\alpha}\right)\Phi_J(\boldsymbol{r};\boldsymbol{R}).\end{aligned} \tag{2.52}$$

This underlines the fact that in FMS all the initial parent TBFs are coupled from the beginning and will be coupled to all the additional children TBFs created throughout the dynamics.

The important question arising at this point is: When and how are basis functions added to the dynamics? From Eq. (2.45) it can be seen that nonadiabatic population transfer is mediated by the interstate couplings between TBFs. Therefore, whenever a TBF encounters a region of high nonadiabatic coupling to another state, a new TBF is created on the other state. The most commonly used spawning algorithm[160] is schematically shown in figure 2.3. Throughout the dynamics, every TBF monitors the strength of the nonadiabatic coupling (the effective coupling, $[T_{IJ}^{\text{eff}}(\boldsymbol{R})]$ between the state it evolves in and all other states. The coupling strength is most straightforwardly evaluated as the absolute value of the nonadiabatic coupling vector at the position of the centre of the TBF, so $T_{IJ}^{\text{eff}}(\bar{\boldsymbol{R}}_m)$ is defined as

$$T_{IJ}^{\text{eff}}(\bar{\boldsymbol{R}}_m) = |\boldsymbol{d}_{IJ}(\bar{\boldsymbol{R}}_m)| \,. \tag{2.53}$$

An alternative criterion that is commonly used monitors the projection of the NACV on the classical velocity of the TBF:

$$T_{IJ}^{\text{eff}}(\bar{\boldsymbol{R}}_m) = |\boldsymbol{d}_{IJ}(\bar{\boldsymbol{R}}_m) \cdot \dot{\bar{\boldsymbol{R}}}_m| \,. \tag{2.54}$$

As soon as one TBF encounters a coupling that exceeds a predefined threshold, the propagation of the complex coefficients (of all TBFs in the dynamics) is stopped. At this time, t_{entry}, the respective TBF enters the *spawning mode* (see centre panels in figure 2.3): only this TBF is propagated forward until it reaches the point where T_{IJ}^{eff} is maximal. At this point, a new child TBF is spawned on the new state if certain criteria are fulfilled:[161–163] i) the energy can be conserved, i.e. the kinetic energy is large enough to compensate for the increase in potential energy, ii) the child TBF overlaps sufficiently with the parent TBF and iii) the child TBF does not overlap too much with other TBFs on the same state. Under these conditions, the successful spawn is created as a TBF with the identical properties as the parent, but its momentum is rescaled for energy conservation and the complex coefficient are set to zero. The child TBF is propagated backwards in time, until $t = t_{\text{entry}}$. At this point, the spawning mode is terminated and the normal FMS dynamics can resume with the extended basis: now, the equations of motion include the amplitude of the new child TBF and in the subsequent dynamics it can receive and transfer amplitude from and

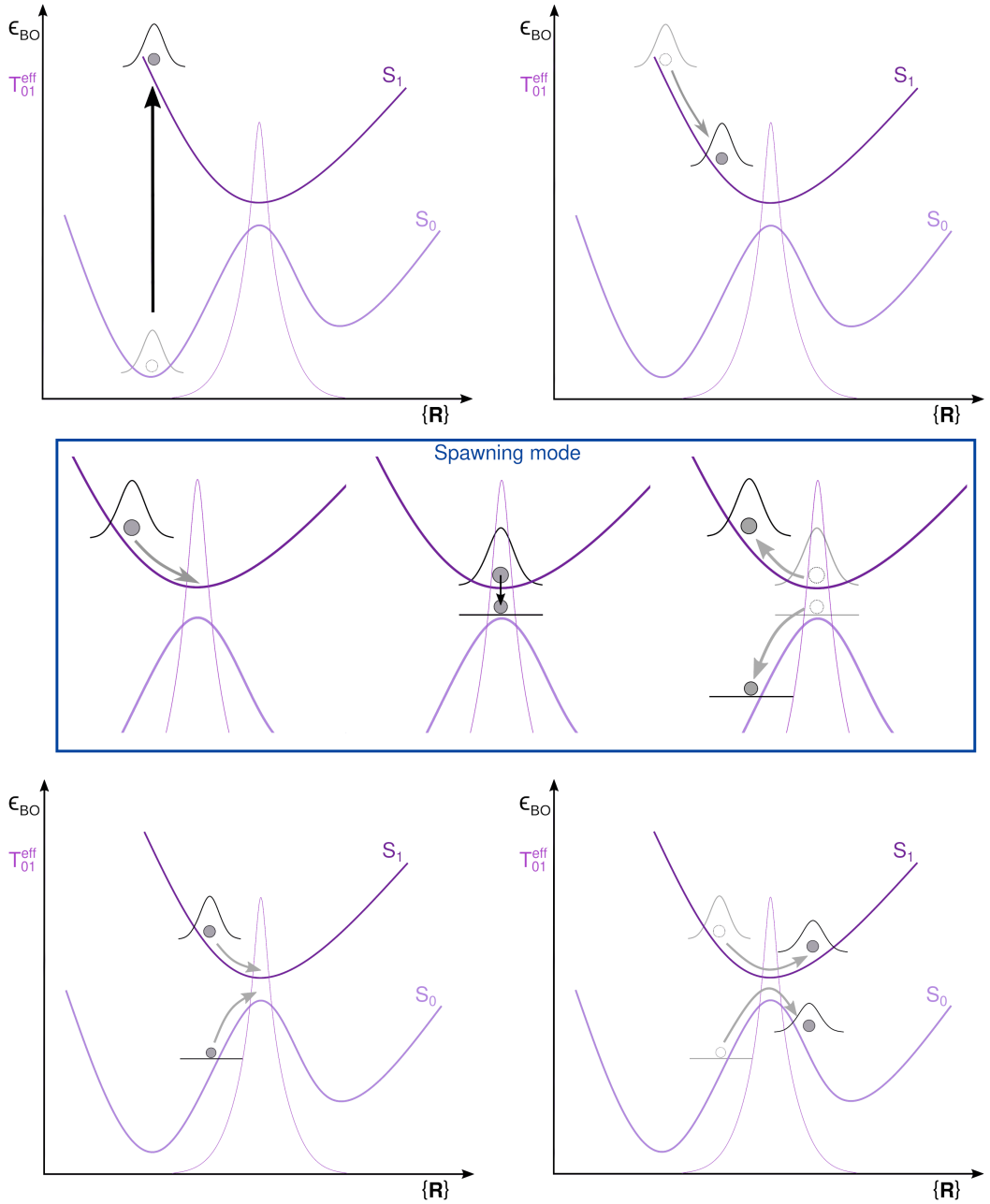

Fig. 2.3.: Schematic illustration of a spawning process in FMS. Top plots: photoexcitation and evolution of the TBF until the effective coupling succeeds a threshold. Middle plots: Spawning mode - forward propagation, spawning, backward propagation. Bottom plots: Forward propagation and exchange of amplitude between parent and child TBF.

to all other TBFs included. This spawning algorithm ensures that the parent and child TBF have a maximal overlap at the point where the effective coupling between their respective states becomes maximal.

Hamiltonian matrix elements

Having established how the Gaussians in FMS are moving and being created, their couplings between each other will be investigated closer.[¶]

Looking at the Hamiltonian matrix elements in more detail, for FMS there are two main types of couplings: the *intrastate* coupling for TBFs in the same electronic state, so for $I = J\ \forall k, m$; and the *interstate* couplings for TBFs in different electronic states, so for $I \neq J\ \forall k, m$. For an intrastate coupling, the Hamiltonian matrix element $[\left(H_{km}^{JJ}\right)_{\mathrm{FMS}}]$ between two TBFs, k and m, evolving in the same electronic state J, becomes[14,79,150]

$$\begin{aligned}\left(H_{km}^{JJ}\right)_{\mathrm{FMS}} = \left(\langle \tilde{\chi}_k^{(J)} \Phi_J | \, \hat{H}_{\mathrm{m}} \, | \Phi_J \tilde{\chi}_m^{(J)} \rangle_{\boldsymbol{r},\boldsymbol{R}}\right)_{\mathrm{FMS}} &= -\sum_{\rho}^{3N_{\mathrm{n}}} \frac{\hbar^2}{2M_\rho} \langle \tilde{\chi}_k^{(J)} | \, \partial_{R_\rho}^2 \, | \tilde{\chi}_m^{(J)} \rangle_{\boldsymbol{R}} \\ &+ \langle \tilde{\chi}_k^{(J)} | \, \epsilon_{\mathrm{BO}}^{(J)} \, | \tilde{\chi}_m^{(J)} \rangle_{\boldsymbol{R}} - \sum_{\rho}^{3N_{\mathrm{n}}} \frac{\hbar^2}{2M_\rho} \langle \tilde{\chi}_k^{(J)} | \, D_{JJ}^{\rho} \, | \tilde{\chi}_m^{(J)} \rangle_{\boldsymbol{R}} \, . \end{aligned} \tag{2.55}$$

The terms on the right-hand side encode the contributions of the nuclear kinetic energy operator, the electronic energy, and the DBOC introduced earlier. An interstate coupling is characterised by a matrix element $[\left(H_{km}^{IJ}\right)_{\mathrm{FMS}}]$, where the two TBFs, k and m, are evolving in different electronic states, I and J, as

$$\begin{aligned}\left(H_{km}^{IJ}\right)_{\mathrm{FMS}} = \left(\langle \tilde{\chi}_k^{(I)} \Phi_I | \, \hat{H}_{\mathrm{m}} \, | \Phi_J \tilde{\chi}_m^{(J)} \rangle_{\boldsymbol{r},\boldsymbol{R}}\right)_{\mathrm{FMS}} &= -\sum_{\rho}^{3N_{\mathrm{n}}} \frac{\hbar^2}{2M_\rho} \langle \tilde{\chi}_k^{(I)} | \, d_{IJ}^{\rho} \, | \tilde{\chi}_m^{(J)} \rangle_{\boldsymbol{R}} \\ &- \sum_{\rho}^{3N_{\mathrm{n}}} \frac{\hbar^2}{2M_\rho} \langle \tilde{\chi}_k^{(I)} | \, D_{IJ}^{\rho} \, | \tilde{\chi}_m^{(J)} \rangle_{\boldsymbol{R}} \, . \end{aligned} \tag{2.56}$$

The right-hand side of this equation shows that the non-BO coupling between two TBFs is mediated by the first-order NACVs and the second-order NACs. These formally exact Hamiltonian matrix elements given above include the integrations of electronic-structure quantities over the nuclear coordinates. This requires that electronic-structure quantities —- electronic energies, NACVs, DBOCs, and NACs — should be known over the full nuclear

[¶]For simplicity, there will be no differentiation of the different branches of TBFs as this was mainly a tool to visualise their origin, but does not have a meaning in FMS, since all TBFs are coupled equally, so it will be considered that $\tilde{\chi}_{k\beta'}^{(I)} = \tilde{\chi}_k^{(I)}$ and $\tilde{\chi}_{m\beta}^{(J)} = \tilde{\chi}_m^{(J)}$.

configuration space. This requirement dramatically limits the applicability of FMS to molecular systems, as it does not allow for on-the-fly dynamics.

Therefore, for the study of the dynamics of molecules in their full dimensionality, it is necessary to rely on controlled approximations to the couplings between the TBFs, which leads to the framework of AIMS.

2.5.3 *Ab initio* multiple spawning

AIMS introduces two main approximations to the way the TBFs are coupled throughout the dynamics to make it accessible for larger molecules: the *independent first generation approximation* (IFGA) and the *saddle point approximation of order zero* (SPA0).

Independent first generation approximation

As described above, in FMS, the initial wavefunction is prepared as N_{ini} coupled initial Gaussian functions, that mimic the initial nuclear wavepacket. Assuming the dynamics of a molecule, a high-dimensional system, after photoexcitation, the nuclear wavepacket is expected to spread rapidly in phase space. Therefore, the initial TBFs rapidly move away from each other and become uncoupled. Subsequently each initial TBF evolves independently and create new TBFs in its branch.

Within AIMS, the so-called IFGA exploits this behaviour: the initial parent TBFs are considered uncoupled from the very beginning of the dynamics.[159,161] This approximation greatly simplifies the dynamics and its initialisation. Within the IFGA, independent initial conditions for each parent TBF can simply be sampled from a Wigner distribution (cf. Sec. 2.4.1) and subsequently be run independently. Consequently, it is also assumed that not only are the initial TBFs evolving independently of each other but also all children TBFs in a certain branch β are independent of any TBFs in any other branch β'. At the end of the dynamics, all observables, as well as the populations of the electronic states, can be reconstructed as an incoherent sum over all initial conditions.

The IFGA provides two great advantages in the practical application of AIMS dynamics: 1) As the initial conditions are each run independently, it allows for a higher degree of parallelisation. 2) Convergence of the dynamics with respect to the number of initial conditions can be determined on the fly. One can add additional runs of initial conditions until convergence is reached.

Saddle-point approximation

The second approximation, the saddle-point approximation directly acts on the Hamiltonian matrix elements. As mentioned before, an exact evaluation of the matrix elements requires integration of electronic energies, NACVs, NACs and DBOCs over the whole nuclear configuration space and therefore requires precomputed potentials. This makes an application for molecules in their full dimensionality impractical and on-the-fly dynamics impossible. Therefore, in AIMS, these matrix elements are approximated. The first approximation is to neglect the NACs and DBOCs, i.e. all $D_{IJ}(\boldsymbol{R})$ and $D_{JJ}(\boldsymbol{R})$ terms, because of their small size.

Additionally, the remaining contributions — the electronic energies $[\epsilon_{\mathrm{BO}}^{(J)}(\boldsymbol{R})]$ and NACVs $[\boldsymbol{d}_{IJ}(\boldsymbol{R})]$ — are evaluated locally at the positions of the TBFs, by introducing the so-called saddle-point approximation of order zero (SPA0). Thanks to the characteristic that TBFs are spatially localised, one can see that the product of two Gaussians yields another Gaussian at the centroid position between the two original Gaussians. This is exploited in the SPA0, as the electronic energy and the NACV are Taylor expanded around this centroid position and the resulting integral can then be solved analytically.[160,161,164,165] Looking for example at the expansion of the electronic energy $[\epsilon_{\mathrm{BO}}^{(J)}(\boldsymbol{R})]$ between two TBFs, $[\tilde{\chi}_k^{(J)}(\boldsymbol{R},t)$ and $\tilde{\chi}_m^{(J)}(\boldsymbol{R},t)]$, around the centroid position $[\bar{\boldsymbol{R}}_{km} = (\bar{\boldsymbol{R}}_k + \bar{\boldsymbol{R}}_m)/2]$, one would obtain

$$\begin{aligned}\epsilon_{\mathrm{BO}}^{(J)}(\boldsymbol{R}) = \epsilon_{\mathrm{BO}}^{(J)}(\bar{\boldsymbol{R}}_{km}) &+ \sum_{\rho}^{3N_\mathrm{n}} (R_\rho - \bar{R}_{km,\rho}) \left.\frac{\partial \epsilon_{\mathrm{BO}}^{(J)}(\boldsymbol{R})}{\partial R_\rho}\right|_{R_\rho = \bar{R}_{km,\rho}} \\ &+ \frac{1}{2} \sum_{\rho,\rho'}^{3N_\mathrm{n}} (R_\rho - \bar{R}_{km,\rho}) \left.\frac{\partial^2 \epsilon_{\mathrm{BO}}^{(J)}(\boldsymbol{R})}{\partial R_\rho \partial R_{\rho'}}\right|_{R_\rho = \bar{R}_{km,\rho}, R_{\rho'} = \bar{R}_{km,\rho'}} (R_{\rho'} - \bar{R}_{km,\rho'}) + \cdots . \end{aligned} \tag{2.57}$$

In AIMS, the Taylor series is truncated after the zeroth order term, (thus, the name, SPA0), and the intrastate coupling elements become

$$\left(\langle \tilde{\chi}_k^{(J)} \Phi_J | \, \hat{H}_\mathrm{m} \, | \Phi_J \tilde{\chi}_m^{(J)} \rangle_{\boldsymbol{r},\boldsymbol{R}} \right)_{\mathrm{AIMS}}^{\mathrm{SPA0}} = - \sum_{\rho}^{3N_\mathrm{n}} \frac{\hbar^2}{2M_\rho} \langle \tilde{\chi}_k^{(J)} | \, \partial_{R_\rho}^2 \, | \tilde{\chi}_m^{(J)} \rangle_{\boldsymbol{R}} + \epsilon_{\mathrm{BO}}^{(J)}(\bar{\boldsymbol{R}}_{km}) \, \langle \tilde{\chi}_k^{(J)} | \tilde{\chi}_m^{(J)} \rangle \ . \tag{2.58}$$

For the interstate couplings, the NACV is expanded within the SPA0 to become

$$\left(\langle \tilde{\chi}_k^{(I)} \Phi_I | \, \hat{H}_\mathrm{m} \, | \Phi_J \tilde{\chi}_m^{(J)} \rangle_{\boldsymbol{r},\boldsymbol{R}} \right)_{\mathrm{AIMS}}^{\mathrm{SPA0}} = - \sum_{\rho}^{3N_\mathrm{n}} \frac{\hbar^2}{M_\rho} d_{IJ}^{\rho}(\bar{\boldsymbol{R}}_{km}) \, \langle \tilde{\chi}_k^{(I)} | \, \partial_{R_\rho} \, | \tilde{\chi}_m^{(J)} \rangle_{\boldsymbol{R}} \ . \tag{2.59}$$

The SPA0 addresses elegantly the complexity arising from the $\boldsymbol{R}$-dependence of the electronic energies and NACVs: It allows to simply calculate the Hamiltonian matrix elements by performing at each time step a single point calculation at the position of each TBF and at the centroid position between each pair of TBFs, and with that to evaluate the complex coefficients on the fly.

An important consideration has been swept under the carpet in the presentation of the AIMS approximations above: neglecting the NACs in the interstate matrix elements should break the hermiticity of the Hamiltonian [$\mathbf{H}_{IJ} \neq \mathbf{H}_{JI}$].[166] This is a result of the NACVs being anti-Hermitian [$\boldsymbol{d}_{IJ}(\boldsymbol{R}) = -\boldsymbol{d}_{JI}(\boldsymbol{R})$], and would have the dramatic consequence that AIMS dynamics should not conserve the norm of the wavefunction. Interestingly, the use of the SPA0 compensates for the neglect of the NACs.[79] Looking closely at the definition of the AIMS interstate Hamiltonian matrix elements in the SPA0 (Eq. (2.59)), one can see that the AIMS Hamiltonian *is* Hermitian, as $\boldsymbol{d}_{IJ}(\bar{\boldsymbol{R}}_{km}) = -\boldsymbol{d}_{JI}(\bar{\boldsymbol{R}}_{km})$ and $\langle \tilde{\chi}_k^{(I)} | \nabla_{\boldsymbol{R}} | \tilde{\chi}_m^{(J)} \rangle_{\boldsymbol{R}} = -\langle \tilde{\chi}_m^{(J)} | \nabla_{\boldsymbol{R}} | \tilde{\chi}_k^{(I)} \rangle_{\boldsymbol{R}}$. This compensation between the SPA0 and the neglect of the NACs explains the Hermitian nature of the AIMS Hamiltonian and its norm-conserving dynamics. However, this observation also indicates that one needs to be extremely careful when trying to modify or improve the interstate Hamiltonian matrix elements in AIMS to preserve its Hermitian nature, as will be exemplified in the following.

Ab initio multiple spawning beyond the zeroth-order saddle point approximation

Improving the quality of the AIMS matrix elements beyond the SPA0 appears to be a trivial task: one can simply include higher-order terms in the Taylor expansion discussed above. In the following, it will be shown that care has to be taken with the interstate couplings.[55]

Applying the saddle-point approximation to first order (SPA1) to the intrastate Hamiltonian matrix elements is straightforward as it only requires the addition of the first-order term of the Taylor expansion for the electronic energy – the nuclear gradient – evaluated at

the centroid position of the two TBFs considered. The general expression for the intrastate couplings is then

$$\left(\langle\tilde{\chi}_k^{(J)}\Phi_J|\,\hat{H}_{\rm m}\,|\Phi_J\tilde{\chi}_m^{(J)}\rangle_{\boldsymbol{r},\boldsymbol{R}}\right)_{\rm AIMS}^{\rm SPA1} = -\sum_{\rho}^{3N_{\rm n}}\frac{\hbar^2}{2M_\rho}\,\langle\tilde{\chi}_k^{(J)}|\,\partial_{R_\rho}^2\,|\tilde{\chi}_m^{(J)}\rangle_{\boldsymbol{R}} + \epsilon_{\rm BO}^{(J)}(\bar{\boldsymbol{R}}_{km})\,\langle\tilde{\chi}_k^{(J)}|\tilde{\chi}_m^{(J)}\rangle_{\boldsymbol{R}} + \sum_{\rho}^{3N_{\rm n}}\left.\frac{\partial\epsilon_{\rm BO}^{(J)}(\boldsymbol{R})}{\partial R_\rho}\right|_{R_\rho=\bar{R}_{km,\rho}}\langle\tilde{\chi}_k^{(J)}|\,(R_\rho-\bar{R}_{km,\rho})\,|\tilde{\chi}_m^{(J)}\rangle_{\boldsymbol{R}}\,, \tag{2.60}$$

where the evaluation of the last term on the right-hand side only requires the calculation of a nuclear gradient of the electronic energy for state J at the centroid position.

Deriving the SPA1 for the interstate Hamiltonian matrix elements is substantially more challenging for two reasons. The first issue comes from the fact that adding the first-order term of the Taylor expansion for these matrix elements implies the evaluation of the Jacobian of the NACVs – a quantity not commonly available in electronic-structure packages. The Jacobian of the NACVs $[\mathbf{J}_{\boldsymbol{d}_{IJ}}(\boldsymbol{R})]$ is defined as

$$\mathbf{J}_{\boldsymbol{d}_{IJ}}(\boldsymbol{R}) = \frac{\partial}{\partial\boldsymbol{R}}\boldsymbol{d}_{IJ}(\boldsymbol{R}) = \begin{pmatrix}\frac{\partial}{\partial\boldsymbol{R}}d_{IJ}^1(\boldsymbol{R})\\ \vdots\\ \frac{\partial}{\partial\boldsymbol{R}}d_{IJ}^{3N_{\rm n}}(\boldsymbol{R})\end{pmatrix} = \begin{pmatrix}\frac{\partial}{\partial R_1}d_{IJ}^1(\boldsymbol{R}) & \cdots & \frac{\partial}{\partial R_{3N_{\rm n}}}d_{IJ}^1(\boldsymbol{R})\\ \vdots & \ddots & \vdots\\ \frac{\partial}{\partial R_1}d_{IJ}^{3N_{\rm n}}(\boldsymbol{R}) & \cdots & \frac{\partial}{\partial R_{3N_{\rm n}}}d_{IJ}^{3N_{\rm n}}(\boldsymbol{R})\end{pmatrix}. \tag{2.61}$$

(The explicit form of the Jacobian for the NACVs for a two-state two-dimensional case is given in the appendix A.) Considering that one can obtain $\mathbf{J}_{\boldsymbol{d}_{IJ}}(\boldsymbol{R})$, the interstate couplings within the SPA1 would be given by

$$\left(\langle\tilde{\chi}_k^{(I)}\Phi_I|\,\hat{H}_{\rm m}\,|\Phi_J\tilde{\chi}_m^{(J)}\rangle_{\boldsymbol{r},\boldsymbol{R}}\right)_{\rm AIMS}^{\rm SPA1} = -\sum_{\rho}^{3N_{\rm n}}\frac{\hbar^2}{M_\rho}d_{IJ}^{\rho}(\bar{\boldsymbol{R}}_{km})\,\langle\tilde{\chi}_k^{(I)}|\,\partial_{R_\rho}\,|\tilde{\chi}_m^{(J)}\rangle_{\boldsymbol{R}} - \sum_{\rho}^{3N_{\rm n}}\sum_{\rho'}^{3N_{\rm n}}\frac{\hbar^2}{M_\rho}\left(\mathbf{J}_{\boldsymbol{d}_{IJ}}(\bar{\boldsymbol{R}}_{km})\right)_{\rho\rho'}\langle\tilde{\chi}_k^{(I)}|\,(R_{\rho'}-\bar{R}_{km,\rho'})\partial_{R_\rho}\,|\tilde{\chi}_m^{(J)}\rangle_{\boldsymbol{R}}\,. \tag{2.62}$$

with $\left(\mathbf{J}_{\boldsymbol{d}_{IJ}}(\bar{\boldsymbol{R}}_{km})\right)_{\rho\rho'}$ being the element $\rho\rho'$ of the Jacobian matrix (see Eq. (2.61)). Without considering the difficulties in obtaining the Jacobian, Eq. (2.62) reveals the second issue mentioned above: it is non-Hermitian. Upon expanding the integrand of the Gaussian integral in the last term of the right hand-side in Eq. (2.62), it becomes clear that most resulting contributions are Hermitian, with the exception of the term $[\sum_{\rho}^{3N_{\rm n}}\frac{\hbar^2}{2M_\rho}\left(\mathbf{J}_{\boldsymbol{d}_{IJ}}(\bar{\boldsymbol{R}}_{km})\right)_{\rho\rho}\langle\tilde{\chi}_k^{(I)}|\tilde{\chi}_m^{(J)}\rangle_{\boldsymbol{R}}]$.

This term is anti-Hermitian, as $\left(\mathbf{J}_{\boldsymbol{d}_{IJ}}(\bar{\boldsymbol{R}}_{km})\right)_{\rho\rho} = -\left(\mathbf{J}_{\mathbf{d}_{JI}}(\bar{\boldsymbol{R}}_{km})\right)_{\rho\rho}$ and $\langle\tilde{\chi}_k^{(I)}|\tilde{\chi}_m^{(J)}\rangle_{\boldsymbol{R}} = \langle\tilde{\chi}_m^{(J)}|\tilde{\chi}_k^{(I)}\rangle_{\boldsymbol{R}}$. An explicit discussion of all the contributing terms for a two-level two-dimensional system can be found in the appendix A.

From the above analysis of the SPA1 interstate couplings, it becomes clear that the original approximations in AIMS places this method in a sweet spot where the SPA0 compensates for the loss of hermiticity caused by neglecting the NACs in the interstate couplings. One may now wonder whether including back the NACs could resolve the hermiticity issue observed within the SPA1.

Including the second order couplings in *ab initio* multiple spawning – two-state systems

Based on the findings above that the SPA1 breaks the hermiticity of the AIMS interstate couplings, it will be investigated whether including back the (long-neglected) NACs could lead to Hamiltonian matrix elements that are Hermitian. At this opportunity, also the inclusion of the DBOCs in the interstate matrix elements will be discussed, as they originate from the second-order couplings. Discussions of the role of NACs and DBOCs in AIMS have been previously proposed in Refs. [167, 168], for example.

To simplify the analysis, it is restricted to a two-state model (for example the two-state two-dimensional system introduced in Eq. (2.9)), which allows simplifying the expressions for the NACs and DBOCs. One can start by expanding the NACs into a symmetrised form,

$$D_{IJ}^{\rho}(\boldsymbol{R}) = \langle\Phi_I|\,\partial_{R_\rho}^2\,|\Phi_J\rangle_{\boldsymbol{r}} = \partial_{R_\rho}\langle\Phi_I|\,\partial_{R_\rho}\,|\Phi_J\rangle_{\boldsymbol{r}} - \langle\partial_{R_\rho}\Phi_I|\partial_{R_\rho}\Phi_J\rangle_{\boldsymbol{r}}\,. \tag{2.63}$$

Inserting the resolution of the identity $[\sum_K |\Phi_K\rangle\langle\Phi_K| = \mathbf{1}]$ into the last term of the right hand-side in Eq. (2.63), one obtains

$$D_{IJ}^{\rho}(\boldsymbol{R}) = \langle\Phi_I|\,\partial_{R_\rho}^2\,|\Phi_J\rangle_{\boldsymbol{r}} = \partial_{R_\rho}\langle\Phi_I|\,\partial_{R_\rho}\,|\Phi_J\rangle_{\boldsymbol{r}} - \sum_K \langle\partial_{R_\rho}\Phi_I|\Phi_K\rangle_{\boldsymbol{r}}\langle\Phi_K|\partial_{R_\rho}\Phi_J\rangle_{\boldsymbol{r}}\,. \tag{2.64}$$

For a two-state system, from Eq. (2.64) a simplified expression can be derived for the DBOCs

$$D_{JJ}^{\rho}(\boldsymbol{R}) = \langle\Phi_J|\,\partial_{R_\rho}^2\,|\Phi_J\rangle_{\boldsymbol{r}} = -|\,\langle\Phi_1|\,\partial_{R_\rho}\,|\Phi_2\rangle_{\boldsymbol{r}}\,|^2 = -|d_{12}^{\rho}(\boldsymbol{R})|^2\,, \tag{2.65}$$

and the NACs,

$$D_{IJ}^{\rho}(\boldsymbol{R}) = \langle \Phi_I | \, \partial_{R_\rho}^2 \, | \Phi_J \rangle_{\boldsymbol{r}} = \partial_{R_\rho} \langle \Phi_I | \, \partial_{R_\rho} \, | \Phi_J \rangle_{\boldsymbol{r}} = \partial_{R_\rho} d_{IJ}^{\rho}(\boldsymbol{R}) \, . \tag{2.66}$$

Hence, both the DBOCs and the NACs can be readily obtained from the NACVs for a two-state model.

Now the definitions of DBOCs and NACs provided by Eqs. (2.65) and (2.66) can be used in the AIMS matrix elements within the SPA0. The additional term in any matrix elements incorporating the DBOC reads, within the SPA0, as

$$\left(\sum_{\rho}^{3N_\mathrm{n}} \frac{\hbar^2}{2M_\rho} \langle \tilde{\chi}_k^{(J)} | \, D_{JJ}^{\rho} \, | \tilde{\chi}_m^{(J)} \rangle_{\boldsymbol{R}} \right)_{\mathrm{AIMS}}^{\mathrm{SPA0}} = - \sum_{\rho}^{3N_\mathrm{n}} \frac{\hbar^2}{2M_\rho} |d_{12}^{\rho}(\bar{\boldsymbol{R}}_{km})|^2 \, \langle \tilde{\chi}_k^{(J)} | \tilde{\chi}_m^{(J)} \rangle_{\boldsymbol{R}} \, , \tag{2.67}$$

while the one containing the NACs is

$$\left(\sum_{\rho}^{3N_\mathrm{n}} \frac{\hbar^2}{2M_\rho} \langle \tilde{\chi}_k^{(I)} | \, D_{IJ}^{\rho} \, | \tilde{\chi}_m^{(J)} \rangle_{\boldsymbol{R}} \right)_{\mathrm{AIMS}}^{\mathrm{SPA0}} = \sum_{\rho}^{3N_\mathrm{n}} \frac{\hbar^2}{2M_\rho} \left(\mathbf{J}_{\boldsymbol{d}_{IJ}}(\bar{\boldsymbol{R}}_{km}) \right)_{\rho\rho} \langle \tilde{\chi}_k^{(I)} | \tilde{\chi}_m^{(J)} \rangle_{\boldsymbol{R}} \, . \tag{2.68}$$

In light of the discussion of Eq. (2.62), it is known that the interstate coupling term (Eq. (2.68)) is anti-Hermitian, as $\left(\mathbf{J}_{\boldsymbol{d}_{IJ}}(\bar{\boldsymbol{R}}_{km}) \right)_{\rho\rho} = - \left(\mathbf{J}_{\mathbf{d}_{JI}}(\bar{\boldsymbol{R}}_{km}) \right)_{\rho\rho}$ while $\langle \tilde{\chi}_k^{(I)} | \tilde{\chi}_m^{(J)} \rangle_{\boldsymbol{R}} = \langle \tilde{\chi}_m^{(J)} | \tilde{\chi}_k^{(I)} \rangle_{\boldsymbol{R}}$. However, this anti-Hermitian contribution coming from Eq. (2.68) is exactly the same as the anti-Hermitian contribution obtained from the expansion of the last term of the right hand-side of Eq. (2.62) (interstate coupling within the SPA1). Hence, if one combines the SPA1 for the NACVs with the SPA0 for the NACs, the two anti-Hermitian parts cancel out, providing an overall Hermitian Hamiltonian. Note that expanding the interstate matrix elements to different orders of the SPA allows to include all terms that contain the NACVs up to their first-order derivatives.

In summary, one can propose the following AIMS Hamiltonian matrix elements for a two-state system, using a combination of the SPA0 and SPA1 for both the intrastate couplings,

$$\left(\langle\tilde{\chi}_k^{(J)}\Phi_J|\,\hat{H}_\mathrm{m}\,|\Phi_J\tilde{\chi}_m^{(J)}\rangle_{\boldsymbol{r},\boldsymbol{R}}\right)_\mathrm{AIMS}^\mathrm{SPA1'} = -\sum_\rho^{3N_\mathrm{n}}\frac{\hbar^2}{2M_\rho}\langle\tilde{\chi}_k^{(J)}|\,\partial_{R_\rho}^2\,|\tilde{\chi}_m^{(J)}\rangle_{\boldsymbol{R}} + \epsilon_\mathrm{BO}^{(J)}(\bar{\boldsymbol{R}}_{km})\,\langle\tilde{\chi}_k^{(J)}|\tilde{\chi}_m^{(J)}\rangle_{\boldsymbol{R}}$$
$$+\sum_\rho^{3N_\mathrm{n}}\left.\frac{\partial\epsilon_\mathrm{BO}^{(J)}(\boldsymbol{R})}{\partial R_\rho}\right|_{R_\rho=\bar{R}_{km,\rho}}\langle\tilde{\chi}_k^{(J)}|\,(R_\rho-\bar{R}_{km,\rho})\,|\tilde{\chi}_m^{(J)}\rangle_{\boldsymbol{R}}$$
$$+\sum_\rho^{3N_\mathrm{n}}\frac{\hbar^2}{2M_\rho}|d_{12}^\rho(\bar{\boldsymbol{R}}_{km})|^2\,\langle\tilde{\chi}_k^{(J)}|\tilde{\chi}_m^{(J)}\rangle_{\boldsymbol{R}}\,, \tag{2.69}$$

and the interstate couplings,

$$\left(\langle\tilde{\chi}_k^{(I)}\Phi_I|\,\hat{H}_\mathrm{m}\,|\Phi_J\tilde{\chi}_m^{(J)}\rangle_{\boldsymbol{r},\boldsymbol{R}}\right)_\mathrm{AIMS}^\mathrm{SPA1'} = -\sum_\rho^{3N_\mathrm{n}}\frac{\hbar^2}{M_\rho}d_{IJ}^\rho(\bar{\boldsymbol{R}}_{km})\,\langle\tilde{\chi}_k^{(I)}|\,\partial_{R_\rho}\,|\tilde{\chi}_m^{(J)}\rangle_{\boldsymbol{R}}$$
$$-\sum_\rho^{3N_\mathrm{n}}\sum_{\rho'}^{3N_\mathrm{n}}\frac{\hbar^2}{M_\rho}\left(\mathbf{J}_{\boldsymbol{d}_{IJ}}(\bar{\boldsymbol{R}}_{km})\right)_{\rho\rho'}\langle\tilde{\chi}_k^{(I)}|\,(R_{\rho'}-\bar{R}_{km,\rho'})\partial_{R_\rho}\,|\tilde{\chi}_m^{(J)}\rangle_{\boldsymbol{R}}$$
$$-\sum_\rho^{3N_\mathrm{n}}\frac{\hbar^2}{2M_\rho}\left(\mathbf{J}_{\boldsymbol{d}_{IJ}}(\bar{\boldsymbol{R}}_{km})\right)_{\rho\rho}\langle\tilde{\chi}_k^{(I)}|\tilde{\chi}_m^{(J)}\rangle_{\boldsymbol{R}}\,. \tag{2.70}$$

This combination of approximations for the Hamiltonian matrix elements will be denoted *SPA1'*. The SPA1' is the simplest approximation to the FMS Hamiltonian matrix elements that allows for the inclusion of the NACs and DBOCs while preserving hermiticity.

2.5.4 Stochastic-selection *ab initio* multiple spawning

The accuracy of AIMS, thanks to the coupling between the TBFs, comes at the cost of two drawbacks: nonlinear scaling of the computational effort with respect to the number of TBFs and high sensitivity to numerical issues and instabilities during the propagation. Since all TBFs of one initial branch are coupled in AIMS, the number of required electronic structure calculations scales quadratically with the number of TBFs, leading to almost infeasible computational costs of AIMS dynamics for long-time propagation or a large number of electronic states. Additionally, the fully-coupled propagation of the complex coefficients implies that as soon as an error occurs during any electronic structure calculation for any TBF the whole AIMS dynamics cannot continue. To the end of overcoming these bottlenecks, a very straightforward solution has been proposed recently: using the

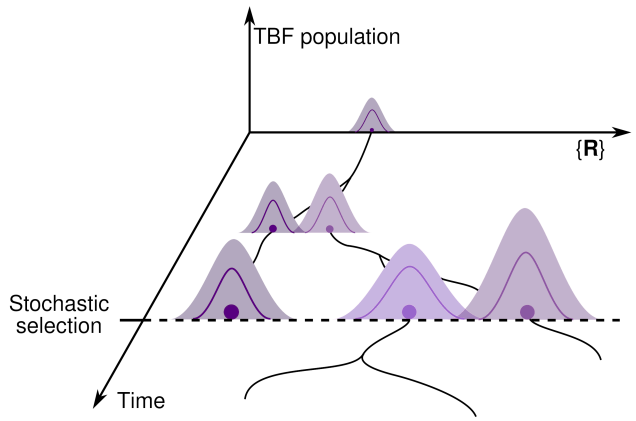

Fig. 2.4.: Schematic representation of the evolution of a TBF in a typical SSAIMS run. An initial (parent) TBF evolves in time and spawns new TBFs throughout the dynamics. The coupling between TBFs is constantly monitored during the dynamics, and when TBFs become uncoupled (indicated by the dashed line), a stochastic-selection process is triggered. Only one TBF, or a group of coupled TBFs, survives the stochastic-selection process – in the present scheme, the parent TBF becomes uncoupled from a group of two child TBFs and is therefore discarded.

naturally occurring decoupling between groups of TBFs to reduce the number of TBFs by stochastically selecting one of the groups.[169]

The important consideration is how an introduced death process for decoupled TBFs affects observable results. In AIMS, the expectation value of an operator $[\hat{O}]$ for the nuclear wavefunction for state J is given by

$$O_J(t) = \frac{\sum_{km}^{N^J(t)} C_k^{(J)*}(t) C_m^{(J)}(t) \langle \tilde{\chi}_k^{(J)} | \hat{O} | \tilde{\chi}_m^{(J)} \rangle_{\boldsymbol{R}}}{\sum_{km}^{N^J(t)} C_k^{(J)*}(t) C_m^{(J)}(t) (\boldsymbol{S})_{km}^{JJ}} . \tag{2.71}$$

In most cases local operators are of interest, meaning for TBFs well separated in phase space the matrix elements in the numerator goes to zero, leaving only pairs of TBFs close to each other. In the limit of all TBFs being very distant, Eq. (2.71) reduces to

$$O_J(t) \approx \frac{\sum_{k}^{N^J(t)} |C_k^J(t)|^2 \langle \tilde{\chi}_k^{(J)} | \hat{O} | \tilde{\chi}_k^{(J)} \rangle_{\boldsymbol{R}}}{\sum_{k}^{N^J(t)} |C_k^J(t)|^2} . \tag{2.72}$$

Similarly, for TBFs in different electronic states, the important interference terms are localised in nonadiabatic regions where the TBFs overlap. Following this observation, the new approach of stochastic-selection *ab initio* multiple spawning (SSAIMS) dynamics seems reasonable: in the case of (groups of) TBFs becoming uncoupled, it is unnecessary to follow the complete dynamics as the interference terms vanish and subsequently, allows

stochastic selection of one of the blocks to pursue the dynamics. The main approximation invoked in this scheme is the following assumption: If a group of TBFs decouples from all other TBFs at one point during the dynamics, they will remain uncoupled to all other TBFs throughout the whole dynamics.

Within this scheme, it is of utmost importance to be careful when TBFs are defined as uncoupled. In the ESSAIMS method (where the E comes from the energy units of the threshold), the off-diagonal matrix elements of **H** between the running TBFs (represented by the bold dashed lines in figure 2.4) are compared to a predefined threshold $[\varepsilon]$ throughout the dynamics. In the overlap based formalism, OSSAIMS, the relevant criterion is the overlap between the TBFs. It is important to note that this criterion in OSSAIMS does not distinguish between the electronic state the TBFs are evolving on, whereas in ESSAIMS interstate and intrastate couplings are differentiated. A connectivity matrix $[\mathbf{M}]$ between the TBFs is constructed and for $|(\mathbf{H})_{km}| > \varepsilon$ (if TBFs k and m are coupled) $(\mathbf{M})_{km}$ is set to unity, and zero otherwise. Iterative multiplications of the connectivity matrix by itself identifies higher order couplings between TBFs, i.e. when two TBFs are coupled via one or more other TBFs, and is performed until idempotency is reached.

Having established the coupling pattern between the TBFs, the coherent population $[p_\alpha]$ of an uncoupled block $[\alpha]$ of $N_\alpha^J(t)$ coupled trajectories in each state J is calculated as

$$p_\alpha = \sum_J \sum_{km}^{N_\alpha^J(t)} C_k^{(J)*}(t) C_m^{(J)}(t) S_{km}^{JJ} \,. \tag{2.73}$$

In the case of multiple uncoupled blocks, one of them $[\nu]$ is selected stochastically for further propagation if for a random number $[\xi]$ generated in the interval $[0:1]$

$$\sum_\alpha^{\nu-1} p_\alpha \leq \xi \leq \sum_\alpha^{\nu} p_\alpha \,. \tag{2.74}$$

The simulation is continued with only the TBFs of the νth block, which are rescaled to preserve wavefunction normalisation. It is important to note that during the spawning mode the stochastic selection process is suspended for the newly created TBF to ensure its survival until the spawning time since at the point of entry the new TBF is usually only weakly coupled.

The parameter ε has to be chosen individually for each system of interest and depending on the choice of ε SSAIMS can be an approximation to AIMS with only a few stochastic

trajectories, while still ensuring a proper description of regions of high nonadiabaticity (spawning regions), or by decreasing the threshold it eventually converges to the AIMS population distribution between the electronic states. In chapter 6, a detailed analysis of ESSAIMS vs. OSSAIMS for the dynamics of complex molecular systems is presented and the results and computational cost of the method are compared to those of AIMS and TSH.

2.6 Nonadiabatic dynamics based on trajectories

In contrast to the previously introduced methods based on trajectory basis functions, a different approach to dynamics, based on classically moving trajectories will be introduced. While the previously introduced strategies all preserve the quantum nature of the nuclei, mixed quantum/classical approaches use a classical approximation for the nuclei, keeping only the quantum description of the electrons and an approximate description of nonadiabatic effects.[15] The nuclei move as classical particles, following Newton's equation of motion, but the nuclear forces are derived from the potential energies that need to account for nonadiabatic effects.[170,171] A trajectory β, describing the nuclear configuration $[\boldsymbol{R}^{\beta}(t)]$ at time t feels the classical nuclear force $[\boldsymbol{F}^{\beta}(t)]$,

$$\boldsymbol{F}^{\beta}(t) = -\nabla_{\boldsymbol{R}} \epsilon(\boldsymbol{R})\big|_{\boldsymbol{R}=\boldsymbol{R}^{\beta}(t)}\,, \tag{2.75}$$

from a potential $[\epsilon(\boldsymbol{R})]$. The obvious question arising now is: How can one define $\epsilon(\boldsymbol{R})$ in a way that it incorporates nonadiabatic effects?[15,172]

2.6.1 Ehrenfest dynamcis

A common choice for the potential would be a mean-field potential energy giving rise to the so-called *Ehrenfest dynamics*..[170,173,174] Ehrenfest dynamics emerges from a classical limit of the time-dependent self-consistent field equations, where the molecular wavefunction is approximated as a product of a time-dependent nuclear and electron wavefunction. Subsequently, in Ehrenfest dynamics, a mean-field potential energy is used to propagate the purely classical nuclei. The force is then calculated as the gradient of the expectation value of the BO Hamiltonian as

$$\boldsymbol{F}^{\beta}(t) = -\nabla_{\boldsymbol{R}} \left\langle \Phi(t;\boldsymbol{R}^{\beta}(t)) \right| \hat{H}_{\mathrm{BO}}(\boldsymbol{R}^{\beta}(t)) \left| \Phi(t;\boldsymbol{R}^{\beta}(t)) \right\rangle_{\boldsymbol{r}}\,. \tag{2.76}$$

If the electronic states involved in photoprocesses are of similar character, Ehrenfest dynamics can efficiently provide good results for short term dynamics. However, if the PESs involved in the photoprocess differ strongly, the mean-field nature can lead to artificial nuclear dynamics.

Since the trajectories are propagated on the support of an average potential, Ehrenfest dynamics cannot represent different physical situations found after encountering regions of high nonadiabaticity.

2.6.2 Trajectory surface hopping

One of the most famous and widely used mixed quantum/classical methods is trajectory surface hopping (TSH). In a way, TSH has a resemblance with a classical approximation to AIMS: Invoking an independent trajectory approximation (ITA), replace moving Gaussians by classical (and fully independent) trajectories and spawning events are replaced by *hops*, i.e. trajectories are allowed to change the running state based on nonadiabatic effects.

Postulated in the 1970s[175,176], it became widely known and used since the formulation of the *fewest switches surface hopping* (FSSH) algorithm in 1990.[16,177] In TSH the classical nuclei are propagated on the adiabatic PESs, so their nuclear force felt by a trajectory β is

$$\boldsymbol{F}^{\beta}(t) = -\nabla_{\boldsymbol{R}} \epsilon_{\mathrm{BO}}^{(*)}(\boldsymbol{R})\big|_{\boldsymbol{R}=\boldsymbol{R}^{\beta}(t)}\,, \tag{2.77}$$

where $\epsilon_{\mathrm{BO}}^{(*)}$ indicates that the electronic state, in which the trajectory evolves, can change during the dynamics. Each trajectory β is associated with a time-dependent electronic wavefunction which is a linear combination of the electronic states $[\Phi_J(\boldsymbol{r};\boldsymbol{R}^{\beta})]$

$$\tilde{\Phi}_J(\boldsymbol{r},t;\boldsymbol{R}^{\beta}) = \sum_J C_{\beta}^{(J)}(t)\Phi_J(\boldsymbol{r};\boldsymbol{R}^{\beta})\,, \tag{2.78}$$

with complex coefficients $[C_{\beta}^{(J)}(t)]$ associated with each state. Inserting this expansion into the time-dependent *electronic* Schrödinger equation, yields a set of equations of motion for the complex amplitudes:

$$\dot{C}_{\beta}^{(I)}(t) = -\frac{i}{\hbar}\epsilon_{\mathrm{BO}}^{(J)}(\boldsymbol{R}^{\beta})C_{\beta}^{(I)}(t) - \sum_J \dot{\boldsymbol{R}}^{\beta}(t)\cdot\boldsymbol{d}_{IJ}(\boldsymbol{R}^{\beta})C_{\beta}^{(J)}(t)\,, \tag{2.79}$$

which includes the projection of the NACV $[\boldsymbol{d}_{IJ}(\boldsymbol{R}^{\beta})]$ onto the nuclear velocity vector $[\dot{\boldsymbol{R}}^{\beta}(t)]$. At time $t = 0$, the initial state of the trajectory is chosen by setting the coefficient of this state to 1 and all other coefficients to 0. After each nuclear time step, the coefficients are propagated and a probability for a hop from the running electronic state to another is calculated. Then, based on a stochastic algorithm, it is decided whether the trajectory hops or remains in its state. Within the fewest switches algorithm, this hopping probability is calculated as

$$\mathcal{P}^{\beta}_{J\to I} = \max\left[0, -\frac{2\Re\left[C^{(J)*}_{\beta}(t)C^{(I)}_{\beta}(t)\dot{\boldsymbol{R}}^{\beta}(t)\cdot\boldsymbol{d}_{IJ}(\boldsymbol{R}^{\beta})\right]}{|C^{(J)}_{\beta}(t)|^2}\mathrm{d}t\right]. \tag{2.80}$$

A random number ξ is created at each step (from the uniformous interval $[0:1]$) and a hop from J to I occurs if

$$\sum_{K<I}\mathcal{P}^{\beta}_{J\to K} \le \xi \le \sum_{K\ge I}\mathcal{P}^{\beta}_{J\to K}. \tag{2.81}$$

So at each step, every trajectory has the opportunity to hop and this possibility is mediated by the nonadiabatic coupling between the electronic state and complex coefficients. For an accurate description of the nonadiabatic processes, a large number of trajectories is necessary to converge the stochastic algorithm (in addition to the convergence of the sampling of initial conditions).

In comparison to the previously introduces SSAIMS, there is an undeniable analogy between the selection process in SSAIMS strongly and the idea of hops in TSH. However, TSH is never guaranteed to converge to the exact physical result. In contrast, a large number of stochastic runs and a small threshold in SSAIMS reproduces the AIMS result.

2.6.3 Issues with trajectory surface hopping

Since the TSH algorithm has not been derived from first principles, some aspects of the dynamics require *ad hoc* adjustments. The most critical corrections are the momentum rescaling to ensure energy conservation during hops, the approach to handle frustrated hops and the problem of overcoherence.[178]

Energy conservation and frustrated hops

In TSH, each trajectory should conserve classical energy throughout the dynamics. However, since hops induce an instantaneous gain or loss of potential energy, this needs to be

compensated. There is no unique way to do this,[178–180] but several approaches to scale the nuclear kinetic energy have been proposed. The original method proposed by Tully[16] is to rescale the nuclear momentum vector in the direction of the NACV [$\boldsymbol{d}_{IJ}(\boldsymbol{R})$] of the two states, I,J, involved in the hop. Thereby, the potential energy variation of the hopping event is transformed into the work of a force acting on the nuclei. However, since the nonadiabatic coupling vectors might not always be available during the dynamics, an isotropic rescaling, i.e. simply rescaling along the nuclear velocity, is also widely used. It should be noted that both these common methods do not conserve angular momentum, however, using the rescaling along the NACVs can restore this conservation once a projection operator is applied to remove the translational and rotational components.[181]

An issue closely related to the rescaling of the momentum is frustrated hops. A hop is considered frustrated if the gain of potential energy during the hop exceeds the kinetic energy. In these cases, it has been argued in the past that the nuclear momentum should subsequently be inverted, but also the opposite has been argued. Again, if one chooses to invert the nuclear momentum after a frustrated hop, this can either be done parallel to the NACV or the full momentum vector can be inverted.[177,179,182,183] Generally, hops are more likely to be frustrated when rescaling along the NACV as only the portion of kinetic energy parallel to the NACV is available.[178]

Decoherence failure

Another troubling aspect of TSH is its *overcoherent* nature, a consequence of the disconnection of the evolution of nuclei and electrons: while the nuclei evolve on individual BO PESs and instantaneously hop between them, the electronic evolution remains in a coherent superposition of BO states throughout.[178] This problem is exemplified in Fig. 2.5. Consider a trajectory β initially fully evolving on one state, e.g. S_1, with complex coefficients at time t_0 as $C_\beta^{(S_0)}(t_0) = 0.0$ and $C_\beta^{(S_1)}(t_0) = 1.0$. Once the two states come close in energy, because of the stochastic algorithm no hop occurs, so the nuclear dynamics of the trajectory still follows the force of the S_1 state. However, in the vicinity of the coupling region, electronic population is transferred between the states through the equations of motion for the complex amplitudes. Thus, after passing the coupling region, the complex coefficients are for example $C_\beta^{(S_0)}(t_1) = \sqrt{0.3}$ and $C_\beta^{(S_1)}(t_1) = \sqrt{0.7}$. As the trajectory is following the force of S_1, all electronic population is also forced to follow the force of the running state, leading to an artificial overcoherence of the population.

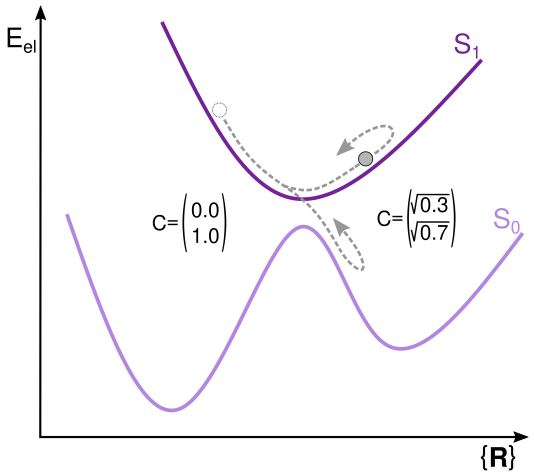

Fig. 2.5.: Schematic representation of the overcoherence problem of TSH. A trajectory, with initial coefficient $[C_\beta^{(S_1)}(t_0) = 1.0]$ evolves on the S_1 state. In the coupling region no hop occurs but electronic population gathers in the ground state $[C_\beta^{(S_0)}(t_1) = \sqrt{0.3}]$. However, all electronic population has to follow the running trajectory and therefore, the electronic population on the S_0 overcoherently goes against the force of its state.

A direct consequence of the overcoherence of TSH is a loss of *internal consistency*:[184] The fraction of trajectories in any electronic state J at any time t $[\Pi_J(t) = \frac{N_J(t)}{N_{\text{traj}}}]$, should equal the averaged electronic population $[\bar{p}_J(t) = \frac{1}{N_{\text{traj}}} \sum_\beta^{N_{\text{traj}}} \left|C_\beta^{(J)}\right|^2]$. Many *ad hoc* decoherence correction schemes have been proposed that aim at restoring internal consistency.[184] One of the simplest schemes is the *energy based decoherence correction* (EDC) proposed by Granucci and Persico.[184] Based on earlier work by Truhlar and coworkers in the context of mean-field methods,[185,186] the idea of EDC is to apply an exponential dampening function to the electronic populations of the nonactive states after each integration step. For a trajectory β in state J, the electronic population of each nonactive state $[p_I^\beta(t) = \left|C_\beta^{(I)}(t)\right|^2]$ is dampened according to

$$p_I^{\beta\prime}(t) = \left|C_\beta^{(I)}(t)\right|^2 \exp\left(-\frac{\Delta t}{\tau_{IJ}}\right), \tag{2.82}$$

for a time-step $[\Delta t]$ and a decoherence rate $[\tau_{IJ}]$, which is computed as

$$\tau_{IJ}^{\text{EDC}} = \frac{\hbar}{|\epsilon_{\text{BO}}^{(J)} - \epsilon_{\text{BO}}^{(I)}|}\left(1 + \frac{C}{T_{\text{n}}}\right) \tag{2.83}$$

and depends on the energy gap between the active state J and the nonactive state I, as well as on the kinetic energy $[T_{\text{n}}]$. The parameter C is a constant that could be adjusted

but is usually set to 0.1 E_h. Zhu et al. observed that their results was quite insensitive to the parameter $[C]$[185] and were the first to use 0.1 E_h which subsequently also became the usual default value for C in the context of TSH. It should be noted that although originally this decay was intended to be applied to the populations, multiple softwares implemented the EDC to be dampening coefficients. However, numerical comparisons between the two approaches for a subset of molecules do not reveal significant practical differences in predicted population decay.[17,187]

A different approach is the so-called *augmented fewest switches surface hopping* (A-FSSH)[188] where the decoherence rate is obtained from how fast trajectories propagated on different surfaces move away from each other. Each trajectory is associated with auxiliary trajectories evolving on the other nonactive states. The decoherence rate is calculated as

$$\frac{1}{\tau_{IJ}^{\text{A-FSSH}}} = \frac{\delta \boldsymbol{F}_{IJ} \cdot \delta \boldsymbol{R}_{IJ}}{2\hbar} - \frac{2\left|\boldsymbol{d}_{IJ} \cdot \boldsymbol{R}(\epsilon_{\text{BO}}^{(J)} - \epsilon_{\text{BO}}^{(I)})\delta \boldsymbol{R}_{IJ} \cdot \boldsymbol{R}\right|}{\hbar |\boldsymbol{R}|^2}, \tag{2.84}$$

where $\delta \boldsymbol{R}_{IJ} = \boldsymbol{R}_I - \boldsymbol{R}_J$ refers to the position difference between the auxiliary trajectory on state I and the trajectory on the active state J, and $\boldsymbol{F}_{IJ} = -\nabla_{\boldsymbol{R}}(\epsilon_{\text{BO}}^{(I)} - \epsilon_{\text{BO}}^{(J)}(\boldsymbol{R}_J))$ to the force difference. This decoherence rate is not directly applied, but used in a stochastic collapse process: if $\Delta t/\tau_{IJ}^{\text{A-FSSH}}$ is greater than a random number, the amplitude of nonactive state $[C_\beta^{(I)}]$ is collapsed to zero, while the coefficient of the active state is increased to conserve the total amplitude.

A similar approach with propagating auxiliary trajectories is taken in the *decoherence-induced surface hopping based on exact factorisation* (DISH-XF).[189] In DISH-XF, an additional term $[\eta_\beta^{(I)}(t)]$ is added to the equations of motion of the complex coefficients (see Eq. (2.79)) that accounts for the decoherence. This term has the form

$$\eta_\beta^{(I)}(t) = \sum_J \sum_\rho^{N_n} \frac{1}{M_\rho} \frac{\nabla_{\boldsymbol{R}_\rho}|\chi(\boldsymbol{R},t)|}{|\chi(\boldsymbol{R},t)|}\Big|_{\boldsymbol{R}^\beta(t)} \cdot (f_{\beta,\rho}^{(J)}(t) - f_{\beta,\rho}^{(I)}(t))|C_\beta^{(J)}(t)|^2 C_\beta^{(I)}(t), \tag{2.85}$$

and it contains the quantum momentum term $[\frac{\nabla_{\boldsymbol{R}_\rho}|\chi(\boldsymbol{R},t)|}{|\chi(\boldsymbol{R},t)|}\big|_{\boldsymbol{R}^\beta(t)}]$ and the accumulated force, i.e. the difference in force along the BO PES integrated along the trajectory $[f_{\beta,\rho}^{(J)}(t) = -\int_0^t \nabla_{\boldsymbol{R}_\rho}\epsilon_{\text{BO}\,\rho}^{(J)}(t')\mathrm{d}t']$. The dependence on the population of the different states leads to this term being active as soon as population is distributed between different states. It has been shown that this term $[\eta_\beta^{(I)}(t)]$ leads to decoherence and wavepacket splitting in model systems.[27,28] At this point, the question arises, how can one compute (approximately)

the quantum momentum, since we have an approximation of classical trajectories and therefore do not have a nuclear wavefunction. To this end, auxiliary trajectories are propagated: for each initial active trajectory β, auxiliary trajectories β' are propagated on all nonactive states. Then, the nuclear wavefunction is approximately reconstructed by a Gaussian broadening of each of the trajectories and from this, the quantum momentum is approximately reconstructed.

It should be noted that these are not the only ways to account for decoherence in surface hopping but a large number of approaches have been proposed in the past.[35,185,190–193]

2.6.4 Trajectory surface hopping vs. *ab initio* multiple spawning

Having presented the two widely used ansätze for nonadiabatic dynamics provided by AIMS and TSH, it is an interesting step to compare how they evaluate their complex amplitudes.[14,79]

Assuming a system including two electronic states I and J, in TSH the equations of motion for the complex coefficients associated with the two states for a trajectory β are calculated as

$$\begin{pmatrix} \dot{C}_\beta^{(I)}(t) \\ \dot{C}_\beta^{(J)}(t) \end{pmatrix} = -\frac{i}{\hbar} \begin{pmatrix} H_\beta^{II} & H_\beta^{IJ} \\ H_\beta^{JI} & H_\beta^{JJ} \end{pmatrix} \begin{pmatrix} C_\beta^{(I)}(t) \\ C_\beta^{(J)}(t) \end{pmatrix}, \tag{2.86}$$

with the Hamiltonian matrix elements, according to Eq. (2.79), being defined as

$$H_\beta^{JJ} = \epsilon_{\mathrm{BO}}^{(J)}(\boldsymbol{R}^\beta) \tag{2.87}$$

$$H_\beta^{IJ} = -i\hbar \boldsymbol{d}_{IJ}(\boldsymbol{R}^\beta) \cdot \dot{\boldsymbol{R}}^\beta \,. \tag{2.88}$$

In contrast, for AIMS, as a simple, exemplary case, two TBFs evolving on state I and one TBF evolving on state J are assumed. This then leads the following equations of motion

$$\begin{pmatrix} S_{11}^{II} & S_{12}^{II} & 0 \\ S_{12}^{II} & S_{22}^{II} & 0 \\ 0 & 0 & S_{33}^{JJ} \end{pmatrix} \begin{pmatrix} \dot{C}_1^{(I)}(t) \\ \dot{C}_2^{(I)}(t) \\ \dot{C}_3^{(J)}(t) \end{pmatrix} = \left[-\frac{i}{\hbar} \begin{pmatrix} H_{11}^{II} & H_{12}^{II} & H_{13}^{IJ} \\ H_{21}^{II} & H_{22}^{II} & H_{23}^{IJ} \\ H_{31}^{JI} & H_{32}^{JI} & H_{33}^{JJ} \end{pmatrix} - \begin{pmatrix} \dot{S}_{11}^{II} & \dot{S}_{12}^{II} & 0 \\ \dot{S}_{12}^{II} & \dot{S}_{22}^{II} & 0 \\ 0 & 0 & \dot{S}_{33}^{JJ} \end{pmatrix} \right] \begin{pmatrix} C_1^{(I)}(t) \\ C_2^{(I)}(t) \\ C_3^{(J)}(t) \end{pmatrix}, \tag{2.89}$$

with the Hamiltonian matrix elements, following Eqs. (2.58) and (2.59), being obtained as

$$H_{km}^{IJ} = \epsilon_{\mathrm{BO}}^{(J)}(\bar{\boldsymbol{R}}_{km}) \langle \tilde{\chi}_k^{(J)} | \tilde{\chi}_m^{(J)} \rangle_{\boldsymbol{R}} \tag{2.90}$$

$$H_{km}^{IJ} = -\sum_{\rho}^{3N_{\mathrm{n}}} \frac{\hbar^2}{M_\rho} d_{IJ}^{\rho}(\bar{\boldsymbol{R}}_{km}) \langle \tilde{\chi}_k^{(I)} | \frac{\partial}{\partial R_\rho} | \tilde{\chi}_m^{(J)} \rangle_{\boldsymbol{R}} \ . \tag{2.91}$$

Comparison of these two sets of equations of motion highlights the conceptual difference between the coupled TBFs in AIMS and the independent trajectories in TSH. As a consequence of the ITA, there are neither interstate nor intrastate interactions between different trajectories within TSH while the interstate couplings (for a given trajectory β) are exclusively evaluated at the location of the trajectory at time t.

While the ITA is the reason behind the simplicity (and success) of the TSH algorithm and allows for a computational cost scaling linearly with the number of TSH trajectories, it is clear from the previous analysis that the trajectories produced might suffer from some artefact. In particular, TSH might suffer in cases where the nuclear wavepacket branches in a nonadiabatic region, leading to a separation of the nuclear components on the two coupled surfaces – in the case of decoherence, as detailed in the previous section. This is in stark contrast with AIMS, where the use of coupled TBFs, possibly evolving on different electronic states, allows for the description of splitting wavepackets.

Surface hopping approach to *ab initio* multiple spawning

Armed with the detailed comparison between TSH and AIMS provided above, is a good starting position for close investigation of the effect of their differences on the excited-state dynamics. Comparing the two sets of equations of motion of TSH and AIMS clearly highlights the difference between the ITA inherent to TSH and the coupled TBFs strategy employed by AIMS. Apart from the complete neglect of intrastate couplings in TSH, a vast difference becomes evident upon the comparison of the interstate elements of the Hamiltonian. The interstate couplings of the AIMS Hamiltonian read (upon evaluation of the Gaussian integral[153,164])

$$\begin{aligned}\left(H_{km}^{IJ}\right)_{\mathrm{AIMS}} &= \sum_{\rho} d_{IJ}^{\rho}(\bar{\boldsymbol{R}}_{km}^{(IJ)}(t)) \frac{\hbar^2}{M_\rho} \langle \tilde{\chi}_k^{(I)} | \frac{\partial}{\partial R_\rho} | \tilde{\chi}_m^{(J)} \rangle \\ &= \sum_{\rho} d_{IJ}^{\rho}(\bar{\boldsymbol{R}}_{km}^{(IJ)}(t)) \frac{\hbar^2}{M_\rho} \left[-\frac{i}{\hbar} \bar{P}_{km,\rho} - \alpha_\rho \Delta R_{km,\rho}^{(IJ)} \right] \langle \tilde{\chi}_k^{(I)} | \tilde{\chi}_m^{(J)} \rangle \ ,\end{aligned} \tag{2.92}$$

with $\bar{P}^{(IJ)}_{km,\rho} = \frac{1}{2}(\bar{P}^{(J)}_{m,\rho} + \bar{P}^{(I)}_{k,\rho})$.
In comparison, interstate couplings in TSH are computed as

$$H^{IJ}_{\beta} = -i\hbar \boldsymbol{d}_{IJ}(\boldsymbol{R}^{\beta}) \cdot \dot{\boldsymbol{R}}^{\beta}(t)\,. \tag{2.93}$$

Which kind of approximations need to be performed on the AIMS matrix elements to bridge the equations of motion of AIMS to those of TSH? The most obvious approximation is to set the overlap $[S^{II}_{km}]$ and Hamiltonian matrix elements of the type $\dot{S}^{II}_{km}$ and H^{II}_{km} to zero in Eq (2.89). This uncouples the TBFs evolving on the same state and prevents amplitude transfer between them. Recovering the interstate couplings of TSH from the AIMS equations would require to enforce that the two coupled TBFs, evolving on different states, follow the same trajectory, leading to a perfect overlap between them at all times. Hence, setting the intrastate couplings to 0 and enforcing the following three approximations to the interstate couplings of AIMS constitute the framework called *surface hopping approach to ab initio multiple spawning* (SHAIMS):

1. Enforcing perfect overlap between the TBFs: $\langle \tilde{\chi}^{(I)}_{k} | \tilde{\chi}^{(J)}_{m} \rangle = 1$
2. The two TBFs need to be placed at the same position and propagated identically, i.e. $\Delta \boldsymbol{R}^{(IJ)}_{km} = 0$ and $\bar{\boldsymbol{P}}^{(IJ)}_{km} = \bar{\boldsymbol{P}}^{(I)}_{k} = \bar{\boldsymbol{P}}^{(J)}_{m}$
3. Instead of the NACV at the centroid position $[\boldsymbol{d}_{IJ}(\bar{\boldsymbol{R}}^{(IJ)}_{km}(t))]$ only the one of one TBF $[\boldsymbol{d}_{IJ}(\boldsymbol{R}^{(J)}_{m}(t))]$ is considered.

At this point, it is important to note that SHAIMS was developed and implemented as a tool to investigate differences between TSH and AIMS rather than an actual dynamics method.

3 A photochemical reaction in different theoretical representations

This chapter is based on the publication:
L. M. Ibele, B. F. E. Curchod and F. Agostini, "A photochemical reaction in different theoretical representations" submitted (2021)

3.1 Introduction

As introduced in the previous section, our way of picturing molecules and chemical processes has been greatly shaped by the Born-Oppenheimer (BO) approximation, the assumption that the motion of electrons and nuclei can be treated separately in a molecule.[13,194] Photochemistry inherently goes beyond this picture as photon absorption by a molecule makes transitions to different electronic states possible.[10,17,195–199] A legitimate strategy to move beyond the BO approximation would be to try to supplement the BO picture with more electronic eigenstates and account for their mutual couplings mediated by nuclear motion (see Sec. 2.2). This approach is equivalent to expanding the molecular wavefunction in a basis of time-independent electronic eigenfunctions, with time-dependent coefficients given by the nuclear wavefunctions. Importantly, this post BO model relies on the use of quantities originally defined within the framework of the BO approximation – like the potential energy surfaces obtained from the electronic Schrödinger equation for fixed nuclear degrees of freedom – in a context that is at the opposite of their initial *raison d'être*: strong electron-nuclear couplings.[52] Analogously, our way to regard photochemical processes, and the vocabulary used for such processes is intrinsically shaped by BO concepts: potential energy surfaces,[195] conical intersections,[44,45] geometric phase,[43,200] transition dipole moment (the electric dipole moment for the transition between two electronic states).

This chapter explores the different steps of a typical photochemical experiment described in sections 2.2.1 and 2.3.1, within the standard Born-Oppenheimer (BO) picture (as introduced in Sec. 2.2) that generates the model that underlies our common understanding of photochemistry. This model is contrasted with an alternative representation of the coupled electron-nuclear dynamics of a molecule, the exact factorisation (EF, see Sec. 2.3).[66,67] The EF introduces a framework exempt of the ideas emanating from the BO picture – there is no mention of electronic states or static potential energy surfaces. Instead, the EF depicts the dynamics of a molecular system by a nuclear wavefunction whose dynamics is dictated by a single time-dependent vector and scalar potential. Earlier works[64,65,74,201] showed that this formalism proposes a radically different model of nonadiabatic molecular dynamics. In particular, the concepts of transition between electronic states, conical intersections (CIs), or geometric phase (GP) do not appear in the EF. Hence, there is a real curiosity to unravel how the EF would describe a full photochemical experiment for a two-dimensional two-state molecular model, from the photoexcitation with a laser pulse to the formation of photoproducts, and to compare this picture to the more conventional BO representation. In addition, these simulations will allow shedding light on other interesting aspects of an *in-silico* photochemical experiment, such as (*i*) the effect of the Condon approximation, (*ii*) the analysis of the dynamics using representation-free quantities, and (*iii*) the use of classical and quantum trajectories to depict the entire nuclear dynamics during a photochemical process.

This chapter is organised as follows. I first define the two-state two-dimensional model Hamiltonian and the light-matter interaction Hamiltonian with and without the Condon approximation in Sec. 3.2. In the same section, I also highlight some important considerations on the model and provide the computational details. I then present the results of this *in-silico* photochemical experiment, starting with the more conventional BO picture (Sec. 3.3) and then moving to the EF (Sec. 3.4). An additional topic that this chapter addresses is the representation of an *in-silico* photochemical experiment using purely the concept of nuclear trajectories, which will allow opening a broader discussion on the steps towards excited-state molecular dynamics simulations. In Sec. 3.5, nuclear trajectories are used for nonadiabatic dynamics in the context of the EF, since well-defined nuclear forces can be identified and provide a clear distinction between classical and quantum trajectories.

3.2 Presentation of the two-state two-dimensional model

3.2.1 Computational details

A two-dimensional, two-state molecular model is used for this study. In the diabatic representation, the general form of the Hamiltonian is given by

$$\hat{\mathbf{H}}^{\mathrm{dia}}(\boldsymbol{R}) = \hat{T}_{\mathrm{n}}(\boldsymbol{R})\mathbf{1} + \begin{pmatrix} V_{11}(\boldsymbol{R}) & V_{12}(\boldsymbol{R}) \\ V_{12}(\boldsymbol{R}) & V_{22}(\boldsymbol{R}) \end{pmatrix}, \tag{3.1}$$

with the following diabatic electronic energies:

$$\begin{aligned} V_{11}(\boldsymbol{R}) &= \frac{k_X}{2}(X - X_1)^2 + \frac{k_Y}{2}Y^2 \\ V_{22}(\boldsymbol{R}) &= \frac{k_X}{2}(X - X_2)^2 + \frac{k_Y}{2}Y^2 + \Delta \\ V_{12}(\boldsymbol{R}) &= \gamma Y \exp(-\alpha(X - X_3)^2)\exp(-\beta Y^2), \end{aligned} \tag{3.2}$$

using $\boldsymbol{R} = (X, Y)$. The parameters $k_X = 0.02\ E_h a_0^{-2}$, $k_Y = 0.1\ E_h a_0^{-2}$, $\Delta = 0.01\ E_h$, $\gamma = 0.01\ E_h a_0^{-1}$, $\alpha = 3\ a_0^{-2}$, and $\beta = 1.5\ a_0^{-2}$, $M_X = 20000.0\ m_e$, and $M_Y = 6667.0\ m_e$ are based on Refs. [201, 202], and here, it was set that $X_1 = 6\ a_0$, $X_2 = 2\ a_0$, and $X_3 = 3.875\ a_0$.

Nuclear wavepackets are propagated with numerically-exact quantum dynamics, using for the initial state a Gaussian function with widths $\sigma_X = 0.15\ a_0^{-1}$ and $\sigma_Y = 0.197\ a_0^{-1}$ initialised in the adiabatic ground electronic state with zero initial nuclear momentum. The nuclear wavefunction is initially positioned at the Franck-Condon (FC) point $\boldsymbol{R}_{\mathrm{init}} = (2.0, 0.0)\ a_0$.

The external time-dependent electric field of a laser pulse under study here is given by

$$\mathbf{E}(t) = \boldsymbol{\varepsilon}^{\lambda} B_0 \exp\left(-\frac{(t - t_0)^2}{T^2}\right)\left(-2\frac{(t - t_0)}{T^2} \cdot \sin(\omega t) + \omega\cos(\omega t)\right), \tag{3.3}$$

with amplitude $B_0 = 0.065\ \hbar(ea_0)^{-1}$, centered at $t_0 = 350.0\ \hbar E_h^{-1}$, with duration $T = 141.421356\ \hbar E_h^{-1}$, and frequency $\omega = 0.15\ E_h\hbar^{-1}$. $\boldsymbol{\varepsilon}^{\lambda}$ is the polarisation vector, set to $\frac{1}{\sqrt{2}}(1.0, 1.0)$ for all calculations. The transition dipole moment in the diabatic representation is chosen as $\boldsymbol{\mu}_{12}(\boldsymbol{R}) = (f_X(X - X_0), f_Y(Y - Y_0))$, with $f_X = 0.2\ e$, $f_Y = 2.0\ e$, $X_0 = -1.0\ a_0$

and $Y_0 = -0.5\ a_0$. In the Condon approximation, $\boldsymbol{\mu}_{12}(\boldsymbol{R} = \boldsymbol{R}_{\text{init}})$ is used. The diagonal elements of the dipole operator are set to zero.

The full time-dependent Schrödinger equation is solved numerically in the diabatic representation employing a split-operator formalism[203,204] with a time step of 0.01 $\hbar E_h^{-1}$. A spatial grid of 800 points per coordinate is used over the range $X \in [0.0, 8.0]\ a_0$ and $Y \in [-2.0, 2.0]\ a_0$. Diabatic quantities are consequently transformed to give all the respective EF quantities of interest, namely the time-dependent vector potential (TDVP) and the time-dependent potential energy surface (TDPES), as discussed in Sec. 3.2.2 The phase factor $[\zeta(\boldsymbol{R}, t)]$ is here absorbed into the phase $[\mathcal{S}(\boldsymbol{R}, t)]$ of the nuclear wavefunction $[\chi(\boldsymbol{R}, t) = |\chi(\boldsymbol{R}, t)| \exp[(i/\hbar)\mathcal{S}(\boldsymbol{R}, t)]]$ and the gauge is chosen so that the nuclear wavefunction is real and non-negative, i.e., $\chi(\boldsymbol{R}, t) = |\chi(\boldsymbol{R}, t)|\ \forall \boldsymbol{R}, t$. The exact nuclear density is determined as the sum of the squared moduli of the diabatic nuclear wavefunctions and its positive square root yields the nuclear wavefunction $[\chi(\boldsymbol{R}, t)]$ in the chosen gauge. Using the diabatic wavefunctions and the nuclear wavefunctions, the potentials can be easily constructed as discussed previously.[74]

3.2.2 Expressing the TDVP and TDPES within a diabatic basis

The electronic Hamiltonian in this work (Eq. (3.1)) is given in the diabatic basis, thus, in the calculations the state $|\Phi(t; \boldsymbol{R})\rangle$ is represented in such a basis, and the expansion coefficients (or diabatic nuclear amplitudes) are identified as $\chi_l^{(\text{dia})}(\boldsymbol{R}, t)$. All quantities analysed in this work, namely the nuclear density, the TDPES and the TDVP, are obtained by integrating over the electronic degrees of freedom, thus by summing over the diabatic states.

The nuclear density $|\chi(\boldsymbol{R}, t)|^2$ is simply

$$|\chi(\boldsymbol{R}, t)|^2 = \sum_l \left|\chi_l^{(\text{dia})}(\boldsymbol{R}, t)\right|^2 . \tag{3.4}$$

The explicit expression of the TDPES is

$$\begin{aligned}\epsilon(\boldsymbol{R}, t) = &\langle\Phi(t; \boldsymbol{R})|\, \hat{H}_{\text{BO}}\, |\Phi(t; \boldsymbol{R})\rangle_{\boldsymbol{r}} \\ &+ \sum_{\rho=1}^{N_n} \left[\frac{\hbar^2}{2M_\rho} \left\langle \nabla_\rho \Phi(t; \boldsymbol{R})\right| \nabla_\rho \Phi(t; \boldsymbol{R})\right\rangle_{\boldsymbol{r}} - \frac{\mathbf{A}_\rho^2(\boldsymbol{R}, t)}{2M_\rho}\right] \\ &+ \langle\Phi(t; \boldsymbol{R})|\, - i\hbar\partial_t\, |\Phi(t; \boldsymbol{R})\rangle_{\boldsymbol{r}} \ .\end{aligned} \tag{3.5}$$

and can thus be decomposed as the sum of four terms $\epsilon(\boldsymbol{R},t) = \epsilon_{\mathrm{GI1}}(\boldsymbol{R},t) + \epsilon_{\mathrm{GI2}}(\boldsymbol{R},t) + \epsilon_{\mathrm{GI3}}(\boldsymbol{R},t) + \epsilon_{\mathrm{GD}}(\boldsymbol{R},t)$, the first three being gauge invariant (GI) while the last one being gauge dependent (GD) under the (gauge) transformations discussed in Sec. 2.3. Transforming the integration over $\boldsymbol{r}$ to the sum over the diabatic states, considering that the nonadiabatic coupling vectors are identically zero in this basis, and using the notation for the matrix elements of electronic Hamiltonian introduced in Eq. (3.1), the terms in the expression of the TDPES are

$$\epsilon_{\mathrm{GI1}}(\boldsymbol{R},t) = \sum_{l,k} \frac{\chi_k^{(\mathrm{dia})^*}(\boldsymbol{R},t)\chi_l^{(\mathrm{dia})}(\boldsymbol{R},t)}{|\chi(\boldsymbol{R},t)|^2} V_{kl}(\boldsymbol{R}) \tag{3.6}$$

$$\epsilon_{\mathrm{GI2}}(\boldsymbol{R},t) = \sum_{\rho} \frac{\hbar^2}{2M_\rho} \sum_{l} \left| \nabla_\rho \frac{\chi_l^{(\mathrm{dia})}(\boldsymbol{R},t)}{\chi(\boldsymbol{R},t)} \right|^2 \tag{3.7}$$

$$\epsilon_{\mathrm{GI3}}(\boldsymbol{R},t) = -\sum_{\rho} \frac{\mathbf{A}_\rho^2(\boldsymbol{R},t)}{2M_\rho} \tag{3.8}$$

$$\epsilon_{\mathrm{GD}}(\boldsymbol{R},t) = -i\hbar \sum_{l} \frac{\chi_l^{(\mathrm{dia})^*}(\boldsymbol{R},t)}{\chi^*(\boldsymbol{R},t)} \partial_t \frac{\chi_l^{(\mathrm{dia})}(\boldsymbol{R},t)}{\chi(\boldsymbol{R},t)} \,. \tag{3.9}$$

Similarly, the TDVP is given by

$$\mathbf{A}_\rho(\boldsymbol{R},t) = -i\hbar \sum_{l} \frac{\chi_l^{(\mathrm{dia})^*}(\boldsymbol{R},t)}{\chi^*(\boldsymbol{R},t)} \nabla_\rho \frac{\chi_l^{(\mathrm{dia})}(\boldsymbol{R},t)}{\chi(\boldsymbol{R},t)} . \tag{3.10}$$

While the TDPES and TDVP can be expressed in the diabatic basis, as done above, it is critical to note that they *do not* depend on any particular choice of electronic representations.

3.2.3 Some considerations on the proposed model

In this chapter, all the steps of a photochemical process are simulated explicitly for the model system discussed above, as schematically represented in Fig. 3.1. The model system consists of two two-dimensional parabolas shifted in X direction and energy. At time $t = 0$, the molecular system is in its ground vibrational state, in the FC region of the electronic ground state (point (1) in Fig. 3.1). Then, a part of the initial wavefunction is excited to the S_1 excited electronic state via the coupling of the molecule with an explicit ultrashort laser pulse whose frequency is in resonance with the S_0-to-S_1 transition (point (2) in Fig. 3.1). This photoexcitation generates a nuclear wavepacket in the excited electronic state, which will relax towards the CI and funnel through it (point (3) in Fig. 3.1). At this point, the

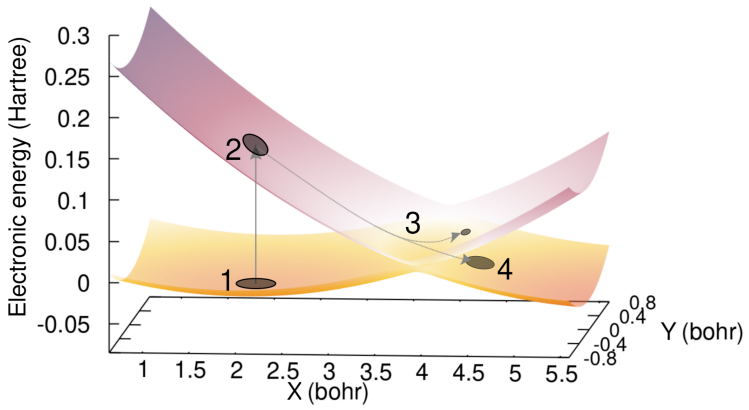

Fig. 3.1.: Schematic representation of the *in-silico* photochemical experiment discussed in this chapter. The adiabatic potential energy surfaces for the ground (S_0) and the excited (S_1) electronic states of the model are represented with a colourmap that shows positive electronic energies in purple and negative values in yellow/orange tones. The black circles and arrows indicate the different steps of the photochemical experiment: (1) initial state of the system in the FC region, (2) photoexcitation from S_0 to S_1 triggered by a laser pulse, (3) relaxation through a CI, and (4) formation of photoproducts.

nuclear wavepacket undergoes a branching, preserving some of its amplitude in the excited electronic state while a good part of it has transferred back to the ground state as a result of nonadiabatic effects, where it now evolves as a photoproduct (point (4) in Fig. 3.1).

It should be stressed at this stage that the schematic representation of a photochemical experiment depicted in Fig. 3.1 is deeply rooted in a (post) BO picture. In the following (Sec. 3.3), the details of this dynamics will be discussed in terms of time-dependent nuclear wavepackets and static potential energy surfaces, thus adopting such a BO vocabulary. In Sec. 3.4, this analysis will be revisited from the perspective of the EF, where the overall dynamics is examined in terms of a time-dependent nuclear wavepacket evolving according to a single time-dependent vector and scalar potential.

Another aspect that requires attention at this stage is the coupling of an external time-dependent electric field – here a laser pulse – to a molecule. As described above, a semiclassical approach is used here to couple an external time-dependent electric field to the molecular dipole operator. Introducing a given basis for the electronic states – once more preserving here a BO picture – yields couplings between the time-dependent electric field and the transition dipole moment between the pair of electronic states considered (here S_0 and S_1) $[\boldsymbol{\mu}_{12}(\boldsymbol{R})]$. The magnitude and direction of the transition dipole moment depend on the nuclear position, as depicted by the colourmap and white arrows in the left panel of Fig. 3.2. This $\boldsymbol{R}$-dependence of the transition dipole moment implies that, within the long-wavelength approximation, the time-dependent electric field *cannot* be

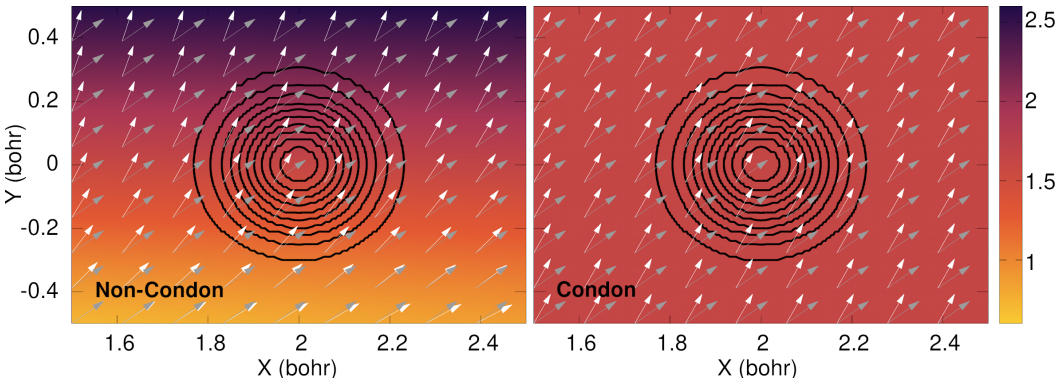

Fig. 3.2.: Representation of the transition dipole moment (white arrows give its direction and colourmap its intensity in ea_0) in the non-Condon case (left panel) and Condon case (right panel), around the FC region. The gray arrows indicate the polarisation vector of the time-dependent electric field. The black contour lines show the nuclear density of the initial wavefunction at time $t = 0$.

considered as always aligned with the transition dipole moment (see grey arrows in Fig. 3.2, symbolising the electric-field polarisation vector) and one has to take the scalar product between the two quantities. The situation when the explicit $\boldsymbol{R}$-dependence of the transition dipole moment is accounted for will be referred to as 'non-Condon' in the following. The Condon approximation proposes to consider the transition dipole moment as a constant, set to its value at the FC point $[\boldsymbol{\mu}_{12}(\boldsymbol{R}_{\mathrm{FC}})]$ (right panel of Fig. 3.2). Hence, only within the Condon approximation, it is valid to consider that the time-dependent electric field is always polarised along the transition dipole moment, for all nuclear configurations (note that this is not the case in the present chapter).

In the non-Condon case, the strength of the coupling between the molecular system and the time-dependent electric field, given by

$$\mathbf{V}^{(\mathrm{dia})}(\boldsymbol{R}, t) = \begin{pmatrix} 0 & -\boldsymbol{\mu}_{12}(\boldsymbol{R}) \cdot \mathbf{E}(t) \\ -\boldsymbol{\mu}_{12}(\boldsymbol{R}) \cdot \mathbf{E}(t) & 0 \end{pmatrix}, \tag{3.11}$$

depends on $\boldsymbol{R}$ as well. Conversely, in the Condon approximation the relative orientation of the transition dipole moment and the polarisation vector of the time-dependent electric field is constant, leading to a $\boldsymbol{R}$-independent coupling term in the Hamiltonian.

3.3 Photochemical experiment in the Born-Oppenheimer picture

3.3.1 Nuclear dynamics

In a BO picture (as introduced generally and depicted for a one-dimensional case in the theory section 2.2) , the overall dynamics of an electronically-excited molecule is analysed by following the evolution of nuclear wavepackets on the potential energy surfaces (as depicted schematically in Fig. 3.1). At time $t = 0$ the nuclear wavefunction is a stationary state in the adiabatic ground state S_0 (first column in Fig. 3.3). The interaction with the time-dependent external field – *laser pulse* in the following – induces the electronic excitation of part of the original wavefunction to the first excited state S_1 (second column in Fig. 3.3). The state created in S_1 is a nuclear wavepacket, which evolves and decays back to the ground state through the CI (third column in Fig. 3.3).

First, let us investigate the quantum dynamics obtained in the non-Condon case (upper two rows of panels in Fig. 3.3). The colourmap shows the potential energy of the S_1 (top row) and S_0 (second row from top) states, and the location of two critical points of the potential energy surfaces – the FC point and CI – are marked throughout the plots with a cross and triangle for reference. Focusing on the BO picture of a photochemical process, the potential energy surfaces of the two adiabatic states do not move or change during the dynamics, but can rather be seen as the electronic landscape on the support of which the nuclear wavepackets evolve. The nuclear densities associated with the S_0 and S_1 states are superimposed onto the respective potentials in Fig. 3.3 and indicated as red and purple contour lines, respectively. At time $t = 0$, the complete nuclear density is found in the S_0 state without any contribution in S_1. During the photoexcitation by the laser pulse ($t = 10.2$ fs in Fig. 3.3), nuclear amplitude is transferred to the excited electronic state. In addition, it can be observed that the nuclear contribution remaining in the ground electronic state is also affected by the action of the laser pulse. Once the short laser pulse is over, the excited portion of the nuclear wavepacket relaxes on the S_1 potential energy surface, and at $t = 31.5$ fs reaches the CI (last column in Fig. 3.3). At this precise moment, part of the nuclear density transfers to the S_0 electronic state due to the influence of nonadiabatic effects. Interestingly, the portion of the nuclear wavepacket that remains in the FC region in S_0 formed a nodal line as a result of the photoexcitation process. This

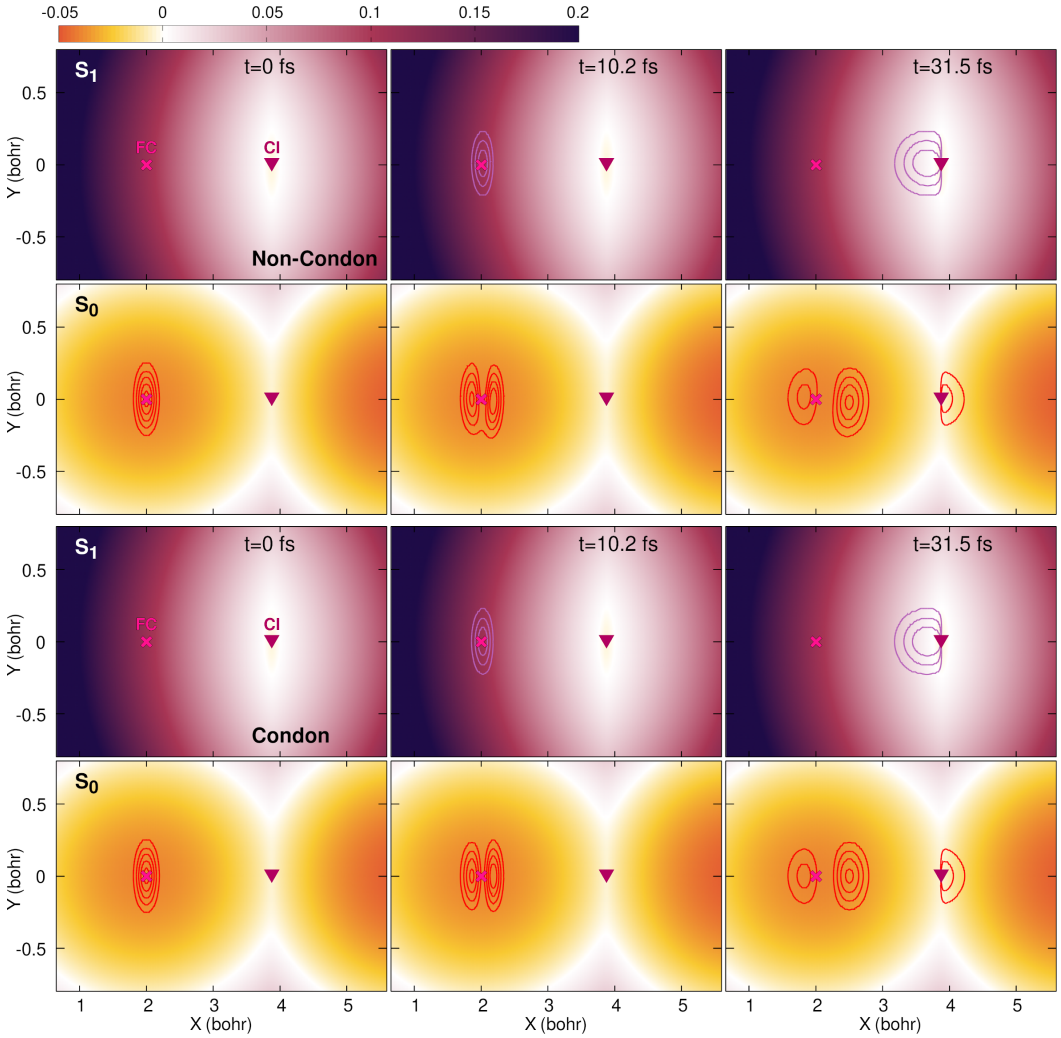

Fig. 3.3.: Snapshots of the nonadiabatic quantum dynamics at times 0, 10.2 and 31.5 fs (from left to right). The colourmaps indicate the (adiabatic) electronic energies of the S_1 and S_0 electronic states (see labels) in hartree (E_h). The adiabatic contribution to the nuclear density in each electronic state for the three snapshots is indicated by red ($|\chi_{S_0}(\boldsymbol{R},t)|^2$) and purple ($|\chi_{S_1}(\boldsymbol{R},t)|^2$) contour lines. The FC point is indicated by a magenta cross and the location of the CI by a burgundy triangle.

nodal line is somehow tilted, that is, not parallel to the Y-axis (see red contour lines on the second row, last column panel of Fig. 3.3).

Within the Condon approximation (bottom two rows in Fig. 3.3), the potential energy surfaces remain identical to the non-Condon case but the transition dipole moment – and as explained above the interaction Hamiltonian – is no more $\boldsymbol{R}$-dependent. The overall dynamics is very similar to the one observed in the non-Condon case, with the main difference being that the nodal line, observed after the laser pulse on the ground-state nuclear wavepacket, appears to be parallel to the Y-axis, rather than tilted as in the non-Condon case. This feature can be clearly observed at times $t = 10.2$ fs and $t = 31.5$ fs in the S_0 portion of the nuclear density (bottom panels of Fig. 3.3).

It is worth commenting further on the development of the nodal line in the ground-state portion of the nuclear wavefunction after the laser pulse. This nodal line suggests the formation of a higher vibrational eigenstate in the electronic ground state in the FC region. The asymmetry of the nuclear density in S_0 observed at $t = 31.5$ fs testifies from the anharmonic nature of the S_0 potential energy surface for the low vibrational states. From a more general perspective, this observation unravels an interesting question related to the analysis of a photochemical experiment, where the outcome of a light-induced process – photoproducts or hot ground-state molecules – are thought to be coming from the excited-state dynamics following photoexcitation. This observation hints towards the possibility of forming vibrationally-excited molecules without nonadiabatic processes, simply as a result of the coupling with a laser pulse. However, nonadiabatic dynamics simulations are often initiated directly from the formed nuclear wavepacket in a given excited electronic state, neglecting the remaining ground-state nuclear amplitude. While that is often an adequate approximation, the simple example presented here could indicate that the influence of a laser pulse on the contribution remaining in the ground electronic state may not be negligible.

3.3.2 Analysis of the nuclear dynamics

A more quantitative analysis of the photochemical dynamics described in Section 3.3.1 can be obtained by monitoring the electronic population evolution and the formation of photoproducts (Fig. 3.4).

Initially, the electronic population is fully in the ground state (see left panel of Fig. 3.4). Due to the coupling between the molecule and the laser pulse, the population starts to be

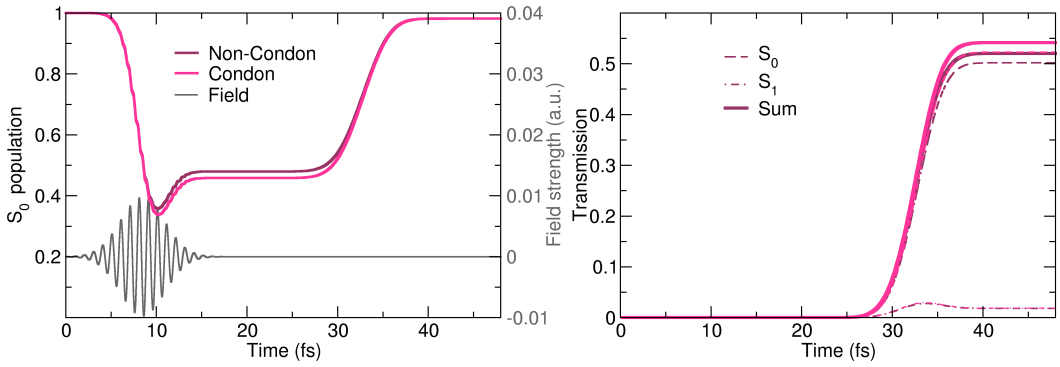

Fig. 3.4.: Left panel: Time trace of the ground-state (S_0) population for the non-Condon (purple) and Condon (magenta) quantum dynamics simulations, and strength of the electric component of the laser pulse (gray line) in E_h/ea_0. Right panel: Time trace of the transmission probability through the CI for the non-Condon (purple lines) and Condon simulation (magenta lines). Solid lines indicate the total (S_0+S_1) probability, while the dashed (dotted) lines give the S_0 (S_1) population contribution.

transferred to the excited state just before 5 fs. A maximum of around 64% (non-Condon) and 67% (Condon) of the population is excited to S_1 at $t = 10.2$ fs, shortly after the laser pulse reaches its maximum intensity. The ground-state population subsequently plateaus at 48% (non-Condon) and 46% (Condon). After 26 fs, the excited-state population starts to decay back to the ground state as the S_1 nuclear wavepacket reaches the CI (see discussion above in Sec. 3.3.1). This ground-state population finally reaches a final plateau at about 98% after about 39 fs. Overall, the evolution of the ground-state population is very similar in the non-Condon and Condon quantum dynamics simulations, with only minor quantitative differences emerging.

It is important at this stage to stress that the electronic population dynamics reported in the left panel of Fig. 3.4 and discussed above is a *representation-dependent* quantity. In other words, this quantity is not (strictly speaking) an observable and the assignment of an adiabatic electronic state is intrinsically linked to the BO picture. Hence, the earlier observations are complemented with an analysis of the evolution of the nuclear density in the configuration space. To this end, the transmission probability through the CI along the reaction coordinate (along X) is calculated, based on the proposition that X_{CI}, i.e., the position of the CI in the X coordinate, delimits two regions: the photoreactant region ($X < X_{CI}$) and the photoproduct region ($X > X_{CI}$). Therefore, the formation of photoproducts can be estimated by integrating the nuclear density over all values of Y and for $X > 3.86\ a_0$ (that is, $X > X_{CI}$). In the case of a real photochemical experiment, the formation of photoproducts could be probed,[196] and the passage through a CI can open up

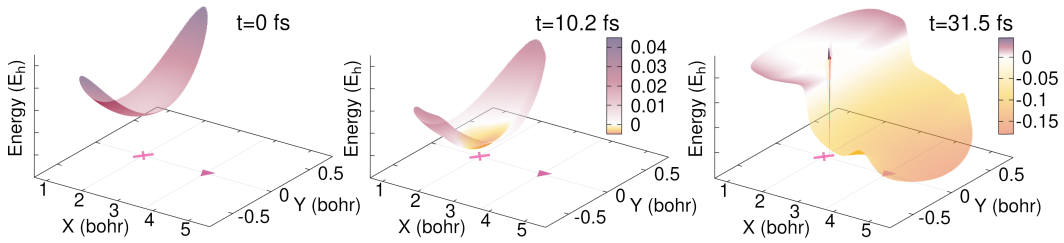

Fig. 3.5.: Schematic representation of the full TDPES at three different times during the dynamics: 0 fs, 10.2 fs, and 31.5 fs. The position of the FC (magenta cross) point and CI (burgundy triangle) are marked for reference. The colourbar is given in hartree (E_h) and its negative range has been extended for the t = 31.5 fs snapshot. The TDPES is represented only in the regions of nuclear configuration space where the total nuclear density is 10^{-8} or larger.

pathways on the ground electronic state that would have been inaccessible by thermal evolution.

The transmission probability for the non-Condon and Condon cases is shown in the right panel of Fig. 3.4. Within the Condon approximation, 54.2% of the population is transferred to the photoproduct region. In the non-Condon case, this value is slightly lower, reaching 52.0%. The transmission probability can be decomposed in ground- and excited-state contributions, going back to a BO picture. The majority of the photoproducts are formed in their ground state, 50.2% (non-Condon) and 52.3% (Condon). Hence, the slight differences between non-Condon and Condon excitations observed in the representation-dependent population dynamics are reflected in this 'representation-free' observable.

3.4 Photochemical experiment in the exact-factorisation picture

Having discussed this *in-silico* photochemical experiment from a BO perspective, the findings are reinterpreted in the following using the tools offered by the EF picture by transforming the diabatic quantities to the TDVP and TDPES as described in Sec. 3.2.2. The representation of the EF proposes to replace the concepts of static potential energy surfaces associated with adiabatic electronic states and their nonadiabatic couplings by a single TDPES and TDVP. With the EF, one moves away from the representation of multiple electronic states visited by time-dependent nuclear wavefunctions and focus solely on a single nuclear wavefunction evolving under the influence of the single TDPES and TDVP.

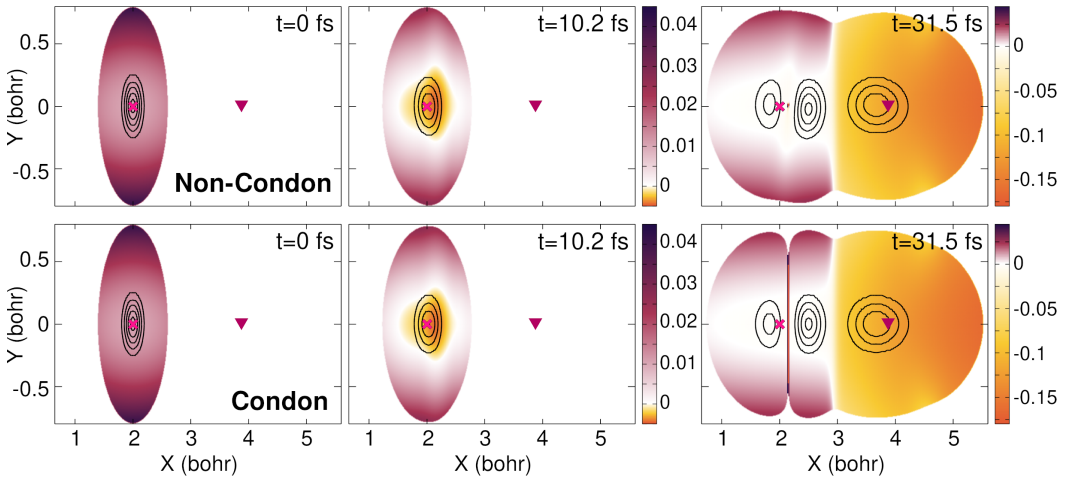

Fig. 3.6.: Time-dependent potential energy surface at three different times – 0, 10.2 and 31.5 fs (from left to right) – for the non-Condon (top row) and Condon quantum dynamics (bottom row). The colourbar is given in hartree (E_h). The nuclear density is superimposed (black contour lines). The position of the FC (magenta cross) point and CI (burgundy triangle) are marked for reference.

This picture was introduced and the features depicted generally for a one-dimensional case in the section 2.3 of the Theory chapter.

For the non-Condon dynamics, Fig. 3.5 depicts schematically the behaviour of the TDPES for the three same times along the dynamics as in the previous section, i.e., $t = 0, 10.2, 31.5$ fs. At time $t = 0$, the TDPES exhibits a single well in the FC region, basically reproducing the shape of the S_0 potential energy surface in this region (see Fig. 3.1). When the laser pulse is interacting with the molecule ($t = 10.2$ fs in Fig. 3.5), the minimum of the TDPES gets lower in energy and becomes asymmetrical around the FC point. This distortion is due to the fact that the TDPES includes the effect of the time-dependent external field via $v_{\text{int}}(\boldsymbol{R}, t)$ (see Sec. 2.3). At later times ($t = 31.5$ fs in Fig. 3.5), the TDPES develops a step, separating the two portions of the nuclear wavepacket: one portion is localised in the FC region while the second one can be found in the vicinity of the CI. In addition, the nodal line observed for the nuclear wavefunction in the FC region is reflected in the TDPES as a potential barrier, reaching high positive and negative values. This section provides a deeper analysis of the TDPES and its companion the TDVP for the studied photochemical experiment.

3.4.1 Nuclear and electronic dynamics

As in Sec. 3.3, the quantum dynamics obtained with and without invoking the Condon approximation are compared, but this time from an EF perspective.

Let us first focus on the evolution of the TDPES. In Fig. 3.6, the full TDPES is plotted as a colourmap with superimposed black contour lines indicating the areas where the (full) nuclear density is mainly localised. At $t = 0$, both the non-Condon and the Condon simulations show an identical picture, where the TDPES shows a minimum around the centre of the initial nuclear wavefunction and is curved upwards to higher energies towards the borders, mainly reproducing the shape of the S_0 potential energy surface (as discussed above for Fig. 3.5). When the laser pulse reaches its maximum intensity (at around $t = 10.2$ fs), the TDPES is lower in energy in the area just around the centre of the nuclear wavefunction in comparison to the previously shown time step, where the yellow/orange areas correspond to negative energy values. At this time step, no significant differences appear between the TDPES computed with and without the Condon approximation. Later in time, after the laser pulse (Fig. 3.6, $t = 31.5$ fs), a step appears within the TDPES: the portion of the TDPES with $X > 3\ a_0$ is significantly lower than that at $X < 3\ a_0$. Furthermore, a marked difference between the non-Condon and Condon calculations emerges when looking at the TDPES in the region where the nodal line appears on the nuclear wavefunction around the FC position. In the non-Condon case, a localised peak can be observed between the two portions of the nuclear wavefunction, whereas a barrier forms within the Condon approximation, almost parallel to the Y-axis and stretching all through the TDPES. It is worth stressing that the interesting features of the TDPES at $t = 31.5$ fs are all localised around the FC point and caused by the formation of an eigenstate in this portion of the configuration. The TDPES in the region where a CI would be observed in the BO picture is blatantly featureless, basically leading the nuclear wavepacket towards the photoproduct region ($X > X_{\mathrm{CI}}$).

The TDPES is one of the time-dependent quantities of interest within the EF. Another key ingredient of this formalism is the TDVP. For a physical understanding of the TDVP, it is important to note that the nuclear momentum field computed from the molecular wavefunction $[\Psi(\boldsymbol{r}, \boldsymbol{R}, t)]$ can be decomposed as the sum of a curl-free contribution, which is related to the phase $[\mathcal{S}(\boldsymbol{R}, t)]$ of the nuclear wavefunction $[\chi(\boldsymbol{R}, t)]$, and a (in general) not-irrotational contribution, which is given by the TDVP $[\boldsymbol{A}_\rho(\boldsymbol{R}, t)]$. Thus, in the chosen gauge, where $\mathcal{S}(\boldsymbol{R}, t) = 0$, the TDVP is equivalent to the nuclear momentum field.

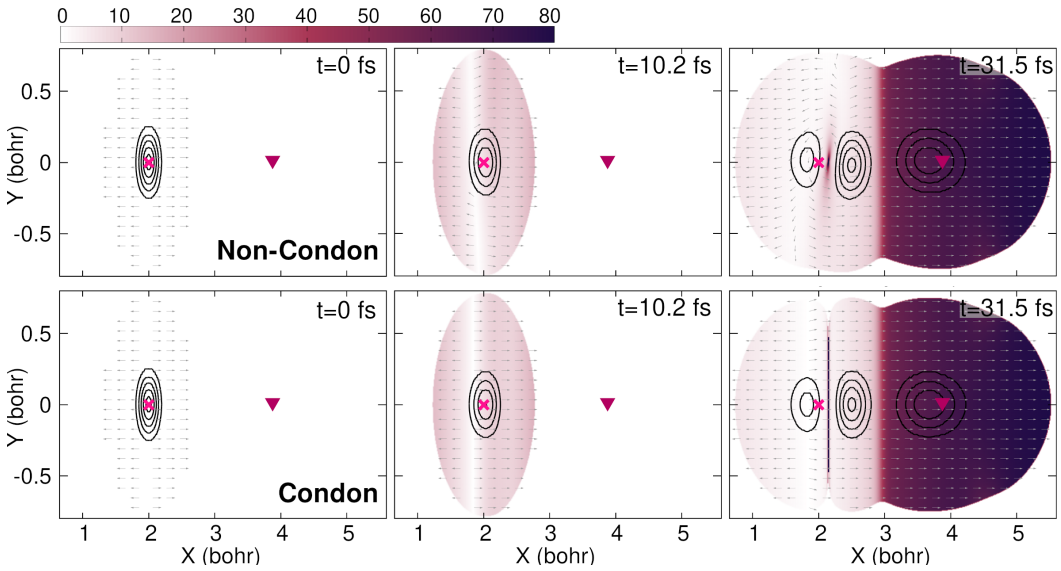

Fig. 3.7.: Time-dependent vector potential at three different times – 0, 10.2 and 31.5 fs (from left to right) – for the non-Condon (top row) and Condon quantum dynamics (bottom row). The colourmap indicates the absolute value of the TDVP in $\hbar/a_0$, while the gray unit vectors show the orientation of the vector potential. The nuclear density is superimposed (black contour lines). The position of the FC (magenta cross) point and CI (burgundy triangle) are marked for reference.

Fig. 3.7 shows the TDVP for the three critical times of the dynamics, with and without the Condon approximation. At time $t = 0$, the magnitude of the TDVP is very small. This can be understood from the definition of the initial condition for the dynamics, which is the ground vibrational state for the ground electronic state, at FC point. From a quantum trajectory perspective, the momentum field corresponding to a nuclear (real) eigenstate would be zero everywhere.[205] During the excitation, the TDVP increases in magnitude and triggers the dynamics of the nuclear wavepacket. Conversely to the earlier observations with the TDPES, the TDVP already develops some differences at $t = 10.12$ fs depending on the use of the Condon approximation or not. In the non-Condon simulation, the TDVP shows a non-negligible contribution along the Y-direction, while within the Condon approximation such contribution is almost zero and the vector potential has components only along the X-axis (see unit arrows in Fig. 3.7). In both cases, however, one can observe an abrupt change of direction of the TDVP along the X-axis at around $X = 1.9\ a_0$, for all values of Y. At $t = 31.5$ fs, the TDVP develops two clear portions. In the region $X > 3\ a_0$, the TDVP shows overall a larger magnitude. In this region, the nuclear wavepacket is indeed pushed towards larger X values following the slope of the TDPES. Interestingly, and consistently with the observation on the TDPES, this portion of

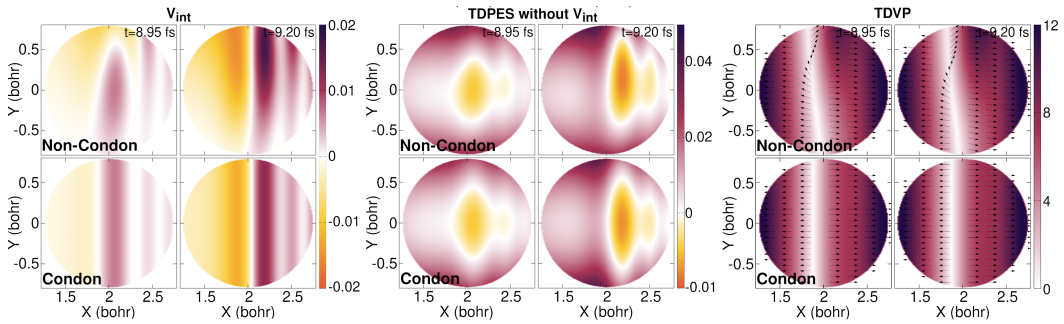

Fig. 3.8.: Time-dependent potential energy surface and vector potential during the laser pulse, for the non-Condon (top row of each panel) and Condon (bottom row of each panel) dynamics. Left panel: v_{int} – contribution to the TDPES coming from an external potential (here the interaction between the laser pulse and the molecule). Middle panel: TDPES without the external potential. Right panel: TDVP, where the colourmap indicates the absolute value, while the black unit vectors show the orientation. The FC point is indicated by a magenta cross in all plots. Colorbars for the left and middle panels are given in hartree (E_h), while that of the right panel is given in $\hbar/a_0$.

the TDVP is smooth and does not reveal any features that would testify from a specific electron-nuclear coupling. This observation is particularly important if one considers that, in the BO picture, the nuclear wavepacket is passing through a CI at this specific time (see Fig. 3.3). Such a behaviour of the TDPES and the TDVP simply highlights that the coupled electron-nuclear dynamics presented here should be seen as a non-event – with a molecule simply relaxing in energy, driven by the TDPES and TDVP. However, a BO picture enforces the description of this process with adiabatic electronic states, which are not representative of a single electronic character. As a result, the S_1 nuclear wavepacket in the BO picture suffers a nearly singular nonadiabatic coupling to transfer to the S_0 electronic state, hence preserving its electronic character. Conical intersections and singular nonadiabatic coupling terms, therefore, emanate from the intrinsic limitations posed by the adiabatic representation of the BO picture, and the EF remedies naturally to this issue by eliminating the notion of electronic states altogether.

Around the FC position, the TDVP shows significantly smaller values at $t = 31.5$ fs, highlighting the rather stationary nature of the portion of the nuclear wavefunction localised in this region (Fig. 3.7). In the region around $X = 2.1$ a_0, where the nuclear density splits, an intense localised peak appears on the TDVP in the non-Condon case while the Condon simulation leads to the appearance of an intense 'delocalised' barrier, parallel to the Y-axis. In the non-Condon case, the unit vectors of the TDVP betray the fact that the nuclear wavepacket is somehow rotating around $X = 2.1, Y = 0$ a_0.

To further unravel the differences observed in the TDPES and TDVP for the non-Condon *versus* Condon treatment of quantum dynamics, the TDPES is decomposed into $\epsilon(\boldsymbol{R}, t)$ and $v_{\text{int}}(\boldsymbol{R}, t)$ at two times close to the maximum of the field envelop. The time 8.95 fs corresponds to a snapshot before the electric field of the laser pulse reaches a maximum while the other snapshot, $t = 9.20$ fs, is just after the maximum is passed. Fig. 3.8 presents a zoom of the TDPES and TDVP around the FC region for these two specific times. Looking only at the contribution to the TDPES coming from the coupling of the laser pulse to the molecule – $v_{\text{int}}(\boldsymbol{R}, t)$ in Eq. (2.29) ('v_{int}', left panels in Fig. 3.8) – it can be observed in the non-Condon case that an anisotropy along the Y-direction is created, absent in the Condon approximation. This anisotropy is also visible in the term $\epsilon(\boldsymbol{R}, t)$ (TDPES without v_{int}, middle panels in Fig. 3.8), where for instance the negative contributions of the TDPES are not symmetric along the Y-direction in the non-Condon case. The variation of the TDPES caused by the interferences between the two components of the nuclear wavefunction is reminiscent of the observations of interferences in nonadiabatic processes.[206] Zooming on the TDVP (right panels of Fig. 3.8) highlights some additional interesting features. The TDVP already exhibits strong contributions along the Y-direction at the early stage of the dynamics in the non-Condon case, when the laser pulse is present, while in the Condon case no Y-contribution can be observed. The line along which the X-component of the TDVP changes sign is not parallel to the Y-axis in the non-Condon simulation, conversely to the Condon one.

The observations presented in this section show that the EF formalism offers an alternative perspective of a photochemical process to the conventional BO picture. The contribution to the molecular Hamiltonian coming from the light-matter interaction is fully encoded in the TDPES, and the evolution of the nuclear wavepacket is driven by the (single) TDPES and TDVP, which, in turn, encode the effect of the electronic dynamics on the nuclei. In the particular gauge chosen in this chapter, the TVDP is identified as the nuclear momentum field. Furthermore, it was highlighted how the combined effects of the TDPES and TDVP induce the splitting of the nuclear wavepacket into two portions in the FC region, resembling the formation of a higher vibrational state of the electronic ground-state potential. Instead, the TDPES and TDVP are smooth where, in the BO picture, the nuclear wavepacket passes through a CI and suffers singular nonadiabatic couplings.

The EF and its time-dependent potential also highlight another interesting fact about photochemistry and photophysics. The presence of potential energy surfaces in a BO

picture invites us to think of photochemical processes similarly to chemical reactions in the ground electronic state: by looking at these static potentials and possibly looking at their critical points and how they connect via minimum-energy paths. However, it is crucial to realise that such concepts are often not sufficient or valid to understand a given photochemical process.[163] In other words, a molecule does not have *per se* a defined photochemical reactivity, but such a photochemical reactivity depends on the initialisation of the process (type of photoexcitation) and the following out-of-equilibrium dynamics on the coupled potential energy surfaces. The EF highlights this fact by exhibiting different time-dependent potentials even for subtly different photochemical dynamics (here, simply employing or not the Condon approximation).

3.5 Analysis of a photochemical process with trajectories

Since the EF encodes all the coupled electron-nuclear dynamics in the TDPES and TDVP, this framework naturally lends itself to the propagation of nuclear trajectories, which can be used to further analyse the nuclear quantum dynamics without the need of introducing additional approximations. The challenge of propagating trajectories in a BO picture to describe nonadiabatic dynamics is notorious and caused by the presence of the lack of well-defined nuclear forces due to the presence of different (sometimes coupled) potential energy surfaces.[15,73]

3.5.1 Trajectory-based solution of the nuclear exact factorisation equation

As the coupled nuclear and electronic equations of motion give rise to a single TDVP and a single TDPES in the EF, one intriguing question is how one can exploit this characteristic and represent the nuclear probability density with trajectories evolving based on the two potentials. Previous works[204,207] showed that by inserting the polar form of the nuclear wavefunction $[\chi(\boldsymbol{R},t) = |\chi(\boldsymbol{R},t)| \exp(\frac{i}{\hbar}\mathcal{S}(\boldsymbol{R},t))]$ into the time-dependent Schrödinger

equation, one can derive an evolution equation for the phase that can furthermore be identified as a (nuclear) Hamilton-Jacobi equation (with $\nabla_{\boldsymbol{R}_\rho}\mathcal{S}(\boldsymbol{R},t)=\tilde{\boldsymbol{P}}_\rho(\boldsymbol{R},t)$):

$$-\frac{\partial}{\partial t}\mathcal{S}(\boldsymbol{R},t)=H_{\mathrm{n}}(\tilde{\boldsymbol{P}},\boldsymbol{R},t)=\sum_\rho\frac{[\tilde{\boldsymbol{P}}_\rho(\boldsymbol{R},t)+\boldsymbol{A}_\rho(\boldsymbol{R},t)]^2}{2M_\rho} + \epsilon(\boldsymbol{R},t)+v_{\mathrm{int}}(\boldsymbol{R},t)+\sum_\rho\frac{-\hbar^2}{2M_\rho}\frac{\nabla_\rho^2|\chi(\boldsymbol{R},t)|}{|\chi(\boldsymbol{R},t)|}\,. \tag{3.12}$$

The last term on the right-hand side is the so-called quantum potential $[Q_{\mathrm{pot}}(\boldsymbol{R},t)]$ which is responsible for an important portion of the nuclear quantum effects. The term containing the nuclear momentum field $[\boldsymbol{P}_\rho(\boldsymbol{R},t)=\tilde{\boldsymbol{P}}_\rho(\boldsymbol{R},t)+\boldsymbol{A}_\rho(\boldsymbol{R},t)]$ is the nuclear kinetic energy and the sum $[\epsilon(\boldsymbol{R},t)+v_{\mathrm{int}}(\boldsymbol{R},t)+Q_{\mathrm{pot}}(\boldsymbol{R},t)]$ represents the potential energy. As discussed in an earlier work,[204] this Hamilton-Jacobi partial differential equation can be solved by using the method of characteristics. This results in Hamilton-like evolution equations (which are, an *a priori* infinite, set of ordinary differential equations) for the trajectories $[\boldsymbol{R}(t)\equiv\{\boldsymbol{R}_\rho(t)\}_{\rho=1,\ldots,N_{\mathrm{n}}}]$, with corresponding momenta $[\boldsymbol{P}(t)\equiv\{\boldsymbol{P}_\rho(t)\}_{\rho=1,\ldots,N_{\mathrm{n}}}]$:

$$\dot{\boldsymbol{R}}_\rho(t)=\frac{\tilde{\boldsymbol{P}}_\rho(t)+\boldsymbol{A}_\rho(\boldsymbol{R}(t),t)}{M_\rho} \tag{3.13}$$

$$\dot{\tilde{\boldsymbol{P}}}_\rho(t)=-\nabla_{\boldsymbol{R}_\rho}H_{\mathrm{n}}(\tilde{\boldsymbol{P}}(t),\boldsymbol{R}(t),t)\,, \tag{3.14}$$

or equivalently

$$\dot{\boldsymbol{R}}_\rho(t)=\frac{\boldsymbol{P}_\rho(t)}{M_\rho} \tag{3.15}$$

$$\dot{\boldsymbol{P}}_\rho(t)=-\nabla_{\boldsymbol{R}_\rho}H_{\mathrm{n}}(\boldsymbol{P}(t),\boldsymbol{R}(t),t)+\dot{\mathbf{A}}_\rho(\boldsymbol{R}(t),t)\,. \tag{3.16}$$

Enforcing the choice of gauge for this work $[\mathcal{S}(\boldsymbol{R},t)=0]$ in the characteristics representation of the nuclear dynamics, yields that Eqs. (3.13) and (3.14) simplify to

$$\dot{\boldsymbol{R}}_\rho(t)=\frac{\boldsymbol{A}_\rho(\boldsymbol{R}(t),t)}{M_\rho} \tag{3.17}$$

$$\dot{\tilde{\boldsymbol{P}}}_\rho(t)=0\,, \tag{3.18}$$

proving that the TDVP fully accounts for the nuclear momenta of the trajectories. It is worth noting that, within the EF, the nuclear momentum field computed with $\Psi(\boldsymbol{r},\boldsymbol{R},t)$ is

the sum of a curl-free term – the gradient of $\mathcal{S}(\boldsymbol{R}, t)$ – and a (in general not irrotational) contribution due to the TDVP, as shown in Ref. [73]. With the choice of gauge used in this work, the irrotational part becomes zero. The following section will present an analytical proof of the identity given in Eq. (3.18) and show that, in the chosen gauge, $\nabla_{\boldsymbol{R}_\rho} H_\mathrm{n}(\tilde{\boldsymbol{P}}(t), \boldsymbol{R}(t), t) = 0$.

Propagating trajectories either using solely Eq. (3.17) or the coupled Eqs. (3.15) and (3.16) yields what is referred to as *quantum trajectories*. In particular, Eq. (3.17) corresponds to the Bohmian definition of the velocity field for quantum-mechanical particles described by a real wavefunction in the presence of an external vector potential.[208] By neglecting the quantum potential in $H_\mathrm{n}(\boldsymbol{P}(t), \boldsymbol{R}(t), t)$, the nuclear Hamiltonian becomes classical, i.e., $H_\mathrm{n}^\mathrm{cl}(\boldsymbol{P}(t), \boldsymbol{R}(t), t)$. This classical approximation is used when integrating Eqs. (3.15) and (3.16) to generate *classical trajectories*. The corresponding evolution equations for the classical trajectories then read

$$\dot{\boldsymbol{R}}_\rho(t) = \frac{\boldsymbol{P}_\rho(t)}{M_\rho} \tag{3.19}$$

$$\dot{\boldsymbol{P}}_\rho(t) = -\nabla_{\boldsymbol{R}_\rho} H_\mathrm{n}^\mathrm{cl}(\boldsymbol{P}(t), \boldsymbol{R}(t), t) + \dot{\mathbf{A}}_\rho(\boldsymbol{R}(t), t)\,. \tag{3.20}$$

Nuclear forces for the quantum trajectories

In this section, Eq. (3.18) of the previous section is proven by demonstrating that, within the chosen gauge [$\mathcal{S}(\boldsymbol{R}, t) = 0$], $\nabla_{\boldsymbol{R}_\rho} H_\mathrm{n}(\tilde{\boldsymbol{P}}, \boldsymbol{R}, t) = 0$.

The nuclear Hamiltonian identified in the Hamilton-Jacobi equation in Eq. (3.12) reads

$$H_\mathrm{n}(\boldsymbol{R}, t) = \sum_\rho \frac{\boldsymbol{A}_\rho(\boldsymbol{R}, t)^2}{2M_\rho} + \epsilon(\boldsymbol{R}, t) + v_\mathrm{int}(\boldsymbol{R}, t) + \sum_\rho \frac{-\hbar^2}{2M_\rho} \frac{\nabla_\rho^2 |\chi(\boldsymbol{R}, t)|}{|\chi(\boldsymbol{R}, t)|}\,, \tag{3.21}$$

when imposing the gauge as $\tilde{\boldsymbol{P}} = 0$. Following its definition given in Sec. 2.3, the time-dependent scalar potential [$\epsilon(\boldsymbol{R}, t)$] is

$$\begin{aligned}\epsilon(\boldsymbol{R}, t) = &\langle \Phi(t; \boldsymbol{R})|\, \hat{H}_\mathrm{BO}(\boldsymbol{R})\, |\Phi(t; \boldsymbol{R})\rangle_{\boldsymbol{r}} + \sum_\rho \frac{\hbar^2}{2M_\rho} \langle \nabla_{\boldsymbol{R}_\rho} \Phi(t; \boldsymbol{R}) | \nabla_{\boldsymbol{R}_\rho} \Phi(t; \boldsymbol{R})\rangle_{\boldsymbol{r}} \\ &- \sum_\rho \frac{\boldsymbol{A}_\rho(\boldsymbol{R}, t)^2}{2M_\rho} + \langle \Phi(t; \boldsymbol{R})| - i\hbar \frac{\partial}{\partial t} |\Phi(t; \boldsymbol{R})\rangle_{\boldsymbol{r}}\,,\end{aligned} \tag{3.22}$$

where the second and third terms follows from the $\hat{U}_\mathrm{en}[\Phi, \chi](\boldsymbol{R}, t)$ contribution. The third term of Eq. (3.22) cancels out with the kinetic energy in Eq. (3.21) and it is identified

$\epsilon_{\mathrm{BO}}(\boldsymbol{R},t) = \epsilon_{\mathrm{GI1}}(\boldsymbol{R},t)$ and $\epsilon_{\mathrm{bBO}}(\boldsymbol{R},t) = \epsilon_{\mathrm{GI2}}(\boldsymbol{R},t)$. As a result, the full nuclear Hamiltonian reads:

$$H_{\mathrm{n}}(\boldsymbol{R},t) = \epsilon_{\mathrm{BO}}(\boldsymbol{R},t) + \epsilon_{\mathrm{bBO}}(\boldsymbol{R},t) + \epsilon_{\mathrm{GD}}(\boldsymbol{R},t) + v_{\mathrm{int}}(\boldsymbol{R},t) + Q_{\mathrm{pot}}(\boldsymbol{R},t) \tag{3.23}$$

with

$$\epsilon_{\mathrm{BO}}(\boldsymbol{R},t) = \langle \Phi(t;\boldsymbol{R})|\, \hat{H}_{\mathrm{BO}}(\boldsymbol{R})\, |\Phi(t;\boldsymbol{R})\rangle_{\boldsymbol{r}} \tag{3.24}$$

$$\epsilon_{\mathrm{bBO}}(\boldsymbol{R},t) = \sum_{\rho} \hbar^2 \frac{\langle \nabla_{\boldsymbol{R}_\rho}\Phi(t;\boldsymbol{R})|\nabla_{\boldsymbol{R}_\rho}\Phi(t;\boldsymbol{R})\rangle_{\boldsymbol{r}}}{(2M_\rho)} \tag{3.25}$$

$$\epsilon_{\mathrm{GD}}(\boldsymbol{R},t) = \langle \Phi(t;\boldsymbol{R})|\, -i\hbar\partial_t\, |\Phi(t;\boldsymbol{R})\rangle_{\boldsymbol{r}} \tag{3.26}$$

It is easy to prove that, while $\epsilon_{\mathrm{BO}}(\boldsymbol{R},t)$ (BO term) and $\epsilon_{\mathrm{bBO}}(\boldsymbol{R},t)$ (beyond-BO term) are gauge-invariant contributions, since they remain unchanged if the electronic wavefunction is modified by a phase factor that only depends on $\boldsymbol{R}$ and t, $\epsilon_{\mathrm{GD}}(\boldsymbol{R},t)$ is gauge-dependent (GD).[73] Furthermore, it might seem that in the chosen gauge the nuclear Hamiltonian is purely potential energy. This is not actually the case, since it has been shown in Refs. [67, 209] that $\epsilon_{\mathrm{bBO}}(\boldsymbol{R},t)$ contributes to the nuclear kinetic energy – despite appearing as a scalar potential included in the expression of $\epsilon(\boldsymbol{R},t)$.

With the aim to manipulate previous equations, here the definition of the electronic wavefunction as $\Phi(\boldsymbol{r},t;\boldsymbol{R}) = \frac{\Psi(\boldsymbol{r},\boldsymbol{R},t)}{|\chi(\boldsymbol{R},t)|}$ is used. This expression is inserted into the definitions of the $\epsilon_{\mathrm{BO}}(\boldsymbol{R},t)$ and $\epsilon_{\mathrm{GD}}(\boldsymbol{R},t)$ potentials. Writing explicitly the expectation values as integrals over the electronic configuration space, this yields for these contributions

$$\epsilon_{\mathrm{BO}}(\boldsymbol{R},t) = \frac{1}{|\chi(\boldsymbol{R},t)|^2}\int \mathrm{d}\boldsymbol{r}\Psi^*(\boldsymbol{r},\boldsymbol{R},t)\hat{H}_{\mathrm{BO}}(\boldsymbol{r},\boldsymbol{R})\Psi(\boldsymbol{r},\boldsymbol{R},t) \tag{3.27}$$

$$\begin{aligned}\epsilon_{\mathrm{GD}}(\boldsymbol{R},t) &= \int \mathrm{d}\boldsymbol{r}\frac{\Psi^*(\boldsymbol{r},\boldsymbol{R},t)}{|\chi(\boldsymbol{R},t)|}(-i\hbar\frac{\partial}{\partial t})\frac{\Psi(\boldsymbol{r},\boldsymbol{R},t)}{|\chi(\boldsymbol{R},t)|} \\ &= \int \mathrm{d}\boldsymbol{r}\frac{\Psi^*(\boldsymbol{r},\boldsymbol{R},t)}{|\chi(\boldsymbol{R},t)|}(-i\hbar)\frac{(\frac{\partial}{\partial t}\Psi(\boldsymbol{r},\boldsymbol{R},t))|\chi(\boldsymbol{R},t)| - \Psi(\boldsymbol{r},\boldsymbol{R},t)\frac{\partial}{\partial t}|\chi(\boldsymbol{R},t)|}{|\chi(\boldsymbol{R},t)|^2} \\ &= \frac{1}{|\chi(\boldsymbol{R},t)|^2}\int \mathrm{d}\boldsymbol{r}\Psi^*(\boldsymbol{r},\boldsymbol{R},t)(-i\hbar\frac{\partial}{\partial t})\Psi(\boldsymbol{r},\boldsymbol{R},t)\,.\end{aligned} \tag{3.28}$$

The second term in $\epsilon_{\mathrm{GD}}(\boldsymbol{R},t)$, being purely imaginary, is identically zero since the whole expression is purely real.

The contribution to the time-dependent scalar potential arising from the external field, i.e., $v_{\text{int}}(\boldsymbol{R}, t)$, can also be rewritten as

$$v_{\text{int}}(\boldsymbol{R}, t) = \frac{1}{|\chi(\boldsymbol{R}, t)|^2} \int \mathrm{d}\boldsymbol{r} \Psi^*(\boldsymbol{r}, \boldsymbol{R}, t) \hat{V}_{\text{ext}}(\boldsymbol{r}, \boldsymbol{R}, t) \Psi(\boldsymbol{r}, \boldsymbol{R}, t) \,. \tag{3.29}$$

The "kinetic" part of the time-dependent scalar potential, $\epsilon_{\text{bBO}}(\boldsymbol{R}, t)$, becomes

$$\begin{aligned} \epsilon_{\text{bBO}}(\boldsymbol{R}, t) &= \sum_{\rho} \frac{\hbar^2}{2M_\rho} \int \mathrm{d}\boldsymbol{r} \left(\nabla_{\boldsymbol{R}_\rho} \Phi(\boldsymbol{r}, t; \boldsymbol{R}) \right)^* \left(\nabla_{\boldsymbol{R}_\rho} \Phi(\boldsymbol{r}, t; \boldsymbol{R}) \right) \\ &= \sum_{\rho} \frac{\hbar^2}{2M_\rho} \left[\nabla_{\boldsymbol{R}_\rho} \int \mathrm{d}\boldsymbol{r} \Phi^*(\boldsymbol{r}, t; \boldsymbol{R}) \nabla_{\boldsymbol{R}_\rho} \Phi(\boldsymbol{r}, t; \boldsymbol{R}) - \int \mathrm{d}\boldsymbol{r} \Phi^*(\boldsymbol{r}, t; \boldsymbol{R}) \nabla^2_{\boldsymbol{R}_\rho} \Phi(\boldsymbol{r}, t; \boldsymbol{R}) \right] . \end{aligned} \tag{3.30}$$

Here, the chain rule for the derivative with respect to $\boldsymbol{R}_\rho$, namely $\nabla_{\boldsymbol{R}_\rho}$, is used. Applying once more the chain rule to the first term on the right-hand side of Eq. (3.30) yields

$$\begin{aligned} &\int \mathrm{d}\boldsymbol{r} \Phi^*(\boldsymbol{r}, t; \boldsymbol{R}) \nabla_{\boldsymbol{R}_\rho} \Phi(\boldsymbol{r}, t; \boldsymbol{R}) \\ &\quad = \nabla_{\boldsymbol{R}_\rho} \int \mathrm{d}\boldsymbol{r} \Phi^*(\boldsymbol{r}, t; \boldsymbol{R}) \Phi(\boldsymbol{r}, t; \boldsymbol{R}) - \int \mathrm{d}\boldsymbol{r} \left(\nabla_{\boldsymbol{R}_\rho} \Phi(\boldsymbol{r}, t; \boldsymbol{R}) \right)^* \Phi(\boldsymbol{r}, t; \boldsymbol{R}) \,. \end{aligned} \tag{3.31}$$

Using the partial normalisation condition $[\int d\boldsymbol{r} |\Phi(\boldsymbol{r}, t; \boldsymbol{R})|^2 = 1 \; \forall \boldsymbol{R}, t]$ to show that the first term on the right-hand side of Eq. (3.31) is identically zero, implies that

$$\int \mathrm{d}\boldsymbol{r} \Phi^*(\boldsymbol{r}, t; \boldsymbol{R}) \nabla_{\boldsymbol{R}_\rho} \Phi(\boldsymbol{r}, t; \boldsymbol{R}) = - \int \mathrm{d}\boldsymbol{r} \left(\nabla_{\boldsymbol{R}_\rho} \Phi(\boldsymbol{r}, t; \boldsymbol{R}) \right)^* \Phi(\boldsymbol{r}, t; \boldsymbol{R}) \,, \tag{3.32}$$

proving that Eq. (3.32) is purely imaginary. However, $\epsilon_{\text{bBO}}(\boldsymbol{R}, t)$ is real overall, which implies that such purely imaginary contribution, from the first integral in its definition (Eq. (3.30)), should be canceled out exactly by the imaginary part of its second term. As a result, Eq. (3.30) can be rewritten as

$$\epsilon_{\text{bBO}}(\boldsymbol{R}, t) = -\Re \left[\sum_{\rho} \frac{\hbar^2}{2M_\rho} \int \mathrm{d}\boldsymbol{r} \Phi^*(\boldsymbol{r}, t; \boldsymbol{R}) \nabla^2_{\boldsymbol{R}_\rho} \Phi(\boldsymbol{r}, t; \boldsymbol{R}) \right] . \tag{3.33}$$

Summarising the results obtained so far, the nuclear Hamiltonian can be expressed as

$$H_{\mathrm{n}}(\boldsymbol{R},t) = \frac{1}{|\chi(\boldsymbol{R},t)|^2}\int \mathrm{d}\boldsymbol{r}\Psi^*(\boldsymbol{r},\boldsymbol{R},t)\left(-i\hbar\frac{\partial}{\partial t}+\hat{H}_{\mathrm{BO}}(\boldsymbol{r},\boldsymbol{R})+\hat{V}_{\mathrm{ext}}(\boldsymbol{r},\boldsymbol{R},t)\right)\Psi(\boldsymbol{r},\boldsymbol{R},t) \\ -\Re\left[\sum_\rho \frac{\hbar^2}{2M_\rho}\int \mathrm{d}\boldsymbol{r}\Phi^*(\boldsymbol{r},t;\boldsymbol{R})\nabla^2_{\boldsymbol{R}_\rho}\Phi(\boldsymbol{r},t;\boldsymbol{R})\right]+Q_{\mathrm{pot}}(\boldsymbol{R},t)\,. \tag{3.34}$$

Note that the first integral of Eq. (3.34) can be simplified using the time-dependent Schrödinger equation. In fact, the operator in parenthesis equals (minus) the nuclear kinetic energy, i.e., $(-i\hbar\frac{\partial}{\partial t}+\hat{H}_{\mathrm{BO}}(\boldsymbol{r},\boldsymbol{R})+\hat{V}_{\mathrm{ext}}(\boldsymbol{r},\boldsymbol{R},t)) = -\hat{T}_{\mathrm{n}}(\boldsymbol{R})$, and the whole integral is (minus) the expectation value of $\hat{T}_{\mathrm{n}}(\boldsymbol{R})$ over the molecular wavefunction. Hence, now one can define the condition for (the nuclear gradient of) $H_{\mathrm{n}}(\boldsymbol{R},t)$ to be equal to zero:

$$-\Re\left[\sum_\rho \frac{\hbar^2}{2M_\rho}\int \mathrm{d}\boldsymbol{r}\Phi^*(\boldsymbol{r},t;\boldsymbol{R})\nabla^2_{\boldsymbol{R}_\rho}\Phi(\boldsymbol{r},t;\boldsymbol{R})\right] \\ \stackrel{!}{=}\sum_\rho \frac{-\hbar^2}{2M_\rho}\int \mathrm{d}\boldsymbol{r}\frac{\Psi^*(\boldsymbol{r},\boldsymbol{R},t)\nabla^2_{\boldsymbol{R}_\rho}\Psi(\boldsymbol{r},\boldsymbol{R},t)}{|\chi(\boldsymbol{R},t)|^2}-Q_{\mathrm{pot}}(\boldsymbol{R},t)\,. \tag{3.35}$$

Using once again the definition of $\Phi(\boldsymbol{r},t;\boldsymbol{R})$ in terms of the molecular and nuclear wavefunctions, and applying $\nabla^2_{\boldsymbol{R}_\rho}$ on the left-hand side of Eq. (3.35), yields

$$-\sum_\rho \frac{\hbar^2}{2M_\rho}\int \mathrm{d}\boldsymbol{r}\Phi^*(\boldsymbol{r},t;\boldsymbol{R})\nabla^2_{\boldsymbol{R}_\rho}\Phi(\boldsymbol{r},t;\boldsymbol{R}) \\ =-\sum_\rho \frac{\hbar^2}{2M_\rho}\int \mathrm{d}\boldsymbol{r}\frac{\Psi^*(\boldsymbol{r},\boldsymbol{R},t)}{|\chi(\boldsymbol{R},t)|}\left(\frac{\nabla^2_{\boldsymbol{R}_\rho}\Psi(\boldsymbol{r},\boldsymbol{R},t)}{|\chi(\boldsymbol{R},t)|}-\frac{2\nabla_{\boldsymbol{R}_\rho}\Psi(\boldsymbol{r},\boldsymbol{R},t)\nabla_{\boldsymbol{R}_\rho}|\chi(\boldsymbol{R},t)|}{|\chi(\boldsymbol{R},t)|^2}\right. \\ \left.-\frac{\Psi(\boldsymbol{r},\boldsymbol{R},t)\nabla^2_{\boldsymbol{R}_\rho}|\chi(\boldsymbol{R},t)|}{|\chi(\boldsymbol{R},t)|^2}+\frac{2\Psi(\boldsymbol{r},\boldsymbol{R},t)\left(\nabla_{\boldsymbol{R}_\rho}|\chi(\boldsymbol{R},t)|\right)^2}{|\chi(\boldsymbol{R},t)|^3}\right) \\ =\sum_\rho \frac{\hbar^2}{2M_\rho}\left(-\int \mathrm{d}\boldsymbol{r}\frac{\Psi^*(\boldsymbol{r},\boldsymbol{R},t)\nabla^2_{\boldsymbol{R}_\rho}\Psi(\boldsymbol{r},\boldsymbol{R},t)}{|\chi(\boldsymbol{R},t)|^2}+\frac{\nabla^2_{\boldsymbol{R}_\rho}|\chi(\boldsymbol{R},t)|}{|\chi(\boldsymbol{R},t)|}\right. \\ \left.+2\int \mathrm{d}\boldsymbol{r}\frac{\Psi^*(\boldsymbol{r},\boldsymbol{R},t)\nabla_{\boldsymbol{R}_\rho}\Psi(\boldsymbol{r},\boldsymbol{R},t)}{|\chi(\boldsymbol{R},t)|^2}\frac{\nabla_{\boldsymbol{R}_\rho}|\chi(\boldsymbol{R},t)|}{|\chi(\boldsymbol{R},t)|}-2\frac{(\nabla_{\boldsymbol{R}_\rho}|\chi(\boldsymbol{R},t)|)^2}{|\chi(\boldsymbol{R},t)|^2}\right). \tag{3.36}$$

Therefore, the condition given by Eq. (3.35) would be fulfilled if, by taking the real part of Eq. (3.36), the last two terms would cancel out.

To show that, the real part of the contribution depending on the full molecular wavefunction is investigated, where $\Psi(\boldsymbol{r}, \boldsymbol{R}, t) = \Phi(\boldsymbol{r}, t; \boldsymbol{R})|\chi(\boldsymbol{R}, t)|$ is used, namely

$$\begin{aligned}\Re\left[\int \mathrm{d}\boldsymbol{r} \frac{\Psi^*(\boldsymbol{r}, \boldsymbol{R}, t)}{|\chi(\boldsymbol{R}, t)|} \frac{\nabla_{\boldsymbol{R}_\rho}\Psi(\boldsymbol{r}, \boldsymbol{R}, t)}{|\chi(\boldsymbol{R}, t)|}\right] &= \Re\left[\int \mathrm{d}\boldsymbol{r}\Phi^*(\boldsymbol{r}, t; \boldsymbol{R})\nabla_{\boldsymbol{R}_\rho}\Phi(\boldsymbol{r}, t; \boldsymbol{R})\right] \\ &+\Re\left[\int \mathrm{d}\boldsymbol{r}\Phi^*(\boldsymbol{r}, t; \boldsymbol{R})\Phi(\boldsymbol{r}, t; \boldsymbol{R}) \frac{\nabla_{\boldsymbol{R}_\rho}|\chi(\boldsymbol{R}, t)|}{|\chi(\boldsymbol{R}, t)|}\right] \end{aligned} \tag{3.37}$$

The first term on the right-hand side of Eq. (3.37) is identically zero as it is purely imaginary (see Eq. (3.32)); the integral in the second term yields 1 thanks to the partial normalisation condition. This results in

$$\Re\left[\int \mathrm{d}\boldsymbol{r} \frac{\Psi^*(\boldsymbol{r}, \boldsymbol{R}, t)\nabla_{\boldsymbol{R}_\rho}\Psi(\boldsymbol{r}, \boldsymbol{R}, t)}{|\chi(\boldsymbol{R}, t)|^2} \frac{\nabla_{\boldsymbol{R}_\rho}|\chi(\boldsymbol{R}, t)|}{|\chi(\boldsymbol{R}, t)|}\right] = \frac{(\nabla_{\boldsymbol{R}_\rho}|\chi(\boldsymbol{R}, t)|)^2}{|\chi(\boldsymbol{R}, t)|^2}, \tag{3.38}$$

proving that when taking the real part of the last two terms of Eq. (3.36), they exactly cancel out. Therefore, the condition posed by Eq. (3.35) is fulfilled, as stated above.

Finally it can be shown that the nuclear Hamiltonian of Eq. (3.34) is zero in the chosen gauge

$$\begin{aligned} H_{\mathrm{n}}(\boldsymbol{R}, t) =& \frac{\langle\Psi(\boldsymbol{R}, t)| - i\hbar\frac{\partial}{\partial t} + \hat{H}_{\mathrm{BO}}(\boldsymbol{R}) + \hat{V}_{\mathrm{ext}}(\boldsymbol{R}, t) + \hat{T}_{\mathrm{n}}(\boldsymbol{R})\,|\Psi(\boldsymbol{R}, t)\rangle_{\boldsymbol{r}}}{|\chi(\boldsymbol{R}, t)|^2} \\ &- Q_{\mathrm{pot}}(\boldsymbol{R}, t) + Q_{\mathrm{pot}}(\boldsymbol{R}, t) = 0\,, \end{aligned} \tag{3.39}$$

meaning that its gradient is zero as well.

3.5.2 Computational details for the quantum and classical trajectories

For the quantum and classical trajectory dynamics, the 1000 initial nuclear positions are sampled from the probability density given by the initial nuclear wavefunction. Special care needs to be taken when selecting the initial nuclear momenta. While for classical trajectories, nuclear positions and momenta can be regarded as independent variables, this is no more the case for quantum trajectories – their nuclear position and momentum at each time step are related. As shown above, the nuclear momentum at time t and position $\boldsymbol{R}$ is given by the TDVP $\boldsymbol{A}(\boldsymbol{R}, t)$. Thus, the 1000 initial nuclear momenta for the sampled initial nuclear positions $\boldsymbol{R}_0$ are given by $\boldsymbol{A}(\boldsymbol{R}_0, 0)$. For classical trajectories,

the initial nuclear momenta are sampled from the momentum probability distribution computed from the Wigner transform of the initial nuclear wavefunction (in position representation). For the propagation of the trajectories, a time-step of 10 $\hbar E_h^{-1}$ is used, and one uses the exact time-dependent vector and scalar potentials as obtained from the quantum dynamics. The time-dependent potentials are not (numerically) available when the nuclear density is small ($< 10^{-8}$). Furthermore, classical trajectories are propagated according to the force computed as (minus) the gradient of the time-dependent scalar potential. Therefore, numerical errors due to the calculation of the nuclear gradients can cause the trajectories to move in a region of space where the time-dependent potential is not available. Those trajectories need to be removed from the ensemble. For this dynamics, an energy-conservation criterion can be used to remove such unstable trajectories. To this end, it was imposed that the classical energy should be conserved within a deviation of 0.01 E_h from the initial value at the end of the laser pulse. A maximum of 51 classical trajectories has been excluded based on this criterion in any of the simulations. It is noted that the propagation of the quantum and classical trajectories in this framework was based on the previously obtained exact quantities (TDVP and TDPES) which both require knowledge of the full nuclear denisty.

3.5.3 Analysis of the trajectories

As discussed above, quantum trajectories can be propagated easily within the EF by using the TDVP as a nuclear momentum field, integrating Eq. (3.17). While the initial nuclear positions can be randomly sampled from the initial nuclear density, the initial nuclear momenta have to be chosen as $\boldsymbol{A}(\boldsymbol{R}_0, t = 0)$ (where $\boldsymbol{R}_0$ stands for the whole set of initial positions), as positions and momenta are not independent variables. 1000 quantum trajectories are propagated using the TDVP calculated at all times from the quantum dynamics simulations, without and with the Condon approximation.

As expected from their definition, the quantum trajectories follow closely the nuclear density of the quantum wavepacket at all three times previously discussed (see Fig. 3.9). Only the results for the non-Condon dynamics are shown as the Condon ones are very similar. Several observations can be made by looking at the time evolution of the quantum trajectories in the non-Condon case (as shown in the movies of the Supporting Information of Ref. [70]). First, it can be seen that the motion of the quantum trajectories is dominated by an evolution in the X direction. Second, the trajectories forming the two split portions

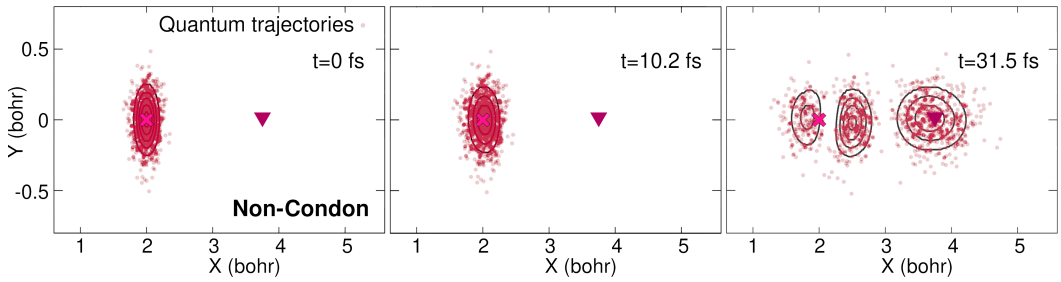

Fig. 3.9.: Positions of the quantum trajectories at three different times – 0, 10.2 and 31.5 fs (from left to right) – for a non-Condon dynamics. The full nuclear density from the quantum dynamics is superimposed (black contour lines). The position of the FC (magenta cross) point and CI (burgundy triangle) are marked for reference.

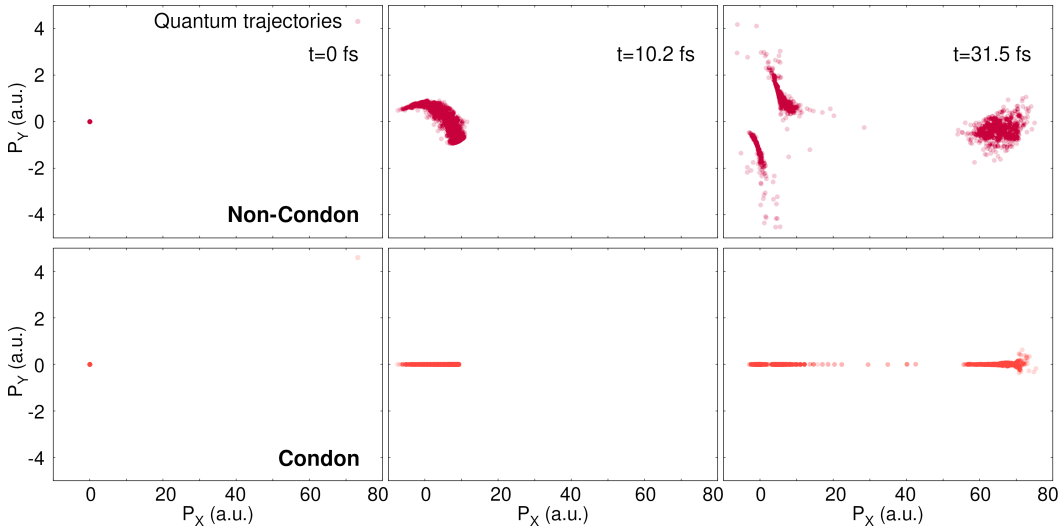

Fig. 3.10.: Components of the nuclear momentum in X (P_X) and Y (P_Y) for each quantum trajectory at three different times – 0, 10.2 and 31.5 fs (from left to right) – for a non-Condon (top row) and Condon (bottom row) dynamics. The label a.u. stands for $\hbar/a_0$.

of the nuclear wavepacket that remain in the vicinity of the FC region appear to rotate around a point close to the initial position of the nuclear wavefunction (but not exactly at the FC point due to the anharmonicity of the potential energy surface in this region). Such behaviours were predicted earlier based on the analysis of the shape of the TDVP (see Sec. 3.4.1). Conversely, within the Condon approximation, the quantum trajectories representing the nuclear wavepacket around the FC region do not significantly move once the splitting is complete. This behaviour further supports the stationary nature of the driving wavefunction in this region and attests that the Y-contribution of the momentum field is almost zero at later times in this region (as observed in Fig. 3.7).

The distribution of the nuclear momenta for each quantum trajectory of the swarm highlights striking differences between the non-Condon and Condon dynamics at all

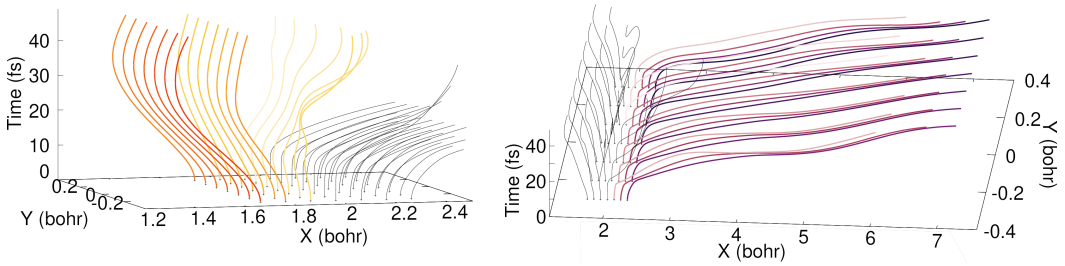

Fig. 3.11.: Traces of quantum trajectories in space and time for the non-Condon dynamics. These quantum trajectories were specially initialised on an equally-spaced grid in configuration space to enhance clarity. The left panel shows in yellow/orange the trajectories remaining in the FC region. The right panel depicts in pink/purple the trajectories moving away from the FC region to reach the photoproduct region. The same trajectories are shown in both panels.

times (Fig. 3.10). At $t = 0$, the TDVP is very small in magnitude, i.e., close to zero, which is why the distribution of initial momenta appears highly localised around (0.0,0.0). Subsequently, the quantum trajectories acquire larger momenta and start spreading to finally be distributed in three distinct areas by $t = 31.5$ fs in the non-Condon case (top right panel in Fig. 3.10). The first group of trajectories shows large (positive) values for P_X – between 60 and 80 $\hbar a_0^{-1}$ – and represents the photoproduct trajectories. Two groups of trajectories with comparably smaller P_X values spread along two lines, reaching values of $-4\ \hbar a_0^{-1}$ or $4\ \hbar a_0^{-1}$ for P_Y. These last two groups depict the slow quantum trajectories in the region where a stationary state is formed. The distribution of nuclear momenta for the dynamics conducted within the Condon approximation looks significantly different to the non-Condon case described above (bottom row in Fig. 3.10). At $t = 10.2$ fs, all the trajectories have a dominant X-contribution to their nuclear momenta. At $t = 31.5$ fs, a partition of the trajectories in momentum space is visible, as observed in the non-Condon case, forming two main groups – trajectories with a large P_X value, and those with smaller momenta in the X direction. Note that the group with a smaller P_X contribution appears to be further split at the same position in X as in the non-Condon case. A small portion of the trajectories with very large P_X contribution at $t = 31.5$ fs also start to spread along P_Y.

The fate of the quantum trajectories over time is made clearer by plotting their traces in time and space (Fig. 3.11). Note that the quantum trajectories presented here were initialised from an equally-spaced grid to improve the clarity of the plots in Fig. 3.11. The trace representation of the quantum trajectories highlights the presence of two groups of quantum trajectories: the remainders that evolve around the FC region (left panel of Fig. 3.11) and the leavers that translate the formation of photoproducts (right panel of

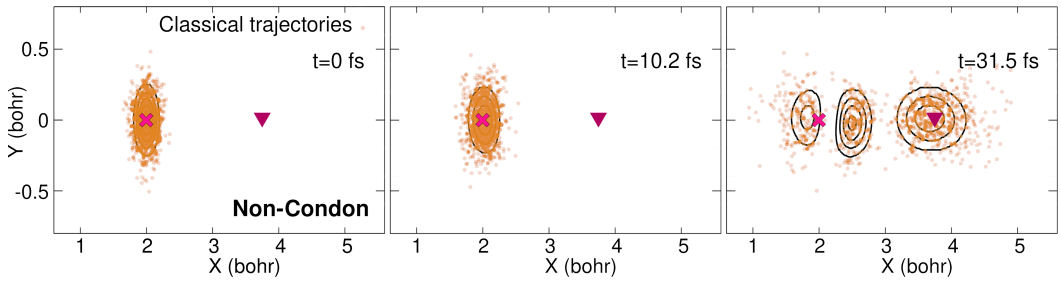

Fig. 3.12.: Positions of the classical trajectories at three different times – 0, 10.2 and 31.5 fs (from left to right) – for a non-Condon dynamics. The full nuclear density from the quantum dynamics is superimposed (black contour lines). The position of the FC (magenta cross) point and CI (burgundy triangle) are marked for reference.

Fig. 3.11). Interestingly, it appears from this analysis that quantum trajectories with a larger X value in the FC region are more likely to follow the photoproduct path than those started at $t = 0$ fs at a smaller value of X. This trace representation for the quantum trajectories also offers an opportunity to show that they do not cross in configuration space.[210] This non-crossing rule is a strict requirement for quantum trajectories and a direct consequence of the single-valuedness of the nuclear wavefunction.

An interesting feature of quantum trajectories is that they can easily be transformed into their more classical analogues by neglecting the so-called quantum potential, which acts as a non-local glue for the trajectories (see Appendix 3.5.1). Classical trajectories can therefore be propagated by using the TDPES and TDVP computed from the quantum wavepacket dynamics, but removing the contribution from the quantum potential $Q_{\text{pot}}(\boldsymbol{R}, t)$. Hence, the classical trajectories – initialised from 1000 nuclear positions and momenta sampled from a Wigner distribution – directly come from the integration of Eqs. (3.19) and (3.20).

The positions of these classical trajectories at $t = 0, 10.2, 31.5$ fs show a rather good agreement with the nuclear wavepacket (Fig. 3.12), even if it is clear by comparison with Fig. 3.9 that the classical trajectories spread more in both X and Y direction over time.* Looking at the full evolution of the classical trajectories over time further reinforces this observation (as can be seen in movies of the Supporting Information of Ref. [70]) with trajectories exhibiting important oscillations along the Y coordinate.

The projection of the classical trajectories in nuclear momentum space for the three selected times (Fig. 3.13) is strikingly different from that of the quantum trajectories discussed earlier (Fig. 3.10). The distribution of nuclear momenta for the classical trajectories is spread at all times and does not exhibit the peculiar structure observed for the quantum

*Note that the same initial positions were used for the classical and quantum trajectories.

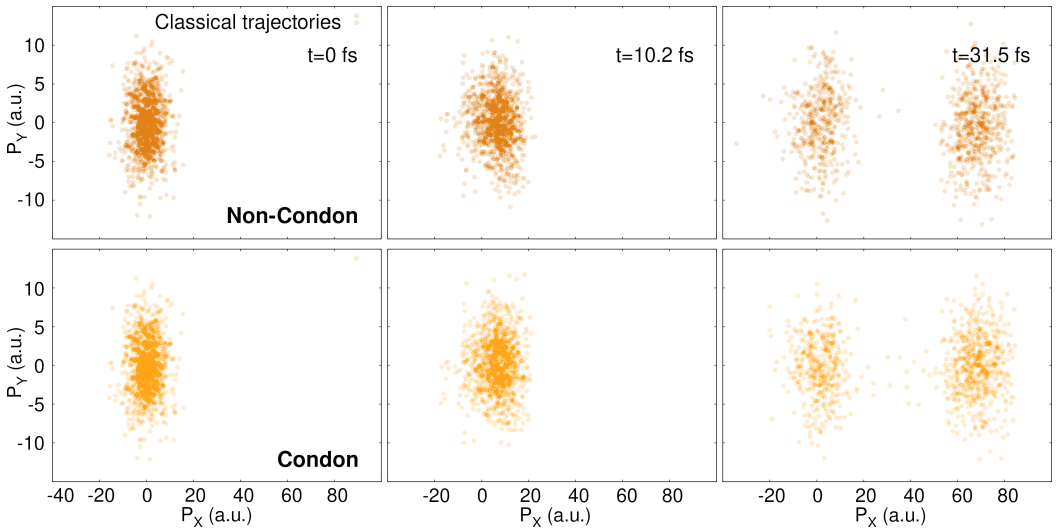

Fig. 3.13.: Components of the nuclear momentum in X (P_X) and Y (P_Y) for each classical trajectory at three different times – 0, 10.2 and 31.5 fs (from left to right) – for a non-Condon (top row) and Condon (bottom row) dynamics. The label a.u. stands for $\hbar/a_0$.

trajectories. The magnitude of the nuclear momenta is also significantly larger in the X and more specifically in the Y direction. This observation explains the oscillating behaviour in the Y coordinate described above for the classical trajectories. At $t = 31.5$ fs, the momenta distribution separates into only two regions (Fig. 3.13) – one part with momenta distributed around $P_X = 0$ while the other part is distributed around $P_X = 70\ \hbar a_0^{-1}$. Interestingly, the distribution of classical nuclear momenta in the non-Condon case closely resembles the one in the Condon case, as if the removal of the quantum potential washed out the fine differences observed during the formation of the stationary state.

To conclude this analysis, the transmission towards photoproducts is calculated, as performed in Sec. 3.3.2, but here based on the distribution of the quantum and classical trajectories over time. To this end, the trajectories with $X > 3.86\ a_0$ are counted for both quantum and classical trajectories, and in non-Condon and Condon dynamics. Quantum trajectories appear to slightly underestimate the reference transmission probability (from the quantum dynamics) by around 0.01 for the non-Condon dynamics and 0.02 for the Condon dynamics (left panel of Fig. 3.14). The classical trajectories overestimate the transmission probability in both non-Condon and Condon cases by 0.04 and 0.05, respectively (right panel of Fig. 3.14). This deviation is marginal and both quantum and classical trajectory-based dynamics reproduce reasonably well the qualitative evolution of the nuclear density while providing quantitative good estimates for the transmission

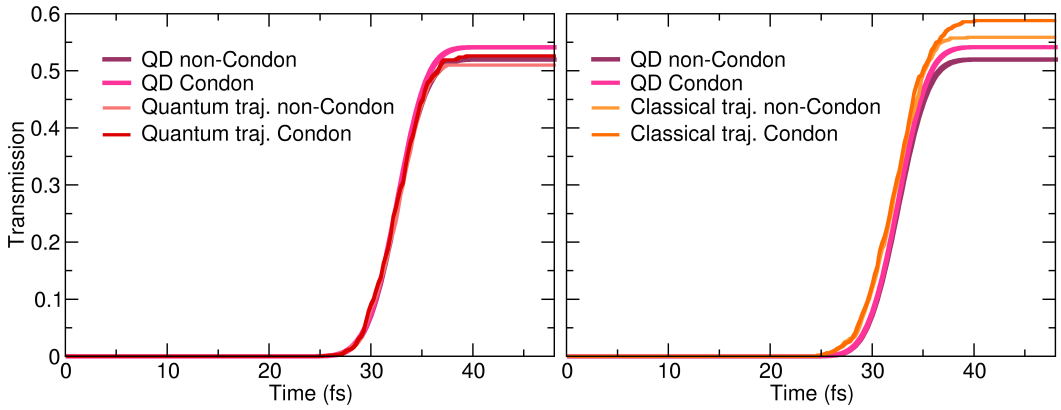

Fig. 3.14.: Time trace of the transmission probabilities through the line defined by $X > 3.86\ a_0$ obtained for the quantum (left panel, red lines) and classical trajectories (right panel, orange lines), in the non-Condon and Condon case. The results from quantum dynamics (QD) are given for reference (non-Condon with purple lines and Condon with magenta lines).

probability – an observable that would, for a real molecule, connect to the formation of photoproducts and thus, to the quantum yield of a photochemical reaction.

One important aspect that needs to be stressed at this point is the fact that both quantum and classical trajectories benefited from the definition of the time-dependent potentials used to propagate them thanks to the formalism of the EF (and within the choice of gauge). More specifically, simulating a full photochemical experiment as done here using quantum or classical trajectories within a BO picture would have dramatically complexified the simulations. Transfers, hops, averaging, or spawns would have to be invoked to allow the trajectories to visit different electronic states due to the influence of a laser pulse or nonadiabatic transitions. The EF simplifies that by providing the single TDPES and TDVP.

3.6 Conclusions

This chapter introduced a comparison between the BO and EF models of an *in-silico* photochemical experiment, from the initial photoexcitation with an ultrashort laser pulse to the formation of photoproducts. The extensive analysis of the subsequent photodynamics revealed how to picture a photochemical reaction in the EF formalism and how its quantities – namely the time-dependent vector and scalar potentials – behave when an external laser pulse shakes the electronic wavefunction and triggers the formation of a nuclear wavepacket. As a side-product of the excitation with a laser pulse, the formation of a stationary state could also be observed in the FC region and the corresponding behaviour

of the time-dependent potentials. The Condon approximation can alter the dynamics of the nuclear wavepacket, even if the formation of photoproducts – a representation-free quantity – does not suffer from this approximation in the presented model. Interestingly, the passage through a CI in the BO picture becomes a non-event in the EF – the singularities and degeneracies at CIs are in stark contrast with the featureless time-dependent potentials of the EF. Last but not least, one of the exciting features of the EF was highlighted in the context of a full photochemical process: the possibility to naturally introduce trajectories as an approximation for the nuclear dynamics. The propagation of these trajectories is trivial as the EF has only a single time-dependent vector and scalar potential, meaning that no hops or spawns are required to describe regions of strong nonadiabaticity. Distinguishing between classical and quantum trajectories, the suitability of using trajectories was evaluated to simulate photochemical processes with the EF and the importance of properly selecting initial conditions was highlighted.

4 Diabolical limitations of AIMS near conical intersections

This chapter is based on the publication:
L. M. Ibele and B. F. E. Curchod, "Dynamics near a conical intersection – a diabolical compromise for the approximations of ab initio multiple spawning", J. Chem. Phys. 155, 174119 (2021)

4.1 Introduction

Conical intersections are one of the most prominent features of the Born-Oppenheimer picture. These points of degeneracy of adiabatic states act as funnels for the electronic population decay and therefore, an accurate description of the nuclear dynamics in the vicinity of conical intersections (CIs) is crucial for any successful approximated nonadiabatic dynamics method. In this chapter, the influence of the approximations of the AIMS method is tested for dynamics in close proximity to a CI. To this end, a series of simple models are used in two dimensions, as this is the lowest dimensionality in which CIs arise.

Earlier works have focused on understanding the influence of the independent first generation approximation approximation (IFGA) and the saddle point approximation (SPA) in the excited-state dynamics of simple model systems.[159,164,211,212] Nevertheless, a grey area still remains around additional contributions to the coupled electron-nuclear dynamics that are typically neglected in any practical implementations of AIMS: the second-order nonadiabatic couplings (NACs) and the diagonal Born-Oppenheimer corrections (DBOCs). As AIMS proposes to perform nonadiabatic dynamics in the adiabatic representation of the electronic states, one may also enquire about the inclusion of geometric-phase (GP) effects in its formalism. Geometric (or Berry) phase effects can emerge when a nuclear wavepacket evolving on adiabatic potential energy surfaces (PESs) encircles a conical intersection (see Sec. 2.2.4).[54] The inclusion of DBOCs in the dynamics of the TBFs in AIMS has been discussed in an earlier work,[168] and the question of how the lack of GP might affect the AIMS dynamics has already been raised in the past.[213–215] No work has,

however, tested the performance of the AIMS approximations to describe the nonadiabatic dynamics through conical intersections and the influence of the missing NACs, DBOCs, and GP terms mentioned above.

In this chapter, I want to closely investigate the quality of the coupling elements between TBFs in AIMS in the context of a dynamics through a conical intersection. In particular, the attention will be focused on the neglected contributions to these coupling terms in the original formulation of AIMS. For a reasonable estimation of the capability of AIMS dynamics, a numerical comparison is carried out between AIMS, numerically-exact quantum dynamics (QD), and TSH, for a series of challenging two-state two-dimensional model systems. The model systems are parametrised to reproduce key features of the excited-state dynamics of bis(methylene)adamantyl (BMA), butatriene cation, and pyrazine.[54,61] The discussion of the quality of the results is not only based on the excited-state population traces but also the (reconstructed) ground-state nuclear densities for the different nonadiabatic methods. In addition to the fully approximate framework of AIMS, it is investigated how including NACs, DBOCs, and GP effects in the coupling terms affects the dynamics. Another aspect that is questioned is the use of Born-Huang *versus* Born-Oppenheimer PESs for the dynamics of the TBFs. Overall, it is shown how the original AIMS formalism can capture qualitatively well the excited-state dynamics on these model systems and that including additional terms challenges the existing practical approximations of AIMS.

This chapter is organised as follows. First, in Sec. 4.2 it is introduced how GP effects can be included within the AIMS framework while keeping its practical approximations and on-the-fly character. The two-state two-dimensional model systems used in this chapter are introduced and the details of the simulations are given in Sec. 4.3 The excited state population traces obtained with AIMS, numerically-exact QD, and TSH are compared and discussed for all three models in Sec. 4.4.1, before focusing on the challenging butatriene cation model and analysing the reconstructed ground-state nuclear densities (Sec. 4.4.2). Subsequently, it is shown how some of the AIMS approximations can be lifted and how the dynamics respond to the inclusion of NACs, DBOCs, and GP effects, reaching the limitations of the AIMS framework (Sec. 4.5). Additionally, in Sec. 4.6, it is shown how a propagation on BH PESs is limited by the AIMS approximations and highlights the missing GP effects. The conclusions are finally drawn in Sec. 4.7.

4.2 Inclusion of the geometric phase in AIMS for a two level system

As introduced in Sec. 2.2.4, a GP arises in the vicinity of conical intersections when using the adiabatic representation of the electronic states, i.e. the eigenfunctions of $\hat{H}_{\mathrm{BO}}(\boldsymbol{r}, \boldsymbol{R})$, $\{\Phi_J(\boldsymbol{r}; \boldsymbol{R})\}_{J=1}^{\infty}$, which depend parametrically on the nuclear coordinates. When following a closed path in (parametric) nuclear coordinates, an adiabatic electronic wavefunction acquires a phase. This phase is exactly π if the path encircles a conical intersection, leading to a change in sign of the (real) electronic wavefunction that breaks its single-valuedness. To counteract this effect and ensure that the molecular wavefunction is singled valued, one can introduce a position-dependent phase factor $[e^{i\gamma_J(\boldsymbol{R})}]$ for the corresponding nuclear wavefunction that also changes sign when encircling a conical intersection. Based on the seminal work by Mead and Truhlar[43] on the topic, this phase factor is the same for both states considered in a two-state system.Hence, one can chose $\gamma_1(\boldsymbol{R}) = \gamma_2(\boldsymbol{R}) = \gamma(\boldsymbol{R})$ for a two state-system.

The diabatic Hamiltonian of the two-state model system used for this chapter has the form

$$\hat{\mathbf{H}}_{\mathrm{dia}}(\boldsymbol{R}) = \hat{T}_{\mathrm{n}}(\boldsymbol{R})\mathbf{1} + \begin{pmatrix} V_{11}(\boldsymbol{R}) & V_{12}(\boldsymbol{R}) \\ V_{12}(\boldsymbol{R}) & V_{22}(\boldsymbol{R}) \end{pmatrix}. \tag{4.1}$$

This is in analogy to the Hamiltonian defined the Theory Sec. 2.2.2 (Eq. (2.9)). The transformation to diabatic states is mediated again by the adiabatic-to-diabatic transformation angle $\theta(\boldsymbol{R})$ (Eq. (2.12)). Closer investigation of $\theta(\boldsymbol{R})$ shows that upon encircling a conical intersection (a point of degeneracy of the adiabatic electronic eigenstates), the phase of the adiabatic electronic wavefunction (Eq. 2.11) will change by a factor of π.[43,59–63] This factor of π means that the (real) adiabatic wavefunctions, given by Eq. (2.11), will change their sign by circling around a conical intersection. This phase shift and subsequent flip of sign is a manifestation of the geometric phase.[59,60] However, the geometric phase leads to a double-valuedness of the electronic wavefunctions. For a proper description of the molecular wavefunction (which is now doubled-valued), one would need to use doubled-valued boundary conditions for the nuclear wavefunctions as well.

To perform quantum dynamics in the adiabatic representation, it can be more convenient to perform a transformation of the adiabatic molecular Hamiltonian $[\hat{H}_{\mathrm{m}}(\boldsymbol{r}, \boldsymbol{R})]$ to include the effect of a GP while keeping the standard nuclear wavefunctions.[61] As suggested by

Mead and Truhlar[43], the mixing angle $\theta(\boldsymbol{R})$ can be related to the geometric phase and the adiabatic molecular Hamiltonian can be transformed as

$$\hat{H}^{\mathrm{GP}}_{\mathrm{adi}}(\boldsymbol{R}) = e^{i\theta(\boldsymbol{R})}\hat{H}_{\mathrm{adi}}(\boldsymbol{R})e^{-i\theta(\boldsymbol{R})}\,. \tag{4.2}$$

The choice of $e^{i\theta(\boldsymbol{R})}$ for the geometric phase is valid in the two-state models used in this chapter, but it is not universal. A detailed discussion of this choice, its validity, and further implications are provided in Refs. [52, 216].

This approach will be used for the inclusion of the geometric phase in AIMS. The molecular Hamiltonian used in full multiple spawning (FMS), $\hat{H}_{\mathrm{m}}(\boldsymbol{r},\boldsymbol{R})$, will be transformed into $\hat{H}_{\mathrm{m}}(\boldsymbol{r},\boldsymbol{R}) \rightarrow \hat{H}^{\mathrm{GP}}_{\mathrm{m}}(\boldsymbol{r},\boldsymbol{R}) = e^{i\theta(\boldsymbol{R})}\hat{H}_{\mathrm{m}}(\boldsymbol{r},\boldsymbol{R})e^{-i\theta(\boldsymbol{R})}$. Using this transformed Hamiltonian in FMS leads to a new set of equations for the Hamiltonian matrix elements, where for the intrastate couplings the action of the Laplacian (coming from the nuclear kinetic energy operator) on the phase gives rise to new terms and the FMS matrix elements from equation 2.55 transform to:

$$\begin{aligned}\left(\langle\tilde{\chi}^{(J)}_k\Phi_J|\,\hat{H}^{\mathrm{GP}}_{\mathrm{m}}\,|\Phi_J\tilde{\chi}^{(J)}_m\rangle_{\boldsymbol{r},\boldsymbol{R}}\right)^{\mathrm{GP}}_{\mathrm{FMS}} &= -\sum_{\rho}^{3N_{\mathrm{n}}}\frac{1}{2M_\rho}\langle\tilde{\chi}^{(J)}_k|\,\partial^2_{R_\rho}\,|\tilde{\chi}^{(J)}_m\rangle_{\boldsymbol{R}} + \langle\tilde{\chi}^{(J)}_k|\,E^{\mathrm{el}}_J\,|\tilde{\chi}^{(J)}_m\rangle_{\boldsymbol{R}}\\ &+\sum_{\rho}^{3N_{\mathrm{n}}}\frac{1}{2M_\rho}\langle\tilde{\chi}^{(J)}_k|\,|d^\rho_{12}|^2\,|\tilde{\chi}^{(J)}_m\rangle_{\boldsymbol{R}} + \sum_{\rho}^{3N_{\mathrm{n}}}\frac{1}{2M_\rho}\langle\tilde{\chi}^{(J)}_k|\,(\partial_{R_\rho}\theta)^2\,|\tilde{\chi}^{(J)}_m\rangle_{\boldsymbol{R}}\\ &-\sum_{\rho}^{3N_{\mathrm{n}}}\frac{i}{2M_\rho}\langle\tilde{\chi}^{(J)}_k|\left(\partial^2_{R_\rho}\theta\right)|\tilde{\chi}^{(J)}_m\rangle_{\boldsymbol{R}} - \sum_{\rho}^{3N_{\mathrm{n}}}\frac{i}{M_\rho}\langle\tilde{\chi}^{(J)}_k|\left(\partial_{R_\rho}\theta\right)\partial_{R_\rho}\,|\tilde{\chi}^{(J)}_m\rangle_{\boldsymbol{R}}\end{aligned} \tag{4.3}$$

The last three terms on the right-hand side are the additional terms arising from the geometric phase.

For the interstate couplings, the presence of the $\nabla_{\boldsymbol{R}}$ operator (with the NACVs term) gives rise to an additional term (last term on the right hand-side) with respect to the FMS matrix elements given in equation 2.55:

$$\begin{aligned}\left(\langle\tilde{\chi}^{(I)}_k\Phi_I|\,\hat{H}^{\mathrm{GP}}_{\mathrm{m}}\,|\Phi_J\tilde{\chi}^{(J)}_m\rangle_{\boldsymbol{r},\boldsymbol{R}}\right)^{\mathrm{GP}}_{\mathrm{FMS}} &= -\sum_{\rho}^{3N_{\mathrm{n}}}\frac{1}{M_\rho}\langle\tilde{\chi}^{(I)}_k|\,d^\rho_{IJ}\partial_{R_\rho}\,|\tilde{\chi}^{(J)}_m\rangle_{\boldsymbol{R}}\\ &-\sum_{\rho}^{3N_{\mathrm{n}}}\frac{1}{2M_\rho}\langle\tilde{\chi}^{(I)}_k|\left(\partial_{R_\rho}d^\rho_{IJ}\right)|\tilde{\chi}^{(J)}_m\rangle_{\boldsymbol{R}}\\ &-\sum_{\rho}^{3N_{\mathrm{n}}}\frac{i}{M_\rho}\langle\tilde{\chi}^{(I)}_k|\,d^\rho_{IJ}\left(\partial_{R_\rho}\theta\right)|\tilde{\chi}^{(J)}_m\rangle_{\boldsymbol{R}}\,.\end{aligned} \tag{4.4}$$

As stated in Eq. (2.13), it is possible to connect the derivative of the mixing angle $\nabla_{\boldsymbol{R}}\theta(\boldsymbol{R})$ and the NACVs $\mathbf{d}_{12}(\boldsymbol{R})$. Thus, we can rewrite Eqs. (4.3) and (4.4) with the additional contributions now given in terms of the NACVs $d_{12}^{\rho}(\boldsymbol{R})$ as

$$\begin{aligned}\left(\langle\tilde{\chi}_k^{(J)}\Phi_J|\,\hat{H}_{\mathrm{m}}^{\mathrm{GP}}\,|\Phi_J\tilde{\chi}_m^{(J)}\rangle_{\boldsymbol{r},\boldsymbol{R}}\right)_{\mathrm{FMS}}^{\mathrm{GP}} = &-\sum_{\rho}^{3N_{\mathrm{n}}}\frac{1}{2M_\rho}\,\langle\tilde{\chi}_k^{(J)}|\,\partial_{R_\rho}^2\,|\tilde{\chi}_m^{(J)}\rangle_{\boldsymbol{R}} + \langle\tilde{\chi}_k^{(J)}|\,E_J^{\mathrm{el}}\,|\tilde{\chi}_m^{(J)}\rangle_{\boldsymbol{R}}\\ &+\sum_{\rho}^{3N_{\mathrm{n}}}\frac{1}{M_\rho}\,\langle\tilde{\chi}_k^{(J)}|\,|d_{12}^{\rho}|^2\,|\tilde{\chi}_m^{(J)}\rangle_{\boldsymbol{R}}\\ &-\sum_{\rho}^{3N_{\mathrm{n}}}\frac{i}{2M_\rho}\,\langle\tilde{\chi}_k^{(J)}|\,\left(\partial_{R_\rho}d_{12}^{\rho}\right)\,|\tilde{\chi}_m^{(J)}\rangle_{\boldsymbol{R}}\\ &-\sum_{\rho}^{3N_{\mathrm{n}}}\frac{i}{M_\rho}\,\langle\tilde{\chi}_k^{(J)}|\,d_{12}^{\rho}\partial_{R_\rho}\,|\tilde{\chi}_m^{(J)}\rangle_{\boldsymbol{R}}\,,\end{aligned} \tag{4.5}$$

and

$$\begin{aligned}\left(\langle\tilde{\chi}_k^{(I)}\Phi_I|\,\hat{H}_{\mathrm{m}}^{\mathrm{GP}}\,|\Phi_J\tilde{\chi}_m^{(J)}\rangle_{\boldsymbol{r},\boldsymbol{R}}\right)_{\mathrm{FMS}}^{\mathrm{GP}} = &-\sum_{\rho}^{3N_{\mathrm{n}}}\frac{1}{M_\rho}\,\langle\tilde{\chi}_k^{(I)}|\,d_{IJ}^{\rho}\partial_{R_\rho}\,|\tilde{\chi}_m^{(J)}\rangle_{\boldsymbol{R}}\\ &-\sum_{\rho}^{3N_{\mathrm{n}}}\frac{1}{2M_\rho}\,\langle\tilde{\chi}_k^{(I)}|\,\left(\partial_{R_\rho}d_{IJ}^{\rho}\right)\,|\tilde{\chi}_m^{(J)}\rangle_{\boldsymbol{R}} \qquad (4.6)\\ &-\sum_{\rho}^{3N_{\mathrm{n}}}\frac{i}{M_\rho}\,\langle\tilde{\chi}_k^{(I)}|\,d_{IJ}^{\rho}d_{12}^{\rho}\,|\tilde{\chi}_m^{(J)}\rangle_{\boldsymbol{R}}\,. \qquad (4.7)\end{aligned}$$

From this set of equations, one can now derive a practical expression for AIMS by applying a series of approximations. One can expand the electronic energy term as well as all terms including the NACVs within the SPA to first order (SPA1), while all the DBOCs

and NACs terms (including $|d_{12}^{\rho}(\boldsymbol{R})|^2$ and $\partial_{R_\rho} d_{IJ}^{\rho}(\boldsymbol{R})$) are expanded to zeroth order (SPA0). This framework results in the following equation for the intrastate couplings

$$\begin{aligned}
\left(\langle\tilde{\chi}_k^{(J)}\Phi_J|\,\hat{H}_{\mathrm{m}}^{\mathrm{GP}}\,|\Phi_J\tilde{\chi}_m^{(J)}\rangle_{\boldsymbol{r},\boldsymbol{R}}\right)_{\mathrm{AIMS}}^{\text{GP-SPA1'}} &= -\sum_{\rho}^{3N_{\mathrm{n}}}\frac{\hbar^2}{2M_\rho}\langle\tilde{\chi}_k^{(J)}|\,\partial_{R_\rho}^2\,|\tilde{\chi}_m^{(J)}\rangle_{\boldsymbol{R}} + \epsilon_{\mathrm{BO}}^{(J)}(\bar{\boldsymbol{R}}_{km})\,\langle\tilde{\chi}_k^{(J)}|\tilde{\chi}_m^{(J)}\rangle_{\boldsymbol{R}} \\
&\quad + \sum_{\rho}^{3N_{\mathrm{n}}}\left.\frac{\partial\epsilon_{\mathrm{BO}}^{(J)}(\boldsymbol{R})}{\partial R_\rho}\right|_{R_\rho=\bar{R}_{km,\rho}}\langle\tilde{\chi}_k^{(J)}|\,(R_\rho-\bar{R}_{km,\rho})\,|\tilde{\chi}_m^{(J)}\rangle_{\boldsymbol{R}} \\
&\quad + \sum_{\rho}^{3N_{\mathrm{n}}}\frac{\hbar^2}{M_\rho}|d_{12}^{\rho}(\bar{\boldsymbol{R}}_{km})|^2\,\langle\tilde{\chi}_k^{(J)}|\tilde{\chi}_m^{(J)}\rangle_{\boldsymbol{R}} \\
&\quad - \sum_{\rho}^{3N_{\mathrm{n}}}\frac{i\hbar^2}{M_\rho}d_{IJ}^{\rho}(\bar{\boldsymbol{R}}_{km})\,\langle\tilde{\chi}_k^{(J)}|\,\partial_{R_\rho}\,|\tilde{\chi}_m^{(J)}\rangle_{\boldsymbol{R}} \\
&\quad - \sum_{\rho}^{3N_{\mathrm{n}}}\sum_{\rho'}^{3N_{\mathrm{n}}}\frac{i\hbar^2}{M_\rho}\left(\mathbf{J}_{\boldsymbol{d}_{IJ}}(\bar{\boldsymbol{R}}_{km})\right)_{\rho\rho'}\langle\tilde{\chi}_k^{(J)}|\,(R_{\rho'}-\bar{R}_{km,\rho'})\partial_{R_\rho}\,|\tilde{\chi}_m^{(J)}\rangle_{\boldsymbol{R}} \\
&\quad - \sum_{\rho}^{3N_{\mathrm{n}}}\frac{i\hbar^2}{2M_\rho}\left(\mathbf{J}_{\boldsymbol{d}_{IJ}}(\bar{\boldsymbol{R}}_{km})\right)_{\rho\rho}\langle\tilde{\chi}_k^{(J)}|\tilde{\chi}_m^{(J)}\rangle_{\boldsymbol{R}}\,,
\end{aligned} \tag{4.8}$$

and the following one for the interstate couplings

$$\begin{aligned}
\left(\langle\tilde{\chi}_k^{(I)}\Phi_I|\,\hat{H}_{\mathrm{m}}^{\mathrm{GP}}\,|\Phi_J\tilde{\chi}_m^{(J)}\rangle_{\boldsymbol{r},\boldsymbol{R}}\right)_{\mathrm{AIMS}}^{\text{GP-SPA1'}} &= -\sum_{\rho}^{3N_{\mathrm{n}}}\frac{\hbar^2}{M_\rho}d_{IJ}^{\rho}(\bar{\boldsymbol{R}}_{km})\,\langle\tilde{\chi}_k^{(I)}|\,\partial_{R_\rho}\,|\tilde{\chi}_m^{(J)}\rangle_{\boldsymbol{R}} \\
&\quad - \sum_{\rho}^{3N_{\mathrm{n}}}\sum_{\rho'}^{3N_{\mathrm{n}}}\frac{\hbar^2}{M_\rho}\left(\mathbf{J}_{\boldsymbol{d}_{IJ}}(\bar{\boldsymbol{R}}_{km})\right)_{\rho\rho'}\langle\tilde{\chi}_k^{(I)}|\,(R_{\rho'}-\bar{R}_{km,\rho'})\partial_{R_\rho}\,|\tilde{\chi}_m^{(J)}\rangle_{\boldsymbol{R}} \\
&\quad - \sum_{\rho}^{3N_{\mathrm{n}}}\frac{\hbar^2}{2M_\rho}\left(\mathbf{J}_{\boldsymbol{d}_{IJ}}(\bar{\boldsymbol{R}}_{km})\right)_{\rho\rho}\langle\tilde{\chi}_k^{(I)}|\tilde{\chi}_m^{(J)}\rangle_{\boldsymbol{R}} \\
&\quad - \sum_{\rho}^{3N_{\mathrm{n}}}\frac{i\hbar^2}{M_\rho}d_{IJ}^{\rho}(\bar{\boldsymbol{R}}_{km})d_{12}^{\rho}(\bar{\boldsymbol{R}}_{km})\,\langle\tilde{\chi}_k^{(I)}|\tilde{\chi}_m^{(J)}\rangle_{\boldsymbol{R}}\,.
\end{aligned} \tag{4.9}$$

Evaluating the AIMS matrix elements within a SPA1' for the GP-transformed Hamiltonian $\hat{H}_{\mathrm{m}}^{\mathrm{GP}}(\boldsymbol{r},\boldsymbol{R})$ yields intrastate and interstate couplings containing both contributions from the DBOCs and the NACs. It is important to note that this framework preserves the hermiticity of the AIMS Hamiltonian. These two equations are those employed in the following under the name GP-SPA1'.

4.3 Computational details

For this study, a series of two-dimensional, two-state linear vibronic coupling (LVC) models is used. In the diabatic representation, the general form of the Hamiltonian is given by

$$\hat{\mathbf{H}}_{\mathrm{dia}}(\boldsymbol{R}) = \hat{T}_{\mathrm{n}}(\boldsymbol{R})\mathbf{1} + \begin{pmatrix} V_{11}(\boldsymbol{R}) & V_{12}(\boldsymbol{R}) \\ V_{12}(\boldsymbol{R}) & V_{22}(\boldsymbol{R}) \end{pmatrix}, \tag{4.10}$$

with the following diabatic electronic energies

$$\begin{aligned} V_{11}(\boldsymbol{R}) &= \frac{\omega_1^2}{2}\left(X + \frac{a}{2}\right)^2 + \frac{\omega_2^2}{2}Y^2 + \frac{\Delta}{2} \\ V_{22}(\boldsymbol{R}) &= \frac{\omega_1^2}{2}\left(X - \frac{a}{2}\right)^2 + \frac{\omega_2^2}{2}Y^2 - \frac{\Delta}{2} \\ V_{12}(\boldsymbol{R}) &= cY \end{aligned} \tag{4.11}$$

with $\boldsymbol{R} = (X, Y)$. The parameters a, ω_1, ω_2, Δ and c are obtained from Ref. [61] and chosen to create three models representative of the conical intersection for the molecules bis(methylene)adamantyl (BMA), butatriene cation, and pyrazine. The model potentials describe, in a diabatic picture, two parabolas displaced in the x direction and shifted in energy by the parameter Δ. Fig. 4.1 depicts the general shape of the adiabatic potential energy surfaces for the different molecules. The ground electronic state is indicated by green contour lines and the excited state with purple ones. We note that in the case of BMA, $\Delta = 0.0\ E_h$, which means that the model is symmetric with a CI at $\boldsymbol{R}_{\mathrm{CI}} = (X_{\mathrm{CI}}, Y_{\mathrm{CI}}) = (0.0, 0.0)a_0$ (see Fig. 4.1). In the following, units for the nuclear coordinates are given in a_0.

The nonadiabatic passage of a nuclear wavepacket through a conical intersection is simulated using three different methods: AIMS, numerically-exact QD, and TSH.

In the QD simulations, the initial state is given by a Gaussian nuclear wavepacket with widths $\sigma_X = \sqrt{\frac{2}{\omega_1}}$ and $\sigma_Y = \sqrt{\frac{2}{\omega_2}}$ initialised in the adiabatic excited electronic state with zero initial nuclear momenta. The widths (σ_X, σ_Y) are set to $(16.07, 17.30)a_0^{-1}$ for BMA, $(14.47, 24.43)a_0^{-1}$ for butatriene cation, and $(23.41, 21.86)a_0^{-1}$ for pyrazine. Following earlier work by Izmaylov and coworkers,[61,63] the nuclear wavepacket is initially positioned on the Franck-Condon point of the corresponding full-dimensional model, which gives $(15.53, 0.0)a_0$ for BMA, $(-2.08, 0.0)a_0$ for the butatriene cation, and $(5.10, 0.0)a_0$ for pyrazine. The full time-dependent Schrödinger equation is solved numerically in the diabatic representation employing a split-operator formalism.[203,204]

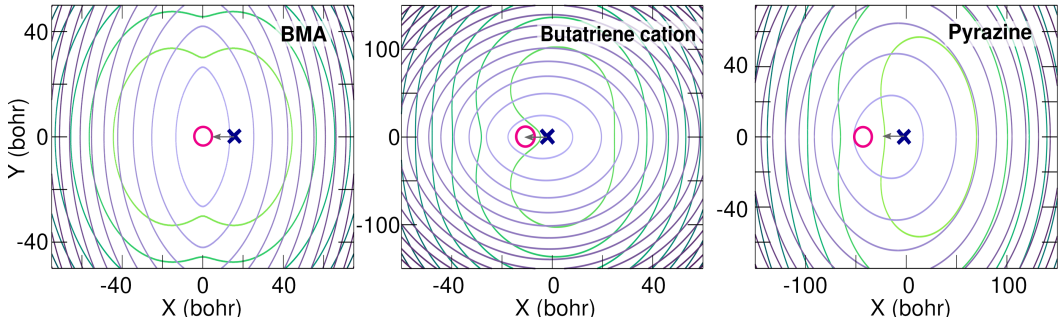

Fig. 4.1.: Contour lines of the adiabatic ground (green) and excited (purple) potential energy surfaces for the three model systems: BMA, butatriene cation, and pyrazine (from top to bottom). Higher energies are depicted by darker colours. The pink circles indicate the location of the conical intersection, and the dark blue crosses locate the centre of the initial Gaussian nuclear wavepacket, with an arrow indicating the initial motion of the nuclear wavepacket upon relaxation.

The TSH dynamics are carried out with the LVC interface of the SHARC 2.1 program.[217,218] For consistency, the dynamics obtained from the LVC interface and the analytical potential routine of SHARC have been compared and have given identical results. A nuclear time step of 0.05 fs, that is $\sim 2\ \hbar E_h^{-1}$ (atomic time units, atu), is used for the classical propagation of the nuclei. The energy-based decoherence correction was used with the standard parameter $a = 0.1 E_h$. Only the component of the nuclear velocities parallel to the NACVs was rescaled after a hop, or reflected after a frustrated hop.

The AIMS dynamics were performed with a modified version of the FMS90 code implemented in MOLPRO.[160] The additional correction terms — the GP effects (Sec. 4.2) and for the DBOC, NACs and SPA1 of the NACVs (Sec. 2.5.3) — were included into the overlap module of FMS90. A time step of $1\ \hbar E_h^{-1}$ was used for the propagation of the TBFs, which was reduced to $0.25\ \hbar E_h^{-1}$ in regions of strong nonadiabaticity. The threshold to enter the spawning mode (absolute value of the nonadiabatic coupling) was set to $0.0001\ a_0^{-1}$, with a minimum population of 0.001 required for a TBF to spawn. The widths of the Gaussians was chosen to be the same as the initial nuclear wavepacket in the quantum dynamics, and all AIMS simulations presented employed the independent first generation approximation (IFGA).

The AIMS and TSH dynamics used the same 2000 initial conditions, obtained by sampling randomly the Wigner distribution corresponding to the initial Gaussian nuclear wavepacket used in each QD simulations. The additional terms included in AIMS and discussed in Sec. 4.5 caused some numerical instabilities for the AIMS dynamics of a

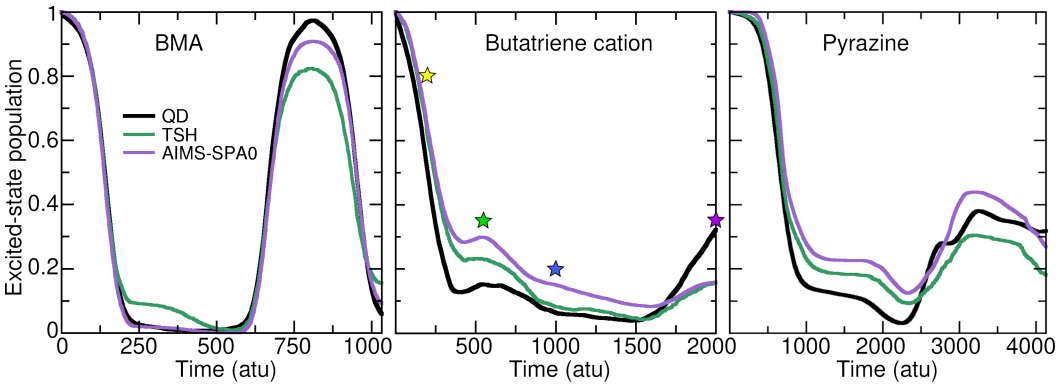

Fig. 4.2.: Excited-state population decays for the model of (a) BMA, (b) butatriene cation, and (c) pyrazine. Three different nonadiabatic dynamics strategies are compared for each model: QD (black), TSH (green), and AIMS-SPA0 (purple). The colored stars in panel (b) mark different time snapshots that will be investigated in more detail in the Figs. 4.3 and 4.4.

few initial conditions. As a result, the number of initial conditions used for the different dynamics discussed in Sec. 4.5 varies between 1980 and 2000.

4.4 Comparison of the nuclear dynamics

4.4.1 Excited-state population decay

To begin with, the excited-state population decay will be investigated for the three different models, comparing the QD results to the decays predicted by TSH and AIMS within the SPA0 (Eqs. (2.58) and (2.59)).

The BMA model is set up to recreate the diabatic trapping occurring in the excited-state dynamics of the full molecule. As a result, the numerically-exact QD dynamics exhibits an almost complete depletion of the initial excited-state population within the first 250 $\hbar E_h^{-1}$ (black line in Fig. 4.2a), rapidly followed by a complete revival of the excited-state population after 625 $\hbar E_h^{-1}$. The excited-state population then decays again back to the ground electronic state after around 1000 $\hbar E_h^{-1}$. TSH reproduces quite closely the QD results for the excited-state population (green line in Fig. 4.2a). Deviations are observed after the first decay (at around 250 $\hbar E_h^{-1}$), where TSH does not fully decay the excited-state population. Another marked difference can be observed during the revival of the excited-state population (at around 750 $\hbar E_h^{-1}$), where TSH predicts that nearly 20% of the population remains in the ground state. These results are entirely consistent with the analysis of Izmaylov and coworkers, who rationalised the overall good performance of TSH

for dynamics around conical intersections by compensation of errors between neglecting DBOCs and GP effects.[219,220] The population trace obtained with AIMS-SPA0 for BMA (purple line in Fig. 4.2a) is almost identical to that obtained with QD, with only a small deviation observed from the reference during the revival of the excited-state population. This deviation is smaller than what is observed for TSH, with only 10% of population left on the ground state for AIMS-SPA0.

The second model is based on the excited-state dynamics of the butatriene cation. The excited-state population described by QD suffers an immediate decay, leaving ~ 15% of population in the excited state after 350 $\hbar E_h^{-1}$ of dynamics (black line in Fig. 4.2b). A brief increase of this population is observed at around 550 $\hbar E_h^{-1}$ before it carries on its decay. A sudden repopulation of the excited state is however observed between 1500 to 2000 $\hbar E_h^{-1}$, from around 5% to over 30%. The time-trace of the excited-state population is reproduced qualitatively by both TSH and AIMS-SPA0 (green and purple lines in Fig. 4.2b). The overall shape of the population trace obtained with AIMS is comparably similar to the QD reference than that of TSH, but AIMS-SPA0 underestimates the overall decay of population. The TSH population trace matches that of QD between 850 and 1600 $\hbar E_h^{-1}$. Perhaps more noticeable, both approximate methods miss the strong repopulation of the excited state after 1500 $\hbar E_h^{-1}$.

The third and last model studied is based on the photodynamics of pyrazine. The QD population trace shows an initial decay starting after ~ 400 $\hbar E_h^{-1}$ of dynamics until the excited-state population reaches ~ 15% of population after 1000 $\hbar E_h^{-1}$ (black line in Fig. 4.2c). While the population decay dramatically slows down after this first transfer, the excited-state population decreases to less than 5% after 2250 $\hbar E_h^{-1}$ of dynamics. A significant repopulation of the excited state occurs at this time, leading to a maximum of the excited-state population at around 3200 $\hbar E_h^{-1}$ before a decrease is again observed. This rather complex population trace is quite well mimicked by TSH and AIMS-SPA0 (green and purple lines in Fig. 4.2c). Both approximate methods describe the initial fast decay of excited-state population, with AIMS transferring slightly less population to the ground state than TSH. The plateau is then reached with, for both TSH and AIMS, a slightly higher excited-state population than what QD predicts (20% with TSH and 23% with AIMS). In contrast with the dynamics of the butatriene cation described above, both AIMS-SPA0 and TSH manage to describe the repopulation of the excited state after 2250 $\hbar E_h^{-1}$. The overall shape of the repopulation (and then decay) observed during the QD is better reproduced

by AIMS, while the variation of population depicted by TSH is smaller (overestimation before the repopulation and underestimation after it).

Overall, the TSH and AIMS-SPA0 agree surprisingly well with the QD reference for these three non-trivial dynamics through a conical intersection. The excellent agreement between the AIMS and QD results obtained for BMA comes somehow as a surprise as it is important to remember that the AIMS-SPA0 dynamics presented here uses the saddle point approximation of zeroth order (SPA0) and the independent first generation approximation (IFGA). The latter was originally justified for the study of molecules in their full dimensionality, but in resonance with previous work[212,221] the IFGA appears to perform well for models with a small number of nuclear degrees of freedom. While these approximations can explain in part the deviations in population between AIMS and QD observed for the two other models, it is crucial to realise that the AIMS dynamics presented here do not account for geometric phase (GP) effects and neglect the diagonal Born-Oppenheimer correction (DBOCs) and second order nonadiabatic coupling terms (NACs). As observed by Izmaylov for mixed-quantum classical methods,[219,220] the somewhat encouraging results obtained for the three models with AIMS-SPA0 seem to imply that AIMS benefits from a similar cancelation of errors as TSH – the lack of GP effects in AIMS is compensated by the neglect of DBOCs. We note that the BMA model is characterised by a rather asymmetric DBOC in the branching space, while the models for butatriene cation and pyrazine show a more symmetric DBOC.[61,219] These observations and the results above suggest that the approximations of AIMS-SPA0 may perform best in general for molecules with less symmetric DBOCs.

The results reported here are somehow reassuring for the use of AIMS-SPA0 to describe the dynamics through conical intersections for molecular systems. Given that AIMS-SPA0 encodes more nuclear quantum effects than a mixed quantum/classical method like TSH, it was not given that AIMS-SPA0 would perform well in nonadiabatic dynamics around conical intersections when NACs and geometric effects are significant. Differences are, however, non-negligible, and therefore, in the following, the influence of the different missing terms in the AIMS Hamiltonian matrix elements will be investigated more closely. From here onward, it will be focused on the butatriene cation model (Fig. 4.2b) as it appears to be the most challenging model for AIMS-SPA0.

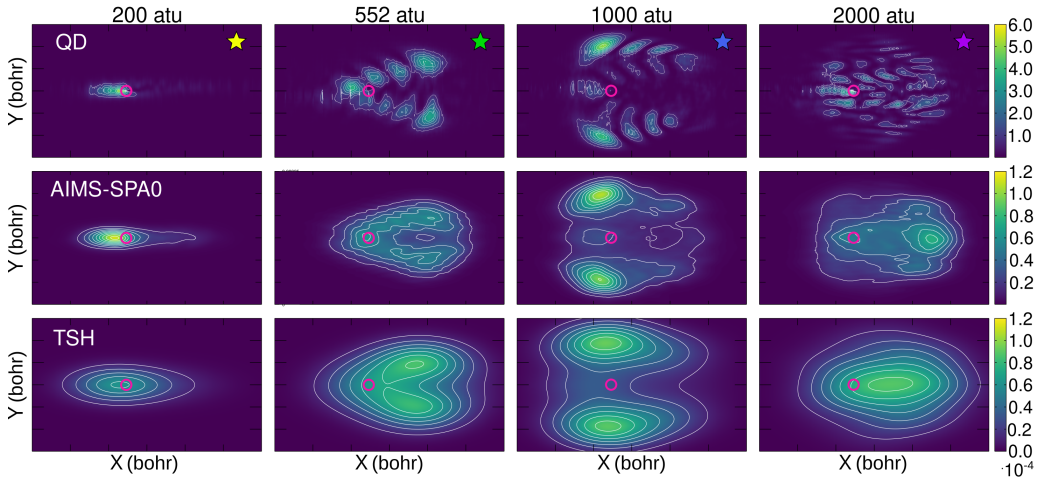

Fig. 4.3.: Snapshots of the ground-state nuclear density taken at four characteristic times of the nonadiabatic dynamics of the butatriene cation. The four different times selected are indicated by the corresponding colored stars in Fig. 4.2. The ground-state nuclear density is reconstructed for QD (top panels), AIMS-SPA0 (middle panels), and TSH (lower panels). Pink circles indicate the location of the conical intersection. The colorbar range is rescaled by a factor of two for the snapshots at 200 $\hbar E_h^{-1}$ (left panels).

4.4.2 Ground-state nuclear dynamics for the butatriene cation model

To complement the analysis of the excited-state population dynamics, the ground-state nuclear density will be visualised as obtained with the different methods. This quantity is straightforward to access in the QD simulation (it should be noted here that the adiabatic ground-state nuclear density is plotted). In AIMS-SPA0, the ground-state nuclear density can be easily reconstructed from the TBFs and their complex coefficients, owing to the FMS ansatz discussed above. We note that the use of the IFGA implies that the nuclear density is reconstructed for each AIMS-SPA0 run (each parent TBF with their respective child) individually. The overall AIMS-SPA0 nuclear density is obtained by performing an incoherent average over the nuclear density of each AIMS-SPA0 run. TSH does not offer an ansatz for the nuclear wavefunctions due to its independent trajectory approximation. Hence, the nuclear density in TSH is approximated by broadening each TSH trajectory with a Gaussian function, whose width is chosen to be identical to that of the TBFs in AIMS-SPA0.

The ground-state nuclear density is compared at four different times for the butatriene dynamics – 200, 552, 1000, and 2000 $\hbar E_h^{-1}$, indicated by colored stars in Fig. 4.2b. These times were selected as they correspond to a specific behaviour in the excited-state population trace: the initial decay of the population (200 $\hbar E_h^{-1}$), the maximum of the weak repopulation

(552 $\hbar E_h^{-1}$), the beginning of the plateau (1000 $\hbar E_h^{-1}$), and the end of the dynamics after the repopulation (2000 $\hbar E_h^{-1}$). Fig. 4.3 shows the different snapshots of the ground-state nuclear density for the QD, AIMS-SPA0, and TSH dynamics (from top to bottom), reconstructed at these four times. The pink circle in the plots indicates the location of the conical intersection.

At 200 $\hbar E_h^{-1}$, nuclear density starts to appear in the ground electronic state. While the location of the nuclear density given by AIMS-SPA0 and TSH matches that of the QD result, the QD nuclear density shows a nodal region near the position of the conical intersection, which is not reproduced by either AIMS-SPA0 or TSH. The approximations of AIMS-SPA0 can be held responsible for this deviation from the QD result, considering that the AIMS-SPA0 simulation presented invokes the SPA0 and the IFGA (and no geometric effects are included). At later times, the ground-state nuclear density spreads on the ground-state potential energy surface (see Fig. 4.1), ending up being mostly delocalised by $t = 2000\ \hbar E_h^{-1}$. While AIMS-SPA0 and TSH both reproduce well the overall shape and localisation of the nuclear density at most times, it is surprising to see how qualitatively well AIMS-SPA0 captures the main features of the structure of the QD nuclear density, in particular at $t = 552\ \hbar E_h^{-1}$ and $t = 1000\ \hbar E_h^{-1}$, considering the crude approximation of its Hamiltonian matrix elements and the use of the IFGA. This good match between QD and AIMS-SPA0 is further observed in the actual movies of the evolution of the ground-state nuclear density (as can be seen in the movies of the Supporting Information of Ref. [55]). This evolution further highlights that the good agreement between the QD and AIMS-SPA0 nuclear densities is not coincidental at the selected times. Comparing the evolution for the AIMS-SPA0 and TSH dynamics offers a clear illustration of the fundamental difference between the two methods. The TSH movie makes it obvious that the motion of the nuclear density is simply correlated to the dynamics of the independent classical trajectories on the ground-state potential energy surface. Conversely, the AIMS-SPA0 movie shows that the complex amplitude is transferred between the TBFs, which serve as moving grid points on which the nuclear density is distributed.

This observation is further supported by comparing the positions of the TSH trajectories with that of the TBFs centers in AIMS-SPA0 at the various snapshot times (Fig. 4.4). Both simulations, AIMS-SPA0 and TSH start with 2000 independent initial conditions, in AIMS-SPA0 each of these initial conditions spawns additional Gaussians throughout the dynamics. In AIMS-SPA0, the TBFs evolve from being mainly around $Y = 0$ at 200 $\hbar E_h^{-1}$ to

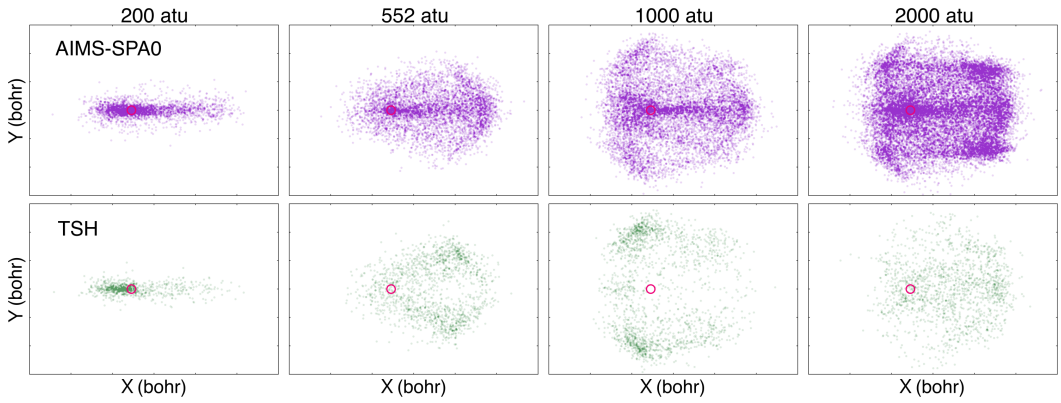

Fig. 4.4.: Snapshots of the positions of the AIMS-SPA0 TBFs (upper panel) and the TSH trajectories (lower panel) evolving on the ground state at four characteristic times for the nonadiabatic dynamics of the butatriene cation. The snapshot times are the same as those presented in Fig. 4.3 and indicated by colored stars in Fig. 4.2b. Pink circles indicate the location of the conical intersection.

mostly everywhere in space at later times – an essential element for the success of the method if one considers that the actual positions of the TBFs are not critical as long as they offer a proper support to describe the nuclear wavepacket dynamics, described in AIMS-SPA0 via the complex coefficients. This coverage of the configuration space by the TBFs is made possible by the spawning algorithm, which increases the number of TBFs continuously during the dynamics. This growing distribution and spreading of the TBFs are in stark contrast with the distribution of the TSH trajectories.

4.5 Including new contributions in *ab initio* multiple spawning

Having characterised the nonadiabatic dynamics obtained with AIMS-SPA0 for the different models, in the following it will be investigated how additional contributions to the AIMS Hamiltonian matrix elements affect the dynamics, focusing in particular to some terms that are usually neglected in AIMS – GP effect, DBOCs, and NACs – and discussed above in Sec. 4.2 and 2.5.3. Figure 4.5 provides an overview of the various 'flavours' of AIMS that

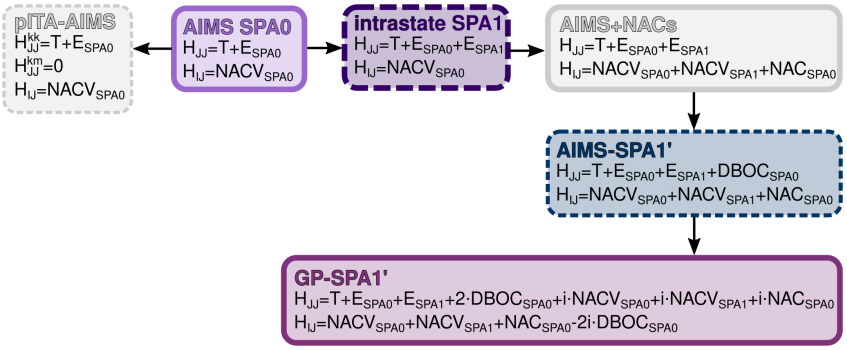

Fig. 4.5.: Schematic overview of the hierarchy of the different 'flavours' of AIMS that will be discussed in this section, and the terms included in the respective matrix elements.

will be used to simulate the photodynamics of the butatriene cation in the following. The various matrix elements are given in a symbolic notation, defined as:

$$\mathrm{T} \equiv -\sum_{\rho}^{3N_\mathrm{n}} \frac{1}{2M_\rho} \langle \tilde{\chi}_k^{(J)} | \, \partial^2_{R_\rho} \, | \tilde{\chi}_m^{(J)} \rangle_{\boldsymbol{R}} \tag{4.12}$$

$$\mathrm{E}_{\mathrm{SPA0}} \equiv \epsilon_{\mathrm{BO}}^{(J)}(\bar{\boldsymbol{R}}_{km}) \, \langle \tilde{\chi}_k^{(J)} | \tilde{\chi}_m^{(J)} \rangle_{\boldsymbol{R}} \tag{4.13}$$

$$\mathrm{E}_{\mathrm{SPA1}} \equiv \sum_{\rho}^{3N_\mathrm{n}} \left. \frac{\partial \epsilon_{\mathrm{BO}}^{(J)}(\boldsymbol{R})}{\partial R_\rho} \right|_{R_\rho = \bar{R}_{km,\rho}} \langle \tilde{\chi}_k^{(J)} | \, (R_\rho - \bar{R}_{km,\rho}) \, | \tilde{\chi}_m^{(J)} \rangle_{\boldsymbol{R}} \tag{4.14}$$

$$\mathrm{NACV}_{\mathrm{SPA0}} \equiv -\sum_{\rho}^{3N_\mathrm{n}} \frac{1}{M_\rho} d^\rho_{IJ}(\bar{\boldsymbol{R}}_{km}) \, \langle \tilde{\chi}_k^{(I)} | \, \partial_{R_\rho} \, | \tilde{\chi}_m^{(J)} \rangle_{\boldsymbol{R}} \tag{4.15}$$

$$\mathrm{NACV}_{\mathrm{SPA1}} \equiv -\sum_{\rho}^{3N_\mathrm{n}} \sum_{\rho'}^{3N_\mathrm{n}} \frac{1}{M_\rho} \left(\mathbf{J}_{\mathbf{d}_{IJ}}(\bar{\boldsymbol{R}}_{km}) \right)_{\rho\rho'} \langle \tilde{\chi}_k^{(I)} | \, (R_{\rho'} - \bar{R}_{km,\rho'}) \partial_{R_\rho} \, | \tilde{\chi}_m^{(J)} \rangle_{\boldsymbol{R}} \tag{4.16}$$

$$\mathrm{NAC}_{\mathrm{SPA0}} \equiv -\sum_{\rho}^{3N_\mathrm{n}} \frac{1}{2M_\rho} \left(\mathbf{J}_{\mathbf{d}_{IJ}}(\bar{\boldsymbol{R}}_{km}) \right)_{\rho\rho} \langle \tilde{\chi}_k^{(I)} | \tilde{\chi}_m^{(J)} \rangle_{\boldsymbol{R}} \tag{4.17}$$

$$\mathrm{DBOC}_{\mathrm{SPA0}} \equiv \sum_{\rho}^{3N_\mathrm{n}} \frac{1}{2M_\rho} |d^\rho_{12}(\bar{\boldsymbol{R}}_{km})|^2 \, \langle \tilde{\chi}_k^{(J)} | \tilde{\chi}_m^{(J)} \rangle_{\boldsymbol{R}} \, . \tag{4.18}$$

First, the influence of improving the quality of the intrastate matrix elements in AIMS-SPA0 is considered by moving to the SPA1 (*intrastate-SPA1* in Fig. 4.6a, dark purple dashed line), that is, by using Eq. (2.60) for the intrastate couplings and maintaining the SPA0 (Eq. (2.59)) for the interstate couplings. No major variations of the population trace can be observed by improving the intrastate couplings. This observation could be rationalised by the fact that, within a given AIMS run, TBFs might separate in phase space sufficiently such that they are not strongly affected by their respective intrastate couplings. An interesting

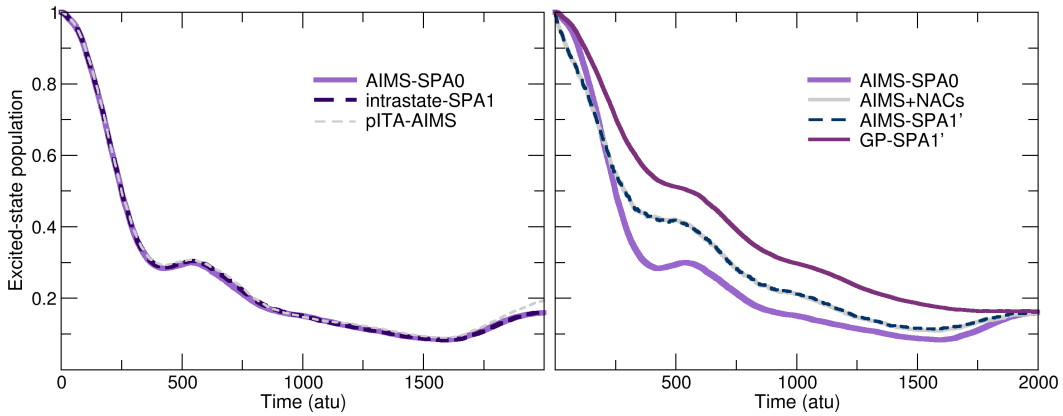

Fig. 4.6.: Excited-state population decay for the butatriene cation model using different flavors of AIMS. a) Alterations of the intrastate coupling terms: standard AIMS formulation using the SPA0 for all coupling terms (*AIMS-SPA0*, purple line, identical to the population depicted in Fig. 4.2), using an SPA1 for the intrastate couplings (*intrastate-SPA1*, dark purple dashed lines), and removing all intrastate couplings (*pITA-AIMS*, grey dashed line). b) Modifications of both inter- and intrastate couplings: the standard AIMS formulation for reference (*AIMS-SPA0*, purple line), using the SPA1 and including NACs (*AIMS+NACs*, grey line), using the SPA1 and including both NACs and DBOCs (*AIMS-SPA1'*, dark blue dashed line), using the SPA1' and adding the GP correction (*GP-SPA1'*, palatinate line). The exact QD result is given in black for reference.

test to validate the importance of the coupling between TBFs on the same state consists in removing all intrastate couplings (pseudo-independent trajectory approximation in AIMS, *pITA-AIMS*, in Fig. 4.6a, grey dashed line). Once more, the population trace obtained within this approximation does not significantly deviate from the original AIMS one, validating the weak influence of the intrastate coupling within the current approximations. It is important to note that removing the IFGA may significantly alter this result, as all parent TBFs and their child TBFs would become coupled. Before moving to the next step and including the NACs and GP effects, it is noted the bra-ket averaged Taylor (BAT) expansion to order zero proposed in Ref. [153] has been tested for the NACVs (instead of the SPA0) and has yielded a population trace in very close agreement with AIMS-SPA0.

At this point, it is possible to consider including terms in the Hamiltonian matrix elements that are usually neglected within the conventional AIMS framework, based on the analysis in Sec. 2.5.3. The first step consists in including the NACs in the interstate couplings. As discussed in the analysis in Sec. 2.5.3, preserving the hermiticity of the Hamiltonian matrix requires using the SPA1 for the interstate couplings. The resulting strategy (*AIMS+NACs*, grey line in Fig. 4.6b), uses the SPA1 for the intrastate couplings (Eq. (2.60)) and the interstate couplings (Eq. (2.70)), including the NACs. AIMS+NACs

shows a population transfer initially accelerated in comparison to AIMS-SPA0, but this acceleration rapidly slows down, and a significantly smaller population transfer towards the ground state is observed between 400 $\hbar E_h^{-1}$ and 750 $\hbar E_h^{-1}$. The excited-state population then slowly converges towards that of AIMS-SPA0. Based on the earlier consideration with intrastate-SPA1 and pITA-AIMS, it does not come as a surprise that adding the DBOCs to this dynamics (*AIMS-SPA1'*, dark blue dashed line in Fig. 4.6b, using Eq. (2.69) for intrastate couplings and Eq. (2.70) for interstate couplings) does not alter the population transfer in comparison to AIMS+NACs, since it uses the identical expression for the interstate couplings and only adds the DBOC to the intrastate couplings. Overall, the inclusion of NACs and DBOCs appears to slow down the population transfer for the butatriene cation model – an observation for AIMS in resonance with earlier findings on TSH, where the inclusion of DBOCs was found to slow down significantly the population transfer.[219] (See Sec. 4.6 below for additional information on the inclusion of DBOCs in AIMS.) The final contribution that can be included is the GP correction within a SPA1' (*GP-SPA1'*, palatinate line in Fig. 4.6), using Eq. (4.8) for intrastate couplings and Eq. (4.9) for interstate couplings. The population trace obtained with AIMS under the GP-SPA1' approximation deviates even more from the AIMS-SPA0 (and QD result), exhibiting a dramatic slow down of the excited-state population transfer. This result is surprising as one would expect, based on earlier works,[61,219] that including a GP correction in the interstate coupling terms should increase the nonadiabatic transfer of population.

To shed further light on this observation, it will be focused now on a representative parent-child TBF pair and their interstate coupling will be monitored when approaching the conical intersection.* Following the strength of the interstate coupling for each TBF using AIMS-SPA0 (Fig. 4.7b), one can see how the TBFs meet in configuration space when their coupling strength is maximal – a behavior encoded in the spawning algorithm. When now monitoring the strength of the interstate couplings for the same pair of TBFs but including GP effects (GP+SPA1', Fig. 4.7c), one can immediately observe that the nonadiabatic strength is almost ten times stronger than without the GP effects. Hence, it appears that, as expected, the nonadiabatic strength is dramatically enhanced when GP effects are included in AIMS. What happens then to the population transfer between this pair of TBFs?

*It should be noted that this parent-child TBF pair has been randomly chosen from the set of initial conditions and that the vast majority of parent-child TBF pairs exhibits similar behaviour.

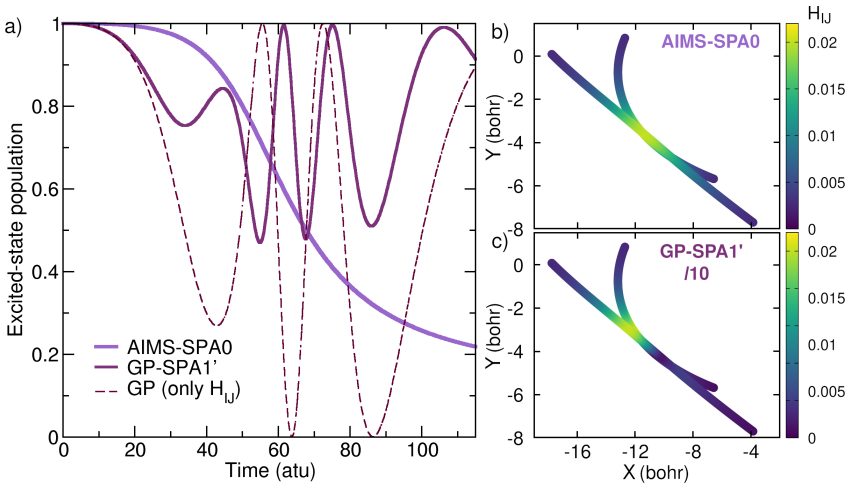

Fig. 4.7.: Early dynamics of a representative parent-child TBF pair evolving in different electronic state: a) Excited-state population transfer with AIMS-SPA0 (purple line), AIMS including GP effects within the SPA1' (*GP-SPA1'*, palatinate, solid line), and AIMS including only the interstate coupling corrections for the GP with the SPA1' (*GP*, dashed palatinate line). b) The effective nonadiabatic coupling strength (norm of the Hamiltonian matrix element for interstate couplings, $|H^{IJ}_{\mathrm{m},km}|$) between the two TBFs present in the simulation, depicted along each TBF for the first 115 $\hbar E_h^{-1}$ of AIMS-SPA0 dynamics. c) The effective nonadiabatic coupling strength (norm of the Hamiltonian matrix element for interstate couplings – $|H^{\mathrm{GP},IJ}_{\mathrm{m},km}|$) between the two TBFs present in the simulation, depicted along each TBF for the first 115 $\hbar E_h^{-1}$ of AIMS GP-SPA1' dynamics. Note that the scale of the color bar for this panel has been divided by a factor of 10 in comparison to panel (b), i.e., the effective nonadiabatic coupling strength is a factor of 10 larger than it is for AIMS-SPA0.

The norm of the Hamiltonian matrix element for the interstate coupling for AIMS-SPA0, $\left(H^{IJ}_{\mathrm{m},km}\right)^{\mathrm{SPA0}}_{\mathrm{AIMS}}$, or for GP-SPA1', $\left(H^{\mathrm{GP},IJ}_{\mathrm{m},km}\right)^{\mathrm{GP\text{-}SPA1'}}_{\mathrm{AIMS}}$, are taken as proxies for the nonadiabatic coupling strength in a situation without or with GP effects. We start by monitoring the excited-state population trace for this pair of TBFs, using AIMS-SPA0 and GP+SPA1' for the matrix elements (Fig. 4.7a). The population trace using AIMS-SPA0 shows a smooth and monotonic decay. However, upon inclusion of the GP effects, one sees that, while the population starts to decay earlier than in AIMS-SPA0, it then exhibits some rapid oscillations between 1.0 and 0.5, hindering the population transfer. While the TBFs feel a much stronger mutual interstate coupling, the nuclear amplitude oscillates in a Rabi-way between the two TBFs without a stable transfer to the ground-state one. One reason for that could be that there are at this time only two TBFs in the dynamics (one on each state), and therefore that once transferred to the TBF in the ground state, the amplitude cannot spread towards other ground-state TBFs and remains trapped on the child TBF, still strongly coupled with the parent TBF – leading to an oscillation of the amplitude between the two TBFs, a sort of overcoherent effect due to the locality of the parent/child TBF pair. Including the GP effects only in the interstate couplings (palatinate dashed line in Fig. 4.7a) further enhances these oscillations. Hence, it appears to have reached in this particular case one of the limitations of AIMS: the use of the IFGA, which limits the number of coupled TBFs at the early times. To circumvent this issue, it would be necessary to start the dynamics with a large number of coupled TBFs. While this solution would potentially be tractable for a model system, its cost would simply be prohibitive for molecular systems.

This leads to the interesting conclusion that including GP effects in AIMS would likely require getting rid of some of the practical approximations (SPA0 and IFGA) that made AIMS a successful strategy to investigate the nonadiabatic dynamics of molecular systems. These tests also reveal that these nonadiabatic processes can be easily described within these strong approximations by relying on cancellation of errors – a reason why TSH performs so well for molecular systems. However, trying to account properly for additional quantum effects like GP in AIMS would require a dramatic improvement of its underlying approximations.

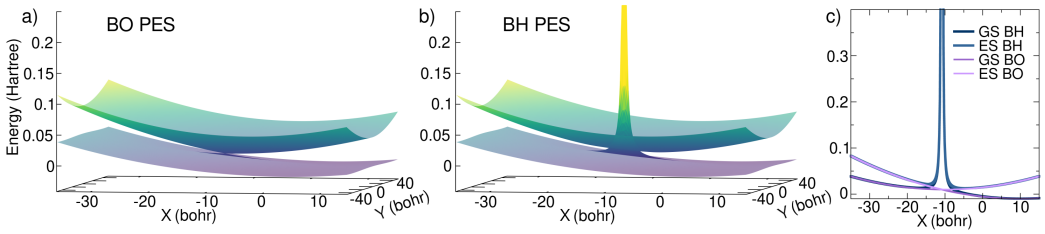

Fig. 4.8.: Comparison of the potential energy surfaces for the ground state (GS) and the excited state (ES) of the butatriene cation around the conical intersection. a) Born-Oppenheimer potential energy surfaces (BO PES). b) Born-Huang potential energy surfaces (BH PES). c) Cut through the BO PESs (light and dark purple lines) and the BH PESs (light and dark blue lines) along the axis $Y = 0$.

4.6 Born-Oppenheimer vs. Born-Huang Potential energy surfaces

Up to this point, the attention has been focused only on the Hamiltonian matrix elements connecting the TBFs. However, one should keep in mind that, while the dynamics of the complex coefficients is obtained via the time-dependent Schrödinger equation, the TBFs are propagated classically and meant to follow the dynamics of the nuclear wavepackets. In the standard version of AIMS (AIMS-SPA0), the TBFs evolve on the Born-Oppenheimer potential energy surfaces (BO PESs) given by $\epsilon_{\mathrm{BO}}^{(J)}(\boldsymbol{R})$. Considering the inclusion of DBOCs in the Hamiltonian matrix elements of AIMS-SPA0 (see Eq. (2.69)) raises the question of also including these terms in the dynamics of the TBFs. The resulting Born-Huang (BH) PESs are then defined for the electronic state J as $\epsilon_{\mathrm{BO}}^{(J)}(\boldsymbol{R}) + D_{JJ}(\boldsymbol{R})$. The BH PESs have been investigated extensively for electron transfer processes in the context of non-Born-Oppenheimer effects.[222–224] The BO PESs are very similar to the BH PESs for a given molecule as long as electronic states are far apart in energy. However, one can show for a two-level system that the DBOCs are proportional to the squared norm of the NACVs (as discussed earlier, see Eq. (2.65)). Hence, the shape of the BH PESs will dramatically differ from that of the BO PESs in the vicinity of a conical intersection, as the NACVs are inversely proportional to the electronic energy gap between the two coupled states. Looking at the model for the butatriene cation, one can see that the typical conical shape of the BO PES (Fig. 4.8a) is completely altered by the inclusion of the DBOCs, leading to BH PESs both displaying a singularity at the exact location of the conical intersection (Fig. 4.8b). The addition of this singular barrier on both BH PESs is made more visible in Fig. 4.8c by performing a cut on the BH and BO PESs along the $Y = 0$ axis.

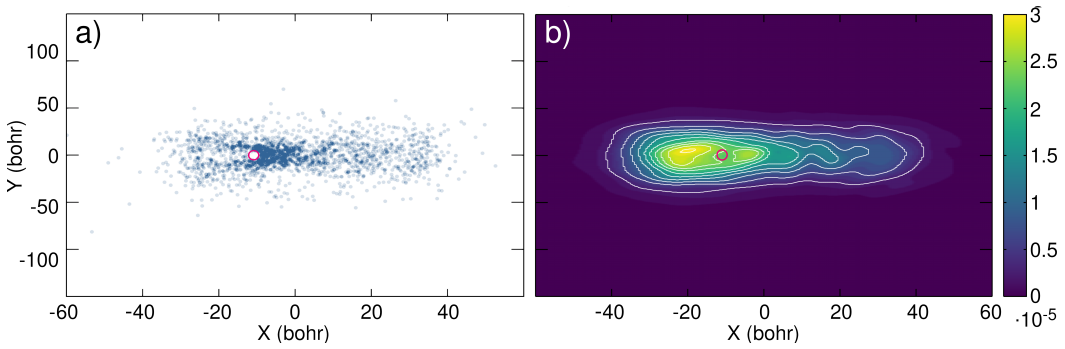

Fig. 4.9.: Snapshot at 200 $\hbar E_h^{-1}$ of the (a) AIMS ground-state nuclear density and (b) TBFs centers, for an AIMS dynamics where the TBFs are evolved on BH PESs for the butatriene cation model. Pink circles indicate the location of the conical intersection.

This comparison between the shape of BO and BH PESs makes it clear that nonadiabatic dynamics methods based on classical trajectories will be strongly affected by this additional barrier. Earlier work on TSH showed that including the DBOCs in the propagation of the classical trajectories dramatically hampers the nonadiabatic population transfer.[219,220] Hence, focusing now on AIMS-SPA0, it does not come as a surprise that the TBFs are avoiding the regions of the conical intersection when evolving on the BH PESs (Fig. 4.9b). Interestingly though, the width of the TBFs makes that the reconstructed ground-state nuclear density (Fig. 4.9a), combined with the approximate nature of the interstate and intrastate couplings, still displays some nuclear density in the direct vicinity of the conical intersection. As expected from the distribution of the TBFs, the overall excited-state population decay predicted by AIMS-SPA0 when employing BH PESs to propagate the TBFs is dramatically decelerated (light-blue line in Fig. 4.10) in comparison to the AIMS-SPA0 on BO PES (purple line in Fig. 4.10). This observation is in line with earlier findings on propagating TBFs on BH PESs within the AIMS-SPA0 formalism,[168] and earlier work on the inclusion of DBOCs only in QD and TSH.[54,61,219,220]

Accounting for GP effects into the AIMS dynamics on BH PESs (at the GP-SPA1' level, see Sec. 4.5 above) results in a slight speed-up of the excited-state population transfer. This behavior is expected due to the enhanced interstate couplings resulting from the inclusion of the GP (see Fig. 4.7) and shows that TBFs can still interact next to the conical intersection. However, the classical motion of the TBFs on the BH PESs, combined with the limitations in the description of the interstate and intrastate couplings and the IFGA (described above), do not allow for an overall improved description of the excited-state

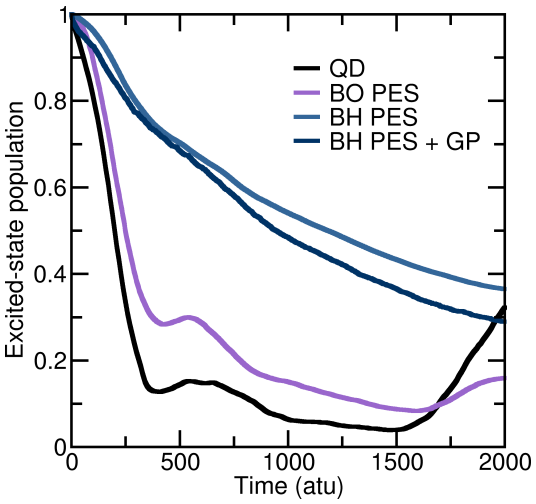

Fig. 4.10.: Excited-state population decay with AIMS-SPA0, with TBFs evolving on standard BO PESs (purple line) or BH PESs (light blue line). The dark blue line shows the propagation on the BH PES but including the GP corrections in the Hamiltonian matrix elements (BH PES + GP). The exact QD result is given in black for reference.

population transfer. This finding reinforces earlier work on the incorporation of DBOCs in AIMS.[167,168]

4.7 Conclusions

In this chapter, the influence of the missing contributions to the Hamiltonian matrix elements was analysed in the AIMS method for nonadiabatic dynamics around conical intersections. Based on three two-dimensional model systems, it was shown that AIMS – in its original formulation, which means using the SPA0 and IFGA and neglecting the NACs, DBOCs and GP corrections – offers a least a qualitatively correct description of the dynamics through a conical intersection. The results obtained with AIMS align with what is observed for the mixed quantum/classical method TSH. As AIMS is not per se a mixed quantum/classical method but is derived from the in-principle exact FMS framework, possible improvements of the method can be envisaged. A set of equations was derived aiming at improving the Hamiltonian matrix elements coupling the TBFs by including GP corrections. Interestingly, adding terms in the interstate or intrastate couplings outside of the realm of the original AIMS approximations does not appear to improve the description of population transfer at a conical intersection. The limited accuracy in the Hamiltonian matrix elements combined with the IFGA seems to be responsible for such shortcomings. Considering that the complexity related to dynamics through a conical

intersection is particularly enhanced in the three low-dimensional models presented in this chapter, the adequate behaviour of the original AIMS in such conditions offers an empirical validation for the simulation of nonadiabatic processes in higher dimensions using this method. The shortcomings of AIMS when improving its Hamiltonian matrix elements in the adiabatic representation are also highly stimulating for developing new TBF-based strategies for nonadiabatic dynamics employing dedicated (time-dependent) diabatic electronic quantities.[168,225–227]

Testing nonadiabatic molecular dynamics methods in the vicinity of CIs is of high importance, since CIs are ubiquitous in molecules and act as funnels for the population decay. The topology of the CI has a strong influence on the dynamics of the nuclear wavefunction of the molecular system. Understanding the limitations of methods at describing the dynamics around CI is a fundamental step towards the applicability of the method for full dimensional nonadiabatic molecular dynamics.

5 Molecular models to challenge nonadiabatic dynamics

This chapter is based on the publications:
L. M. Ibele and B. F. E. Curchod, "A Molecular Perspective on Tully Models for Nonadiabatic Dynamics", Phys. Chem. Chem. Phys., 22, 15183 (2020).
P. Vindel-Zandbergen, L. M. Ibele*, J.-K. Ha, S. K. Min, B. F. E. Curchod and N. T. Maitra, "A study of the decoherence correction derived from the exact factorization approach for nonadiabatic dynamics", J. Chem. Theory Comput., 17, 3852 (2021)
*Contribution: carried out all the TSH-EDC calculations, contributed to the analysis and writing of the final draft of the manuscript.
L. M. Ibele†, Y. Lassmann, T. J. Martínez and B. F. E. Curchod, "Comparing (stochastic-selection) ab initio multiple spawning with trajectory surface hopping for the photodynamics of cyclopropanone, fulvene, and dithiane", J. Chem. Phys., 154, 104110 (2021)
†Contribution: carried out all the TSH and AIMS calculations, all SSAIMS calculations on dithiane, part of the SSAIMS calculations on cyclopropanone, analysed the data and wrote the initial draft of the manuscript.

5.1 Introduction

Prior to any actual application aiming at either explaining experimental observations or predicting a particular molecular behaviour, one has to duly test the approximations of a given nonadiabatic method and determine the limitations that such approximations impose on the use of the technique. To this end, model systems are a crucial tool to test and challenge nonadiabatic dynamics methods.In the context of low-dimensional analytical test systems, a given model is composed of (*i*) predefined potential energy curves and nonadiabatic couplings between electronic states – with the focus being on the nuclear dynamics and not the electronic structure – and (*ii*) initial conditions for the nuclear dynamics – initial position and momentum of the nuclear wavepacket/trajectories. Models are usually designed to probe specific difficult situations of nonadiabatic dynamics, for

example, decoherence and recoherence, dephasing, etc.[16,228] While testing on analytical and low dimensional models is an important first step of assessing the capabilities of nonadiabatic dynamics methods, ultimately these methods will be used on full-dimensional molecules. Therefore, two questions need to be addressed: Can processes probed by low dimensional molecules be related to the nonadiabatic dynamics of real, molecular systems? And can we transfer the concept of models to real, molecular systems?

The first question is legitimate already from an electronic structure perspective, as moving from one to two nuclear degrees of freedom forces us to account for conical intersections (in the adiabatic representation).[43–46] Moving to an even higher number of nuclear degrees of freedom allows defining a two-dimensional branching space – coordinates along which the electronic degeneracy is lifted – as well as the $3N_n - 8$ intersection seam – along which the electronic degeneracy is preserved. Conical intersections are known to be ubiquitous in the photodynamics of molecular systems and responsible for ultrafast funnelling processes between electronic states. Is it therefore possible, to connect some typical nonadiabatic processes occurring in molecular systems to some of the features of common low-dimensional models? Achieving this goal will offer a series of molecular models to compare nonadiabatic molecular dynamics methods among each other in the full nuclear dimensionality of molecules. There is a consensus in the community that such unified *hard* benchmark tests,[47] using models in higher dimensions, would be highly beneficial for benchmarking the different methods available and dissecting their approximations. The Libra library is a project going in this direction.[48]

When it comes to the second question, it is important to realise that the key interest of analytical models in few dimensions is that they are easily transferable to any nonadiabatic methods because they are based on analytical potential energy curves and couplings as well as on a clear definition of the initial conditions. Such transferability is more challenging to achieve for *ab initio* nonadiabatic molecular dynamics, especially since it is desirable to compute the electronic structure quantities on the fly. What one needs to make accessible are all the initial conditions, parameters, and simulation protocol of the nonadiabatic dynamics.

This chapter proposes three molecules — ethylene, 4-*N*,*N*'-dimethylaminobenzonitrile (DMABN) and fulvene — serving as typical examples of key nonadiabatic processes for molecular systems. The photophysical processes these molecules undergo are reminiscent of the physics probed by the three so-called *Tully models* that were proposed by Tully in

his seminal articles on TSH.[16] These molecules can therefore be seen as a set of *molecular Tully models* and a new tool towards a more general mean of comparison between methods for nonadiabatic dynamics.

This chapter is organised as follows. First, an overview of the original Tully models is provided in Sec. 5.2.1. These models are then related to an exemplary set of molecules in Sec. 5.2.2. Sec. 5.3.1 provides all the computational details so that the exact same dynamics can be reproduced, especially concerning the initial conditions and electronic structure. The population traces of the nonadiabatic dynamics of the three molecules obtained with AIMS and TSH with and without a decoherence correction (dTSH and TSH, respectively) are shown in Secs. 5.3.2, 5.3.3, and 5.3.4. The observed dynamics allows us to highlight connections with the photophysical processes observed in the original Tully models, and how these molecular model can probe specific strengths and limitations of the different nonadiabatic methods. Subsequently, in Sec. 5.4 two examples are provided that illustrate how some of these proposed molecular models can be used to assess the performance of newly proposed flavours of nonadiabatic dynamics methods: The capabilities and cost of ESSAIMS and OSSAIMS are compared on fulvene with AIMS and TSH in Sec. 5.4.1. DISH-XF is evaluated in comparison to uncorrected TSH, other common decoherence corrections (EDC and A-FSSH) and AIMS on two of the proposed molecular Tully models, ethylene and fulvene, in Sec. 5.4.2. Finally, the conclusions are drawn in Sec. 5.5

5.2 Original Tully models and relation to molecular systems

5.2.1 Original Tully models

In 1990, Tully proposed a series of three tests in his seminal article on TSH, later called the *Tully models*, which are depicted in the upper panel of Fig. 5.1. The Tully models are one-dimensional, and the potential energy curves and couplings are expressed analytically (in a diabatic representation).

The main goal of these three models was to test different processes observed during a typical nonadiabatic dynamics and see how approximate methods performed in comparison to exact quantum dynamics simulations. The Tully model I (Fig. 5.1a) exemplifies a simple nonadiabatic event where a one-dimensional particle, whose initial state is described

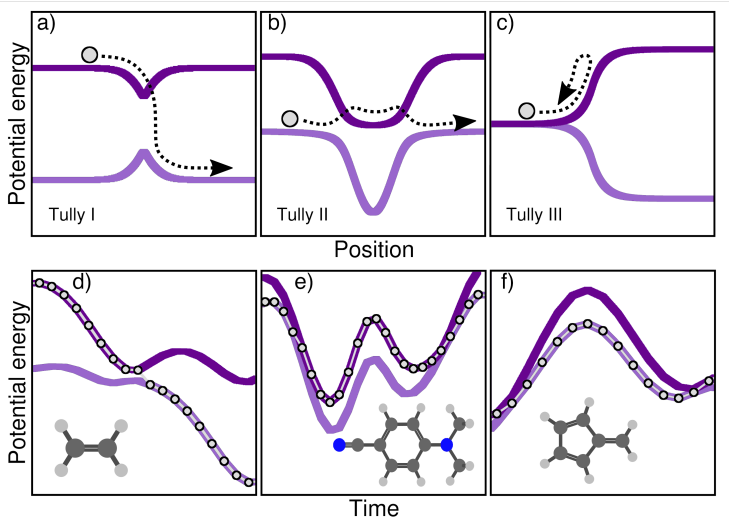

Fig. 5.1.: Schematic depiction of the original Tully models (upper panels, a-c) and the molecular Tully models proposed in this chapter (lower panels, d-e). Upper panel: potential energy curves as a function of a one-dimensional reactive coordinate for the Tully model I (a, single avoided crossing), II (b, double avoided crossings), and III (c, reflection). The path described by the one-dimensional particle (circle and arrow) exemplifies a possible outcome of the dynamics probed by each model. Lower panel: time traces of the potential energies along a TSH trajectory for ethylene (d), DMABN (e), and fulvene (f). The excited-state dynamics for each molecular Tully model mimics the particle dynamics of the corresponding one-dimensional Tully models depicted in the upper panel.

by a nuclear wavepacket in say the first excited electronic state (blue curve), reaches an avoided crossing and can transfer towards the ground electronic state (green curve). The Tully model II (Fig. 5.1b) depicts a somewhat more complicated process, where the particle encounters two different nonadiabatic regions (dual avoided crossing). The nuclear wavepacket describing the state of the particle can 'branch' in the first coupling region – part of the amplitude in the original electronic state is transferred to the coupled state – and the two wavepackets can meet again in the second coupling region. Interferences are possible if the two nuclear wavepackets *recohere* at the second coupling, and their importance will vary as a function of the initial momentum of the particle. The Tully model III (Fig. 5.1c) offers a way to test reflection processes: the two potential energy curves are nearly degenerate at the beginning of the dynamics, and a nonadiabatic coupling region is located just before the near-degeneracy is lifted. When the particle, initially on the ground state, is transferred onto the upper state after the crossing, it may reflect back towards the coupling region if its momentum is too small to overcome the repulsive potential. We will discuss later how these different processes stress the approximation of nonadiabatic methods.

Since their publication in 1990, the simple model systems described above have been extensively used to assess the quality of newly-developed methods or test new approximations or corrections proposed for existing ones. The diversity of strategies tested with some or all of Tully models is astonishing.

5.2.2 Connecting the original Tully models to molecules in their full dimension

As mentioned earlier, the Tully models probe interesting physical phenomena caused by nonadiabatic effects, but how well do these one-dimensional models connect with the nonadiabatic processes observed in (high-dimensional) molecules? In other words, the original one-dimensional Tully models are employed to test the approximations of nonadiabatic methods which will be used for high-dimensional molecular systems, but are the nonadiabatic mechanisms probed in one dimension representative of the coupled electron-nuclear processes a molecule can suffer?

To begin with, different nonadiabatic processes are highlighted that can take place during the excited-state dynamics of a molecule and be connected to key features of the original Tully models. A *caveat* is needed at this stage: the categories discussed below are not intended to fully represent the huge diversity of mechanisms in nonadiabatic molecular dynamics but are only meant to draw some (hopefully general) parallels with the nonadiabatic processes probed in the original Tully models. Upon photoexcitation, certain molecules exhibit an efficient decay back to the ground electronic state mediated by one or more (peaked) conical intersections. A characteristic of such nonadiabatic dynamics is that electronic states are connected by mostly one efficient nonadiabatic event – or one passage through a conical intersection. Such ultrafast and efficient decay processes are clearly connected with the Tully model I – a single crossing event between a pair of electronic states (Fig. 5.1a). Examples from the literature of such photodynamics could be simple photoisomerisation processes like the one of ethylene,[163] protonated formaldimine,[229] or retinal.[230] Other molecules may suffer a nonradiative decay characterised by numerous passages through a given intersection seam between a pair of electronic states. This behaviour is observed when a pair of electronic states remain close in energy, such that the photoexcited molecule can exchange between them several times. This kind of photodynamics can be related to the Tully model II – multiple crossings between two electronic states (Fig. 5.1b). As examples of this category, one can mention molecules having coupled electronic states

with different characters close in energy (4-*N,N'*-dimethylaminobenzonitrile, DMABN, see below), or molecules suffering photodissociation with electronic states getting close in energy, stimulating multiple crossings (see for example dithiane[231]). Another possible outcome of a nonadiabatic dynamics can be observed when a molecule hits a sloped conical intersection with a specific topography. The molecule can transfer to a different electronic state following the passage through the intersection, but soon after will reflect back towards the same region of the intersection seam where a novel nonadiabatic event can take place. Such a nonradiative decay, involving subsequent passages through a nonadiabatic region caused by a reflection process, is reminiscent of the dynamics observed at low kinetic energy in the Tully model III (Fig. 5.1c). As compared to efficient funnelling processes involving peak conical intersections (as mentioned above), sloped intersections are known to slow down the transfer of populations between the coupled electronic states.[232] Such nonadiabatic dynamics proceeding via a sloped intersection and involving a form or reflection process was observed for example in up-funnelling during collision processes,[233] as one contribution to the nonradiative deactivation of fulvene,[234] or in diabatic trappings.[235]

This chapter presents three molecules that, upon electronic excitation, exemplify the typical nonadiabatic processes described above and therefore constitute a molecular version of the original Tully models. The original model potentials proposed by Tully may look somehow 'artificial' (in particular the second and third model), but the correspondence with the processes described in the previous paragraph becomes clearer if, instead of looking at the potential energy curves as a function of position, one plots them as a function of time. In other words, one could compare the potential energy curves as a function of time, drawn by the dynamics of a molecule. In the upper panel of Fig. 5.1, this dynamics in the Tully models is shown by sketching the trajectory of a particle. The lower panel of Fig. 5.1 shows the electronic energies as a function of time for a full atomistic nonadiabatic molecular dynamics of ethylene, DMABN, and fulvene. In the simple case of ethylene (Fig. 5.1d), one sees a trivial correspondence between the molecular trajectory and the one of the particle, both exhibiting a single nonadiabatic event. For the case of DMABN (Fig. 5.1e), the molecule, originally on the green (potential energy) curve, jumps to the blue curve after a nonadiabatic transition, before going back to the green curve due to a passage through a second different nonadiabatic region. The fulvene case (Fig. 5.1f) shows an example of reflection following nonadiabatic transition, where the molecule

transfers from the blue to the green curve, reflects, and goes back to the same region of the intersection space, mimicking the one-dimensional trajectory of the Tully model III.* At this stage, it is worth noting that several deactivations paths can compete in any nonadiabatic process. For example, the particle in the Tully model II could also remain adiabatically on the lower potential energy curve – a branching of the initial nuclear wavepacket in two contributions after the first nonadiabatic event. Such diversity in the possible outcomes after a nonadiabatic transition is likely to be further enhanced for molecular systems as a natural consequence of the larger number of nuclear degrees of freedom. The increase in nuclear degrees of freedom also comes with alternative fates for the photoexcited molecule. Coming back to the previous example, the original Tully model II offers the possibility to observe a recoherence in the second nonadiabatic region when the branched nuclear wavepackets recombine. In molecular systems, it is likely that, while the molecule may hit multiple times the same intersection seam, it will do so at a different region of the seam, limiting the possibilities of interferences between the branched nuclear wavepackets. Hence, Fig. 5.1 is only an illustration of selected possible trajectories that depict some of the interesting phenomena observed in the original Tully models (a more detailed comparison between the molecular and original models will be proposed below).

In the following, it is shown that ethylene, DMABN, and fulvene offer an interesting molecular version of the original Tully models for testing nonadiabatic molecular dynamics methods. For each molecule, a detailed comparison is provided of the nonadiabatic dynamics obtained with TSH, TSH with decoherence correction (see Sec. 2.6.3), and AIMS, using the same level of electronic-structure theory and defining a common set of initial conditions. While an exact solution of the time-dependent molecular Schrödinger equation is clearly out of reach for such large molecular systems, specific features of the nonadiabatic dynamics for each molecule are highlighted that can be used to probe the approximations of other nonadiabatic methods.

*In this latter case, the reflection for fulvene occurs on the ground state while it takes place on the excited state in the original Tully model III.

5.3 Comparing trajectory surface hopping and *ab initio* multiple spawning

5.3.1 Computational details

Electronic structure

Energies, nuclear gradients of the energies, and nonadiabatic couplings of ethylene are computed at the SA(3)-CASSCF(2/2) level of theory[236,237] (including the π and π^* orbitals in the active space) and a 6-31G* basis set.[238,239] Due to the negligible contribution of S_2, only S_0 and S_1 are included in the nonadiabatic dynamics, as done in earlier works on ethylene.[153,240] The lowest four singlet states of DMABN are described with LR-TDDFT[241–243] within the Tamm-Dancoff approximation employing the LC-PBE functional[244,245] with a range-separation parameter set to 0.3 a_0^{-1} and the 6-31G basis set, using the Gaussian09 program.[246] For fulvene, the electronic structure quantities are computed using SA(2)-CASSCF(6/6)/6-31G* (including three pairs of π and π^* orbitals in the active space). All SA-CASSCF calculations are carried out with the MOLPRO 2012 program package.[247]

Nuclear dynamics

Initial conditions for all dynamics (66 for ethylene, 21 for DMABN, and 18 for fulvene) are sampled stochastically from a Wigner distribution for uncoupled harmonic oscillators constructed from a frequency calculation at the ground-state optimised geometry of the respective molecule. For ethylene and DMABN, both geometries and momenta are sampled from this distribution. In contrast, for fulvene only geometries are Wigner-sampled and initial momenta were set to zero (unless otherwise stated). All initial conditions are available from Ref. [248].

The AIMS dynamics are performed with the FMS90/MOLPRO interface.[160] The TBFs are propagated with a time step of 20 $\hbar E_h^{-1}$, reduced to 5 $\hbar E_h^{-1}$ in coupling regions. The threshold to enter the spawning mode is fixed to 3.0 a_0^{-1} for ethylene and 10.0 a_0^{-1} for fulvene (norm of the nonadiabatic coupling vector). Spawning is only allowed for TBFs with a minimum population of 0.01. For ethylene, TBFs spawned on the ground state are removed from the propagation if they have been uncoupled to any other TBFs for more than 200 $\hbar E_h^{-1}$, and the limit of allowed violation of classical energy is set to 0.03 E_h. This

limit for energy conservation is set to 0.01 E_h for fulvene. The results of AIMS dynamics for DMABN are taken from Ref. [121], where the spawning threshold (defined in this case as the scalar product of the nonadiabatic coupling vectors and the nuclear velocities) is set to $0.005\hbar^{-1}E_h$, and the minimum TBF population required to spawn is 0.1. All AIMS simulations use the independent first generation approximation.

The TSH simulations are carried out with the SHARC 2.0 program.[217,249,250] The same initial conditions as in the AIMS dynamics are used, but every trajectory is repeated using 10 different random seeds to improve the convergence of the fewest-switches stochastic process associated with nonadiabatic transitions as described in Sec. 2.6.2. Hence, a total of 660 TSH runs are performed for ethylene, 210 for DMABN, and 180 for fulvene. A nuclear time step of 0.5 fs is used ($\sim 20\ \hbar E_h^{-1}$), a local diabatisation scheme is employed, and nonadiabatic couplings are obtained from wavefunction overlaps instead of computing explicitly the nonadiabatic coupling vectors.[251] Velocity rescaling following a surface hop is performed along the nuclear momenta (unless otherwise stated).

The TSH simulations are carried out with and without the energy-based decoherence correction[184,187] (EDC), which dampens the electronic amplitudes of TSH in case of decoherence. The EDC is used as implemented by default in SHARC, and the same set of random seeds are used for the simulation with and without decoherence correction to ensure a proper comparison. It has to be noted here that the original implementation of the EDC is used, where the TSH amplitudes of the non-running states are damped. Recent discussions revealed that the TSH populations, instead of amplitudes, should have been corrected, as done for example in Newton-X.[187,252,253] The stability of the results has been tested for both ways of imposing the EDC and no major variations have been observed. Finally, it is noted that all the TSH trajectories employing the EDC strictly satisfy the internal consistency criterion detailed in Ref. [184].

Comparability of AIMS and TSH dynamics

As introduced in Sec. 2.5.2, the number of TBFs will grow during an AIMS run as a result of strong nonadiabatic couplings to account for the transfer of amplitude between electronic states. As such, AIMS does require fewer runs than TSH to converge, as the latter needs more runs to ensure proper convergence of the hopping algorithm.[254] For an optimal comparison between AIMS and TSH, it is desirable to adopt a strategy where a given number of initial conditions are sampled from a Wigner distribution (for uncoupled

harmonic oscillators) and used for both TSH and AIMS. However, in this work, ten TSH runs are generated for each set of initial conditions by altering the seed for the random number generator used in the hopping algorithm.[184] As a result, each TSH run starting from the same initial condition can produce different trajectories due to a different hopping pattern. The strategy of using multiple TSH runs for each initial condition allows for a better convergence of the fewest-switches algorithm and dramatically improves the comparison with the AIMS result while using a common set of initial conditions.[184]

5.3.2 Molecular Tully Model I – Ethylene

Ethylene is the simplest example of a molecule showing photoinduced isomerisation through conical intersections, and its photodynamics highlighted the importance of moving beyond a simple one-dimensional model to study qualitatively this photoisomerisation.[163] The nonadiabatic dynamics of ethylene from its first excited singlet state has been the subject of numerous theoretical studies, employing a variety of approaches such as wavepacket propagation,[255] TSH (see e.g., Refs. [256–261]), AIMS (see for example Refs. [262–267]), MCTDH,[268] MCE,[148] or the partial linearised path-integral and symmetrical quasi-classical approach within a quasi-diabatic propagation.[240]

All methods predict a very similar behaviour for the excited ethylene: after photoexcitation to the bright $\pi\pi^*$ state (S_1), internal conversion to the ground state occurs rapidly through two possible conical intersections. However, the ultrafast deactivation occurs in a Tully-I like manner, that is, the nuclear wavepacket only undergoes a single nonadiabatic event via one or the other conical intersection. Thanks to its straightforward dynamical behaviour, ethylene has already been used in several studies to demonstrate the performance of on-the-fly nonadiabatic molecular dynamics methods, for example in Refs .[148, 153, 240, 260]. However, these benchmarks were not performed on a common set of initial conditions or using similar electronic structure methods, and except for Ref. [240] have not been consistently compared to other nonadiabatic dynamics methods.

The deactivation of ethylene from its S_1 state is simulated with the original TSH, decoherence-corrected TSH (dTSH, see computational details and Sec. 2.6.3 for more information), and AIMS, using a set of common initial conditions and the strategy discussed in Sec. 6.2.2 for an improved comparison. Coining the photodynamics of ethylene a *molecular Tully I model* is validated by looking at the average number of hops performed in dTSH ($< N_{hops} >$, Fig. 5.3b): within the first 82 fs of dynamics, 80 % of the trajectories have

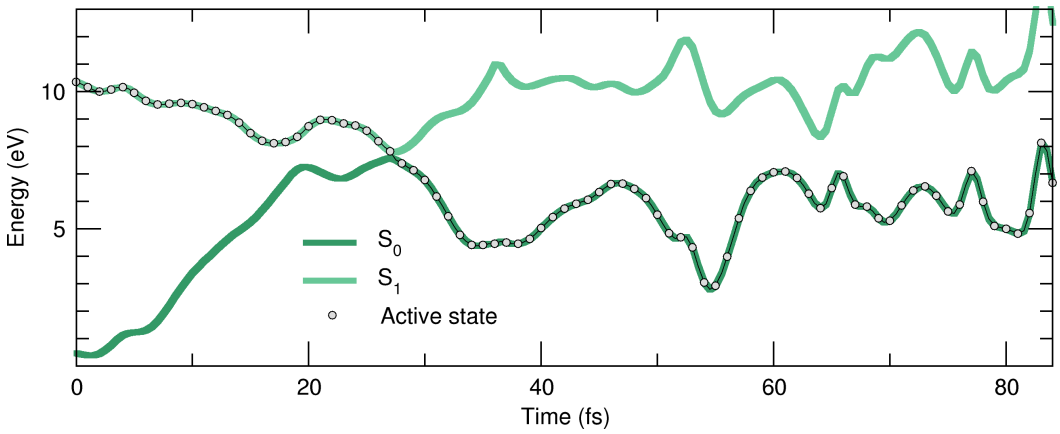

Fig. 5.2.: Photodynamics of ethylene as a molecular Tully model I. Time trace of the potential energies along a representative dTSH trajectory (the active state for the dTSH dynamics is indicated by filled circles).

decayed to the ground state and the average cumulative number of hops has only reached 1.3, indicating that most trajectories perform a single hop from S_1 to the ground state S_0. Thus, the nonadiabatic dynamics of ethylene towards the ground state involves mostly a single crossing event, followed by stable dynamics in S_0, i.e., without hops back to S_1. This behaviour is illustrated by an exemplary TSH trajectory (Fig. 5.2). The two electronic states come energetically close and, following the nonadiabatic transition at around 28 fs when the trajectory hopped to the ground state, they separate again in energy, and the trajectory remains in the ground state. Focusing now on the AIMS dynamics, it can be observed that the average number of child TBFs ($< N_{children} >$), while rising slightly above the average number of hops, remains below two as expected from a dynamics dominated by a single avoided crossing.

The time traces of the S_1 population obtained with the different methods are overall in good agreement (Fig. 5.3a). The decay starts after 11 fs of dynamics and the ground state is largely populated within 80 fs. Despite the overall agreement between the different methods, small differences can be observed. dTSH predicts the fastest decay (with around 20 % of population remaining in the S_1 after 82 fs). It was proposed in previous studies that the more rapid population decay predicted by (d)TSH in comparison to AIMS could be attributed to the intrinsic overcoherence of TSH. Even though the population traces obtained with the different methods are close to each other in the present simulations, as a test it is attempted to reproduce the result obtained with (d)TSH by applying additional approximation to AIMS. Therefore, the following approximations are enforced to the AIMS dynamics: (*i*) setting intrastate couplings between TBFs to zero, (*ii*) propagating the

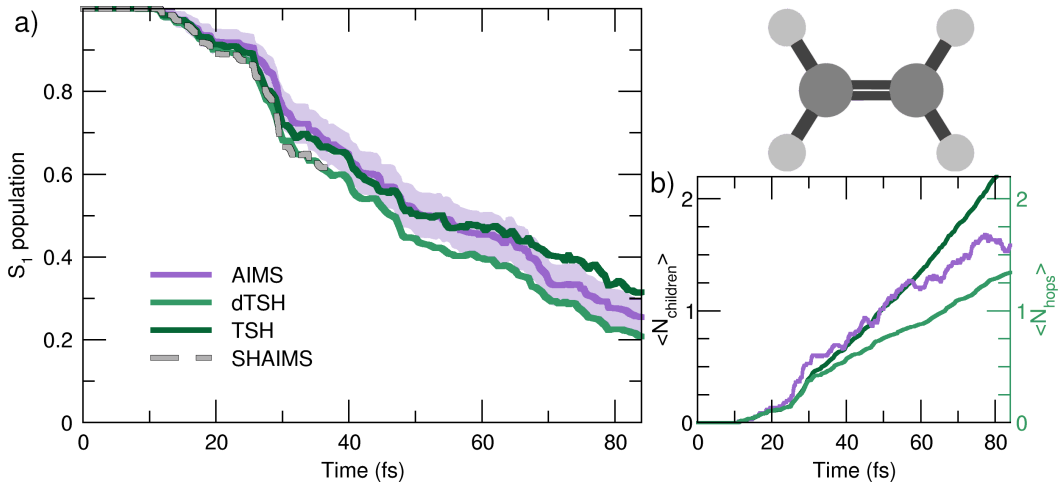

Fig. 5.3.: Photodynamics of ethylene as a molecular Tully model I. a): S_1 population decay as obtained with AIMS (purple, standard error given as a shaded area), TSH (dark green), and decoherence-corrected TSH ('dTSH', light green). The population trace of the surface hopping approach to AIMS (SHAIMS) is given until the approximations underlying this dynamics are no more valid, i.e., when the child TBFs start to spawn back. b): time traces of the average number of child TBFs ($< N_{children} >$) and the average number of hops ($< N_{hops} >$) performed in TSH and dTSH.

amplitudes of the spawned TBFs on the support of the parent TBF, and (*iii*) enforcing a perfect overlap between TBFs. These approximations intend to bridge the equations of motion for the amplitudes in AIMS to those of TSH, and was hence coined *Surface Hopping Approach to AIMS (SHAIMS, c.f. Sec. 2.6.4)*. Interestingly, the nonadiabatic dynamics described by SHAIMS closely follows that of dTSH (dashed line in Fig. 5.3) and shows a faster decay of the S_1 population as compared to AIMS. While care has to be taken when assessing the difference in population decay due to the close agreement of the methods, SHAIMS appears to indicate that a perfect overlap between TBFs would indeed tend to speed up the transfer of population towards the ground state, as observed for TSH and dTSH. TSH and dTSH start to diverge noticeably after 35 fs of dynamics while exhibiting a similar population time trace until this time. This point of divergence is also observed in the average number of hops between the two TSH methods and can be correlated with some hops back to S_1 taking place in the TSH dynamics but prevented in dTSH thanks to the use of the decoherence correction. The fact that the hops back do not take place in dTSH also explains why the SHAIMS strategy agrees more with dTSH after 35 fs (as back spawns are artificially prevented in this analysis method).

In summary, the molecular Tully model I appears to be a good general first test for any newly-developed nonadiabatic dynamics strategy.

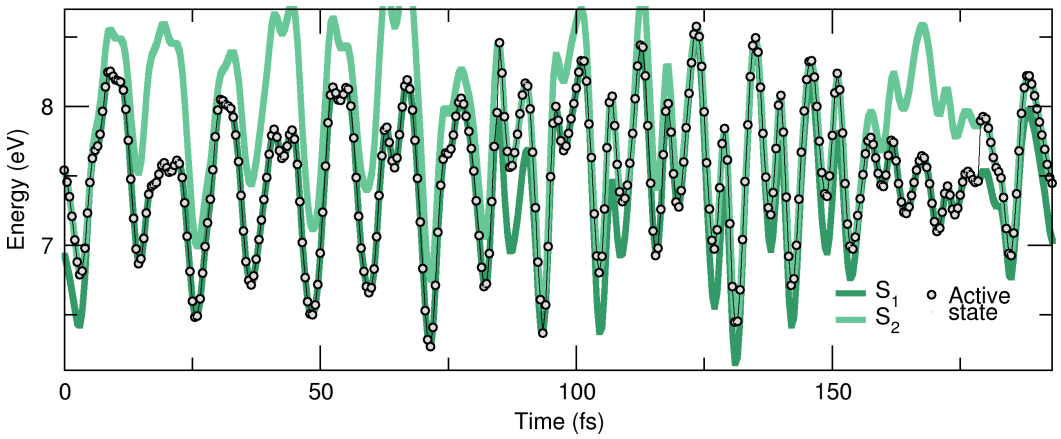

Fig. 5.4.: Photodynamics of DMABN as a molecular Tully model II. Time trace of the potential energies along a representative dTSH trajectory (the active state for the dTSH dynamics is indicated by filled circles).

5.3.3 Molecular Tully Model II – DMABN

As discussed earlier, the original Tully model II depicts a somewhat more complicated case of nonadiabatic dynamics than the model I, where more than one avoided crossings can be encountered during the dynamics. It is shown here that a comparable behaviour is observed at the molecular level during the photodynamics of DMABN. This molecule has been the subject of different studies looking into the details of its ultrafast decay from the photoexcited S_2 state and using different levels of theory for the electronic structure and the nuclear dynamic.[121,269–271] All previous work agreed on the ultrafast relaxation from the S_2 to the S_1 occurring within the first 50 fs of dynamics. This ultrafast decay is also in line with the photodynamics of the parent molecule 4-aminobenzonitrile, studied with MCTDH.[272] However, the S_2 and S_1 states remain close in energy during the excited-state dynamics, and the nuclear wavepackets visit subsequent nonadiabatic regions leading to oscillations of the population between these two states after the initial ultrafast decay. Such multiple crossings between a pair of electronic states link the photodynamics of DMABN to the Tully model II.

The average number of hops during the dTSH dynamics of DMABN rises to more than four within the first 200 fs of dynamics (Fig. 5.5b). In stark contrast with the dynamics of ethylene, the (d)TSH dynamics of DMABN is characterised by a significant number of nonadiabatic transitions *between the same pair of electronic states*, further exemplified by the exemplary trajectory shown in Fig. 5.4. Hops between the two states occur at 7, 85.5, 96, 103, 112, 121, 157, and 179 fs. Importantly, the nonadiabatic transitions do

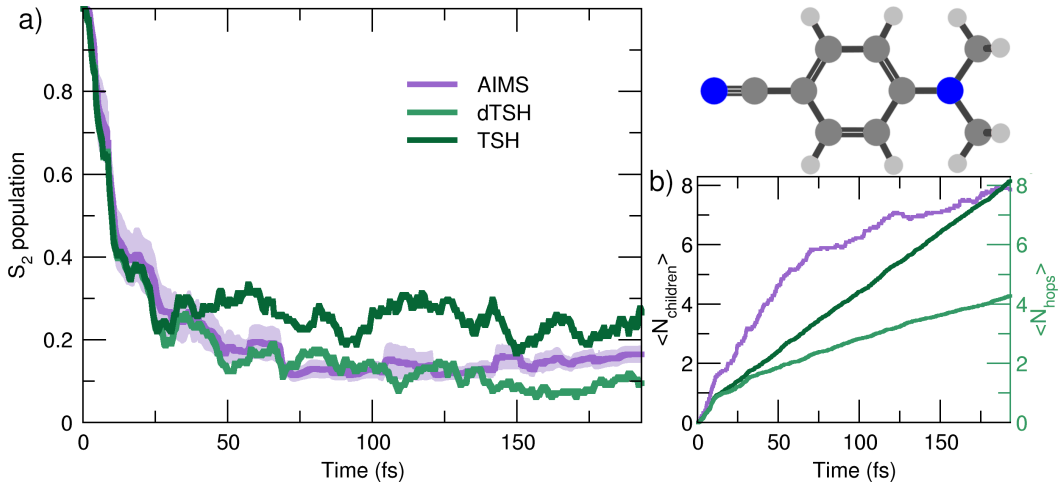

Fig. 5.5.: Photodynamics of DMABN as a molecular Tully model II. a): S_2 population decay as obtained with AIMS (purple, standard error given as a shaded area), TSH (dark green), and decoherence-corrected TSH ('dTSH', light green). b): time traces of the average number of child TBFs ($< N_{children} >$) and the average number of hops ($< N_{hops} >$) performed in TSH and dTSH.

not happen in the same region of the intersection seam (the electronic energies at the different hopping points are different). This observation is crucial as it indicates that the dTSH trajectories do not hop back and forth between S_2 and S_1 in the same region of the intersection seam but instead visit different points of such crossing seam, analogously to the two avoided crossings in Tully model II. As a corollary to this observation, one would expect a branching of the nuclear wavepackets after each nonadiabatic transition without them interfering again at a later time, i.e., with no *recoherence*.[273] This nonadiabatic dynamics contrasts with the Stueckelberg oscillations observed in the original Tully model II[16] that are caused by a modulation of the nonadiabatic interferences between the two wavepackets at the second avoided crossings as a function of the initial momentum of the wavepacket.[206]

All methods – TSH, dTSH, and AIMS (from Ref. [121]) – predict an ultrafast decay of the S_2 population and the corresponding population traces are similar during the first 30 fs (cf. Fig. 5.5a). After this time, the result of the TSH dynamics starts to deviate more strongly from that of the other two methods. Interestingly, this specific behaviour of TSH starts to appear when the average number of hops is reaching 2, indicating that, on average, a TSH trajectory has experienced two hopping events between the same pair of states. Combining this information with the one discussed above (hops in different regions of the intersection space) allows us to assume that TSH, in this particular case, suffers from its lack

of decoherence. While the nuclear wavepackets should branch after each nonadiabatic transition, the ITA forces each TSH trajectories to propagate their amplitudes on the support of a unique trajectory, leading to an overcoherence propagation.[221] Importantly, a large average number of hops between the same pair of states may also defeat the fewest-switches idea of TSH and insufflate a mean-field character to the excited-state dynamics.[16] The described failure of TSH is, however, easily addressed by enforcing decoherence on the amplitudes carried by each trajectory, as showed by the excellent agreement of dTSH with AIMS during the entire nonadiabatic dynamics and its reduced number of average hops. It is noted that decoherence corrections may not offer an adequate patch to TSH if recoherences were present in the dynamics.[273]

The molecular Tully model II can then be used to study the behaviour of a given nonadiabatic molecular dynamics method during excited-state dynamics with multiple crossings between the same pair of electronic states. It also offers an exciting test for novel strategies that aim at incorporating decoherence effects in mixed quantum/classical methods beyond the somehow *ad hoc* corrections of the TSH algorithm.

5.3.4 Molecular Tully Model III – Fulvene

Previous theoretical work on the fulvene molecule has unravelled two possible decay channels upon photoexcitation on the first excited electronic state S_1, see for example Refs. [234, 274–276]. The first deactivation pathway is driven by a *stretch* of the C=CH_2 moiety and involves a strongly sloped conical intersection with S_0, while the second one relies on a *twist* of the same C=CH_2 moiety and decay through a peaked conical intersection. In the first mechanism, the photogenerated nuclear wavepacket passes through the sloped conical intersection and is subsequently reflected on the lower electronic state back towards the nonadiabatic region where a recrossing takes place, leading to a stepwise decay of the S_1 population. Such a nonadiabatic transition involving a reflection is reminiscent of the dynamics generated by the Tully model III (see Fig. 5.1c). More importantly, the previous theoretical studies also highlighted the strong correlation between the initial dynamics of the nuclear wavepacket and the decay channel followed.[234] Hence, one of the two deactivation pathways can be privileged by altering the initial conditions for the dynamics – an observation that will be used in the following to probe the reflection mechanism in the nonadiabatic dynamics of fulvene. To ensure a favoured decay of the nuclear wavepacket through the sloped conical intersections, the initial geometries for the

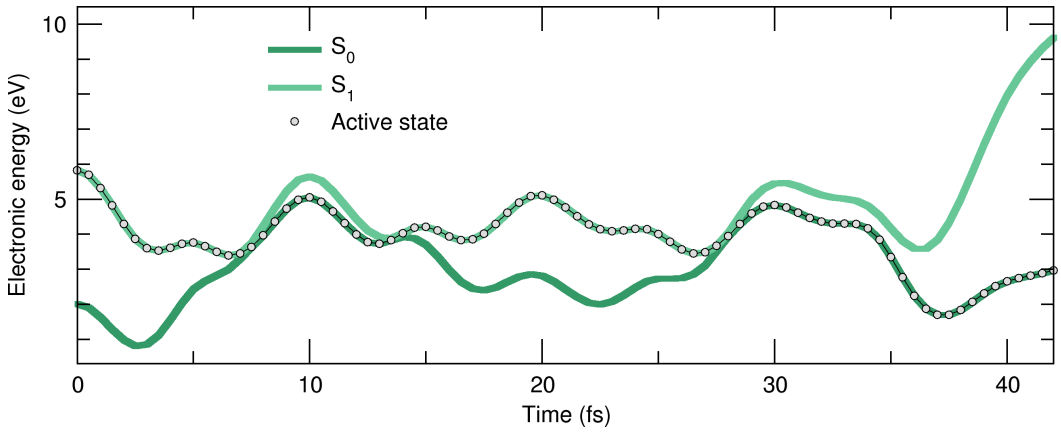

Fig. 5.6.: Photodynamics of fulvene as a molecular Tully model III. Time trace of the potential energies along a representative dTSH trajectory (the active state for the dTSH dynamics is indicated by filled circles).

dynamics are sampled from a Wigner distribution but their initial momenta are set to zero in the first place.

The reflective nature of the nonadiabatic dynamics through the sloped conical intersection is illustrated by the exemplary dTSH trajectory presented in Fig. 5.6. During the dynamics, the two electronic states get closer in energy until the conical intersection is reached at around 7 fs, leading to a net transfer of population from S_1 to S_0. However, the trajectory rapidly reflects and reaches the same region of configuration space again after only 5 fs, where a recrossing occurs and leads to a population back transfer towards S_1. The coupling region is met again after 28 fs of dynamics, this time leading to a stable trajectory in S_0. Importantly, all the recrossings occur at close electronic energies, indicating that the nuclear wavepacket hits each time a similar region of the intersection seam.

AIMS, dTSH, and TSH show all a significant S_1 population decay after 7 fs of dynamics and agree on the remaining population in the excited state: $\sim$ 20% after 10 fs (see Fig. 5.7a). The recrossing leading to back population transfer occurs in all methods shortly after, but its related population transfer depends on the nonadiabatic dynamics method employed. While AIMS predicts that only around 30% of population is in the S_1 state between 15 and 25 fs, the repopulation process of S_1 starts earlier and lasts longer with TSH and dTSH (at around 12 to 30 fs) and the resulting excited-state population plateaus at higher values (40% and 50% of S_1 population with dTSH and TSH, respectively). Interestingly though, all methods appear to agree more closely during the subsequent nonadiabatic event occurring between 35 and 45 fs. The average number of hops tends towards two for TSH and dTSH within the timescale of our simulation. In contrast, the average number of child TBFs

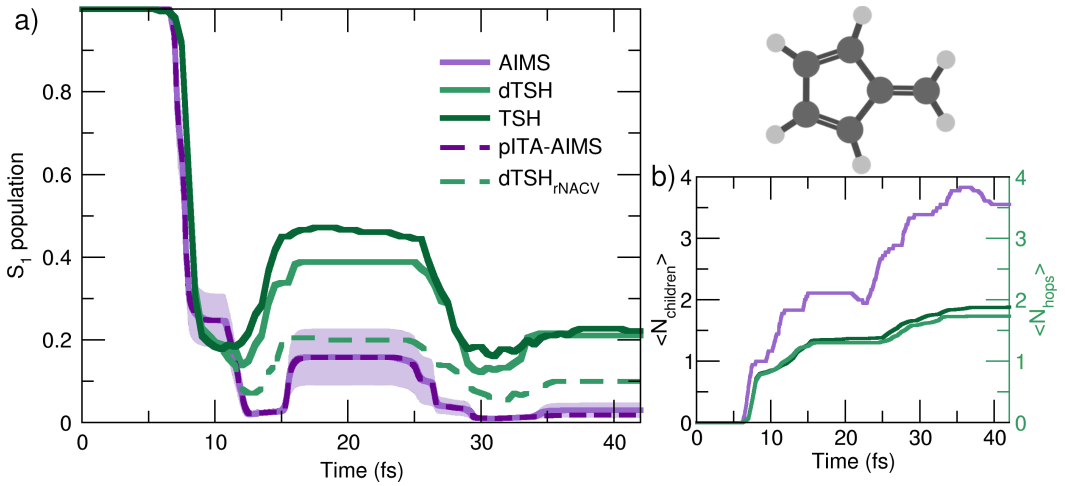

Fig. 5.7.: Photodynamics of fulvene as a molecular Tully model III. a): S_1 population decay as obtained with AIMS (purple, standard error given as a shaded area), TSH (dark green), decoherence-corrected TSH ('dTSH', light green), decoherence-corrected TSH with velocity rescaling performed around the nonadiabatic coupling vectors ('dTSH$_{rNACV}$', dashed green), and pseudo independent trajectory approximation in AIMS ('pITA-AIMS', dashed palatinate with standard error given as a shaded area). b): time traces of the average number of child TBFs ($< N_{children} >$) and the average number of hops performed in (d)TSH ($< N_{hops} >$).

increases stepwise to a value of 5.5 over the same period of time, highlighting that AIMS spawns new TBFs for the different recrossing events (cf. Fig. 5.7b).

To ensure a conservation of total energy along a (d)TSH trajectory, it is necessary to adjust the nuclear kinetic energy after each surface hop to account for the loss or gain in potential energy. Several strategies have been proposed for this task: the most straightforward approach (implemented as default in several TSH codes) is to rescale the nuclear velocity vectors isotropically – a strategy used in all (d)TSH runs above. Alternatively, nuclear velocities can be scaled along the nonadiabatic coupling vectors. This latter strategy is usually encouraged as it can be justified by semiclassical arguments, but in practice, it implies the explicit calculation of the nonadiabatic coupling vectors, which might increase the computational cost of the dynamics. In AIMS, the nuclear kinetic energy of a newly spawned TBF is by default rescaled along the nonadiabatic coupling vectors, but can also be done isotropically. The influence of the nuclear velocity rescaling is tested on the result presented above for dTSH and AIMS. In dTSH, rescaling the nuclear velocities along the nonadiabatic coupling vectors (dTSH$_{rNACV}$ in Fig. 5.7) drastically alters the population dynamics: the S_1 population decays to around 5% during the first nonadiabatic transition and the amount of repopulation of the S_1 state is reduced to only

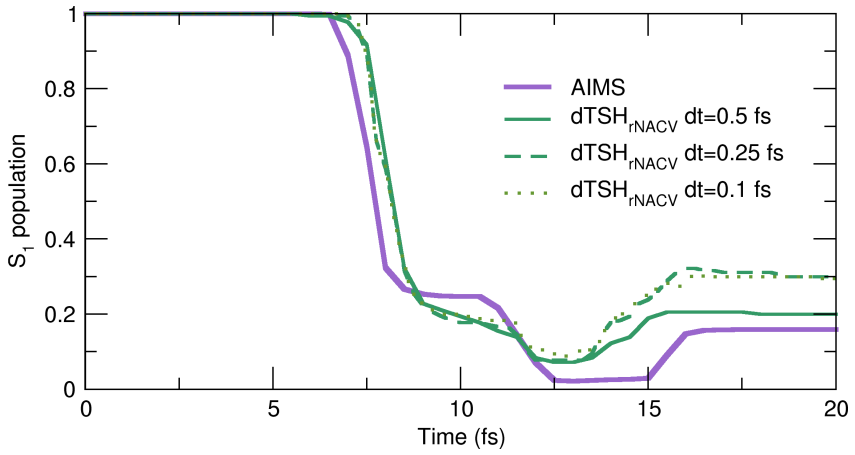

Fig. 5.8.: Convergence of the dTSH$_{rNACV}$ dynamics of fulvene with respect to the timestep.

around 20%. In contrast, the AIMS dynamics is mostly unchanged when the child TBFs nuclear velocities are rescaled along the nonadiabatic coupling vectors or isotropically. However, it can be seen that by reducing the time step during the TSH dynamics, the population curve obtained with dTSH$_{rNACV}$ shows the stronger repopulation as observed with dTSH (see Fig. 5.8).[178] This observation highlights the importance of converging dTSH simulations also with respect to their timestep.

A key difference between AIMS and (d)TSH is that the TBFs in the former are coupled, while the trajectories of the latter are all propagated independently as a result of the ITA (see Sec. 2.6.2). To analyze the role of the role played by the intrastate couplings between TBFs in AIMS, that is, the coupling between the TBFs evolving on the same electronic state, the AIMS dynamics are repeated with removing all direct intrastate couplings by setting the overlap between the TBFs belonging to the same electronic state to zero. This pseudo independent trajectory approximation in AIMS (pITA-AIMS, dark purple dashed line in Fig. 5.7) substantially alters the population dynamics originally observed with AIMS after around 11 fs: an almost complete population decays of S_1 is observed, and the reflection only brings $\sim$ 15% of the S_1 population back. Interestingly, the population dynamics of pITA-AIMS is in quite close agreement with that obtained by dTSH$_{rNACV}$, pointing out the potential importance of the intrastate coupling between TBFs for the decay of fulvene through its sloped intersection. However, it is important to remember at this stage that, while AIMS accounts for both intra- and interstate couplings between the TBFs emanating from a given parent TBF, the Hamiltonian matrix elements responsible for such couplings are approximated using the SPA0 (see Sec. 2.5.3). Interestingly, improving

the description of the intrastate couplings to the SPA1 instead of the SPA0 does not alter the AIMS dynamics, suggesting that the SPA0 may provide a reasonable description of the coupling between the TBFs present in the simulation (see below for an additional discussion on these results).

An exciting aspect of the original one-dimensional Tully models is the possibility to change the initial momentum of the nuclear wavepacket. Such a variation of the initial kinetic energy of the nuclear wavepacket permits to probe the nonadiabatic dynamics in different regimes and also to create specific situations involving nonadiabatic interferences for example (see the discussion on Stueckelberg oscillations above) or transfer of the nuclear wavepacket above a barrier on the potential energy curves. Playing with the initial momenta for a molecular system is more challenging to achieve in a controlled way but was proposed for different molecules as a means of investigating specific photochemical reaction pathways.[234,276,277] It is proposed here to reproduce this specific feature of the original Tully models by testing the influence of the initial momenta on the nonadiabatic dynamics of fulvene.

To achieve this goal, a simplified scheme is proposed here where the same set of initial conditions (described earlier) is used for the nuclear configurations, but to which a (single) set of nuclear momenta is attached that is sampled according to a Wigner distribution where *only* the contribution of the $C{=}CH_2$ stretching mode is incorporated while all other contributions are set to zero (overall kinetic energy of 1.71 meV). This choice is motivated by the discussion above on the deactivation pathways of fulvene: the sloped intersection is reached by a coordinate containing a substantial contribution from the $C{=}CH_2$ stretching. Hence, adding more kinetic energy along this mode will affect the dynamics of fulvene along the reactive coordinate leading to the sloped conical intersection – a test reminiscent of the idea of altering the nuclear momentum of a nuclear wavepacket in the original one-dimensional Tully models. To further enhance the effect of this kick in kinetic energy, a multiplicative factor is applied to the initial set of nuclear velocities (of the (d)TSH trajectories or AIMS TBFs) to generate additional initial conditions with an increasing amount of nuclear kinetic energy. While this offers a simple testbed for the influence of the initial kinetic energy of the system on the branching ratio between electronic states, it has to be duly noted that methods incorporating a more accurate description of the nuclear wavepacket dynamics (such as FMS or vMCG) would also need to correct the initial wavefunction, that is, the amplitudes carried by each travelling Gaussian, to adequately

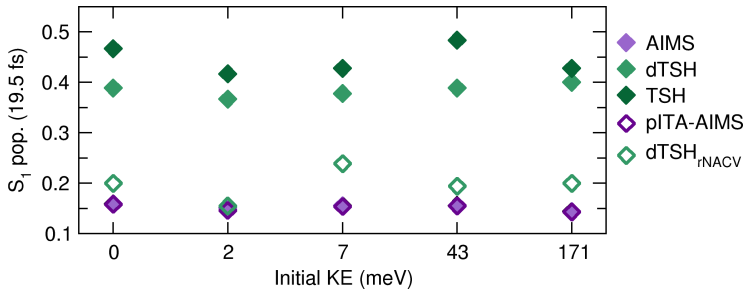

Fig. 5.9.: S_1 population after 19.5 fs of dynamics for initial conditions with different initial nuclear kinetic energy for all methods presented in the central figure.

perform such a test (see for example Ref. [276]). In Figure 5.9 shows the S_1 population after 19.5 fs of dynamics for AIMS and (d)TSH as a function of the initial kinetic energy of the trajectories or TBFs, respectively. While the S_1 population at this time seems to only slightly vary for both TSH and dTSH for different kinetic energies, AIMS shows more variations. The difference between the population decay in dTSH and $dTSH_{rNACV}$ discussed above for the case with zero initial kinetic energy is also visible over the full range of nuclear kinetic energies: a significantly lower population in S_1 is observed after 19.5 fs in $dTSH_{rNACV}$ in all cases. In addition, the good correlation between the result of $dTSH_{rNACV}$ and pITA-AIMS discussed above is also observed for most tests with higher initial kinetic energy – both predicting a significantly lower S_1 population after 19.5 fs than all other methods. It has to be noted that $dTSH_{rNACV}$ shows a stronger repopulation of the S_1 in the case of the initial kinetic energy of 7 meV, leading to a closer agreement with the AIMS dynamics.

From the dynamics proposed here, it appears that the molecular Tully model III requires a proper description of the non-local behaviour of the nuclear wavepackets involved in the dynamics. This is translated in AIMS by the importance of intrastate couplings between the TBFs spawned in S_0. While this could constitute an exciting test for methods describing such couplings[131,146,149] and an example of potential issues with the independent trajectory approximation of (d)TSH, at this stage the earlier *caveat* should be repeated. AIMS can describe both intra- and interstate couplings between TBFs, but the integral mediating such couplings are approximated – see the brief discussion on the SPA in Secs. 2.5.3 and 4.5, and Ref. [212] for more details – and a sufficient number of TBFs are required to ensure an adequate convergence of the result. More specifically, the intrastate coupling is only crudely approximated and higher order of the SPA can be required in cases where such couplings are critical (see also the discussion on time-dependent dipole moments in

Ref. [212]). As mentioned above, additional calculations have been carried out using the SPA up to first order for the set of initial conditions with zero initial kinetic energy, and only minor differences in the population dynamics are observed. While the test comparing the SPA0 and SPA1 is reassuring, the molecular Tully model III will surely stimulate further development of AIMS to ensure that intrastate (and interstate) couplings are adequately described in such cases and to investigate the importance of spawning more child TBFs when intrastate couplings appear to be important.

5.4 Challenging new nonadiabatic dynamics methods with the molecular Tully models

Since their proposition, the molecular Tully models have been used in several contexts to test the limits of nonadiabatic dynamics methods. The methods that have been tested on one or more of the molecular Tully models include fewest switches surface hopping with Baeck-An couplings,[278] ab initio symmetric quasi-classical approach,[279] decoherence induced surface hopping based on the exact factorisation,[178] stochastic selection ab initio multiple spawning,[280] and ab initio multiple spawning with informed stochastic selections.[281] In the following, I want to shortly present two exemplary uses of the molecular Tully models.

5.4.1 Stochastic selection ab initio multiple spawning – fulvene

As introduced in Sec. 2.5.4, the newly proposed SSAIMS method provides an approximation to AIMS dynamics to reduce the computational cost.[169] It monitors the coupling between (groups of) TBFs and once this coupling falls below a predefined threshold, a stochastic process is initiated and one of the groups of TBFs is eliminated and removed from the dynamics. This stochastic process is reminiscent of the stochastic hops employed in TSH even if the stochastic process in SSAIMS does not take place during the nonadiabatic transitions but later on when TBFs become uncoupled. Therefore, it is inviting to compare the formalism of SSAIMS in its two flavours — ESSAIMS and OSSAIMS (using an energy or overlap based criterion for the initialisation of the stochastic selection process, see Sec. 2.5.4) — with AIMS and TSH, for the quality of the predicted population traces as well as the computational efficiency. The molecular Tully model III, fulvene, was shown above to be quite sensitive to the method employed with significant differences between

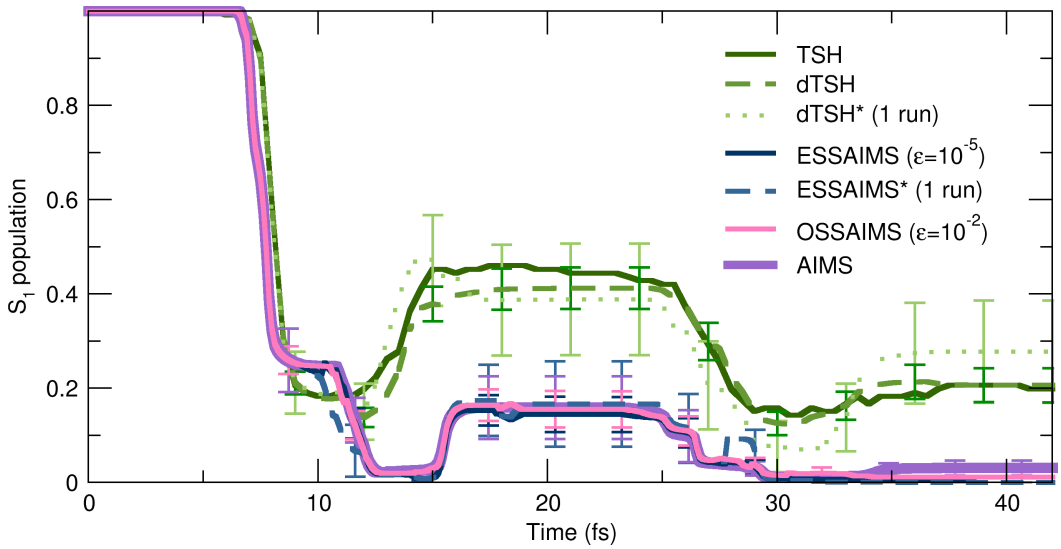

Fig. 5.10.: Photodynamics of fulvene – comparison between AIMS, (E/O)SSAIMS, and (d)TSH. Lower panel: S_1 population decay as obtained with AIMS (purple curve), TSH (dark green curve), dTSH (green dashed curve), ESSAIMS (dark curve, $\epsilon = 10^{-5}$ au), OSSAIMS (light curve, $\epsilon = 10^{-2}$), dTSH* (light green dotted curve, one run per initial condition), and ESSAIMS* (blue dashed curve, one run per initial condition). Error bars indicate standard errors.

the population traces predicted by AIMS and TSH. It is therefore a model of choice for the comparison between (E/O)SSAIMS, AIMS and TSH.

Computational details

The identical AIMS, TSH and dTSH dynamics as described in Sec. 5.3.1 are used for comparison here. The (E/O)SSAIMS dynamics are performed with the FMS90/MOLPRO interface, the same electronic structure and AIMS parameters as described for AIMS in Sec. 5.3.1 are used. The thresholds used for the stochastic selection are 10^{-5} E_h for ESSAIMS and 10^{-2} for OSSAIMS. For convergence of the stochastic algorithm, the SSAIMS dynamics for every initial condition are all repeated 5 times with different random seeds. To ensure a fair comparison, the dTSH dynamics are repeated 7 times with different random seeds, so that the maximum of the standard error in the S_1 populations match between SSAIMS and dTSH.

Results

Fig. 5.10 shows the S_1 population traces for AIMS, ESSAIMS, OSSAIMS, as well as TSH and dTSH. Despite the complexity of the reflection process, both ESSAIMS($\epsilon = 10^{-5}$ au)

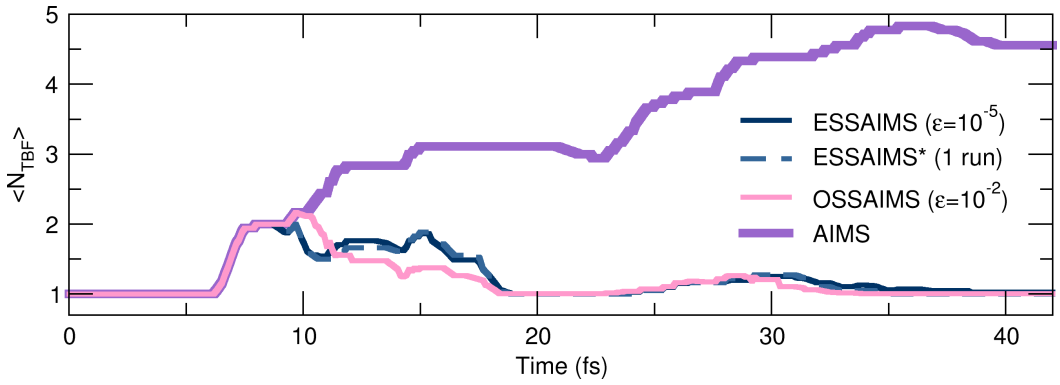

Fig. 5.11.: Computational effort of the photodynamics of fulvene. Top panel: time traces of the average number of TBFs ($< N_{TBF} >$) for each method.

and OSSAIMS($\epsilon = 10^{-2}$) accurately reproduce the initial decay of population and the first revival of S_1 population obtained with AIMS. OSSAIMS predicts the same amount of reflected population as AIMS, while ESSAIMS only slightly underestimates it. The stochastic-selection strategies do not fully capture the second, much weaker reflection process after 35 fs of dynamics using their respective selection criterion. Looking at the average number of TBFs during the dynamics, one can deduce that the stochastic selection algorithm only takes effect after 10 fs of dynamics when 2 TBFs are present on average for all methods. Subsequently, the average number of TBFs in AIMS grows significantly, up to almost 5, while it decreases in ESSAIMS and OSSAIMS and remains well below 2. In contrast with the agreement between (E/O)SSAIMS and AIMS, the population trace predicted by (d)TSH differs significantly from that obtained with AIMS, with more than twice the population appearing in S_1 after the reflection process.[†]

Matching the standard error of (E/O)SSAIMS with that of (d)TSH requires five runs for the former and seven for the latter, for each initial condition. Therefore, for long periods of the simulation, where the number of TBFs in (E/O)SSAIMS remains well below 2, its computational cost is comparable and even lower than the cost of TSH. Interestingly, AIMS is the least expensive method during the first half of the dynamics, until 20 fs of dynamics, at which points its computational effort rises above the one of the fully converged (E/O)SSAIMS.

The ESSAIMS population trace obtained with only one run per initial condition already agrees closely with the fully-converged result – within the standard error of the fully converged ESSAIMS result for most of the simulation, except for the initial decay at 10 fs

[†] As described above, the simulation parameters of dTSH can have an important influence on the population decay in the dynamics of fulvene.

and during the short repopulation at 28 fs. Conversely, the dTSH dynamics with a single run shows significant deviations from its converged result, lying well outside the standard error for most of the dynamics. This example further highlights the difference between the stochastic processes in (E/O)SSAIMS and (d)TSH: in (d)TSH the stochastic process is used to describe the nonadiabatic transitions *per se*, and its convergence is crucial in complex nonadiabatic processes like here with fulvene; in (E/O)SSAIMS, the stochastic processes mostly take place after the nuclear wavepacket branching following a conical intersection, while the nonadiabatic transition itself remains described at the AIMS level.

5.4.2 Decoherence corrections based on the exact factorisation

As introduced in Sec. 2.6.3, a critical aspect when performing a TSH simulation is to account, at least approximately, for decoherence — which TSH in its original formulation fails to do. Therefore, one needs to rely on additional decoherence corrections to overcome the overcoherent nature of TSH. To this end, different schemes have been recently proposed (see Sec. 2.6.3 for a list), among which decoherence induced surface hopping based on the exact factorisation (DISH-XF). The performance of DISH-XF has not been compared yet with other decoherence corrections or with higher-level non-adiabatic dynamics methods (aside from model systems where exact results are available). Therefore, the main objective here is to compare the effects of the decoherence correction arising from the exact factorisation to the widely used energy based decoherence correction (TSH-EDC) and augmented fewest switches surface hopping (A-FSSH). A short explanation of all different decoherence schemes used in this work is provided in Sec. 2.6.3.

Computational details

The same AIMS calculations as detailed in Sec. 5.3.1 are used for reference here. Identical electronic structure and initial conditions as described in Sec. 5.3.1 are used for all the dynamics for both, ethylene and fulvene. The TSH and DISH-XF, calculations are performed with the code PyUNIxMD (UNIversal eXcited state Molecular Dynamics, UNI-xMD).[282] The TSH-EDC and A-FSSH computations are done with the code SHARC 2.0 (Surface Hopping including Arbitrary Couplings)[217,249,250].

The nuclear time-step is taken as $dt = 0.5$ fs unless otherwise stated, while the electronic time-step is taken 10000 times smaller in UNI-xMD, and 25 times smaller in SHARC (the default). It has been checked that decreasing the time-step does not alter the results except

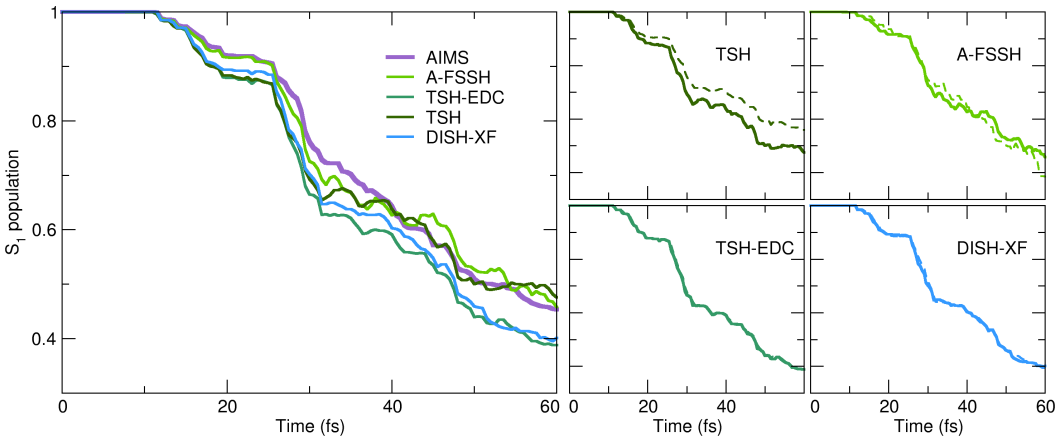

Fig. 5.12.: Population dynamics in ethylene: DISH-XF compared with TSH, TSH-EDC and A-FSSH, all with isotropic velocity adjustment, along with the reference AIMS results. The left panel shows the fraction of trajectories $\Pi_{S_1}(t)$ in the S_1 state. The right panels demonstrates the internal consistency of the surface-hopping methods, with the solid lines showing $\Pi_{S_1}(t)$ again, compared with dashed lines showing the S_1 electronic populations $\rho_{S_1,S_1}(t)$.

for the case of fulvene; the convergence is generally better for the decoherence-corrected schemes than uncorrected ones. As will be discussed, the dynamics in fulvene is somewhat sensitive to the choice of time-step. The large slope of the crossing region means that a large number of trajectories encounter the sharp and localised non-adiabatic coupling.

For TSH and DISH-XF, the explicit NACV were used in the equation of motion, while for TSH-EDC and A-FSSH they were obtained from wavefunction overlaps by default in SHARC.[251] There is little difference in the results when using these two approaches, except for the fulvene molecule where the convergence with respect to time-step is better using the wavefunction overlap scheme, as mentioned earlier. An isotropic velocity adjustment was performed after a surface hop unless otherwise stated.

Ethylene

For each of the surface hopping schemes, 10 trajectories for each initial condition are run but the results are already converged even with 5 trajectories per initial condition. The width of the Gaussian, σ, used to estimate the nuclear density in DISH-XF, is obtained from the initial distribution of the nuclear trajectories of the C=C double bond, and it is set to 0.05.

Fig. 5.12 shows the S_1 populations as determined by both the fraction of trajectories and the electronic populations, computed from the TSH, DISH-XF, TSH-EDC and A-

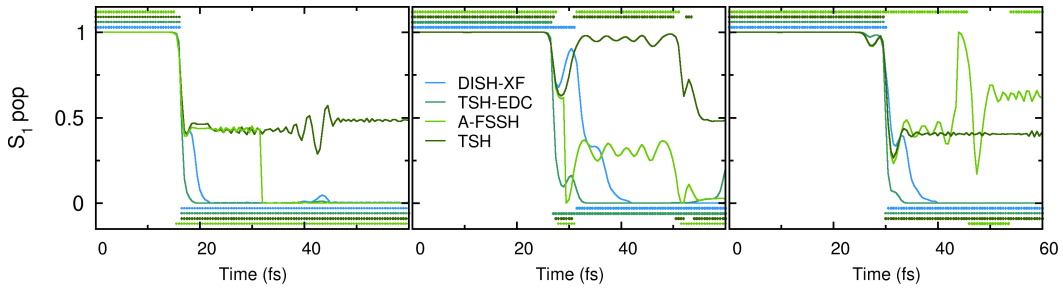

Fig. 5.13.: Comparing population dynamics in ethylene for 3 trajectories with the same initial conditions, TSH, DISH-XF, TSH-EDC and A-FSSH, with isotropic velocity adjustment. Continuous lines show the populations $\rho_{S_1,S_1}(t)$ while the correspondingly coloured symbols indicate the active state. Top panels show the electronic energies during DISH-XF dynamics.

FSSH simulations. For this system, the fraction of trajectories predicted by uncorrected TSH is very close to the reference AIMS, but there is a notable internal consistency error, as expected. Averaged over trajectories, the DISH-XF decoherence correction from exact factorisation and TSH-EDC yield very similar results, increasing the population transfer compared to the uncorrected TSH, and correcting the internal consistency of the uncorrected TSH (the electronic populations are practically on top of the fraction of trajectories in both cases). They appear to agree less well with AIMS but do not deviate too far and would lie within the standard error of AIMS A-FSSH is closer to AIMS, but it shows worse internal consistency than TSH-EDC and DISH-XF.

The close agreement of DISH-XF, TSH-EDC and A-FSSH is not obvious, given the different structure of the corrections discussed earlier. Comparing on an individual trajectory level the electronic populations and active state for the different decoherence corrections, they show a quite different behaviour (see Fig. 5.13 for three randomly chosen trajectories). The TSH-EDC correction damps down the populations after a hop in a mostly (but not entirely) monotonic way, while the DISH-XF tends to be typically non-monotonic, showing more oscillations and generally takes longer to decohere. The stochastic nature of the A-FSSH decoherence correction is evident, and suggests, for this molecule, a longer decoherence time than the other methods.

The different behaviour on an individual trajectory level is reflected in an average over all trajectories of the decoherence indicator,[27,130,131] defined as $\rho_{10}(t) = \sum_J^{N_{\text{traj}}} |C_{S_1}^{(J)} C_{S_0}^{(J)}|^2 / N_{\text{traj}}$. The DISH-XF dynamics grows to a larger coherence and takes a longer time to decohere than TSH-EDC, but the overall structure is similar. On the other hand, as clear from the sample trajectories, A-FSSH remains coherent longer. Although, in the present case, this

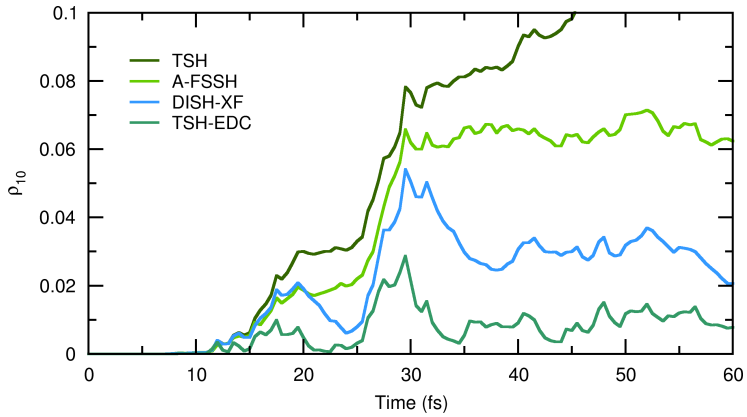

Fig. 5.14.: Decoherence indicator in ethylene: TSH, DISH-XF, TSH-EDC and A-FSSH.

difference does not affect the overall population dynamics very much, nor the nuclear geometries (not shown), it opens the question of whether the different behaviour results in other systems.

Finally, the importance of the choice of velocity adjustment (see Sec. 2.6.3) is evident in Fig. 5.15, where the top panel shows the results of uncorrected TSH with three different ways of velocity adjustment and the lower panel shows the DISH-XF case. The spread in the results shows that, in this case, the choice of velocity adjustment has just about as much effect on the dynamics as the decoherence correction. In particular, while the internal consistency is very well corrected by the decoherence correction when using isotropic scaling, errors remain when scaling along NACVs is performed, consistent with the expectation. When isotropic scaling is used as a "back-up" to scaling along the NACV in the NACV+iso approach, the error in the internal consistency is again small when the decoherence correction is applied; the results are close to the isotropic scaling case for this molecule.

Fulvene

As stated above, fulvene represents a challenging case due to the reflection process on the sloped conical intersection. In addition, it has been observed that the choice surface hopping scheme can have substantial influences on the predicted population decay. Therefore, it seems to present an ideal test system for the effects of DISH-XF. The σ parameter of DISH-XF is chosen as 0.065, which corresponds to the variance of the initial distribution of C=C double bonds of the nuclear trajectories.

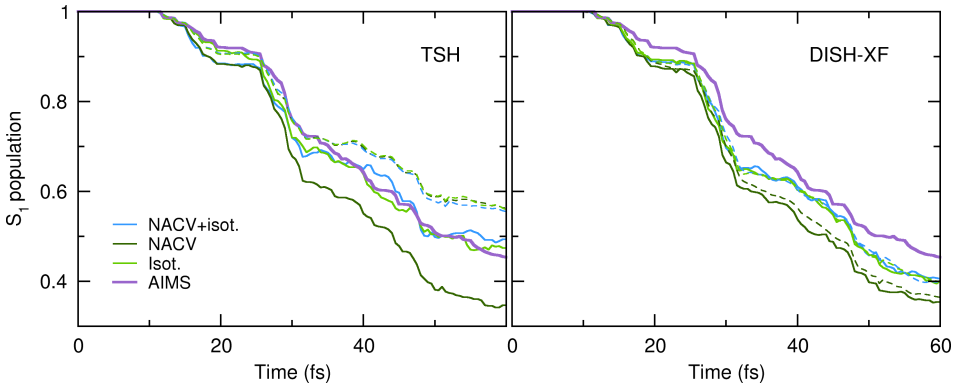

Fig. 5.15.: Comparison of different velocity adjustments in ethylene. Left panel: uncorrected TSH, $\Pi_{S_1}(t)$ and $\rho_{S_1,S_1}(t)$, with velocity adjustments of isotropic, NACV, and NACV-iso; right panel: the same with DISH-XF. AIMS is shown as reference.

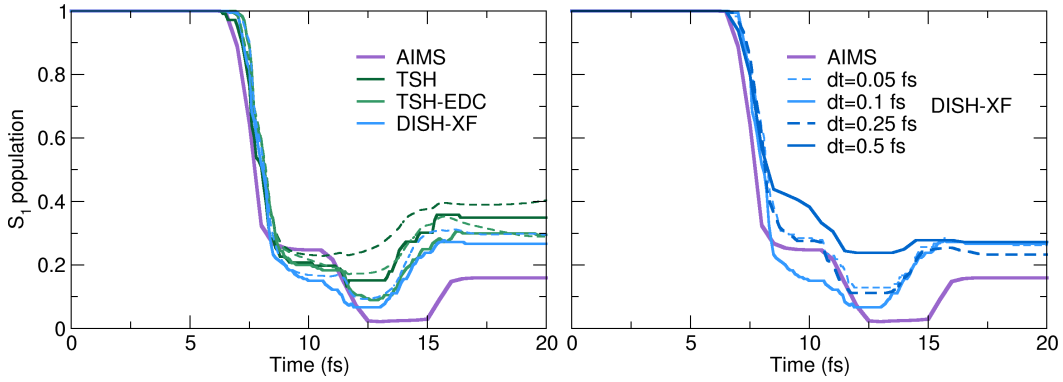

Fig. 5.16.: Fulvene populations. Right panel shows the convergence of Π_{S1} with respect to the nuclear time-step $dt = 0.1, 0.25, 0.5$. Left panel: choosing $dt = 0.1$, the fraction of trajectories Π_{S1} along with ρ_{S_1,S_1} (dashed), for DISH-XF, TSH-EDC, and TSH against the AIMS reference.

The sharply sloped conical intersection gives a large dependence on the time-step dt since the interaction region can be missed. It can be seen that as dt decreases from 0.5, 0.25, 0.1, DISH-XF predicts more population transfer during the initial event (Fig. 5.16, top panel), as expected when the non-adiabatic couplings are sharply peaked. For DISH-XF, the $dt = 0.1$ are close to converged with respect to dt, as shown by the result with $dt = 0.05$. Partially, this dependence can be mitigated by using wavefunction-overlaps to compute the coupling terms, with a local diabatisation scheme. The TSH-EDC calculations in SHARC utilise this scheme, and it was shown in Fig. 5.8 that although TSH-EDC predictions with $dt = 0.5$ (green dash-dot line) plateau to a different level after 15 fs (and is closer to the AIMS result) than that predicted with the $dt = 0.1$ and 0.25 calculations, the results do appear converged with $dt = 0.25$. This example highlights the need to check for convergence with respect to the time-step in these cases. As mentioned earlier, the recent method of Ref. [283] is promising in this regard. AIMS uses an adaptive time-step so does not have such sensitivity.

In the lower panel, it can be seen that both decoherence-corrected schemes increase the population transfer compared to pure TSH, with good internal consistency. Both TSH-EDC and DISH-XF agree quite well with each other, despite their different operation mechanisms.

5.5 Conclusions

In this chapter, a molecular version of the original Tully models was proposed, aiming at offering a unified mean of comparison between the different strategies for on-the-fly nonadiabatic molecular dynamics. First, these tests were used to compare two of the most commonly employed methods for excited-state dynamics, TSH and AIMS.

The molecular Tully model I, ethylene, offers a simple test for nonadiabatic molecular dynamics as it depicts photodynamics dominated by a single nonadiabatic crossing event. As such, all methods tested are in good agreement, with a potential tendency for (d)TSH to exhibit a slightly faster S_1 population decay in the early stage of the excited-state dynamics. The molecular Tully model II, DMABN, stresses the nonadiabatic methods slightly more as the photodynamics from the S_2 excited state involves multiple crossings between S_2 and S_1 – a rather challenging dynamics to describe for TSH without a correction for decoherence. The molecular Tully model III, fulvene, paves the way for numerous

ways of playing with nonadiabatic methods. The reflection of the nuclear wavepacket following passage through the sloped conical intersection as well as the possible intra- and interstate coupling between the nuclear wavepackets makes it a rather stringent test for all methods tested. The population dynamics can be altered by varying the initial conditions (nuclear kinetic energy) of the nonadiabatic dynamics *à la Tully*. The AIMS dynamics indicates that intrastate couplings between TBFs are likely to play a role in the nonadiabatic dynamics of fulvene – a type of couplings not described in (d)TSH due to its independent trajectory approximation. However, while previous dynamics using vMCG seem to confirm the importance of these couplings, the photodynamics of fulvene exemplifies one of the important limitations of the molecular Tully models presented here: the lack of exact solutions for these nonadiabatic processes. Nevertheless, the central goals of these molecular Tully models are to (*i*) compare the strengths and weaknesses of different nonadiabatic molecular dynamics and (*ii*) stimulate the detection of potential improvements by highlighting processes that stress the existing approximations of a given method – for example, the saddle-point approximation of AIMS in the present case of fulvene.

Interestingly, the original Tully models highlighted specific features of nonadiabatic dynamics that were observed in the molecular version of this models, further reinforcing – if needed – the need for challenging models in low dimensions and providing an essential connection between the world of chemical physics (exactly-solvable models) and physical chemistry (photodynamics of molecules).

After their proposition, the molecular Tully models have already been used to test the stability and performance of several nonadiabatic methods. In this chapter, it was exemplified how the two flavours of SSAIMS (ESSAIMS and OSSAIMS) manage to reproduce the AIMS dynamics of fulvene, at a cost comparable to TSH. It could be observed that with equally good agreement, OSSAIMS reduced the cost of the dynamics even further. In addition, on the Tully models I and III, the DISH-XF formalism was compared to other commonly employed decoherence schemes for TSH. It was found that the DISH-XF, TSH-EDC, and A-FSSH decoherence corrections operate in very different ways on an individual trajectory, but at least for the systems studied, when averaged over the full set of trajectories, the results for the electronic populations and nuclear geometry dynamics are similar.

Overall, the molecular Tully models propose a first step towards a generalisation of benchmarks for nonadiabatic dynamics methods for full molecular systems. They are

intended of serving as a set of prototypical molecules, where controlled testing of approximations of nonadiabatic dynamics methods is facilitated, which probe some processes that typically occur in molecules upon photoexcitation.

6 Probing the limits of nonadiabatic dynamics with photoinduced ring-opening reactions

This chapter is based on the publication:
L. M. Ibele*, Y. Lassmann, T. J. Martínez and B. F. E. Curchod, "Comparing (stochastic-selection) ab initio multiple spawning with trajectory surface hopping for the photodynamics of cyclopropanone, fulvene, and dithiane", J. Chem. Phys., 154, 104110 (2021)
*Contribution: carried out all the TSH and AIMS calculations, all SSAIMS calculations on dithiane, part of the SSAIMS calculations on cyclopropanone, analysed the data and wrote the initial draft of the manuscript.

6.1 Introduction

As discussed in Sec. 2.5.3, AIMS can provide very accurate nonadiabatic dynamics simulations on the fly for molecules in their full configuration space. The method is based on a set of fully coupled TBFs that can be expanded during the dynamics whenever necessary. In theory, the number of electronic-structure calculations required per AIMS time step scales quadratically with the number of TBFs, due to their mutual coupling.* As the spawning algorithm is only designed to create new TBFs, it is not unusual that a large number of TBFs is carried throughout the dynamics with the nuclear amplitude only distributed among a few of them – the other TBFs do not contribute to the description of the nuclear wavepackets anymore or are not coupled to the rest of the swarm. The stochastic selection *ab initio* spawning (SSAIMS, cf. Sec. 2.5.4),[169] offers a way to reduce the cost of an AIMS simulation with only a minimal loss of accuracy in the description of the nonadiabatic processes. Proof-of-principle tests of SSAIMS have revealed its potential as a cheaper

*In most implementations of the AIMS algorithm, this scaling is alleviated by neglecting matrix elements between TBFs with vanishing nuclear overlap.

alternative to AIMS, as shown on simplistic molecules in Ref. [169] and this work, on the molecular Tully III, fulvene, in Sec. 5.4.1.

There are (among others) two situations, where the fully coupled nature of the TBFs in AIMS has a strong effect that limits the applicability: i) if one electronic state leads to encounter regions of configuration space where the electronic structure method potentially becomes unstable and ii) if the dynamics encounters repeated and delocalised crossings of two or more electronic states which triggers a large number of spawns. In the first case, the coupling of the TBFs limits the use of AIMS drastically: if one TBF out of the large bundle encounters an instability, the whole dynamics has to be stopped, even if this TBF is not interacting with the bundle anymore. In the latter case, the large number of TBFs will make the dynamics computationally very expensive and therefore limits the time scale and system size accessible in the dynamics. These two situations are both commonly observed in photoinduced ring-opening processes of molecules. i) The photoinduced ring-opening often drives a molecule to the ground state with high kinetic energy and the biradical character facilitates formations of photoproducts which can challenge the electronic structure method, for example when using active space methods. ii) In the limit of bond dissociation, a common occurrence is degeneracies between two or more excited states involving the antibonding or lone-pair orbitals.

Therefore, in this chapter, two prototypical molecules, cyclopropanone and 1,2-dithiane, are used to probe these two limiting cases of nonadiabatic dynamics, highlighting the strengths and limitations of both AIMS and TSH and showing the compromise between accuracy and efficiency provided by SSAIMS. This chapter illustrates how, through careful choice, molecules can be used as model systems to probe specific limiting cases of nonadiabatic dynamics.

To motivate the adoption of cyclopropanone and 1,2-dithiane as a testbed for SSAIMS, their photodynamics is briefly described, illustrated by a schematic depiction of their nonradiative decay (Fig. 6.1). The dynamics of cyclopropanone has been subject to several studies in the past.[284–287] Photoexcitation to the first excited singlet state (S_1) triggers a ring-opening reaction, mediated by carbon-carbon bond breaking followed by subsequent dissociation into ethylene and CO. The S_0 and S_1 potential energy curves along an interpolation in internal coordinates between the ring-closed Franck-Condon and ring-opened minimum energy conical intersection is depicted schematically in Fig. 6.1a. The two electronic states come close in energy during the ring-opening process and separate after

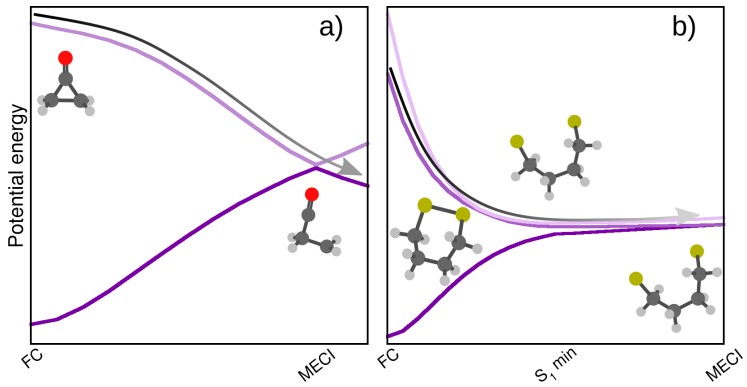

Fig. 6.1.: Schematic depiction of the potential energy curves for (a) cyclopropanone and (b) 1,2-dithiane. The arrows indicate the possible nonradiative pathways. See Computational Details for additional information on the electronic-structure method employed for each case.

the nonadiabatic transition to the ground state. Thus, for cyclopropanone, one expects a relatively straightforward transfer of the nuclear wavepacket from S_1 to S_0, without a significant contribution of the population back transfer to S_1. However, the nonradiative decay is governed by strong geometrical deformations of the molecule – ring-opening and subsequent dissociation – which can challenge the employed electronic structure methods. During an AIMS simulation, it is sufficient that one of the TBFs suffers from an electronic-structure instability to stop the propagation of all the TBFs, even if these are only weakly coupled. SSAIMS could reduce the probability of such a dramatic issue by ensuring that only strongly coupled TBFs are propagated together. 1,2-dithiane shows a sulfur-sulfur ring-opening process upon photoexcitation in its first excited electronic state, followed by complex dynamics where the opened ring recloses within 300 fs.[231] By looking at the three lowest singlet states along a linear interpolation in internal coordinates between the Franck-Condon region, the S_1 minimum geometry, and the S_1/S_0 minimum energy conical intersection (Fig. 6.1b), it becomes apparent that the three singlet states become (and remain) nearly degenerate soon after the ring opens. An accurate theoretical description of the dynamics poses a challenge because of the complex ring-opening and -closing process. Furthermore, the near degeneracy of the three lowest singlet states can induce repeated population transfer – yet another challenge for nonadiabatic dynamics methods.

This chapter is organised as follows: First, the theoretical computational cost of AIMS, SSAIMS and TSH will be elaborated and a scheme for a meaningful comparison of the efficiency of the methods introduced (Sec. 6.1.1. After giving all the computational details

(Sec. 6.2), the photodynamics of cyclopropanone will be analysed (Sec. 6.3). First, a comparison between AIMS and the two flavours of SSAIMS (that use for the initialisation of the stochastic selection either an energy based criterion — ESSAIMS — or the overlap — OSSAIMS) will be undertaken concerning the predicted dynamics and number of TBFs present during the dynamics. Subsequently, the predicted population decay of (SS)AIMS will be compared to the results of (d)TSH and the theoretical computational cost of the methods will be evaluated. For 1,2-dithiane (Sec. 6.4), both schemes (ESSAIMS and OSSAIMS) are compared to dTSH and AIMS, highlighting how a proper stochastic selection is crucial to reproduce the AIMS result. Finally, the conclusions are drawn in Sec. 6.5.

6.1.1 Computational cost of AIMS, SSAIMS, and TSH

This chapter aims not only to compare the performance of SSAIMS in describing complex nonadiabatic dynamics processes with that of AIMS and TSH but also to analyze their respective computational costs.

A comparison of the computational cost in terms of electronic-structure calls or wall time is plagued by the algorithmic details related to the implementation of the method (e.g., adaptive time steps, convergence criteria, or propagation algorithms), which hampers a formal comparison of the computational burden associated to each technique. To provide a comparison that is as fair as possible, it is proposed here to focus on the "theoretical number of electronic-structure calculations" required at each time step of the dynamics, which unravels the computational effort of each method for the different molecular systems presented. In TSH, this number remains constant over time as only one electronic-structure call is necessary for each trajectory at every time step, i.e. it is simply the product of number of initial conditions with the number of repetitions, $N_{\mathrm{ES}}^{\mathrm{TSH}} = n_{\mathrm{rep}} \cdot N_{\mathrm{init}}$. In contrast, the number of electronic structure calls in AIMS and (E/O)SSAIMS will depend on the number of TBFs present in the dynamics at every time step. In the theoretical limit, independently of the algorithmic implementation, assuming that the couplings between all TBFs will be computed, the theoretcial number of electronic structure calculations for AIMS is given by $N_{\mathrm{ES}}^{\mathrm{AIMS}}(t) = \sum_{k=1}^{N_{\mathrm{init}}} \frac{1}{2} N_{\mathrm{TBF}}^{k}(t)(N_{\mathrm{TBF}}^{k}(t)+1)$, while for (E/O)SSAIMS it needs further account for the number of runs per initial condition (and the fact that the number of TBFs created for each initial condition might not be the same within different runs), that is, $N_{\mathrm{ES}}^{\mathrm{(E/O)SSAIMS}}(t) = \sum_{j=1}^{n_{\mathrm{run}}} \sum_{k=1}^{N_{\mathrm{init}}} \frac{1}{2} N_{\mathrm{TBF}}^{k,j}(t)(N_{\mathrm{TBF}}^{k,j}(t)+1)$ The theoretical number of electronic-structure calculations presented in this work is, without any doubt, an idealised

representation of the computational effort of TSH and (E/O)SSAIMS. Still, it offers a formal and straightforward way of comparing the cost of these different methods and unravelling the complexity engendered by the couplings between TBFs in AIMS-based techniques.

6.2 Computational details

6.2.1 Electronic structure

Electronic energies, nuclear gradients of the energies, and nonadiabatic couplings are computed for both molecules studied with SA-CASSCF[236,237] and a 6-31G* basis set.[238,239] For cyclopropanone, an (8/7) active space is used, consisting of the C=O $\pi\pi^*$ orbitals, the $\sigma\sigma^*$ pairs of the adjacent C-C bonds as well as one n lone pair orbital of the oxygen atom, and the state-averaging procedure was performed for the lowest two singlet states. The electronic structure of 1,2-dithiane is described with a (6/4) active space that includes the $\sigma\sigma^*$ pair of the S–S bond as well as two n lone pair orbitals on the sulfur atoms, and with a state averaging for the lowest three singlet states. The SA-CASSCF calculations for 1,2-dithiane are performed with the MOLPRO 2012 program package[247] for the TSH dynamics, and TeraChem[288–292] for the AIMS and (E/O)SSAIMS dynamics.

6.2.2 Nuclear dynamics

The AIMS and (E/O)SSAIMS dynamics for cyclopropanone are performed with the FMS90/MOLPRO interface.[160] For 1,2-dithiane, the AIMS implementation in TeraChem is used.[120,293] All AIMS and (E/O)SSAIMS dynamics share the very same set of parameters for each molecule. The TBFs are propagated with a time step of 20 $\hbar E_h^{-1}$, reduced to 5 $\hbar E_h^{-1}$ in regions of strong nonadiabaticity. The criterion to enter the spawning mode use the norm of the nonadiabatic coupling vectors, with a threshold set to 3.0 a_0^{-1} for cyclopropanone and 20.0 a_0^{-1} for 1,2-dithiane. The minimum population required for a TBF to spawn is 0.01 for cyclopropanone and fulvene, and 0.05 for 1,2-dithiane. The maximum acceptable overlap between a newly-spawned TBF and the existing pool of TBFs is set to 0.6 for fulvene and cyclopropanone, and 0.5 for 1,2-dithiane. For cyclopropanone, the TBFs running on the ground electronic state are stopped if they remained uncoupled with any other TBFs for more than 100 $\hbar E_h^{-1}$. The threshold for total (classical) energy conservation was set to 0.019 E_h for cyclopropanone, 0.005 E_h for 1,2-dithiane. The same set of initial

conditions are used for both (E/O)SSAIMS and AIMS, but the (E/O)SSAIMS runs for each initial condition are repeated five times (with different initial random seeds) to converge the stochastic processes. Different thresholds for the stochastic selection are used and are detailed below.

All TSH simulations are performed with the SHARC 2.0 program.[217,249,250] The TSH trajectories are initiated from the very same set of initial conditions as the AIMS/SSAIMS parent TBFs. Every trajectory is repeated multiple times, typically between 5 and 8 times, with different random seeds to ensure convergence of the stochastic process for the nonadiabatic transitions. The number of repetitions was determined such that the maximum standard error of the S_1 population decay of ESSAIMS and (decoherence-corrected) TSH are in agreement: this criterion was fulfilled with five runs for cyclopropanone and eight for 1,2-dithiane (for each initial condition). The integration time step for the nuclear propagation is set to 0.5 fs (to resemble the 20 $\hbar E_h$ used in (E/OSS)AIMS), a local diabatisation scheme is used, and the nonadiabatic couplings are constructed from wavefunction overlaps to avoid the explicit computation of the nonadiabatic coupling vectors.[251] Following a surface hop, the nuclear kinetic energy is rescaled along the nuclear momenta.

All TSH simulations are carried out with and without the energy-based decoherence correction scheme[184,187] (EDC), which accounts for decoherence through a dampening of the electronic populations in TSH. The decoherence parameter C was set to 0.1 E_h, as proposed in Ref. [187]. The default implementation of the EDC in SHARC is applied, and the same random seeds are used for both TSH and dTSH. [†] All the dTSH trajectories strictly satisfy the internal consistency criterion discussed in Ref [184], and the standard error of the dTSH population decay are calculated using the electronic populations of the trajectories.

6.3 Cyclopropanone – an exemplar scenario of coupled TBFs leading to instabilities in AIMS

The nonadiabatic dynamics of cyclopropanone has been heavily studied in the past employing different combinations of TSH flavors and electronic structure methods.[284–287] All these previous studies highlight the fact that the S_1 population decay of cyclopropanone

[†]The original implementation of the EDC in SHARC is employed, where the amplitudes of the non-running states are damped, instead of the populations, as done, for example, in Newton-X.[187,252,253]

following photoexcitation is rather straightforward – the nuclear wavepacket decays from S_1 to S_0 without any significant back population transfer. The S_1 decay has been characterised by a latency time in S_1 of ~25 fs, followed by a stepwise decay of the S_1 population.[287] However, the structural evolution of the molecule is intriguing: upon excitation, one or two of the C–C bonds adjacent to the carbonyl moiety are broken, leading to dissociation into CO and ethylene within several hundreds of femtoseconds.[284–286] Because of these substantial geometrical rearrangements, a ring-opening process, followed by a full dissociation, cyclopropanone poses an interesting challenge for nonadiabatic dynamics methods, in particular for the underlying electronic structure method.

6.3.1 AIMS versus (E/O)SSAIMS

First, the S_1 population trace is compared as obtained by AIMS for the photodynamics of cyclopropanone with that of (E/O)SSAIMS for different selection thresholds (Fig. 6.2). Due to electronic structure instabilities, AIMS (purple line in Fig. 6.2) can only simulate the first 50 fs of dynamics. The active space employed for SA-CASSCF is not stable when the molecule dissociates on the ground state. While the coupling between TBFs in AIMS permits an adequate description of decoherence processes, it comes with the severe drawback that any instabilities in the propagation of one of the TBFs will prevent the propagation of the entire branch of coupled TBFs. In the particular case of cyclopropanone, a dissociating TBF on the ground state remains coupled, even if only weakly, to other TBFs, and any electronic-structure instability following this dissociation makes it impossible to run the AIMS dynamics for longer times.

This situation highlights one of the key advantages of the stochastic selection algorithm: SSAIMS can detect when a TBF (here evolving on the ground state) is only weakly coupled to the remaining swarm of TBFs, and perform a selection process accordingly. Applying ESSAIMS with the smallest possible energy threshold ($\varepsilon = 10^{-10}\ E_h$) allows to prolong the dynamics up to 75 fs (see light blue dashed curve in Fig. 6.2). The agreement between AIMS and ESSAIMS($\varepsilon = 10^{-10}\ E_h$) in the first 50 fs is excellent, with the ESSAIMS population trace remaining well within the standard error of AIMS. Both methods show that the S_1 population starts decaying after 25 fs, before plateauing at 70 % of S_1 population. ESSAIMS($\varepsilon = 10^{-10}\ E_h$) remains stable enough to describe the beginning of the subsequent S_1 population decay. The average number of TBFs for AIMS peaks at 1.4 TBFs (Fig. 6.3) and stays near this value until the dynamics fails. Despite a relatively low selection threshold,

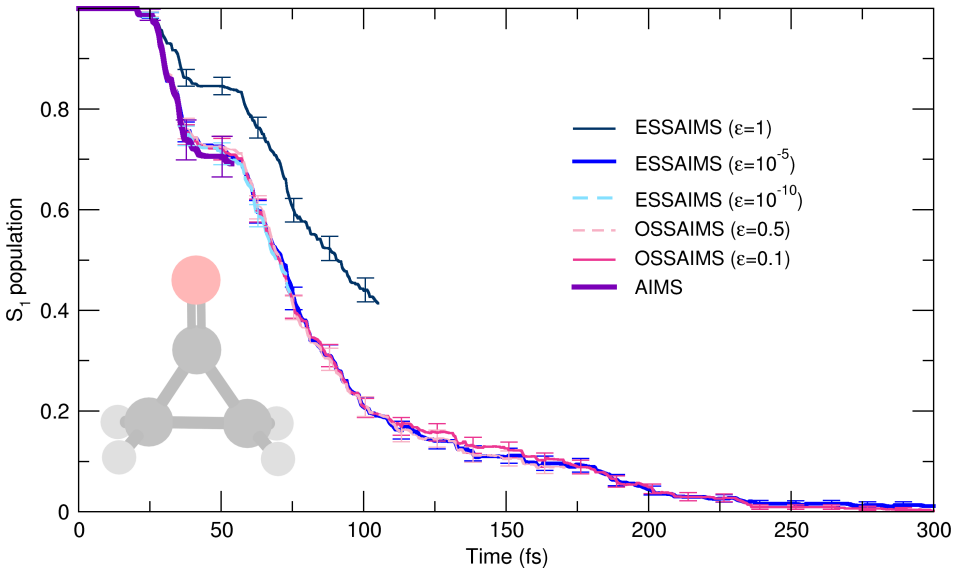

Fig. 6.2.: Photodynamics of cyclopropanone – comparison between AIMS and (E/O)SSAIMS with different thresholds. S_1 population decay as obtained with AIMS (purple curve), ESSAIMS (light blue dashed curve for $\varepsilon = 10^{-10}\ E_h$, blue curve for $\varepsilon = 10^{-5}\ E_h$, and dark blue thin curve for $\varepsilon = 1\ E_h$), and OSSAIMS (light magenta dashed curve for $\varepsilon = 0.5$, magenta curve for $\varepsilon = 0.1$). Error bars indicate standard errors.

the average number of TBFs in ESSAIMS($\varepsilon = 10^{-10}\ E_h$) is already reduced, with a peak under 1.25. This number then drops to 1.0 before rising again for the second decay of the S_1 population. These results show that some TBFs in AIMS are likely to be only very weakly coupled. Using a conservative energy threshold for ESSAIMS allows to stochastically select some weakly-coupled TBFs evolving in S_0, but does not fully resolve the instability issues. Increasing the ESSAIMS threshold permits to enforce a faster uncoupling of the TBFs in the dynamics. This approximation should further help with the remaining instabilities.

With a threshold $\varepsilon = 10^{-5}\ E_h$, ESSAIMS is stable enough to describe the full S_1 population decay (see blue curve in Fig. 6.2). The population trace obtained with this threshold remains within the error bars of AIMS and ESSAIMS($\varepsilon = 10^{-10}\ E_h$). The average number of TBFs does not surpass 1.25 for the ESSAIMS($\varepsilon = 10^{-5}\ E_h$) dynamics – well under the average number of ESSAIMS($\varepsilon = 10^{-10}\ E_h$) – and stays below 1.1 for the largest part of the dynamics. As observed earlier, the average number of TBFs rises initially but drops to almost 1.0 when the first plateau is reached. It then increases again every time new TBFs are spawned, permitting the population transfer to S_0.

Out of curiosity, one can finally test how ESSAIMS would behave when the selection threshold is set to a very high value, here $\varepsilon = 1\ E_h$ (see dark blue thin curve in Fig. 6.2). In this extreme case, the stochastic selection is triggered immediately after the spawn of a

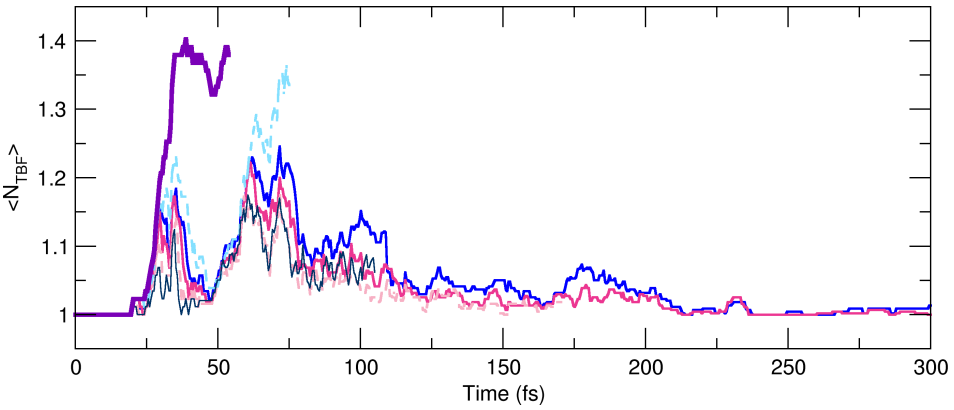

Fig. 6.3.: Photodynamics of cyclopropanone – comparison between AIMS and (E/O)SSAIMS with different thresholds. Time traces of the average number of TBFs ($< N_{TBF} >$) for each method shown in Fig. 6.2.

new TBF (as can be observed in the average number of TBFs), hindering the exchange of amplitude between the two coupled electronic states.

In addition, the performance of OSSAIMS is tested, where the criterion for the coupling between TBFs is given by the overlap between the two TBFs considered. An overlap threshold of $\varepsilon = 0.5$, which may at first glance appear rather large, leads to a very close agreement with the population decay observed in AIMS and ESSAIMS (dashed light magenta curve in Fig. 6.2). Moreover, OSSAIMS achieves this result by requiring a consistently lower average number of TBFs than ESSAIMS($\varepsilon = 10^{-5}\ E_h$). In fact, OSSAIMS($\varepsilon = 0.5$) uses on average nearly the same number of TBFs as the extreme ESSAIMS($\varepsilon = 1.0\ E_h$), with the major difference that ESSAIMS($\varepsilon = 1.0\ E_h$) leads to a poor description of the nonadiabatic processes. Reducing the OSSAIMS threshold to $\varepsilon = 0.1$ does not improve the S_1 population trace significantly, which remains well within the error bars of ESSAIMS($\varepsilon = 10^{-5}\ E_h$). Once more, the OSSAIMS average number of TBFs with $\varepsilon = 0.1$ is consistently lower than for ESSAIMS($\varepsilon = 10^{-5}\ E_h$), indicating that OSSAIMS could offer a better compromise between accuracy and efficiency.

6.3.2 Comparison between AIMS, (E/O)SSAIMS, and (d)TSH

Having shown how (E/O)SSAIMS makes multiple spawning simulations of cyclopropanone possible, these results are compared with the ones obtained using the mixed quantum/-classical method (d)TSH. TSH with and without a decoherence correction (dTSH and TSH, respectively, shown in Fig. 6.4) describes a very similar S_1 population decay for the first 75 fs of dynamics. The population decay starts after 25 fs and plateaus at around 65 % of S_1

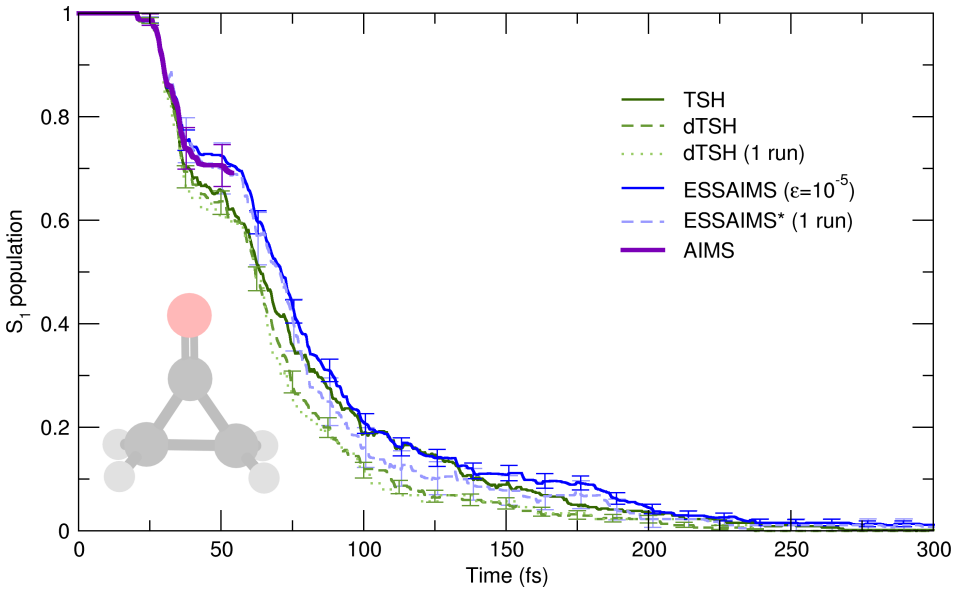

Fig. 6.4.: Photodynamics of cyclopropanone – comparison between AIMS, (E/O)SSAIMS, and (d)TSH.S_1 population decay as obtained with AIMS (purple curve), TSH (dark green curve), dTSH (green dashed curve), ESSAIMS (blue curve, $\varepsilon = 10^{-5}\ E_h$), dTSH* (light green dotted curve, one run per initial condition), and ESSAIMS (light blue dashed curve, one run per initial condition). Error bars indicate standard errors.

population. After 50 fs, the population transfer resumes, and a difference starts appearing between TSH and dTSH after 70 fs of dynamics, the former showing a slower population decay than the latter. This deviation between the two methods can be rationalised as follows. After a hop to the ground state, the decoherence correction enforces a quenching of the dTSH electronic population to the ground state. In TSH, the electronic coefficient for S_1 is not dampened, artificially increasing the probabilities of hops back to the S_1 state, leading to an overall slowdown of the S_1 population decay.

The initial population decay observed in (d)TSH at 25 fs agrees with (E/O)SSAIMS and AIMS. However, the population trace plateaus in (d)TSH at a lower value than the spawning methods and is outside of the AIMS standard error. dTSH then predicts a faster decay of the S_1 population than ESSAIMS($\varepsilon = 10^{-5}\ E_h$). While the population decay of TSH seems to agree well with the ESSAIMS population at later times, this is most likely only an artifact of TSH overcoherence (as detailed above). A similar effect of TSH overcoherence was observed in the photodynamics of ethylene, as detailed in the previous chapter (c.f. Sec. 5.3.2).[17]

Focusing on the computational cost of the different methods compared above (Fig. 6.5), the theoretical number of electronic structure calls per time step is used, as detailed in

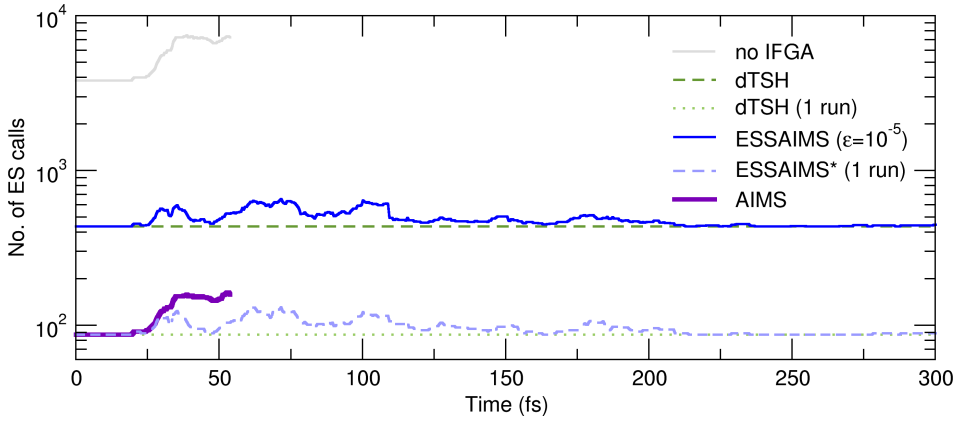

Fig. 6.5.: Photodynamics of cyclopropanone – comparison between AIMS, (E/O)SSAIMS, and (d)TSH. Theoretical number of electronic structure calculation at each time step for all methods presented in Fig. 6.4. The no-IFGA curve corresponds to the theoretical cost of the AIMS dynamics without the independent first generation approximation.

Sec. 6.1.1. The number of electronic structure calls for dTSH (and identically TSH) is constant at 435, as each of the 87 initial conditions were run 5 times. This number is comparable to the one obtained for ESSAIMS, even if it fluctuates to higher values when spawning events take place. In contrast, the average number of electronic structure calls for AIMS is significantly smaller, as there is only one run per initial condition. The AIMS dynamics starts with 87 necessary calls, and this number increases to 163 within 50 fs, before the simulation stops due to the instabilities discussed above. As a curiosity, also the theoretical cost of an AIMS calculation without the IFGA is reported, that is, where all parents would be coupled from $t = 0$ (grey line, Fig. 6.5). The advantage of applying the IFGA in multiple spawning simulations is striking: even for such a trivial nonadiabatic process, the number of electronic structure calls without the IFGA would make an AIMS dynamics intractable. At $t = 0$, 3828 electronic structure calls per time step would be required, increasing to 7381 calls per time step after the first 50 fs.

The use of five runs per initial condition is meant to carefully converge the respective stochastic algorithm of the (E/O)SSAIMS or dTSH dynamics, but it naturally leads to an increase in the computational effort – an effort above that of AIMS for the first part of the dynamics. Interestingly, using a single run per initial condition for dTSH ("dTSH* (1 run)" in Fig. 6.4) only leads to a minor alteration of the population trace. The ESSAIMS result obtained with only one run is similar for the beginning of the dynamics to the converged ESSAIMS one, but deviates slightly after around 80 fs of simulation.

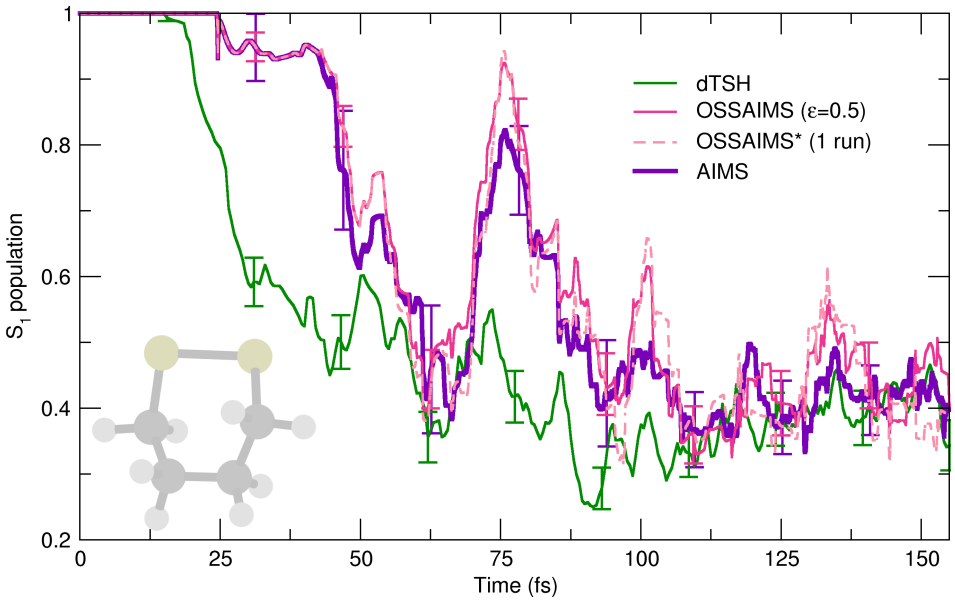

Fig. 6.6.: Photodynamics of 1,2-dithiane – comparison between AIMS, OSSAIMS and dTSH. S_1 population decay as obtained with AIMS (purple curve), dTSH (green curve), OSSAIMS (magenta curve, $\varepsilon = 0.5$), and OSSAIMS* (light magenta dashed curve, one run per initial condition). Error bars indicate standard errors.

6.4 1,2-Dithiane – numerous nonadiabatic transitions caused by nearly degenerate electronic states

The interesting nonadiabatic dynamics of 1,2-dithiane has been revealed in a study employing dTSH:[231] upon photoexcitation, dithiane commences an ultrafast ring-opening process in S_1 mediated by the breaking of its S–S bond, which allows the molecule to reorganise and extend for some time until the S–S bond reforms within 300 fs (in line with earlier experimental work[294]). This intriguing nuclear dynamics represents a challenge for nonadiabatic methods. Besides the evident challenge of describing ring-opening processes from an electronic structure perspective, the excited-state dynamics of dithiane leads to a situation where the three lowest electronic states can become nearly degenerate. The interplay between these electronic states and the nonadiabatic transitions resulting from their near-degeneracy requires a proper treatment of the coupled electron/nuclear dynamics. Hence, this molecule provides an ideal test for SSAIMS, as its nonadiabatic dynamics will produce many TBFs, and their interstate and intrastate interactions will be crucial for an accurate description of the electronic populations.

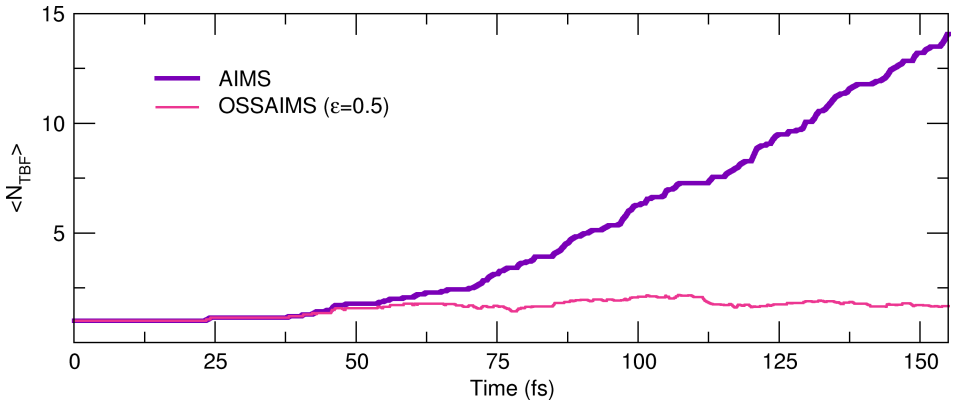

Fig. 6.7.: Photodynamics of 1,2-dithiane – comparison between AIMS, OSSAIMS. Time traces of the average number of TBFs ($< N_{TBF} >$) for AIMS and OSSAIMS.

Following photoexcitation, AIMS predicts that the S_1 population begins to decay after 25 fs (Fig. 6.6), leading to an S_1 population drop to 40 % within 60 fs. Subsequently, the S_1 population experiences a revival – up to 80 % after 75 fs – and then decreases until around 40 % where it stabilises (with some oscillations). OSSAIMS with a high threshold of $\varepsilon = 0.5$ closely reproduces this behaviour: the initial decay and reflection are adequately described, with the only difference being that the S_1 population is overestimated during the revival process. After 100 fs, the S_1 population of OSSAIMS also oscillates around 40 %, in close agreement to AIMS. The average number of TBFs (Fig. 6.7) rises almost exponentially for AIMS, reaching nearly 15 TBFs per initial condition after 155 fs of dynamics. For OSSAIMS with $\varepsilon = 0.5$, this number remains between 1 and 2 and does not surpass 2.5 TBFs. Furthermore, running only a single run per initial condition for OSSAIMS leads to an S_1 population decay in close agreement to our converged run employing five runs per initial condition (light magenta dashed curve in Fig. 6.6).

The decay of the S_1 population in dTSH starts earlier than in (OSS)AIMS, and the revival in the early part of the dynamics is not reproduced by the mixed quantum/classical method (green curve in Fig. 6.6). However, the S_1 population stabilises at the same level as AIMS and OSSAIMS (40 %) after 100 fs of dynamics. The maximum standard error of the S_1 decay of OSSAIMS (using five runs per initial conditions) is reproduced by running each initial condition eight times with dTSH.

Interestingly, while AIMS, OSSAIMS, and dTSH depict a rather similar S_1 population decay, monitoring the S_0 population reveals larger deviations between the methods (Fig. 6.8). OSSAIMS and AIMS show that some population appears in S_0 after 50 fs of dynamics, rising to about 25 % within 100 fs before plateauing between 20 and 25 %. In contrast,

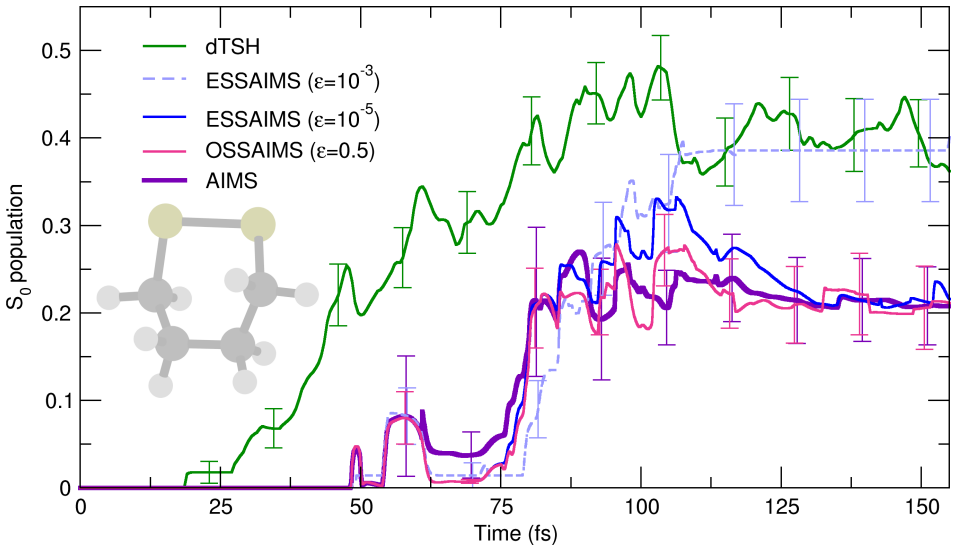

Fig. 6.8.: Photodynamics of 1,2-dithiane – comparison of AIMS, (E/O)SSAIMS and dTSH. S_0 population as obtained with AIMS (purple curve), dTSH (green curve), OSSAIMS ($\varepsilon = 0.5$, magenta curve), ESSAIMS (blue curve for $\varepsilon = 10^{-5}\ E_h$, light blue dashed curve for $\varepsilon = 10^{-3}\ E_h$). Error bars indicate standard errors.

dTSH predicts that the initial rise of the S_0 population takes place earlier (mirroring the behaviour observed for the S_1 decay) and stabilises at a higher population, ~40 % of population after 100 fs. ESSAIMS with a threshold of $\varepsilon = 10^{-3}\ E_h$ appears to capture rather well the S_0 population dynamics up to 100 fs of dynamics (light blue dashed curve in Fig. 6.8). However, the S_0 population continues to grow until it plateaus at around 40 % of population, similar to dTSH. The AIMS results could be recovered only by reducing the selection threshold of ESSAIMS to a value of $\varepsilon = 10^{-5}\ E_h$.[‡]

OSSAIMS($\varepsilon = 0.5$) drastically reduces the cost of the dynamics when a large number of TBFs are present after ~200 fs of dynamics (Fig. 6.9), while nevertheless reproducing the AIMS population dynamics correctly. The cost of ESSAIMS($\varepsilon = 10^{-3}\ E_h$) is lower than that of OSSAIMS($\varepsilon = 0.5$), and even below the theoretical cost of dTSH (as more runs are needed for the latter to achieve a similar level of convergence). However, decreasing the ESSAIMS threshold to $\varepsilon = 10^{-5}\ E_h$ to reach AIMS accuracy leads to a dramatic increase in the computational cost, even higher than that of AIMS for a large part of the dynamics. Hence, OSSAIMS once again appears to offer a good compromise between accuracy and computational cost. It is interesting to note that the S_0 population trace obtained with ESSAIMS($\varepsilon = 10^{-3}\ E_h$) starts to diverge from that of AIMS (at around 90 fs) shortly after the cost of AIMS greatly surpasses the cost of ESSAIMS (at around 75 fs). Adding to

[‡]It is noted that a threshold of $\varepsilon = 10^{-4}\ E_h$ does not improve the dynamics significantly.

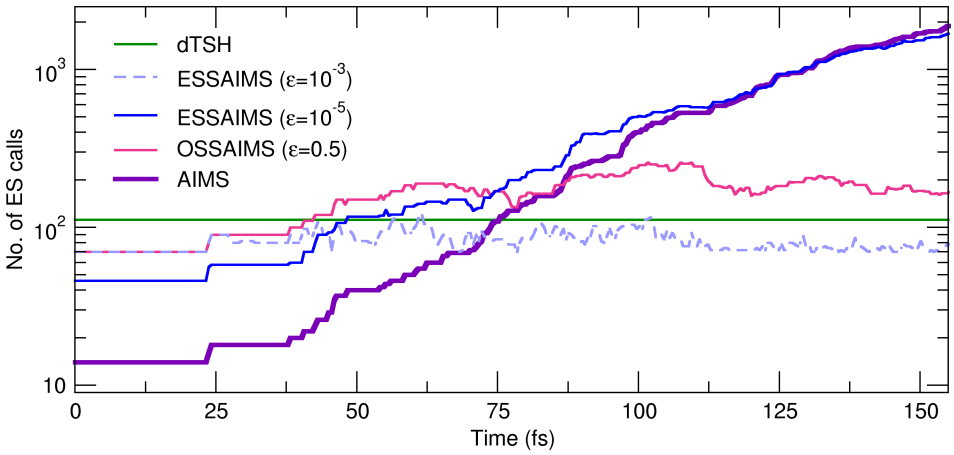

Fig. 6.9.: Photodynamics of 1,2-dithiane – comparison of AIMS, (E/O)SSAIMS and dTSH. Theoretical number of electronic structure calculation at each time step for all methods presented in Figure 6.8.

this observation the similarity between the dTSH and ESSAIMS($\varepsilon = 10^{-3}\ E_h$) population trace, one can infer that the coupling between trajectories (absent in dTSH and limited in ESSAIMS with a high threshold) is likely to play a role in the last part of the dynamics. OSSAIMS, which adequately reproduces the AIMS S_0 population trace, includes more TBFs, and its theoretical cost is comparable to that of AIMS until the plateau is reached after 100 fs of dynamics.

The difference in performance between OSSAIMS and ESSAIMS observed above highlights the importance of the selection criterion. In OSSAIMS, the criterion is solely based on the overlap between TBFs. In ESSAIMS, the selection criterion depends on the off-diagonal elements of the Hamiltonian matrix (in the basis of TBFs). As such, the selection process in ESSAIMS depends on whether the TBFs under consideration evolve on the same state or different states – in the intrastate case, the Hamiltonian matrix element will contain the nuclear kinetic energy operator and the electronic energy, while in the interstate case the Hamiltonian matrix element contains the scalar product of the nonadiabatic coupling vectors with the nuclear gradient. In practice, we observe that ESSAIMS would be more likely to initiate a stochastic selection for TBFs evolving on different states than for TBFs on the same state, as the interstate coupling term is more likely to reach a small value (due to vanishing nonadiabatic coupling terms) than the intrastate one. OSSAIMS, on the other hand, does not differentiate between these two cases and only focuses on the overlap between TBFs. A closer look at the respective Hamiltonian matrix elements during the 1,2-dithiane dynamics provides more insight into the difference between OSSAIMS and

ESSAIMS. During the entire OSSAIMS dynamics, the overlap between TBFs remains rather large, and increasing the selection threshold to 0.7 does not significantly alter the dynamics. Hence, OSSAIMS will preserve any coupled TBFs, irrespective of their electronic state. Such couplings between TBFs appear to be critical to reproduce the AIMS dynamics. (It was found that to recover the result of ESSAIMS with $\varepsilon = 10^{-3}\ E_h$, it was necessary to increase the threshold of OSSAIMS to 0.8.) Focusing now on the off-diagonal elements of the Hamiltonian matrix, we observe that they range between 10^{-3} and $10^{-5}\ E_h$ for most of the dynamics. The ESSAIMS thresholds used in our simulations thus represent two limiting cases – $\varepsilon = 10^{-3}\ E_h$ is larger than the off-diagonal elements between any TBFs and will lead to an immediate stochastic selection, while $\varepsilon = 10^{-5}\ E_h$ is a lower limit that the coupled TBFs only rarely reach. Interestingly, ESSAIMS cannot accurately reproduce the AIMS dynamics even with an intermediate threshold of $\varepsilon = 10^{-4}\ E_h$. This shows that the overlap between TBFs appears to be a robust criterion for SSAIMS, not only for the specific case of 1,2-dithiane but also for the other examples discussed above.

6.5 Conclusion

This chapter illustrated how prototypical molecules undergoing photoinduced ring-opening can be used to challenge nonadiabatic dynamics methods. The novel framework of stochastic-selection *ab initio* multiple spawning (SSAIMS) was applied to describe the photoinduced ring-opening of different molecules systems to highlight its advantages and limitations and compare its performance with the mixed quantum/classical method TSH.

The results obtained for cyclopropanone indicate that both OSSAIMS and ESSAIMS can stabilise an AIMS dynamics suffering from electronic-structure instabilities for weakly coupled TBFs. A very small selection threshold, meaning a dynamics that remains very close to AIMS, could already achieve such a stabilisation. By choosing an adequate selection threshold, the full decay of the S_1 population can be simulated with both flavours of SSAIMS. The computational cost of (E/O)SSAIMS remains close to that of TSH, with OSSAIMS requiring on average fewer TBFs for a result almost identical to ESSAIMS. The challenging photodynamics of 1,2-dithiane requires a large number of TBFs for its depiction. OSSAIMS was able to reproduce the dynamics predicted by AIMS while decreasing the computational cost significantly. Interestingly, ESSAIMS with a loose selection criterion deviates from AIMS and reproduces the dTSH dynamics at longer times, exhibiting the

effect of mimicking the independent trajectory approximation of (d)TSH by considering the TBFs mostly as uncoupled.

Overall, both OSSAIMS and ESSAIMS proved to be stable and reliable strategies that, in many cases, could provide AIMS-quality nonadiabatic dynamics at a much-reduced cost, often competitive with the mixed quantum/classical methods TSH. It has been shown that ESSAIMS and OSSAIMS achieve a very similar accuracy for both cyclopropanone and fulvene, with OSSAIMS necessitating slightly fewer TBFs on average while providing a slightly better agreement with AIMS. For 1,2-dithiane, OSSAIMS predicts the same dynamics as AIMS while reducing the necessary TBFs to below 2.5 on average. In comparison, ESSAIMS captures the early behaviour of the dynamics well, but at later times collapses to the dTSH result when using a threshold leading to a comparable cost with OSSAIMS. Achieving convergence to the AIMS result requires using a dramatically smaller selection criterion for ESSAIMS, resulting in an overall cost surpassing that of AIMS. Hence, these three exemplary molecular test systems indicate that OSSAIMS provides a more reliable and cost-efficient framework for further applications. It remains to be noted that both SSAIMS strategies require several test runs to determine an adequate stochastic-selection criterion.

7 Thiophenone: The interplay of time-resolved spectroscopy and *ab initio* calculations to unravel complex photochemistry

This chapter is based on the publication:
S. Pathak, L. M. Ibele, R. Boll, C. Callegari, A. Demidovich, B. Erk, R. Feifel, R. Forbes, M. Di Fraia, L. Giannessi, C. S. Hansen, D. M. P. Holland, R. A. Ingle, R. Mason, O. Plekan, K. C. Prince, A. Rouzée, R. J. Squibb, J. Tross, M. N. R. Ashfold, B. F. E. Curchod, D. Rolles, Tracking the ultraviolet-induced photochemistry of thiophenone during and after ultrafast ring opening, Nat. Chem., 12, 795 (2020)
All experiments were carried out by collaborators but are still presented briefly for context.

7.1 Introduction

Recent advances in time-resolved experimental techniques and computational methods for studying (coupled) electronic and nuclear dynamics are revolutionising the field of ultrafast photochemistry, enabling direct probing of evolving molecular structures with unprecedented structural and temporal resolution.[295–302] Such studies provide the best test of our knowledge and understanding of light-initiated chemistry. Photoinduced ring-opening/closing reactions are a fundamental photochemical reaction, that also lies at the heart of many processes in nature, for example, the synthesis of previtamin D_3 by sunlight. A direct comparison and synergy of theory and experiments offer the strongest reference model for any nonadiabatic dynamics methods.

The photoinduced ring opening of the polyene 1,3-cyclohexadiene[303] is widely employed as a model system for benchmarking and validating ultrafast methods such as ultrafast X-ray[295,301,302] and electron[300] diffraction, femtosecond transient X-ray absorption[298] and

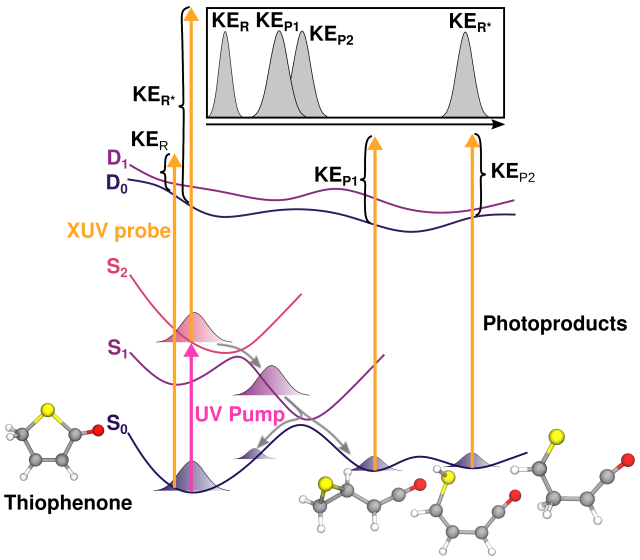

Fig. 7.1.: Schematic of the UV excitation, ring opening and photoionisation of thiophenone. The molecule is photoexcited from its ring-closed ground state (S_0) to an electronically excited state (S_2). It evolves through an optically dark excited state (S_1) back to the (vibrationally excited) S_0 state of several possible reaction products. The XUV probe photon energy is sufficient to ionise thiophenone and all reaction products from both ground and excited states into several ionic final states (D_0, D_1 and so on). The time-evolving electron kinetic energy (KE) spectrum (top) thus consists of contributions from the ground and excited states of thiophenone (denoted as R and R*, respectively) and from the different products.

fragmentation,[304] and time-resolved photoelectron spectroscopy (TRPES).[305,306]. However, few other photoinduced ring-opening reactions have been probed so thoroughly and, of these, even fewer have provided a comprehensive picture of the reaction dynamics on both the excited and ground (S_0) state PESs.

This chapter presents a combined theoretical and experimental study of the UV photoinduced ring opening of a prototypical heterocyclic molecule, 2(5H)-thiophenone (C_4H_4OS, henceforth thiophenone; see Fig. 7.1). Heterocyclic compounds are fundamental building blocks in the synthesis of many organic compounds. Studying these 'single units' may help in validating the (necessarily more complex and less resolvable) photochemistry of ever-larger molecules. The study is conducted in vacuum (that is, under collision-free conditions) and thus reveals information on the purely intramolecular relaxation pathways, without the solvation effects present in previous matrix-isolation[307] and liquid-phase[308] studies of this system. Theory and experiment combine to afford detailed insights into both the mechanism and timescale of the initial ring-opening process and the subsequent evolution of the vibrationally excited ground-state photoproducts.

The experimental study employs the extreme UV (XUV) radiation provided by the free-electron laser (FEL) FERMI.[309] TRPES[310,311] is sensitive to both electronic and structural dynamics, which is essential for any full understanding of the coupled electronic and nuclear dynamics that govern most photoinduced reactions. TRPES also allows access to so-called 'dark' states that may not be amenable to study by linear transient absorption methods. XUV probe pulses (from an FEL or a high harmonic generation source) are sufficiently energetic to ionise molecules in the electronic ground state S_0.

Fig. 7.1 schematically depicts the experiment described in this chapter. Thiophenone, initially in its ground electronic and vibrational state, is excited by a UV pulse (UV pump) to the bright S_2 state. Subsequently, through an elongation and breaking of the C–S bond, it relaxes back to the electronic ground state. Due to its high internal energy, it can form a variety of different photoproducts on the electronic ground state. The experiment can probe the evolution of thiophenone throughout this reaction with an XUV pulse and records the signals of the initial thiophenone (KE_R, in Fig. 7.1, photoexcited thiophenone during the relaxation (KE_{R^*}) and, thanks to the high energy of the XUV pulse, also can probe the ground-state photoproducts (KE_{P1}, KE_{P2}, etc.). By taking the difference of KE and the energy of the probe pulse, one obtains the electron binding energy (BE), i.e. the ionisation potential (IP). Therefore, TRPES can provide a full picture of the photochemical experiment, from the initialisation until the formation of photoproducts.

The importance of computational methods becomes clear at this point as well. While the TRPES provides evidence of the energetic nature of the processes taking place, simulations can directly predict the nuclear dynamics occurring throughout. By computing the ionisation potential (IP) of the structural evolution obtained from the dynamics, a direct comparison with the experiment is possible.

This chapter is structured as follows. First, the experiment and its results will be shortly presented in Sec. 7.2. Subsequently, the computational work carried will be shown. In the first part, the initial ring opening and the excited-state dynamics driving the system back to the ground state are investigated employing static scans (Sec. 7.3.2) as well as using nonadiabatic dynamics using trajectory surface hopping (Sec. 7.3.3). In a second part, the dynamics occurring on the vibrationally excited electronic ground state after deactivation are investigated. Therefore, long time *ab initio* molecular dynamics is run and for validation, the IP of the predicted photoproducts is computed and compared to the experiment (Sec. 7.4.2). In an attempt to explain the long time dynamics, some trajectories

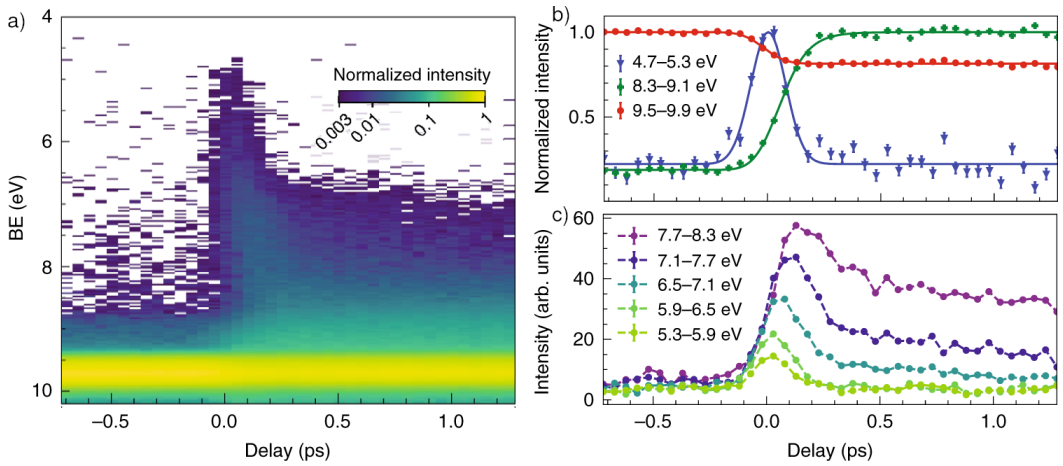

Fig. 7.2.: Time-dependent photoelectron spectra of UV-excited thiophenone. a) Measured photoelectron yield as a function of BE and time delay (Δt) between the pump and probe pulses. Negative Δt corresponds to the FEL pulse preceding the UV pulse and positive Δt to the UV pulse preceding the FEL pulse, while the colour represents the normalised photoelectron intensity. Regions with an intensity below 0.003 are shown in white. b) Delay-dependent photoelectron yields for three BE ranges selected to illustrate the photoinduced depopulation of the S_0 state (red circles), the population of the S_2 state (blue triangles) and the build-up of vibrationally excited $S_0^{\#}$ photoproducts (green crosses). c) Delay-dependent photoelectron yields five contiguous 0.6 eV-wide BE slices that inform on the evolution from photoexcited S_2 to internally excited $S_0^{\#}$ molecules. Statistical error bars are included but are generally smaller than the symbol size. The dashed lines in c just join the dots for better visibility. The data in b) have been normalised such that the maximum value of the fit is at 1 for each curve, whereas the data in c) are displayed on a common intensity scale.

are propagated for up to 100 ps to estimate their behaviour (Sec. 7.4.3). In Sec. 7.5, some preliminary experimental and computational results from ultrafast electron diffraction (UED) experiments are introduced. Finally, conclusions are drawn in Sec. 7.6

7.2 Time-resolved photoelectron spectroscopy

All details on the experiment can be found in Ref. [116]. The experiment measures electron time-of-flight spectra of thiophenone as a function of Δt, which are converted to electron kinetic energy spectra and then, by energy conservation, into spectra of the valence binding energies. Fig. 7.2(a) shows such spectra in the form of a two-dimensional plot of electron yield as functions of binding energy (BE) and Δt. The dominant feature at BE $\sim$ 9.7 eV is due to photoionisation of the "cold" (i.e. non-excited) closed-ring S_0-state thiophenone molecule.[312] This peak is depleted by $\sim$ 20% for positive Δt, as shown in Fig. 7.2(b) (red circles), confirming excitation of ground-state molecules by the UV pulse. A fit to the

delay-dependent yield of photoelectrons originating from S_0-state parent molecules yields an upper limit for the temporal instrument response function of $\sigma = 72 \pm 8$ fs. Fig. 7.2(a) reveals photoelectrons with BEs as low as ~ 5 eV at the shortest positive Δt. The prompt appearance and subsequent decay of this contribution are also emphasised in Fig. 7.2(b), which shows a Gaussian-shaped transient signal with $\sigma = 76 \pm 6$ fs (blue triangles). With increasing delay, the signal at BE ~ 5 eV fades and the peak intensity shifts toward higher BE. As Fig. 7.2(c) shows, the peak in the intensity vs Δt transient obtained by taking contiguous 0.6 eV-wide slices for BE ≥ 5.3 eV shifts to progressively later Δt with increasing BE, and the transients gain an increasingly obvious tail.

The thiophenone cation has close-lying ground (D_0) and first excited (D_1) states at a vertical IP (IP_{vert}) of ~ 9.7 eV, and higher excited states at IP_{vert} values of 10.58 eV (D_2), 12.25 eV (D_3) and 14.1 eV (D_4).[312] Given the present pump photon energy of 4.67 eV, the signal appearing at a binding energy of ~ 5 eV at $\Delta t \approx 0$ is readily attributed to vertical ionisation of photoexcited molecules in the S_2 state to the (unresolved) D_0 and D_1 states. Ionisation to the latter is strongly disfavored due to selection rules. The evolution of the signal at BE ~ 5 eV, the peak shift towards higher BE at later Δt, and the more intense tail in the Δt traces for higher BE slices all reflect the complex evolution of the photo-prepared wavepacket, which the accompanying theory shows involves ultrafast depopulation of the S_2 state to yield "hot", i.e., highly vibrationally excited, S_0 (henceforth $S_0^{\#}$) molecules (revealed by the green stripe in Fig. 2(a) at BE ~ 9 eV). Note that any photoelectrons arising from ionisation of $S_0^{\#}$ molecules to excited D_n ($n > 1$) cation states are likely to appear at BE > 10 eV, and thus do not affect the discussion that follows.

7.3 Initial excited-state dynamics

7.3.1 Computational details

Critical points and linear interpolation in internal coordinates

Critical points of the thiophenone PESs — S_0 minimum, S_1 minima, and S_2/S_1 and S_1/S_0 MECIs — are identified using SA(4)-CASSCF(10/8)[236,237] and a 6-31G* basis set[238,239] as implemented in Molpro 2012[247] . Pathways connecting these different critical points of the PESs are produced by linear interpolations in internal coordinates (LIICs).[313] Electronic energies for thiophenone are computed along the LIIC pathways at the SA(4)-CASSCF(10/8)

and XMS(4)-CASPT2(10/8)[314,315] levels of theory using, in all cases, a 6-31G* basis set. The electronic energies for the thiophenone cation are also computed along the LIICs using SA(4)-CASSCF(9/8) and XMS(4)-CASPT2(9/8). All XMS-CASPT2 calculations are performed with the BAGEL software,[316] employing the corresponding SA-CASSCF wavefunction from Molpro 2012 as a starting point. A level shift[317] of 0.3 E_h is used in all XMS-CASPT2 calculations to prevent the appearance of intruder states.

Trajectory surface hopping dynamics

The excited-state dynamics of thiophenone following photoexcitation are simulated using the mixed quantum/classical dynamics method trajectory surface hopping (TSH), employing the fewest-switches algorithm proposed by Tully.[16] The calculations are performed with the SHARC program package (v2.0)[217,249,250]. 46 initial conditions for the TSH dynamics are sampled stochastically from a Wigner distribution for uncoupled harmonic oscillators constructed from a frequency calculation at the ground-state optimised geometry of thiophenone. All trajectories are initiated in the bright S_2 state of thiophenone. The TSH dynamics employ a time step of 0.5 fs and SA(4)-CASSCF(10/8) for the electronic structure using Molpro 2012. The energy decoherence correction scheme by Granucci and Persico[184] is applied to the electronic coefficients with the default constant of 0.1 E_h. Strict total energy conservation is ensured for each trajectory during the excited-state dynamics. However, the active space showed instabilities within a few tens of femtoseconds in the S_0 state. Such instabilities do not constitute an issue as the TSH dynamics are sufficiently stable to provide initial conditions for the subsequent ground-state AIMD calculations.

7.3.2 Static calculations

To interpret the dynamics revealed in the TRPES spectra, the lowest-lying PESs of thiophenone are computed and different critical points are located. The FC geometry corresponds to the equilibrium structure of the S_0 state of thiophenone, wherein the highest occupied molecular orbital is an out-of-plane π orbital largely localised on the sulfur atom, henceforth labelled n(S). At our chosen pump photon energy, thiophenone is predominantly excited to its S_2 state. At the XMS(4)-CASPT2(10/8) level of theory, the $S_0 \rightarrow S_2$ transition has n(S)/π^* character, a calculated transition energy of 4.67 eV and an appreciable oscillator strength (0.036), reflecting the constructive overlap of the donating n(S) and accepting π^* orbitals. The $S_0 \rightarrow S_1$ transition (with a calculated energy of 4.20 eV), by contrast, is dark

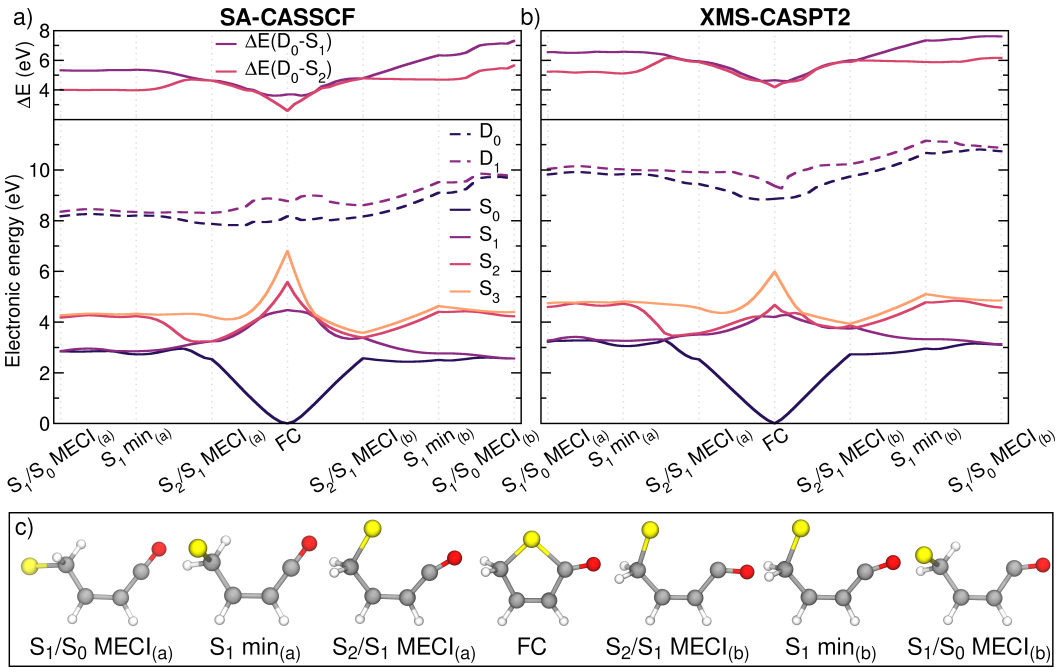

Fig. 7.3.: PESs for the lowest neutral singlet (solid lines; S_0 in dark blue, S_1 in palatinate, S_2 in fuchsia, and S_3 in peach) and cationic doublet (dashed lines) electronic states of thiophenone along LIIC pathways between different critical geometries. Electronic energies are obtained using SA(4)-CASSCF(10/8) for the neutral and SA(4)/CASSCF(9/8) for the cationic form of thiophenone in a) and with XMS(4)-CASPT2(10/8) and XMS(4)/CASPT2(9/8), respectively, in b). Two LIIC paths of minima and MECIs, (a) (left side in both plots) and (b) (right side), are located using the SA(4)-CASSCF(10/8) level of theory, are indicated in with light-grey vertical lines, and the geometries of these critical points on the PESs of neutral thiophenone are shown in c). LIIC pathways are then computed between each critical point, and the upper panels of a) and b) shows the electronic energy gap ΔE between the D_0 state of the cation and the second (S_2) or first (S_1) singlet states of neutral thiophenone for each point along the LIIC pathway.

(the donating O-atom centred, lone pair *n*(O) orbital lies in the plane of the ring and is thus orthogonal to the accepting orbital).

Different minimum energy conical intersections (MECI) are located between the S_2, S_1 and S_0 states of thiophenone, as shown in Fig. 7.3c. All of these MECIs indicate a ring opening in the excited electronic state (that is, formation of a biradical), followed by geometrical relaxation. The pathway (b) leading to the energetically lower S_1/S_0 MECI (indicated as geometries (b) in Fig. 7.3c) shows a ring opening at the S_2/S_1 MECI followed by a bending of the C–C=O moiety, leading to a twisting of the CH_2–S moiety that drives the system to the ground state (S_1/S_0 MECI). An alternative pathway (a) is obtained (the geometries are shown in the left half of Fig. 7.3c). This path differs in that the

critical geometries located for the S_1 minimum and the S_1/S_0 MECI exhibit an out-of-plane configuration and a linear C=C=O moiety.

To determine the possible connections between these critical structures and the relaxation pathways of thiophenone following UV photoexcitation, linear interpolations in internal coordinates (LIICs) are performed using SA(4)-CASSCF(10/8) (Fig 7.3a) and refined with XMS(4)-CASPT2(10/8) (Fig. 7.3b). The overall shape of these pathways is in excellent agreement with that obtained using XMS(4)-CASPT2(10/8), validating the use of SA-CASSCF for the nonadiabatic molecular dynamics. The left side of Figs. 7.3a and 7.3b show the LIIC between the pathway (a), the right side between pathway (b) with the FC geometry (identifcal for both pathways) being in the middle. Starting from the FC geometry, the LIICs smoothly connect the different critical points and confirm that photoexcited thiophenone (S_2) molecules can relax efficiently towards the S_0 state via the S_2/S_1 and S_1/S_0 seams of intersection in the C–S bond extension coordinate.[318] This observation is similar for both simulated pathways (a) and (b). The energies of the low-lying D_0 and D_1 states of the thiophenone cation are also computed along the LIIC pathways (Fig. 7.3, dashed lines). In the FC region, these states are characterised by the removal of an electron from, respectively, the n(S) and n(O) lone pair orbitals. The topographies of the various PESs of neutral thiophenone vary strongly along the LIIC pathways, but the energies of the D_0 and D_1 states of the cation show a smooth and very gradual increase. The energy differences (ΔE) between the D_0 and the S_2/S_1 potentials along the LIIC pathways (top panels in Figs. 7.3a and 7.3b) increase dramatically from the FC point out to the S_1/S_0 MECI.

It may be useful to introduce briefly an electronic argument for focusing the discussion on ionisation to D_0 rather than to the D_1 state. The S_2 state has dominant n(S)/π^* character in the FC region. Importantly, the S atom lone pair remains the dominant donating orbital along the entire decay pathway, from the FC point on S_2 to the S_2/S_1 MECI, and during the relaxation on S_1 towards S_1 minimum, eventually reaching the S_1/S_0 MECI. Similarly, the D_0 state is always formed by loss of an electron from the S atom lone pair along this LIIC pathway, whereas the D_1 state is initially (i.e. in the FC region) characterised by the removal of an electron from the O lone pair before it gains a larger contribution from the n(S) orbital towards the end of the LIIC (when the states get closer in energy). Simple ionisation rules[319] suggest that ionisation should be allowed from the visited electronic state to D_0 along the entire LIIC pathway (S_2 then S_1 after crossing), as their electronic

state characters differ by just a single spin-orbital (the accepting orbital in the excitation of the neutral). The same logic would imply that ionisation from S_2 to D_1 is disfavored, as it necessitates (at least in the first part of the LIIC) a change of more than one spin-orbital in the ionisation step.

The calculations allow assignment of the experimentally observed rapid increase in BE with increasing Δt to the ultrafast depopulation of the S_2 state and electronic deactivation to the S_0 state, resulting in highly vibrationally excited ground-state molecules. The calculated ΔE values are consistently slightly lower than the experimental BE values. Such underestimation of (experimental) IP values by (X)MS-CASPT2 methods is well-known[266] and, in the present case, can also be related to the choice of basis set (benchmarks with increasingly large basis sets show improving agreement with the experimental IP).

7.3.3 Excited-state dynamics

The fates of the photoexcited thiophenone molecules are further explored by running trajectory surface hopping (TSH) calculations from the photoprepared S_2 state at the SA(4)-CASSCF(10/8) level of theory. The trajectories are all initialised on the S_2 state since the computed vertical transitions (at the SA(4)-CASSCF(10/8) level of theory) of 100 Wigner sampled structures indicate that this state is by far the 'brightest' when exciting from the S_0 state and lies[303] at the appropriate energy for the chosen pump wavelength (when the transition energy is computed at the XMS-CASPT2 level of theory).

As expected from inspection of the LIIC pathways, the initial S_2 population rapidly decays to the S_1 state and population appears almost immediately on the S_0 PES, as shown in Fig. 7.4a.* In accord with the LIIC pathways presented above, the nuclear wavepacket created on S_2 exhibits an ultrafast (< 100 fs) decay towards the lower electronic states. The growth of the S_1 population, if fitted by a single exponential, is characterised by a waiting period of 19 fs and a growing time of 83 fs. The entire excited-state population is transferred back to the S_0 state within 350 fs of UV excitation. Fig. 7.4b displays a swarm of 46 TSH trajectories that mimic the relaxation dynamics of the thiophenone wavepacket and demonstrate that the ultrafast deactivation from S_2 to S_1 to S_0 is driven by a ballistic ring-opening process. The trajectories start to spread after ~50 fs; most remain

*The populations are computed as the fraction of trajectories evolving in a given electronic state at a given time. The displayed population traces match well with those computed from the squares of the TSH electronic coefficients, averaged over all trajectories – indicating an internal consistency of the TSH algorithm.

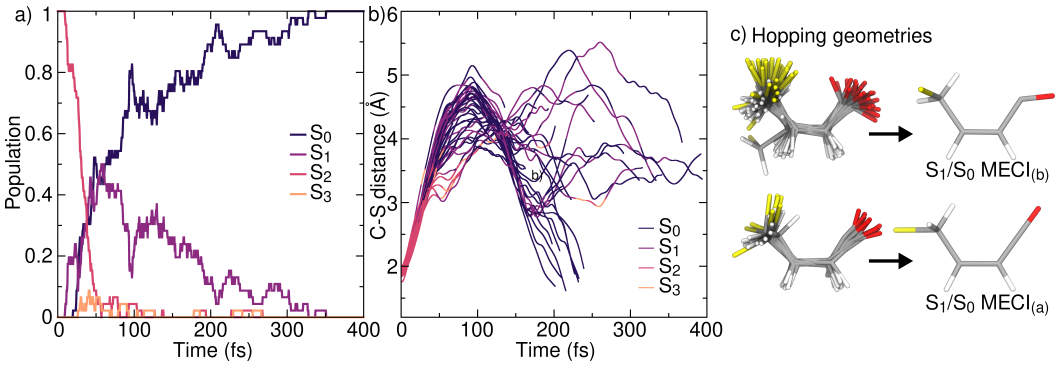

Fig. 7.4.: Simulations of excited-state dynamics, population and structural analysis. a) Time-dependence of the S_3, S_2, S_1 and S_0-state populations provided by the TSH dynamics (46 trajectories). b) Time-evolution of the C–S bond distance for each of these 46 trajectories, illustrating the prompt initial bond extension in all cases and (via the colour coding) the trajectory-dependent evolution from S_2 through S_1 to the S_0 state. The TSH trajectories are propagated until they experienced electronic structure instabilities in the ground state. c) Comparison between hopping an S_1/S_0 MECI geometries (a) and (b) from Fig. 7.3c. Superimposed last S_1/S_0 hopping geometries from the TSH dynamics (shown on the left), grouped into two families according to whether the C=C=O angle corresponds to the bent S_1/S_0 $MECI_{(b)}$ (76% of the hopping geometries, upper panel) or linear S_1/S_0 $MECI_{(a)}$ (24% of the hopping geometries, lower panel).

ring-opened upon becoming $S_0^\#$ molecules, but some readopt a (vibrationally hot) cyclic configuration.

The conclusions from the TSH calculations match well with the experimental time-resolved photoelectron yields for the BE ranges selected to span the predicted IP_{vert} values along the LIIC (Fig. 7.2b,c). The yield in the BE range corresponding to vertical ionisation from the S_2 state (blue trace in Fig. 7.2b) shows a narrow transient signal, the width of which is largely determined by the instrument response function. With increasing Δt, this transient signal shifts to higher BE, broadens somewhat and gains a longer time tail (Fig. 7.2c). Recalling the top panels in Fig. 7.3, these observed changes are all consistent with the wavepacket evolving on the S_2 PES (sampled most cleanly by intensities at BE $\leq$ 5.5 eV) and subsequent non-adiabatic coupling with the S_1 state (which are sampled most efficiently in the 6 $\leq$ BE $\leq$ 7 eV range) and thence with the S_0 PES (which start to be sampled at BE $\geq$ 7 eV). Ionisation of $S_0^\#$ molecules accounts for the tails in the transients for the higher energy BE slices in Fig. 7.2c; the build-up of $S_0^\#$ population (green crosses in Fig. 7.2b) plateaus at $\Delta t \geq$ 300 fs. These comparisons serve to reinforce the interpretation, developed from considering the LIIC pathways (Fig. 7.3) that the experimentally observed increase in BE is a signature of the ultrafast decay of thiophenone (S_2) molecules to high $S_0^\#$ levels.

Looking at the hopping geometries to the S_0 during the TSH calculations (Fig. 7.4c), it can be seen that the majority the majority (76%) of the last S_1-to-S_0 hops observed during the TSH dynamics takes place for molecular configurations similar to the S_1/S_0 $MECI_{(b)}$ of the right half of the LIIC pathway (Fig. 7.3). The majority of the structures show a bending along the C=C=O group, as well as an out-of-plane torsion of the C–S moiety. Therefore, these two structural features might be regarded as the structural signatures of the decay to the ground state.

7.4 Predicting the dynamics of the hot ground state

7.4.1 Computational details

Ab initio molecular dynamics to t = 2 ps and t = 100 ps

AIMD calculations of the photoproducts formed during the TSH dynamics are conducted on the S_0-state PES using unrestricted DFT with the PBE0 exchange/correlation functional[320] and a 6-31G* basis set, employing the GPU-accelerated software TeraChem.[290] The initial conditions (nuclear coordinates and velocities) for each AIMD trajectory (22 in total, drawn randomly from the pool of TSH trajectories) are extracted from the TSH dynamics when the trajectory reached the S_0 state. At this initial point in configuration space, the SA-CASSCF wavefunction already exhibits a dominant closed-shell character (confirmed at the XMS-CASPT2 level of theory). A small (0.1 fs) time step is used to ensure proper total energy conservation for all trajectories, and the length of each (constant total energy) trajectory is set such that the total TSH+AIMD dynamics extend to 2 ps. This strategy necessarily restricts the dynamics to the S_0 PES; the legitimacy of this procedure is validated by test trajectories on S_0, which show the energy separation between the ground and excited electronic states increasing rapidly upon leaving the region of the S_1/S_0 seam of intersection. To explore the long-time dynamics of the different photoproducts, 10 of the 22 trajectories are propagated further, to t = 100 ps, using the same methodology except for a slightly longer time step of 0.25 fs.

Analysis of the 2 ps AIMD and vertical ionisation energy distribution

The 22 AIMD trajectories propagated until t = 2 ps are used to analyse the distribution of IP_{vert} values for the $S_0^{\#}$ photoproducts. For each AIMD trajectory, molecular geometries

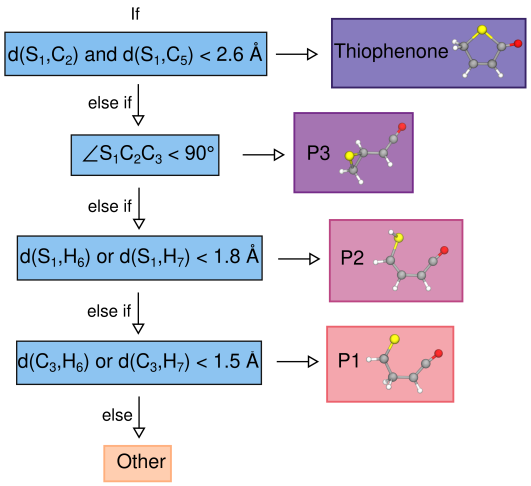

Fig. 7.5.: Decision tree for the identification of photoproducts during the AIMD.

are sampled every 10 fs, leading to a pool of $> 4,000$ S_0 molecular configurations. Each configuration is assigned to one of the possible photoproducts identified by Murdock et al.[308] based on characteristic atomic connectivities determined by measuring bond lengths or angles (see Fig. 7.5). If such assignment is not possible, the configuration is given the label 'Other'. These are often due to a transient configuration between two photoproducts. The IP_{vert} of each configuration is then computed at the MP2-F12/cc-pVDZ-F12 level of theory (this level of theory is benchmarked against CCSD(T)-F12/cc-pVDZ-F12). Table 7.1 illustrates the close agreement between the IP_{vert} values computed with CCSD(T)-F12/cc-pVDZ-F12 and MP2-F12/cc-pVDZ-F12 for different possible photoproducts of thiophenone. All geometries for these benchmarking calculations are optimized at the MP2/6-311+G** level of theory. The table also shows energy differences between the electronic ground state energy of the photoproduct and the parent thiophenone molecule. Convergence of the CCSD(T)-F12 and MP2-F12 results with respect to the basis set size has been tested by comparing the results obtained with cc-pVDZ-F12 and cc-pVTZ-F12 for thiophenone and the P3 isomer. Only minor differences are observed between the two basis sets: for thiophenone, the variation in IP_{vert} values between the two basis sets was 0.05 eV (CCSD(T)-F12) and 0.02 eV (MP2-F12). The level of agreement observed between CCSD(T)-F12 and MP2-F12 for IP_{vert} values and the convergence observed for both methods with the cc-pVDZ-F12 basis validate the use of MP2-F12/cc-pVDZ-F12 for the results presented in the main text.

The resulting distribution of $S_0 \rightarrow D_0$ IP_{vert} values provides an approximation of the low-energy part of the experimental BE spectra. The same methodology, applied to

Tab. 7.1.: Ionization potential of thiophenone and photoproducts. Comparison between CCSD(T)-F12 and MP2-F12 calculated values of the IP_{vert} values of different photoproducts and of their electronic energies relative to that of the S_0 state of thiophenone.

	Thiophenone	P1	P2	P3	P4	P5	P6
						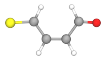	
CCSD(T)-F12							
IP / eV	9.663	9.177	8.310	8.796	9.206	9.223	7.272
relative to thiophenone							
ΔS_0 / eV		1.549	1.410	1.455	1.274	1.396	2.878
Δ IP / eV		-0.486	-1.353	-0.867	-0.458	-0.440	-2.391
MP2-F12							
IP / eV	9.799	9.362	8.368	8.668	9.374	9.392	7.566
relative to thiophenone							
ΔS_0 / eV		1.567	1.417	1.367	1.386	1.512	2.761
Δ IP / eV		-0.436	-1.431	-1.130	-0.425	-0.407	-2.233

ground-state dynamics of cold thiophenone, successfully reproduces the first peak in the experimental He I photoelectron spectrum (cf. Fig. 7.7). All calculations are performed with Molpro 2012.

7.4.2 Computed photoproducts and ionisation potential

One key feature of the present experimental study is that the response of UV-excited thiophenone molecules can be followed not just en route to, but also after reaching, the S_0 PES. To simulate the ground-state dynamics, the foregoing non-adiabatic molecular dynamics calculations using TSH in the lowest four electronic states are combined with *ab initio* molecular dynamics (AIMD) on the S_0 PES. From an electronic structure perspective, this requires switching from a SA-CASSCF description (used for the excited-state dynamics) to an unrestricted density functional theory (UDFT) picture. The SA-CASSCF active space employed for the TSH dynamics becomes unstable when the trajectories are prolonged on the S_0 PES, but AIMD with UDFT is found to offer a stable alternative and allowed long-time simulation of the $S_0^{\#}$ species (see, for example, a previous study by Mignolet et al.[321]). To initiate the $S_0^{\#}$ molecular dynamics after passage through the S_1/S_0 seam of intersection, the AIMD trajectories are launched from the nuclear coordinates and with the momenta extracted from the TSH trajectories after the S_0 state has been reached. Thus, the present AIMD simulations are not per se in a ground-state thermal equilibrium, since the internal energy of the molecule at the start of the S_0-state dynamics calculation depends

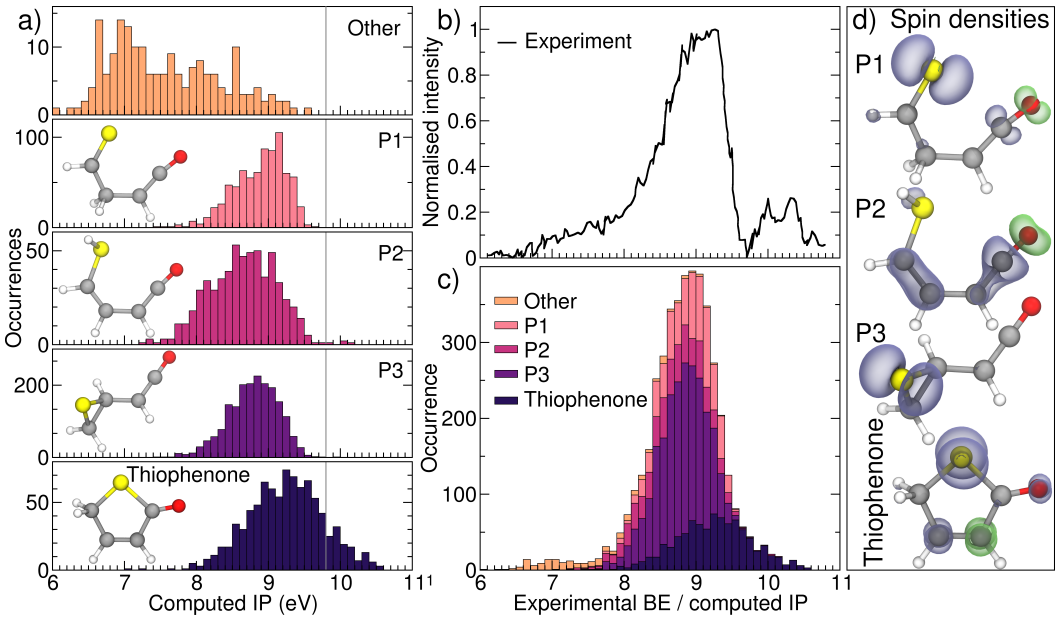

Fig. 7.6.: Dynamics on the S_0 PES following photoexcitation and non-radiative decay. a) Histograms showing the number of occurrences of the various $S_0 \rightarrow D_0$ IP_{vert} values, grouped by similarity to the molecular geometries identified as P1, P2, P3 and closed-ring thiophenone, along with a further small group labelled 'Other' associated with internally hot molecules that are in the act of converting between stable isomeric forms at the time the trajectory is sampled (see text). The calculated IP_{vert} for thiophenone at its optimised ground-state geometry is indicated by a dashed vertical black line. b) Experimental (subtracted) photoelectron spectrum summed over the delay range $0.5 \leq \Delta t \leq 2$ ps; the contribution at BE > 9.8 eV is due to ionisation of $S_0^{\#}$ molecules to excited cationic states, which are not included in the present calculations. c) Sum of the five distributions of IP_{vert} values shown in a. d) Spin densities (blue) of the optimised structures of the photoproducts observed and thiophenone, and their negative contributions (green).

on the history of the TSH trajectory in the excited state. Thereby, the approach allows the description of non-statistical effects in the hot $S_0^{\#}$-state dynamics. In total, 22 AIMD trajectories are propagated until $t = 2$ ps.

Since each AIMD trajectory is a continuation of an excited-state trajectory, the starting configuration in each case involves a ring-opened or highly stretched molecule. The AIMD simulations reveal the formation of several different photoproducts within the earliest timescales of these dynamics. Ring closure (resulting in the reformation of hot thiophenone molecules) is observed, as is the formation of the acyclic isomers 2-thioxoethylketene (P1), 2-(2-sulfanylethyl)ketene (P2) and 2-(2-thiiranyl)ketene (P3) (see Fig. 7.6a for structures). Interconversion between these isomers is observed in most trajectories within 2 ps. The histogram labelled 'Other' in Fig. 7.6a includes all molecular geometries that could not be attributed to P1, P2, P3 or closed-ring thiophenone products. These rare other geometries

often correspond to transient configurations in the act of interconverting between the dominant photoproducts and are mostly observed within 500 fs of accessing the S_0-state PES. It is important to emphasise that these AIMD calculations (and the gas-phase experiments) involve isolated molecules. The potential energy acquired by thiophenone upon photoexcitation is converted, in part, to nuclear kinetic energy during the nonradiative decay to the S_0 state, but these are closed systems: no energy dissipation is possible and the resulting $S_0^\#$ species are highly energetic. Experimentally, the BEs of the $S_0^\#$ species formed via nonradiative de-excitation are concentrated in a narrow (1 eV, full width at half maximum (FWHM)) band centred at $\sim$ 9 eV, as shown in Fig. 7.6b. Yet the AIMD simulations indicate that this ensemble of $S_0^\#$ species must contain a range of structures with high internal energies. Thus, the 22 AIMD outputs are analysed further. Specifically, the molecular geometry is extracted every 10 fs from each AIMD trajectory, yielding a pool of $> 4,000$ geometries. These are grouped by photoproduct and, for each geometry, the IP_{vert} value between the S_0 and D_0 states is calculated using MP2-F12/cc-pVDZ-F12 to provide an estimate of the BE. As Fig. 7.6a shows, the histograms of the IP_{vert} values for each photoproduct span a narrow range, and the ground-state photoproducts P1, P2 and P3 display similar IP_{vert} distributions. This reflects the fact that, in each case, ionisation involves the removal of an electron from an orbital with a high degree of n(S) character. The distribution associated with re-formed closed-ring thiophenone species is centred at slightly higher IP_{vert} values. The 22 AIMD outputs predict a narrow overall distribution of IP_{vert} values (Fig. 7.6c) that, as Fig. 7.6b shows, matches well with the TRPES data summed over the delay range $0.5 \leq \Delta t \leq 2$ ps.

For the electrons identified as being involved in the ionisation process, spin densities are computed (at the MP2/cc-pVDZ level of theory) for the optimised structures of the molecules observed during the AIMD; thiophenone, and the ketene photoproducts P1, P2 and P3 observed in the AIMD calculations. Fig. 7.6d shows the spin densities plotted with an isosurface of 0.02. The spin densities are shown in blue (the green isosurface shows the negative contributions and offers a measure of spin contamination). The spin densities for thiophenone, P1 and P3 are mainly located on the sulfur atom, consistent with the previous conclusion that ionisation occurs mainly from the n(S) orbital. In the case of P2 (second structure in Fig. 7.6d), the spin density is mostly on the C=C double bond, suggesting that ionisation occurs from this π orbital. However, it should be noted that the optimised geometry of the P2 structure may not be fully representative of the

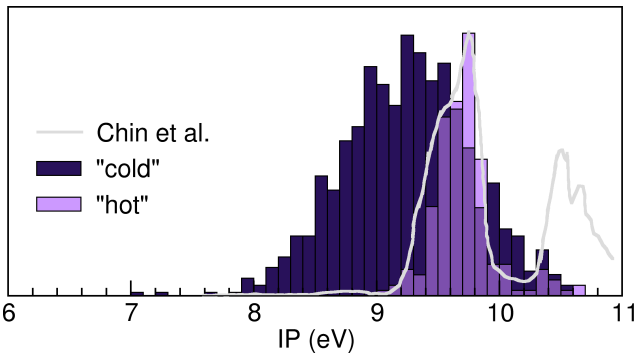

Fig. 7.7.: Comparison of measured (He I) photoelectron spectrum of thiophenone (Chin et al.,[312] solid black trace) and the distributions of computed $S_0 \rightarrow D_0$ IP_{vert} values for 'cold' (lavender) and 'hot' (dark purple) thiophenone molecules. The former histogram, obtained from AIMD simulations of S_0 molecules with internal energy equal to the zero-point energy only, has been scaled vertically to match the experimental spectrum and illustrates the good agreement with the experimental IP. The latter histogram, which shows the distribution of IP_{vert} values associated with closed-ring 'hot' thiophenone species (computed at the MP2/cc-pVDZ-F12 level of theory) produced after photoexcitation and subsequent relaxation has been scaled to have the same maximum. Note that the present protocol has not attempted to model the $S_0 \rightarrow D_2$ ionisation responsible for the BE > 10.4 eV peak in the experimental spectrum.

hot ground-state photoproduct. For the other photoproducts, the histograms of IP_{vert} values calculated for the structures observed during the AIMD are all centred at the IP_{vert} value calculated for the optimised point. For P2, the calculated IP at the optimised point is 8.37 eV, whereas the histogram of IP_{vert} values of the hot photoproduct is centred at $\sim$ 8.7 eV. Additionally, the distribution of IP_{vert} values for P2 is broader than that for any of the other structures. To this end, spin densities are computed for the frames of an AIMD trajectory showing the formation of P2. It is observed that, for such $S_0^{\#}$ geometries, the spin density is localised not only around the C=C bond but also on the sulfur atom. Thus, it can be concluded that the shift to a higher IP_{vert} and the broadening of the IP_{vert} distribution during the AIMD (cf. the IP_{vert} obtained from the ground-state optimised structure) can be understood assuming that ionisation to form D_0 occurs from the π and the n(S) orbitals. The characters of the D_0 photoproducts accord with that observed in the previously discussed XMS(4)-CASPT2(9/8) calculations.

For completeness, it is noted that the predicted distribution of $S_0 \rightarrow D_0$ IP_{vert} values for thiophenone molecules without the extra kinetic energy induced by photoexcitation and subsequent relaxation (derived from AIMD simulations of thiophenone initiated with internal energy equal to the zero-point energy only) is centred at yet higher IP_{vert}, is much

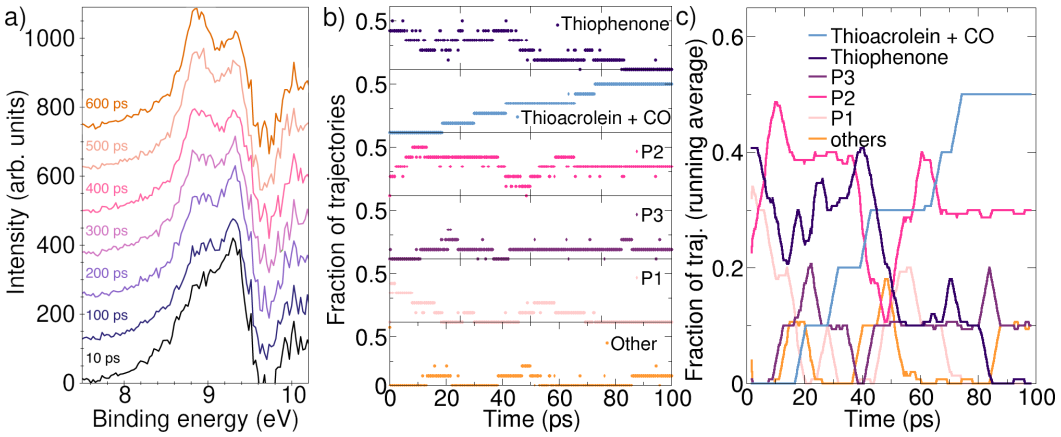

Fig. 7.8.: a) Photoelectron spectra for different pump–probe delays after subtraction of the signal from 'unpumped' thiophenone (S_0) molecule. The spectra are offset vertically for better visibility. b) Distribution of the photoproducts during the long-time AIMD simulations. The dots indicate the proportion of a given photoproduct sampled every 0.25 ps. c) The solid lines show the running average corresponding to the dots of b) (over 15 time steps).

narrower and, as Fig. 7.7 shows, is in very good accord with the lowest energy peak in the measured He I photoelectron spectrum.[312]

7.4.3 Estimation of the long timescale ground-state dynamics

Figure 7.8a shows photoelectron spectra recorded at several pump–probe delays in the range $10 \leq \Delta t \leq 600$ ps. Most of the photoelectron intensity of interest at these large Δt values lies in the range $8.0 \leq \text{BE} \leq 9.6$ eV, and the spectrum appears to consist of different contributions whose weights are Δt dependent; the intensity of the feature at lower BE (peaking at BE $\approx$ 8.8 eV) appears to increase relative to that of the feature peaking at BE $\approx$ 9.3 eV as Δt increases.

To explore the possible evolution of the ground-state photoproducts over longer timescales, 10 AIMD trajectories (out of the initial 22) are propagated until $t = 100$ ps. Issues of particular interest here are (i) whether the 'hot' $S_0^{\#}$ thiophenone photoproducts would eventually ring open, and (ii) whether the primary photoproducts might undergo further fragmentation. At the start of the long-time AIMD simulations (i.e., at t = 2 ps), the chosen pool of 10 molecules involved 4 (i.e. 40%) with 'hot' thiophenone structures, 4 P1 and 2 P2 structures. It should be stressed that these proportions are chosen solely to investigate the possible fate of some specific photoproducts (particularly 'hot' thiophenone) during the long-time exploratory AIMD; they do not reflect the relative photoproduct yields after t = 2 ps (as shown in Fig. 7.8a). Fig. 7.8b and c show how these photoproduct proportions evolve

over the full length of the AIMD. Analysis of the (admittedly small number of) long-time trajectories reveals (1) irreversible conversion of closed-ring to open-ring isomers and (2), in several cases, unimolecular decay of the $S_0^{\#}$ species to CO + Thioacrolein ($CH_2CHC(H)S$) products arising from the decay of both 'hot' thiophenone and photoproduct P1. The computed $S_0 \rightarrow D_0$ IP_{vert} value for thioacrolein (9.04 and 8.99 eV for the Z- and E-isomers, respectively, at the MP2-F12/cc-pVDZ-F12 level of theory) is in very good agreement with the experimental value.[322]

The present long time AIMD analysis is statistically limited, but it serves to highlight possible pathways that can alter the composition of the photoproducts formed on the S_0 PES over time in a manner that could account for the long time variation in the TRPES signal observed in the range $8 \leq BE \leq 9.5$ eV (Fig. 7.8a). Recalling Fig. 7.6a, all closed-ring to open-ring transformations (including the fragmentation process) will cause a net transfer of $S_0^{\#}$ population to species with lower IP_{vert} (that is, lower BE) values—consistent with the experimental observations (Fig. 7.8a).

7.5 Ultrafast electron diffraction

Since the calculations predict photoproducts of a wide variety of nuclear configurations, additional experiments to the TRPES are desirable since TRPES cannot distinguish between the photoproducts of thiophenone. Ultrafast electron diffraction can resolve the position of the nuclei during the photochemical process with femtosecond temporal resolution and sub-angstrom spatial resolution. Therefore, a megaelectron volt UED experiment was carried out at the SLAC-MeV UED facility for thiophenone aiming to verify the formation of the photoproducts predicted by the simulations. The recorded experimental percentage difference signal is shown in Fig. 7.9a. For an interpretation of this experimental data, the computational references are invaluable. In order to provide more accurate reference data, the set of previous 46 TSH trajectories of which only 22 have been extended to 2 ps with AIMD has been extended to 46 AIMD trajectories. All the results presented here are preliminary.

The simulated trajectories are classified in ring-closed thiophenone (which corresponds to the reformation of the hot thiophenone after the deactivation), P3 (2-(2-thiiranyl)ketene) and ring-open species. This summation of ring-open species is done since P1, P2 and "Other" products (bi-radical) from the previous analysis only differ by one hydrogen atom

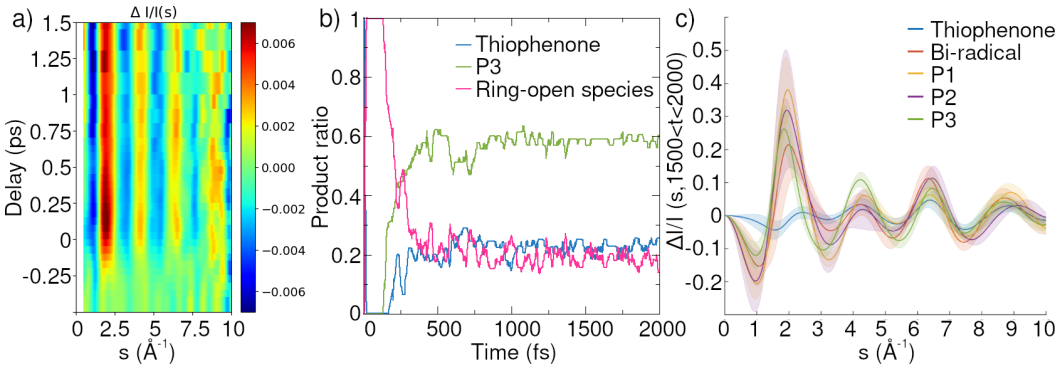

Fig. 7.9.: a) Ultrafast electron diffraction experiment, scattering intensity in reciprocal space as a function of delay time. b) Time evolution of the product ratio from the dynamics simulations. Ring open species includes bi-radical, P1 and P2. c) Simulated reciprocal space signal integrated over time for each of the photoproducts.

and, therefore, yield very similar reciprocal-space signals (see Fig. 7.9c). The time evolution of the computationally predicted ratio of products over time is shown in Fig. 7.9b. It can be seen that immediately after the excitation the ring-open species become dominant, which is in line with the previous observations. Following the results from the previous simulations and experiment, it can be assumed that all ring open species observed in the simulation after 500 fs correspond to either P1 or P2. This is supported by the observation of transient molecules between products as a minor contribution during the long term dynamics. In addition, the AIMD trajectories are initialised once they have assumed predominantly closed-shell character. The simulations predict a majority of P3 being formed with 60 % of the final products corresponding to P3, and similar amounts of thiophenone and ring open species being formed.

The important next step in this study will be to analyse the experimental data using the computational results. By fitting the reciprocal-space signal to the simulated ones of the photoproduct, the experimentally observed photoproducts might be determined. This might offer an estimation of whether the computational prediction of photoproducts is accurate.

7.6 Conclusions

Time-resolved XUV photoelectron spectroscopy studies of the isolated (gas-phase) molecules at a seeded FEL, in combination with high-level *ab initio* theory, have enabled detailed visualisation of the electronic and, particularly, the structural dynamics of this complex

photoinduced ring-opening reaction. The initial motion following photoexcitation is revealed, as well as the non-adiabatic coupling to the S_0 PES as an open-ring biradical, and the subsequent isomerisations and eventual decay of the highly vibrationally excited S_0-state species. The match between theory and experiment spans both the excited-state decay rates and the more challenging athermal rearrangements to photoproducts that occur after non-adiabatic coupling to the S_0 state. The use of sufficiently high-energy probe photons is key to tracking the full decay dynamics, that is, the ultrafast evolution of the photoexcited wavepacket to the S_0 state and the nuclear dynamics of the resulting highly vibrationally excited S_0 molecules. The increase in BE observed immediately post-photoexcitation is a signature of the ultrafast decay of the nuclear wavepacket from the S_2 state, via the S_1 state, towards the electronic ground state, enabled by elongation and eventual scission of the S–CO bond. The evolving molecules couple to the S_0 PES with a range of geometries and nuclear momenta, which govern the subsequent athermal rearrangements of the $S_0^{\#}$ species. These vibrationally excited S_0 molecules are highly fluxional and can adopt at least three identified open-ring structures or re-form the parent thiophenone, and they have sufficient internal energy to dissociate (by loss of a CO moiety). The deduced ground-state dynamics serve to bolster a recent prediction that isomerisation of energised molecules prior to dissociation might well be the rule rather than the exception in many polyatomic unimolecular processes.[323] The IP_{vert} distribution computed from the AIMD trajectories on the S_0 PES reproduces the narrow spread of BEs observed experimentally and can be traced to the localised nature of the sulfur lone pair orbital that is the dominant contributor to the HOMO in each species. Distinguishing the various open-ring products by valence-shell photoelectron spectroscopy is challenging given their very similar first IPs.

Ultrafast electron diffraction studies can address such structural challenges and seem to be able to distinguish some of the computationally predicted photoproducts. It will be of great interest to disclose whether the experimental data can confirm the photoproducts.

8 Conclusion and Outlook

8.1 Summary

The guiding thread of this thesis was to understand what constitutes a good model for nonadiabatic dynamics and how one can adapt such models to depict the key excited-state processes in real-life molecular systems. Models are usually known and used in the context of one-dimensional test systems, where they are applied to assess the capabilities and limitations of newly developed nonadiabatic dynamics methods. However, connections between the one-dimensional test system and the application to real, full dimensional molecules are scarce. This thesis aimed to fill this gap by exploring different models for nonadiabatic dynamics: i) the conceptual models that question our view of photochemistry, ii) the molecular models that are representative of key processes in photochemistry, and iii) the realistic models that can be directly compared with photochemical experiments.

The first part of this thesis mirrored our view of photochemistry, which is heavily based on the Born-Oppenheimer representation, by the picture provided by the exact factorisation. A complete photochemical experiment was simulated on a two-dimensional two-state system, starting from the molecule in its ground state that gets photoexcited by a laser pulse. After this excitation, the excited nuclear wavepacket evolves on the excited state until reaching a region of high nonadiabaticity where the wavepacket decays to the ground state and forms potential photoproducts. This study contrasted this intrinsically BO picture of the dynamics of nuclear wavepackets with static potential energy surfaces, conical intersections, transition dipole moments with the exact factorisation picture, where the nuclear dynamics is governed by a single time-dependent potential energy surface and a single time-dependent vector potential. In addition, this work presented a framework for propagating quantum and classical trajectories based on the exact factorisation potentials. One particular curiosity of this study was the observation that the portion of the wavefunction remaining in the Franck-Condon region was excited to a higher vibrational eigenstate.

After that detailed discussion of the representation of the molecular wavefunction, the next part of this thesis investigated the consequences of the BO picture on approximated nonadiabatic dynamics. The dynamics predicted by AIMS in the vicinity of conical intersections of different topologies were evaluated on the simplest model systems including conical intersections — two dimensional two-state systems — in comparison with exact quantum dynamics and the mixed quantum/classical method TSH. This study found that AIMS is not only capable of reproducing the population decay reasonably well but also predicts the evolution of the ground-state nuclear density in very good agreement with the exact results. This work gave particular attention to the attempt of including higher-order coupling terms as well as geometric phase effect within the AIMS approach. In doing this, one has to be particularly careful to preserve the hermiticity of the employed Hamiltonian. However, the limiting factor of improving the description of the couplings between trajectory basis functions lies in the subtle equilibrium existing between the main approximations of AIMS. Lifting the saddle point approximation of order zero by including additional couplings and geometric phase effects is hampered by the number of trajectory basis functions present in the simulation as a result of the independent first-generation approximation.

Having demonstrated the usefulness of low dimensional models to probe nonadiabatic dynamics methods, the focus was shifted towards applications to real molecular systems in their full dimensionality. This part of the thesis proposed a set of *molecular* models to bridge low dimensional model systems and real molecules. The famous one-dimensional Tully models are taken as inspiration since they have already been extensively used to test nonadiabatic dynamics methods. This work established a connection between the photophysics probed by these models and photoinduced processes occurring in real, full dimensional molecules. As John Tully said himself: *"I have not understood why people have continued to use the over-simplified 1990 models. It is important to test models and design improvements based on realistic, multi-dimensional models."*[324] Subsequently, a set of three molecules, ethylene, DMABN and fulvene, was introduced as the *molecular Tully models*. Based on their dynamics predicted by (decoherence corrected) TSH and AIMS, this work dissected the challenging photophysical processes these models undergo and highlighted how these models can be used to assess the capabilities of new nonadiabatic dynamics methods on full-dimensional molecules. Henceforth, the molecular Tully models have already been used by the nonadiabatic dynamics community to test a variety of

methods: fewest switches surface hopping with Baeck-An couplings,[278] ab initio symmetric quasi-classical approach,[279] decoherence induced surface hopping based on the exact factorisation,[178] stochastic selection ab initio multiple spawning,[280] and ab initio multiple spawning with informed stochastic selections.[281] These examples illustrate that there was a real need within the community for such a set of standardised molecular models. Two examples of their uses were shortly presented: the evaluation of the performance and computational efficiency of stochastic selection AIMS and a comparison of the decoherence induced surface hopping based on the exact factorisation with other, widely used decoherence correction schemes.

Following on the concept of using challenging molecules as model systems to test nonadiabatic dynamics methods, two particularly challenging molecules undergoing photoinduced ring-opening reactions were used to probe the performance and computational efficiency of the recently proposed stochastic selection AIMS method. This study showed how the overlap based formulation of stochastic selection AIMS is capable of reliably reproducing AIMS results at a reduced cost comparable to that of TSH.

Finally, the proof of the pudding is in the direct comparison with time-resolved experiments. This part of the thesis investigated the photoinduced ring-opening reaction of 2(5H)-thiophenone and uncovered its subsequent formation of various photoproducts in the vibrationally excited ground state. The computational study described the excited-state dynamics driven by the ballistic ring opening in great agreement with experimental observables. Immediately upon photoexcitation, the molecule undergoes a ring-opening process that drives the deactivation to the ground state, combined with an out of plane twisting and leads to a significant increase in binding energy recorded in the photoelectron spectrum. Subsequently, ab initio molecular dynamics simulations uncovered a great variety of formed photoproducts by continuing trajectories for 2 ps in the ground state. The ionisation potential was calculated along these ab initio molecular dynamics trajectories and it reproduced well the experimental binding energy. While time-resolved photoelectron spectroscopy is not able to distinguish between the photoproducts of thiophenone, preliminary data of ultrafast electron diffraction experiments and simulations indicate the possibility to dissect between ring-open and three- and five-membered ring-closed species.

Overall, this thesis aimed to give a different view and modern perspective on models within nonadiabatic dynamics and photochemistry. The results presented contribute to

building a stronger bridge between the chemical physics community – that develops new nonadiabatic dynamics methods – and the physical chemistry one – which uses these methods to explain the photodynamics of molecules.

8.2 Outlook

Naturally, this thesis leaves several questions unanswered and triggered new ones too. Starting from the observation of the formation of a vibrationally excited ground-state wavepacket during the photoexcitation by an explicit laser pulse, one question arising is whether this occurs commonly in photochemical experiments. Can this vibrational excitation form a ground-state wavepacket and could this wavepacket contribute to what is called "the photochemical reaction"? Since this is generally neither considered in experiments, where the signature of the equilibrium molecule is subtracted, nor in theory, where excited-state dynamics are often initialised directly in the excited state without describing explicitly the excitation, careful investigation of this phenomenon might be of general interest to the community.

A framework for the propagation of quantum and classical trajectories based on the exact factorisation was introduced, which requires full knowledge of the full nuclear density and necessitates precomputing the quantities of the full nuclear configuration space; however, the choice of gauge simplified the expressions significantly. The coupled trajectory mixed quantum/classical method is a proposition of trajectory-based nonadiabatic dynamics using concepts from the exact factorisation and is applicable to molecules in their full dimensionality. Further developments of nonadiabatic dynamics methods using the exact factorisation will carry on in the future, as this ansatz provides a representation-free description of the dynamics. Given the comparably short history of the exact factorisation — the exact factorisation of the time-dependent electron-nuclear wave function was first published in 2010 —, there are still many avenues to explore. Instead of using coupled classical trajectories propagated on the time-dependent scalar and vector potential, a possibility might be to use an approach based on trajectory basis functions.

One other large focus of this thesis was the development of molecular models to test nonadiabatic dynamics methods. As such, the molecular Tully models have already been used to test newly developed strategies. This set could potentially be extended further, such that a universal benchmark set for nonadiabatic dynamics methods is created, in analogy

to existing benchmark sets for electronic structure methods. It would be desirable to arrive at a point, where more and more nonadiabatic dynamics methods have been tested and compared on a standardised set of real, full dimensional molecules, which ideally probe various scenarios that can occur upon photoexcitation, for example, degeneracies of states, decoherence and recoherence, three state conical intersections, dissociation. This would establish an extensive knowledge on the capabilities of methods, similar to what is done for electronic structure methods, and facilitate greatly the choice of a suitable nonadiabatic dynamics method for a given problem.

All the initial conditions that have been used for the dynamics of the molecular test systems have been made available to facilitate the testing of new methods under the same, controlled framework. However, these initial conditions can only be used for methods based on classical trajectories. For a further generalisation of the molecular Tully models, it would be useful to find a way to perform fair comparisons between methods that are for example based on quantum trajectories or wavepackets. Further investigation in the initialisation between different methods, for example between those using different trajectory basis functions, is of great interest to the field of nonadiabatic dynamics.

Finally, the joint experimental and theoretical studies on thiophenone (amongst other comparable studies) have proven the strengths of the combination of these methods. In the future, due to the increased capabilities of experimental resolution and laser strengths, more comparable studies can be carried out to unravel photochemical processes occurring in molecules. Especially, ultrafast electron diffraction appears as a potentially exciting new approach to probe the photodynamics of molecules as it is directly sensitive to the nuclear configuration of the molecule. Nuclear dynamics simulations, i.e. especially nonadiabatic dynamics and ab initio molecular dynamics, will be crucial tools and their performances will be duly tested since ultrafast electron diffraction allows for a direct comparison with respect to nuclear configurations and predicted product yields.

A Appendix: Explicit form of the SPA1 for the first order nonadiabatic couplings

In the following, a derivation of the full expression for the AIMS interstate couplings within the SPA1 is proposed, neglecting the NACs. Considering a two-dimensional ($\boldsymbol{R} = (X, Y)$) two-state system (such as the ones investigated in the main text) to introduce all the terms explicitly. For clarity, atomic units are used throughout this appendix, meaning that (what is of concern here) $\hbar = 1$ is defined.

First, some notations for the NACVs and their derivatives in a vector form is defined as:

$$\begin{aligned}
\boldsymbol{d}_{IJ}(\boldsymbol{R}) &= \begin{pmatrix} d_{IJ}^{X}(\boldsymbol{R}) \\ d_{IJ}^{Y}(\boldsymbol{R}) \end{pmatrix} \\
\frac{\partial}{\partial X}\boldsymbol{d}_{IJ}(\boldsymbol{R}) &= \begin{pmatrix} \frac{\partial}{\partial X} d_{IJ}^{X}(\boldsymbol{R}) \\ \frac{\partial}{\partial X} d_{IJ}^{Y}(\boldsymbol{R}) \end{pmatrix} = \begin{pmatrix} (d_{IJ}^{X}(\boldsymbol{R}))^{(X)} \\ (d_{IJ}^{Y}(\boldsymbol{R}))^{(X)} \end{pmatrix} \\
\frac{\partial}{\partial Y}\boldsymbol{d}_{IJ}(\boldsymbol{R}) &= \begin{pmatrix} \frac{\partial}{\partial Y} d_{IJ}^{X}(\boldsymbol{R}) \\ \frac{\partial}{\partial Y} d_{IJ}^{Y}(\boldsymbol{R}) \end{pmatrix} = \begin{pmatrix} (d_{IJ}^{X}(\boldsymbol{R}))^{(Y)} \\ (d_{IJ}^{Y}(\boldsymbol{R}))^{(Y)} \end{pmatrix}.
\end{aligned} \tag{A.1}$$

The Taylor expansion to first order for the NACVs around the centroid position, $\bar{\boldsymbol{R}}$, has the general form:

$$\boldsymbol{d}_{IJ}(\boldsymbol{R}) = \boldsymbol{d}_{IJ}(\bar{\boldsymbol{R}}) + \boldsymbol{J}_{\boldsymbol{d}_{IJ}}(\bar{\boldsymbol{R}})(\boldsymbol{R} - \bar{\boldsymbol{R}}) + \ldots \tag{A.2}$$

where

$$\boldsymbol{J}_{\boldsymbol{d}_{IJ}}(\bar{\boldsymbol{R}}) = \begin{pmatrix} (d_{IJ}^{X}(\boldsymbol{R}))^{(X)} & (d_{IJ}^{X}(\boldsymbol{R}))^{(Y)} \\ (d_{IJ}^{Y}(\boldsymbol{R}))^{(X)} & (d_{IJ}^{Y}(\boldsymbol{R}))^{(Y)} \end{pmatrix}\Bigg|_{\boldsymbol{R}=\bar{\boldsymbol{R}}} \tag{A.3}$$

is the Jacobian of the NACVs evaluated at the centroid position.

Using this Taylor expansion to zeroth order as an approximation to the NACVs in the AIMS interstate matrix elements, we obtain

$$\mathrm{NACV}_{\mathrm{SPA0}} \equiv \boldsymbol{M}^{-1}\overline{\boldsymbol{d}_{IJ}}\,\langle\tilde{\chi}_k^{(I)}|\,\frac{\partial}{\partial \boldsymbol{R}}\,|\tilde{\chi}_m^{(J)}\rangle_{\boldsymbol{R}}\,, \tag{A.4}$$

where $\overline{\boldsymbol{d}_{IJ}} = \boldsymbol{d}_{IJ}(\bar{\boldsymbol{R}})$ denotes the nonadiabatic coupling vector evaluated at the centroid position of the two TBFs considered. We used the symbolic notation $\mathrm{NACV}_{\mathrm{SPA0}}$ to designate in a general way the AIMS interstate couplings within the SPA0 and without the NACs (or GP corrections).

The AIMS interstate coupling term between TBFs reads, for the first-order term of the Taylor expansion (Eq. (A.2)),

$$\begin{aligned}\mathrm{NACV}_{\mathrm{SPA1}} &\equiv \langle\tilde{\chi}_k^{(I)}|\,\boldsymbol{M}^{-1}\boldsymbol{J}_{\overline{\boldsymbol{d}_{IJ}}}(\boldsymbol{R}-\bar{\boldsymbol{R}})\frac{\partial}{\partial \boldsymbol{R}}\,|\tilde{\chi}_m^{(J)}\rangle_{\boldsymbol{R}} \\ &= \langle\tilde{\chi}_k^{(I)}|\begin{pmatrix} M_X^{-1} & 0 \\ 0 & M_Y^{-1}\end{pmatrix}\begin{pmatrix} (\bar{d}_{IJ}^X)^{(X)} & (\bar{d}_{IJ}^X)^{(Y)} \\ (\bar{d}_{IJ}^Y)^{(X)} & (\bar{d}_{IJ}^Y)^{(Y)}\end{pmatrix}\begin{pmatrix} X-\bar{X}_{km} \\ Y-\bar{Y}_{km}\end{pmatrix}\begin{pmatrix}\frac{\partial}{\partial X} \\ \frac{\partial}{\partial Y}\end{pmatrix}|\tilde{\chi}_m^{(J)}\rangle_{\boldsymbol{R}}\end{aligned} \tag{A.5}$$

where $\boldsymbol{J}_{\overline{\boldsymbol{d}_{IJ}}}$ is a short-hand notation for $\boldsymbol{J}_{\boldsymbol{d}_{IJ}}(\bar{\boldsymbol{R}})$; $\bar{X}_{km}$ and $\bar{Y}_{km}$ are the X and Y components of the centroid position between the two TBFs $\tilde{\chi}_k^{(I)}$ and $\tilde{\chi}_m^{(J)}$. Developing this expression and separating the terms leads to:

$$\begin{aligned}\mathrm{NACV}_{\mathrm{SPA1}} = \langle\tilde{\chi}_k^{(I)}|\,\Bigg[&M_X^{-1}(\bar{d}_{IJ}^X)^{(X)}(X-\bar{X}_{km})\frac{\partial}{\partial X} + M_X^{-1}(\bar{d}_{IJ}^X)^{(Y)}(Y-\bar{Y}_{km})\frac{\partial}{\partial X} \\ &+ M_Y^{-1}(\bar{d}_{IJ}^Y)^{(X)}(X-\bar{X}_{km})\frac{\partial}{\partial Y} + M_Y^{-1}(\bar{d}_{IJ}^Y)^{(Y)}(Y-\bar{Y}_{km})\frac{\partial}{\partial Y}\Bigg]\,|\tilde{\chi}_m^{(J)}\rangle_{\boldsymbol{R}} \\ =&M_X^{-1}(\bar{d}_{IJ}^X)^{(X)}\left[\langle\tilde{\chi}_k^{(I)}|\,X\frac{\partial}{\partial X}\,|\tilde{\chi}_m^{(J)}\rangle_{\boldsymbol{R}} - \bar{X}_{km}\,\langle\tilde{\chi}_k^{(I)}|\,\frac{\partial}{\partial X}\,|\tilde{\chi}_m^{(J)}\rangle_{\boldsymbol{R}}\right] \\ &+ M_X^{-1}(\bar{d}_{IJ}^X)^{(Y)}\left[\langle\tilde{\chi}_k^{(I)}|\,Y\frac{\partial}{\partial X}\,|\tilde{\chi}_m^{(J)}\rangle_{\boldsymbol{R}} - \bar{Y}_{km}\,\langle\tilde{\chi}_k^{(I)}|\,\frac{\partial}{\partial X}\,|\tilde{\chi}_m^{(J)}\rangle_{\boldsymbol{R}}\right] \\ &+ M_Y^{-1}(\bar{d}_{IJ}^Y)^{(X)}\left[\langle\tilde{\chi}_k^{(I)}|\,X\frac{\partial}{\partial Y}\,|\tilde{\chi}_m^{(J)}\rangle_{\boldsymbol{R}} - \bar{X}_{km}\,\langle\tilde{\chi}_k^{(I)}|\,\frac{\partial}{\partial Y}\,|\tilde{\chi}_m^{(J)}\rangle_{\boldsymbol{R}}\right] \\ &+ M_Y^{-1}(\bar{d}_{IJ}^Y)^{(Y)}\left[\langle\tilde{\chi}_k^{(I)}|\,Y\frac{\partial}{\partial Y}\,|\tilde{\chi}_m^{(J)}\rangle_{\boldsymbol{R}} - \bar{Y}_{km}\,\langle\tilde{\chi}_k^{(I)}|\,\frac{\partial}{\partial Y}\,|\tilde{\chi}_m^{(J)}\rangle_{\boldsymbol{R}}\right].\end{aligned} \tag{A.6}$$

The evaluation of these terms requires the knowledge of the following Gaussian integrals[153,164]

$$
\begin{aligned}
\langle \tilde{\chi}_k^{(I)} | \frac{\partial}{\partial X} | \tilde{\chi}_m^{(J)} \rangle_{\boldsymbol{R}} &= \left[i \left(\bar{P}_m^X + \bar{P}_k^X \right) + \alpha_X (\bar{X}_m - \bar{X}_k) \right] \langle \tilde{\chi}_k^{(I)} | \tilde{\chi}_m^{(J)} \rangle_{\boldsymbol{R}} \\
\langle \tilde{\chi}_k^{(I)} | X \frac{\partial}{\partial X} | \tilde{\chi}_m^{(J)} \rangle_{\boldsymbol{R}} &= -\frac{1}{2} \langle \tilde{\chi}_k^{(I)} | \tilde{\chi}_m^{(J)} \rangle_{\boldsymbol{R}} \\
&\quad + \left[\frac{i}{2} (\bar{X}_k \bar{P}_k^X + \bar{X}_m \bar{P}_m^X) + \frac{\alpha_X}{2} (\bar{X}_m^2 - \bar{X}_k^2) + \frac{1}{8\alpha_X} \left(\left(\bar{P}_k^X \right)^2 - \left(\bar{P}_m^X \right)^2 \right) \right] \langle \tilde{\chi}_k^{(I)} | \tilde{\chi}_m^{(J)} \rangle_{\boldsymbol{R}} \\
\langle \tilde{\chi}_k^{(I)} | Y \frac{\partial}{\partial X} | \tilde{\chi}_m^{(J)} \rangle_{\boldsymbol{R}} &= \Bigg[-\frac{1}{8\alpha_Y} (\bar{P}_m^X + \bar{P}_k^X)(\bar{P}_m^Y - \bar{P}_k^Y) + \frac{i}{4} (\bar{Y}_m + \bar{Y}_k)(\bar{P}_m^X + \bar{P}_k^X) \\
&\quad + \frac{i\alpha_X}{4\alpha_Y} (\bar{X}_m - \bar{X}_k)(\bar{P}_m^Y - \bar{P}_k^Y) + \frac{\alpha_Y}{2} (\bar{X}_m + \bar{X}_k)(\bar{Y}_m + \bar{Y}_k) \Bigg] \langle \tilde{\chi}_k^{(I)} | \tilde{\chi}_m^{(J)} \rangle_{\boldsymbol{R}} ,
\end{aligned}
\tag{A.7}
$$

where α_X and α_Y denote the width of the TBFs in the X and Y direction, $\bar{X}_k$, $\bar{X}_m$, $\bar{Y}_k$, $\bar{Y}_m$ are the central positions of the TBFs $\tilde{\chi}_k^{(I)}$ or $\tilde{\chi}_m^{(J)}$ for the X or Y coordinate, and $\bar{P}_k^X$, $\bar{P}_m^X$, $\bar{P}_k^Y$, $\bar{P}_m^Y$ are the central momenta of the TBFs $\tilde{\chi}_k^{(I)}$ or $\tilde{\chi}_m^{(J)}$ in X or Y.

Inserting the Gaussian integrals from Eq. (A.7) (and their corresponding expressions with inverted X and Y) into Eq. (A.6), we can obtain the final expressions for $\mathrm{NACV}_{\mathrm{SPA1}}$:

$$
\begin{aligned}
\mathrm{NACV}_{\mathrm{SPA1}} = \Bigg(& M_X^{-1}(\bar{d}_{IJ}^X)^{(X)} \left[-\frac{1}{2} + \frac{i}{2}\left(\bar{X}_m\bar{P}_m^X + \bar{X}_k\bar{P}_k^X\right) + \frac{\alpha_X}{2}(\bar{X}_m^2 - \bar{X}_k^2) - \frac{1}{8\alpha_X}\left(\left(\bar{P}_m^X\right)^2 - \left(\bar{P}_k^X\right)^2 \right) \right] \\
& + M_Y^{-1}(\bar{d}_{IJ}^Y)^{(Y)} \left[-\frac{1}{2} + \frac{i}{2}\left(\bar{Y}_m\bar{P}_m^Y + \bar{Y}_k\bar{P}_k^Y\right) + \frac{\alpha_Y}{2}(\bar{Y}_m^2 - \bar{Y}_k^2) - \frac{1}{8\alpha_Y}\left(\left(\bar{P}_m^Y\right)^2 - \left(\bar{P}_k^Y\right)^2 \right) \right] \\
& + M_X^{-1}(\bar{d}_{IJ}^X)^{(Y)} \left[-\frac{1}{8\alpha_Y}\left(\bar{P}_m^X + \bar{P}_k^X\right)\left(\bar{P}_m^Y - \bar{P}_k^Y\right) + \frac{i}{4}(\bar{Y}_m + \bar{Y}_k)\left(\bar{P}_m^X + \bar{P}_k^X\right) \right. \\
& \qquad \left. + \frac{i\alpha_X}{4\alpha_Y}(\bar{X}_m - \bar{X}_k)\left(\bar{P}_m^Y - \bar{P}_m^Y\right) + \frac{\alpha_X}{2}(\bar{Y}_m + \bar{Y}_k)(\bar{X}_m - \bar{X}_k) \right] \\
& + M_Y^{-1}(\bar{d}_{IJ}^Y)^{(X)} \left[-\frac{1}{8\alpha_X}\left(\bar{P}_m^Y + \bar{P}_k^Y\right)\left(\bar{P}_m^X - \bar{P}_k^X\right) + \frac{i}{4}(\bar{X}_m + \bar{X}_k)\left(\bar{P}_m^Y + \bar{P}_k^Y\right) \right. \\
& \qquad \left. + \frac{i\alpha_Y}{4\alpha_X}(\bar{Y}_m - \bar{Y}_k)\left(\bar{P}_m^X - \bar{P}_m^X\right) + \frac{\alpha_Y}{2}(\bar{X}_m + \bar{X}_k)(\bar{Y}_m - \bar{Y}_k) \right] \\
& + M_X^{-1}(\bar{d}_{IJ}^X)^{(X)}\bar{X}_{km} \left[\frac{i}{2}\left(\bar{P}_m^X + \bar{P}_k^X\right) + \alpha_X(\bar{X}_m - \bar{X}_k) \right] \\
& + M_Y^{-1}(\bar{d}_{IJ}^Y)^{(Y)}\bar{Y}_{km} \left[\frac{i}{2}\left(\bar{P}_m^Y + \bar{P}_k^Y\right) + \alpha_Y(\bar{Y}_m - \bar{Y}_k) \right] \\
& + M_X^{-1}(\bar{d}_{IJ}^X)^{(Y)}\bar{Y}_{km} \left[\frac{i}{2}\left(\bar{P}_m^X + \bar{P}_k^X\right) + \alpha_X(\bar{X}_m - \bar{X}_k) \right] \\
& + M_Y^{-1}(\bar{d}_{IJ}^Y)^{(X)}\bar{X}_{km} \left[\frac{i}{2}\left(\bar{P}_m^Y + \bar{P}_k^Y\right) + \alpha_Y(\bar{Y}_m - \bar{Y}_k) \right] \Bigg) \cdot \left(\langle \tilde{\chi}_k^{(I)} | \tilde{\chi}_m^{(J)} \rangle_{\boldsymbol{R}} \right)
\end{aligned}
\tag{A.8}
$$

All terms of this expression are Hermitian with respect to an exchange of the I and J indices, except the first term of the first and second row, highlighted in blue, which upon expansion read:

$$
\left(-\frac{1}{2} M_X^{-1}(\bar{d}_{IJ}^X)^{(X)} - \frac{1}{2} M_Y^{-1}(\bar{d}_{IJ}^Y)^{(Y)} \right) \langle \tilde{\chi}_k^{(I)} | \tilde{\chi}_m^{(J)} \rangle_{\boldsymbol{R}} \tag{A.9}
$$

Upon interchanging of I and J and complex conjugation, the derivatives of the nonadiabatic coupling vectors (at the centroid position) will change sign, $(\bar{d}_{IJ}^X)^{(X)} = -(\bar{d}_{JI}^X)^{(X)}$ and $(\bar{d}_{IJ}^Y)^{(Y)} = -(\bar{d}_{JI}^Y)^{(Y)}$, and in these terms this sign change is not compensated by any other factor. (In contrast, in all other terms of Eq. (A.8) the prefactor before the overlap compensates for that change of sign.)

From this derivation, it becomes clear that the entire AIMS interstate coupling within the SPA1 does not fulfil the hermiticity condition. However, the interstate coupling for the NACs within a SPA0 take the following form:

$$\mathrm{NAC}_{\mathrm{SPA0}} = \frac{1}{2}\left(- M_X^{-1}(\bar{d}_{IJ}^X)^{(X)} - M_Y^{-1}(\bar{d}_{IJ}^Y)^{(Y)} \right) \langle \tilde{\chi}_k^{(I)} | \tilde{\chi}_m^{(J)} \rangle_{\boldsymbol{R}} \ . \tag{A.10}$$

As discussed in Sec. 2.5.3, adding this term to the above expression for $\mathrm{NACV}_{\mathrm{SPA1}}$ leads to a compensation of the two anti-Hermitian contributions and restores the hermiticity of the Hamiltonian.

Bibliography

[1]N. Üstündağ, "The theology of democratic modernity: labor, truth, and freedom", in *Building free life: dialogues with Öcalan* (PM Press, 2020) Chap. 19, pp. 235–260.

[2]G. Nebbia and G. B. Kauffman, "Prophet of solar energy: a retrospective view of Giacomo Luigi Ciamician (1857–1922), the founder of green chemistry, on the 150th anniversary of his birth", Science **317**, 198–199 (2007).

[3]M. Venturi, V. Balzani, and M. T. Gandolfi, "Fuels from solar energy. a dream of Giacomo Ciamician, the father of photochemistry", in Proceedings ISES solar world congress, orlando (usa) (2005).

[4]A. L. Linsebigler, G. Lu, and J. T. Yates Jr, "Photocatalysis on TiO_2 surfaces: principles, mechanisms, and selected results", Chem. Rev. **95**, 735–758 (1995).

[5]M. A. Fox and M. T. Dulay, "Heterogeneous photocatalysis", Chem. Rev. **93**, 341–357 (1993).

[6]A. Fujishima and K. Honda, "Electrochemical photolysis of water at a semiconductor electrode", Naature **238**, 37–38 (1972).

[7]C. K. Prier, D. A. Rankic, and D. W. C. MacMillan, "Visible light photoredox catalysis with transition metal complexes: applications in organic synthesis", Chem. Rev. **113**, 5322–5363 (2013).

[8]M. H. Shaw, J. Twilton, and D. W. C. MacMillan, "Photoredox catalysis in organic chemistry", J. Org. Chem. **81**, 6898–6926 (2016).

[9]C.-S. Wang, P. H. Dixneuf, and J.-F. Soulé, "Photoredox catalysis for building C–C bonds from C(sp2)–H bonds", Chem. Rev. **118**, 7532–7585 (2018).

[10]A. H. Zewail, "Laser femtochemistry", Science **242**, 1645–1653 (1988).

[11]M. Gao, C. Lu, H. Jean-Ruel, L. C. Liu, A. Marx, K. Onda, S.-y. Koshihara, Y. Nakano, X. Shao, T. Hiramatsu, G. Saito, H. Yamochi, R. R. Cooney, G. Moriena, G. Sciaini, and R. J. D. Miller, "Mapping molecular motions leading to charge delocalization with ultrabright electrons", Nature **496**, pages 343–346 (2013).

[12]T. Ishikawa, S. A. Hayes, S. Keskin, G. Corthey, M. Hada, K. Pichugin, A. Marx, J. Hirscht, K. Shionuma, K. Onda, Y. Okimoto, S.-y. Koshihara, T. Yamamoto, H. Cui, M. Nomura, Y. Oshima, M. Abdel-Jawad, R. Kato, and R. J. D. Miller, "Direct observation of collective modes coupled to molecular orbital–driven charge transfer", Science **350**, 1501–1505 (2015).

[13]M. Born and R. Oppenheimer, "Zur Quantentheorie der Molekeln", Ann. Phys. **389**, 457–484 (1927).

[14]L. M. Ibele, A. Nicolson, and B. F. E. Curchod, "Excited-state dynamics of molecules with classically driven trajectories and Gaussians", Mol. Phys. **118**, e1665199 (2020).

[15]F. Agostini and B. F. E. Curchod, "Different flavors of nonadiabatic molecular dynamics", WIREs Comput. Mol. Sci. **9**, e1417 (2019).

[16]J. C. Tully, "Molecular dynamics with electronic transitions", J. Chem. Phys. **93**, 1061–1071 (1990).

[17]L. M. Ibele and B. F. E. Curchod, "A molecular perspective on Tully models for nonadiabatic dynamics", Phys. Chem. Chem. Phys. **22**, 15183–15196 (2020).

[18]T. J. Martínez, M. Ben-Nun, and R. D. Levine, "Multi-electronic-state molecular dynamics: a wave function approach with applications", J. Phys. Chem. **100**, 7884–7895 (1996).

[19]X. Sun and W. H. Miller, "Semiclassical initial value representation for electronically nonadiabatic molecular dynamics", J. Chem. Phys. **106**, 6346–6353 (1997).

[20]S. J. Cotton and W. H. Miller, "A symmetrical quasi-classical spin-mapping model for the electronic degrees of freedom in non-adiabatic processes", J. Phys. Chem. A **119**, 12138–12145 (2015).

[21]X. He, B. Wu, Z. Gong, and J. Liu, "Commutator matrix in phase space mapping models for nonadiabatic quantum dynamics", The Journal of Physical Chemistry A **125**, 6845–6863 (2021).

[22]Y. Wu and M. F. Herman, "Nonadiabatic surface hopping Herman-Kluk semiclassical initial value representation method revisited: applications to Tully's three model systems.", J. Chem. Phys. **123**, 144106 (2005).

[23]V. N. Gorshkov, S. Tretiak, and D. Mozyrsky, "Semiclassical Monte-Carlo approach for modelling non-adiabatic dynamics in extended molecules", Nat. Commun. **4**, 2144 (2013).

[24]T. Zimmermann and J. Vaníček, "Communications: evaluation of the nondiabaticity of quantum molecular dynamics with the dephasing representation of quantum fidelity", J. Chem. Phys. **132**, 241101 (2010).

[25]B. Poirier and G. Parlant, "Reconciling semiclassical and Bohmian mechanics: IV. Multisurface dynamics", J. Phys. Chem. A **111**, 10400–10408 (2007).

[26]R. Baskov, A. J. White, and D. Mozyrsky, "Improved Ehrenfest approach to model correlated electron–nuclear dynamics", J. Phys. Chem. Lett. **10**, 433–440 (2019).

[27]F. Agostini, S. K. Min, A. Abedi, and E. K. U. Gross, "Quantum-classical nonadiabatic dynamics: coupled- vs. independent-trajectory methods", J. Chem. Theory Comput. **12**, 2127–2143 (2016).

[28]G. H. Gossel, F. Agostini, and N. T. Maitra, "Coupled-trajectory mixed quantum-classical algorithm: a deconstruction", J. Chem. Theory Comput. **14**, 4513–4529 (2018).

[29]W. Feng, L. Xu, X.-Q. Li, W. Fang, and Y. Yan, "Nonadiabatic molecular dynamics simulation: an approach based on quantum measurement picture", AIP Adv. **4**, 077131 (2014).

[30]E. R. Dunkel, S. Bonella, and D. F. Coker, "Iterative linearized approach to nonadiabatic dynamics", J. Chem. Phys. **129**, 114106 (2008).

[31]M. Bedard-Hearn, R. Larsen, and B. Schwartz, "Mean-field dynamics with stochastic decoherence (MF-SD): a new algorithm for nonadiabatic mixed quantum/classical molecular-dynamics simulations with nuclear-induced decoherence", J. Chem. Phys. **123**, 234106 (2005).

[32]B. F. E. Curchod, I. Tavernelli, and U. Rothlisberger, "Trajectory-based solution of the nonadiabatic quantum dynamics equations: an on-the-fly approach for molecular dynamics simulations", Phys. Chem. Chem. Phys. **13**, 3231–3236 (2011).

[33]J. C. Burant and J. C. Tully, "Nonadiabatic dynamics via the classical limit Schrödinger equation", J. Chem. Phys. **112**, 6097 (2000).

[34]D. D. Holm, J. I. Rawlinson, and C. Tronci, "The bohmion method in nonadiabatic quantum hydrodynamics", Journal of Physics A: Mathematical and Theoretical **54**, 495201 (2021).

[35]O. V. Prezhdo and P. J. Rossky, "Mean-field molecular dynamics with surface hopping", J. Chem. Phys. **107**, 825–834 (1997).

[36]X. Gao and W. Thiel, "Non-hermitian surface hopping", Phys. Rev. E **95**, 013308 (2017).

[37]G. Tao, "Multi-state trajectory approach to non-adiabatic dynamics: general formalism and the active state trajectory approximation", J. Chem. Phys. **147**, 044107 (2017).

[38]P. Huo and D. F. Coker, "Communication: partial linearized density matrix dynamics for dissipative, non-adiabatic quantum evolution", J. Chem. Phys. **135**, 201101 (2011).

[39]F. A. Shakib and P. Huo, "Ring polymer surface hopping: incorporating nuclear quantum effects into nonadiabatic molecular dynamics simulations", J. Phys. Chem. Lett. **8**, 3073–3080 (2017).

[40]C. C. Martens, "Surface hopping without momentum jumps: a quantum-trajectory-based approach to nonadiabatic dynamics", J. Phys. Chem. A **123**, 1110–1128 (2019).

[41]C. C. Martens, "Surface hopping by consensus", J. Phys. Chem. Lett. **7**, 2610–2615 (2016).

[42]X. Gao, M. A. Sallerr, Y. Liu, A. Kelly, J. O. Richardson, and E. Geva, "Benchmarking quasiclassical mapping hamiltonian methods for simulating electronically nonadiabatic molecular dynamics", J. Chem. Theory Comput. (2020).

[43]C. A. Mead and D. G. Truhlar, "On the determination of Born–Oppenheimer nuclear motion wave functions including complications due to conical intersections and identical nuclei", J. Chem. Phys. **70**, 2284–2296 (1979).

[44]D. R. Yarkony, "Diabolical conical intersections", Rev. Mod. Phys. **68**, 985 (1996).

[45]W. Domcke, D. Yarkony, and H. Köppel, eds., *Conical intersections: electronic structure, dynamics & spectroscopy*, Vol. 15 (World Scientific Pub Co Inc, 2004).

[46]G. A. Worth and L. S. Cederbaum, "Beyond Born-Oppenheimer: molecular dynamics through a conical intersection", Annu. Rev. Phys. Chem. **55**, 127–158 (2004).

[47]S. C. Althorpe, W. Barford, J. Blumberger, C. Bungey, I. Burghardt, A. Datta, S. Ghosh, S. Giannini, T. Grünbaum, S. Habershon, et al., "Emerging opportunities and future directions: general discussion", Faraday Discuss. **221**, 564–581 (2020).

[48]A. V. Akimov, "Libra: an open-source "methodology discovery" library for quantum and classical dynamics simulations", J. Comput. Chem. **37**, 1626–1649 (2016).

[49]E. Schrödinger, "An undulatory theory of the mechanics of atoms and molecules", Phys. Rev. **28**, 1049–1070 (1926).

[50]M. Born and K. Huang, *Dynamical theory of crystal lattices* (Clarendon, Oxford, 1954).

[51]S. Matsika and P. Krause, "Nonadiabatic events and conical intersections", Annu. Rev. Phys. Chem. **62**, 621 (2011).

[52]M. Baer, *Beyond Born-Oppenheimer: Electronic Nonadiabatic Coupling Terms and Conical Intersections* (John Wiley & Sons, Inc., 2006).

[53]S. Gómez, I. F. Galván, R. Lindh, and L. González, "Motivation and basic concepts", in *Quantum chemistry and dynamics of excited states* (John Wiley & Sons, Ltd, 2020) Chap. 1, pp. 1–12.

[54]I. G. Ryabinkin, L. Joubert-Doriol, and A. F. Izmaylov, "Geometric phase effects in nonadiabatic dynamics near conical intersections", Acc. Chem. Res. **50**, 1785–1793 (2017).

[55]L. M. Ibele and B. F. E. Curchod, "Dynamics near a conical intersection—a diabolical compromise for the approximations of ab initio multiple spawning", J. Chem. Phys. **155**, 174119 (2021).

[56]C. A. Farfan and D. B. Turner, "A systematic model study quantifying how conical intersection topography modulates photochemical reactions", Phys. Chem. Chem. Phys. **22**, 20265–20283 (2020).

[57]J. Neumann and E. P. Wigner, "Über das Verhalten von Eigenwerten bei adiabatischen Prozessen", Phys. Zschr. **30** (1929).

[58]D. R. Yarkony, "Conical intersections: the new conventional wisdom", J. Phys. Chem. A **105**, 6277–6293 (2001).

[59]M. V. Berry, "Quantal phase factors accompanying adiabatic changes", Proc. R. Soc. A. **392**, 45–57 (1984).

[60]H. C. Longuet-Higgins, U. Öpik, M. H. L. Pryce, and R. A. Sack, "Studies of the Jahn-Teller effect .II. the dynamical problem", Proc. R. Soc. A **244**, 1–16 (1958).

[61]I. G. Ryabinkin, L. Joubert-Doriol, and A. F. Izmaylov, "When do we need to account for the geometric phase in excited state dynamics?", J. Chem. Phys. **140**, 214116 (2014).

[62]C. A. Mead, "The geometric phase in molecular systems", Rev. Mod. Phys. **64**, 51 (1992).

[63]A. F. Izmaylov, J. Li, and L. Joubert-Doriol, "Diabatic definition of geometric phase effects", J. Chem. Theory Comput. **12**, 5278–5283 (2016).

[64]R. Requist, F. Tandetzky, and E. K. U. Gross, "Molecular geometric phase from the exact electron-nuclear factorization", Phys. Rev. A **93**, 042108 (2016).

[65]S. K. Min, A. Abedi, K. S. Kim, and E. K. U. Gross, "Is the molecular Berry phase an artifact of the Born–Oppenheimer approximation?", Phys. Rev. Lett. **113**, 263004 (2014).

[66]A. Abedi, N. Maitra, and E. Gross, "Exact factorization of the time-dependent electron-nuclear wave function", Phys. Rev. Lett. **105**, 123002 (2010).

[67]A. Abedi, N. T. Maitra, and E. Gross, "Correlated electron-nuclear dynamics: exact factorization of the molecular wavefunction", J. Chem. Phys. **137**, 22A530 (2012).

[68]F. Agostini and E. K. U. Gross, "Exact factorization of the electron–nuclear wave function: theory and applications", in *Quantum chemistry and dynamics of excited states* (John Wiley & Sons, Ltd, 2020) Chap. 17, pp. 531–562.

[69]F. Agostini and E. K. U. Gross, "Ultrafast dynamics with the exact factorization", Eur. Phys. J. B **94**, 179 (2021).

[70]L. M. Ibele, B. F. E. Curchod, and F. Agostini, "A photochemical reaction in different theoretical representations", submitted, 2021.

[71]A. Abedi, F. Agostini, Y. Suzuki, and E. K. U. Gross, "Dynamical steps that bridge piecewise adiabatic shapes in the exact time-dependent potential energy surface", Phys. Rev. Lett. **110**, 263001 (2013).

[72]F. Agostini, A. Abedi, Y. Suzuki, and E. Gross, "Mixed quantum-classical dynamics on the exact time-dependent potential energy surface: a fresh look at non-adiabatic processes", Mol. Phys. **111**, 3625–3640 (2013).

[73]F. Agostini, A. Abedi, Y. Suzuki, S. K. Min, N. T. Maitra, and E. K. U. Gross, "The exact forces on classical nuclei in non-adiabatic charge transfer", J. Chem. Phys. **142**, 084303 (2015).

[74]B. F. E. Curchod and F. Agostini, "On the dynamics through a conical intersection", J. Phys. Chem. Lett. **8**, 831–837 (2017).

[75]F. Agostini and B. F. E. Curchod, "When the exact factorization meets conical intersections...", Eur. Phys. J. B **91**, 141 (2018).

[76]J. Suchan, D. Hollas, B. F. Curchod, and P. Slavíček, "On the importance of initial conditions for excited-state dynamics", Faraday Discuss. **212**, 307–330 (2018).

[77]E. Wigner, "On the quantum correction for thermodynamic equilibrium", Phys. Rev. **40**, 749–759 (1932).

[78]M. Hillery, R. O'Connell, M. Scully, and E. Wigner, "Distribution functions in physics: fundamentals", Phys. Rep. **106**, 121–167 (1984).

[79]B. F. E. Curchod and T. J. Martínez, "Ab initio nonadiabatic quantum molecular dynamics", Chem. Rev. **118**, 3305–3336 (2018).

[80]M Barbatti and K Sen, "Effects of different initial condition samplings on photodynamics and spectrum of pyrrole", Int. J. Quantum Chem. **116**, 762–771 (2016).

[81]L. Favero, G. Granucci, and M. Persico, "Dynamics of acetone photodissociation: a surface hopping study", Phys. Chem. Chem. Phys. **15**, 20651–20661 (2013).

[82]M Persico and G Granucci, "An overview of nonadiabatic dynamics simulations methods, with focus on the direct approach versus the fitting of potential energy surfaces", Theor. Chem. Acc. **133**, 1–28 (2014).

[83]W. Kuhn, "Über das Absorptionsspektrum der Polyene", Helv. Chim. Acta **31**, 1780–1799 (1948).

[84]A. N. Panda, F. Plasser, A. J. A. Aquino, I. Burghardt, and H. Lischka, "Electronically excited states in poly(p-phenylenevinylene): vertical excitations and torsional potentials from high-level ab initio calculations", The Journal of Physical Chemistry A **117**, 2181–2189 (2013).

[85]M. Barbatti, G. Granucci, M. Persico, M. Ruckenbauer, M. Vazda, M. Eckert-Maksić, and H. Lischka, "The on-the-fly surface-hopping program system Newton-X: application to ab initio simulation of the nonadiabatic photodynamics of benchmark systems", J. Photochem. Photobiol. A **190**, 228–240 (2007).

[86]M. Barbatti, "Simulation of excitation by sunlight in mixed quantum-classical dynamics", J. Chem. Theory Comput. **16**, 4849–4856 (2020).

[87]C. A. Ullrich, *Time-dependent density-functional theory* (Oxford University Press, 2012).

[88]A. Dreuw, J. Weisman, and M. Head-Gordon, "Long-range charge-transfer excited states in time-dependent density functional theory require non-local exchange", J. Chem. Phys. **119**, 2943 (2003).

[89]D. Tozer, "Relationship between long-range charge-transfer excitation energy error and integer discontinuity in Kohn–Sham theory", J. Chem. Phys. **119**, 12697 (2003).

[90]O. Gritsenko and E. Baerends, "Asymptotic correction of the exchange–correlation kernel of time-dependent density functional theory for long-range charge-transfer excitations", J. Chem. Phys. **121**, 655 (2004).

[91]A. Dreuw and M. Head-Gordon, "Failure of time-dependent density functional theory for long-range charge-transfer excited states: the zincbacteriochlorin-bacteriochlorin and bacteriochlorophyll-spheroidene complexes", J. Am. Chem. Soc. **126**, 4007–4016 (2004).

[92]N. T. Maitra, "Undoing static correlation: long-range charge transfer in time-dependent density-functional theory", J. Chem. Phys. **122**, 234104 (2005).

[93]P. Wiggins, J. A. G. Williams, and D. J. Tozer, "Excited state surfaces in density functional theory: a new twist on an old problem", J. Chem. Phys. **131**, 091101 (2009).

[94]M. Hellgren and E. K. U. Gross, "Discontinuities of the exchange-correlation kernel and charge-transfer excitations in time-dependent density-functional theory", Phys. Rev. A **85**, 022514 (2012).

[95]B. G. Levine, C. Ko, J. Quenneville, and T. J. Martinez, "Conical intersections and double excitations in density functional theory", Mol. Phys. **104**, 1039 (2006).

[96]C. Hsu, S. Hirata, and M. Head-Gordon, "Excitation energies from time-dependent density functional theory for linear polyene oligomers: butadiene to decapentaene", J. Phys. Chem. A **105**, 451–458 (2001).

[97]N. T. Maitra, F. Zhang, R. J. Cave, and K. Burke, "Double excitations within time-dependent density functional theory linear response", J. Chem. Phys. **120**, 5932 (2004).

[98]R. Cave, F. Zhang, N. Maitra, and K. Burke, "A dressed TDDFT treatment of the 2^1A_g states of butadiene and hexatriene", Chem. Phys. Lett. **389**, 39–42 (2004).

[99]P. Elliott, S. Goldson, C. Canahui, and N. T. Maitra, "Perspectives on double-excitations in TDDFT", Chem. Phys. **391**, 110 –119 (2011).

[100]V. Chernyak and S. Mukamel, "Density-matrix representation of nonadiabatic couplings in time-dependent density functional (TDDFT) theories", J. Chem. Phys. **112**, 3572–3579 (2000).

[101]R. Baer, "Non-adiabatic couplings by time-dependent density functional theory", Chem. Phys. Lett. **364**, 75–79 (2002).

[102]C. Hu, H. Hirai, and O. Sugino, "Nonadiabatic couplings from time-dependent density functional theory: formulation in the Casida formalism and practical scheme within modified linear response", J. Chem. Phys. **127**, 064103 (2007).

[103]C. Hu, H. Hirai, and O. Sugino, "Nonadiabatic couplings from time-dependent density functional theory. II. Successes and challenges of the pseudopotential approximation", J. Chem. Phys. **128**, 154111 (2008).

[104]I. Tavernelli, E. Tapavicza, and U. Rothlisberger, "Nonadiabatic coupling vectors within linear response time-dependent density functional theory", J. Chem. Phys. **130**, 124107 (2009).

[105]I. Tavernelli, B. F. E. Curchod, and U. Rothlisberger, "On nonadiabatic coupling vectors in time-dependent density functional theory", J. Chem. Phys. **131**, 196101 (2009).

[106]R. Send and F. Furche, "First-order nonadiabatic couplings from time-dependent hybrid density functional response theory: consistent formalism, implementation, and performance.", J. Chem. Phys. **132**, 044107 (2010).

[107]Q. Ou, G. D. Bellchambers, F. Furche, and J. E. Subotnik, "First-order derivative couplings between excited states from adiabatic TDDFT response theory", J. Chem. Phys. **142**, 064114 (2015).

[108]I. Tavernelli, B. F. E. Curchod, A. Laktionov, and U. Rothlisberger, "Nonadiabatic coupling vectors for excited states within time-dependent density functional theory and beyond", J. Chem. Phys. **133**, 194104–10 (2010).

[109]A. D. Laurent and D. Jacquemin, "TD-DFT benchmarks: a review", Int. J. Quantum Chem. **113**, 2019–2039 (2013).

[110]M. Caricato, G. W. Trucks, M. J. Frisch, and K. B. Wiberg, "Oscillator strength: how does TDDFT compare to EOM-CCSD?", J. Chem. Theory Comput. **7**, 456–466 (2010).

[111]F. Plasser, R. Crespo-Otero, M. Pederzoli, J. Pittner, H. Lischka, and M. Barbatti, "Surface hopping dynamics with correlated single-reference methods: 9H-adenine as a case study", J. Chem. Theory Comput. **10**, 1395–1405 (2014).

[112]D. Lefrancois, D. Tuna, T. J. Martínez, and A. Dreuw, "The spin-flip variant of the algebraic-diagrammatic construction yields the correct topology of S_1/S_0 conical intersections", J. Chem. Theory Comput. **13**, 4436–4441 (2017).

[113]E. Marsili, A. Prlj, and B. F. E. Curchod, "Caveat when using ADC(2) for studying the photochemistry of carbonyl-containing molecules", Phys. Chem. Chem. Phys. **23**, 12945–12949 (2021).

[114]L. González, D. Escudero, and L. Serrano-Andrés, "Progress and challenges in the calculation of electronic excited states", ChemPhysChem **13**, 28–51 (2012).

[115]B. Mignolet and B. F. E. Curchod, "Steering the outcome of a photochemical reaction—an in silico experiment on the H_2CSO sulfine using few-femtosecond dump pulses", J. Chem. Phys. **150**, 101101 (2019).

[116]S. Pathak, L. M. Ibele, R. Boll, C. Callegari, A. Demidovich, B. Erk, R. Feifel, R. Forbes, M. Di Fraia, L. Giannessi, C. S. Hansen, D. M. P. Holland, R. A. Ingle, R. Mason, O. Plekan, K. C. Prince, A. Rouzée, R. J. Squibb, J. Tross, M. N. R. Ashfold, B. F. E. Curchod, and D. Rolles, "Tracking the ultraviolet-induced photochemistry of thiophenone during and after ultrafast ring opening", Nat. Chem. **12**, 795–800 (2020).

[117]T. Shiozaki, C. Woywod, and H.-J. Werner, "Pyrazine excited states revisited using the extended multi-state complete active space second-order perturbation method", Phys. Chem. Chem. Phys.m **15**, 262–269 (2013).

[118]A Jäckle and H.-D. Meyer, "Product representation of potential energy surfaces", J. Chem. Phys. **104**, 7974–7984 (1996).

[119]H Köppel, W. Domcke, and L. S. Cederbaum, "Multimode molecular dynamics beyond the Born–Oppenheimer approximation", Advances in chemical physics, 59–246 (1984).

[120]J. W. Snyder Jr, B. F. E. Curchod, and T. J. Martínez, "Gpu-accelerated state-averaged complete active space self-consistent field interfaced with ab initio multiple spawning unravels the photodynamics of provitamin D3", J. Phys. Chem. Lett. **7**, 2444–2449 (2016).

[121]B. F. E. Curchod, A. Sisto, and T. J. Martínez, "Ab initio multiple spawning photochemical dynamics of DMABN using GPUs", J. Phys. Chem. A **121**, 265–276 (2017).

[122]S. Pijeau, D. Foster, and E. G. Hohenstein, "Excited-state dynamics of 2-(2-hydroxyphenyl) benzothiazole: ultrafast proton transfer and internal conversion", J. Phys. Chem. A **121**, 4595 (2017).

[123]D. Hollas, L. Sistik, E. G. Hohenstein, T. J. Martínez, and P. Slavicek, "Nonadiabatic ab initio molecular dynamics with the floating occupation molecular orbital-complete active space configuration interaction method", J. Chem. Theory Comput. **14**, 339–350 (2017).

[124]P. O. Dral, M Barbatti, and W Thiel, "Nonadiabatic excited-state dynamics with machine learning", J. Phys. Chem. Lett. **9**, 5660–5663 (2018).

[125]W.-K. Chen, X.-Y. Liu, W Fang, P. O. Dral, and G Cui, "Deep learning for nonadiabatic excited-state dynamics", J. Phys. Chem. Lett. **9**, 6702 (2018).

[126]H. D. Meyer, U. Manthe, and L. S. Cederbaum, "The multi-configurational time-dependent hartree approach", Chem. Phys. Lett. **165**, 73–78 (1990).

[127]M. H. Beck, A. Jäckle, G. A. Worth, and H. D. Meyer, "The multiconfiguration time-dependent hartree (MCTDH) method: a highly efficient algorithm for propagating wavepackets", Phys. Rep. **324**, 1–105 (2000).

[128]G. A. Worth, H. D. Meyer, and L. S. Cederbaum, "Multidimensional dynamics involving a conical intersection: Wavepacket calculations using the MCTDH method", in *Conical intersections: electronic structure, dynamics & spectroscopy*, Vol. 15, edited by W. Domcke, D. R. Yarkony, and H. Köppel, Advanced Series in Physical Chemistry (World Scientific, 2004) Chap. 14, pp. 583–617.

[129]H.-D. Meyer, F Gatti, and G. A. Worth, *Multidimensional quantum dynamics* (John Wiley & Sons, 2009).

[130]S. K. Min, F. Agostini, and E. K. U. Gross, "Coupled-trajectory quantum-classical approach to electronic decoherence in nonadiabatic processes", Phys. Rev. Lett. **115**, 073001 (2015).

[131]S. K. Min, F. Agostini, I. Tavernelli, and E. K. Gross, "Ab initio nonadiabatic dynamics with coupled trajectories: a rigorous approach to quantum (de)coherence", J. Phys. Chem. Lett. **8**, 3048–3055 (2017).

[132]C. W. McCurdy, H. D. Meyer, and W. H. Miller, "Classical model for electronic degrees of freedom in nonadiabatic collision processes: pseudopotential analysis and calculations for $F(^2P_{1/2})+H^+,Xe \rightarrow F(^2P_{3/2})+H^+,Xe$", J. Chem. Phys. **70**, 3177–3187 (1979).

[133]W. H. Miller, "Electronically nonadiabatic dynamics via semiclassical initial value methods", J. Phys. Chem. A **113**, 1405–1415 (2009).

[134]G. Stock and M. Thoss, "Semiclassical description of nonadiabatic quantum dynamics", Phys. Rev. Lett. **78**, 578–581 (1997).

[135]M. Thoss and G. Stock, "Mapping approach to the semiclassical description of nonadiabatic quantum dynamics", Phys. Rev. A **59**, 64–79 (1999).

[136]S. J. Cotton and W. H. Miller, "Symmetrical windowing for quantum states in quasi-classical trajectory simulations: application to electronically non-adiabatic processes", J. Chem. Phys. **139**, 234112 (2013).

[137]W. H. Miller and S. J. Cotton, "Classical molecular dynamics simulation of electronically non-adiabatic processes", Faraday Discuss. **195**, 9–30 (2016).

[138]R. Kapral and G. Ciccotti, "Mixed quantum-classical dynamics", J. Chem. Phys. **110**, 8919–8929 (1999).

[139]S. Nielsen, R. Kapral, and G. Ciccotti, "Mixed quantum-classical surface hopping dynamics", J. Chem. Phys. **112**, 6543–6553 (2000).

[140]D. M. Kernan, G. Ciccotti, and R. Kapral, J. Phys. Chem. B **112**, 424 (2008).

[141]R. E. Wyatt, C. L. Lopreore, and G Parlant, "Electronic transitions with quantum trajectories", J. Chem. Phys. **114**, 5113–5116 (2001).

[142]V. A. Rassolov and S Garashchuk, "Semiclassical nonadiabatic dynamics with quantum trajectories", Phys. Rev. A **71**, 032511 (2005).

[143]B. Poirier and G. Parlant, "Reconciling semiclassical and bohmian mechanics: IV. Multisurface dynamics", J. Phys. Chem. A **111**, 10400–10408 (2007).

[144]G. Worth, M. Robb, and I Burghardt, "A novel algorithm for non-adiabatic direct dynamics using variational Gaussian wavepackets", Faraday Discuss. **127**, 307–323 (2004).

[145]B Lasorne, M. J. Bearpark, M. A. Robb, and G. A. Worth, "Direct quantum dynamics using variational multi-configuration Gaussian wavepackets", Chem. Phys. Lett. **432**, 604–609 (2006).

[146]G. Richings, I Polyak, K. Spinlove, G. Worth, I Burghardt, and B Lasorne, "Quantum dynamics simulations using Gaussian wavepackets: the vMCG method", Int. Rev. Phys. Chem. **34**, 269–308 (2015).

[147]D. Shalashilin, "Quantum mechanics with the basis set guided by Ehrenfest trajectories: theory and application to spin-boson model", J. Chem. Phys. **130**, 244101 (2009).

[148]K Saita and D. V. Shalashilin, "On-the-fly ab initio molecular dynamics with multiconfigurational Ehrenfest method", J. Chem. Phys. **137**, 22A506 (2012).

[149]D Makhov, C Symonds, S Fernandez-Alberti, and D Shalashilin, "Ab initio quantum direct dynamics simulations of ultrafast photochemistry with multiconfigurational Ehrenfest approach", Chem. Phys. **493**, 200 (2017).

[150]T. J. Martínez, M. Ben-Nun, and R. D Levine, "Multi-electronic-state molecular dynamics: A wave function approach", J. Phys. Chem. **100**, 7884 (1996).

[151]T. J. Martínez, M Ben-Nun, and R. D. Levine, "Molecular collision dynamics on several electronic states", J. Phys. Chem. A **101**, 6389–6402 (1997).

[152]T. J. Martínez and R. D. Levine, "Non-adiabatic molecular dynamics: split-operator multiple spawning with applications to photodissociation", J. Chem. Soc., Faraday Trans. **93**, 941–947 (1997).

[153]D. V. Makhov, W. J. Glover, R. J. Martinez, and D. V. Shalashilin, "Ab initio multiple cloning algorithm for quantum nonadiabatic molecular dynamics", J. Chem. Phys. **141**, 054110 (2014).

[154]E. J. Heller, "Wave-packet path integral formulation of semiclassical dynamics", Chem. Phys. Lett. **34**, 321–325 (1975).

[155]E. J. Heller, "Time-dependent approach to semiclassical dynamics", J. Chem. Phys. **62**, 1544–1555 (1975).

[156]E. J. Heller, "The semiclassical way to molecular spectroscopy", Acc. Chem. Res. **14**, 368–375 (1981).

[157]E. J. Heller, "Frozen Gaussians: a very simple semiclassical approximation", J. Chem. Phys. **75**, 2923–2931 (1981).

[158]M. Ben-Nun and T. J. Martínez, "Nonadiabatic molecular dynamics: validation of the multiple spawning method for a multidimensional problem", J. Chem. Phys. **108**, 7244–7257 (1998).

[159]M. D. Hack, A. M. Wensmann, D. G. Truhlar, M Ben-Nun, and T. J. Martínez, "Comparison of full multiple spawning, trajectory surface hopping, and converged quantum mechanics for electronically nonadiabatic dynamics", J. Chem. Phys. **115**, 1172 (2001).

[160]B. G. Levine, J. D. Coe, A. M. Virshup, and T. J. Martinez, "Implementation of ab initio multiple spawning in the Molpro quantum chemistry package", Chem. Phys. **347**, 3–16 (2008).

[161]M. Ben-Nun and T. J. Martínez, "Ab initio quantum molecular dynamics", in *Advances in chemical physics* (John Wiley & Sons, Ltd, 2002) Chap. 7, pp. 439–512.

[162]S. Yang, J. D. Coe, B. Kaduk, and T. J. Martínez, "An "optimal" spawning algorithm for adaptive basis set expansion in nonadiabatic dynamics", J. Chem. Phys. **130**, 04B606 (2009).

[163]B. G. Levine and T. J. Martínez, "Isomerization through conical intersections", Annu. Rev. Phys. Chem. **58**, 613–634 (2007).

[164]M. Šulc, H. Hernández, T. J. Martínez, and J. Vaníček, "Relation of exact Gaussian basis methods to the dephasing representation: theory and application to time-resolved electronic spectra", J. Chem. Phys. **139**, 034112 (2013).

[165]J. P. Alborzpour, D. P. Tew, and S. Habershon, "Efficient and accurate evaluation of potential energy matrix elements for quantum dynamics using Gaussian process regression", J. Chem. Phys. **145**, 174112 (2016).

[166]S. Reiter, D. Keefer, and R. de Vivie-Riedle, "Exact quantum dynamics (wave packets) in reduced dimensionality", in *Quantum chemistry and dynamics of excited states* (John Wiley & Sons, Ltd, 2020) Chap. 11, pp. 355–381.

[167]G. A. Meek and B. G. Levine, "Wave function continuity and the diagonal Born–Oppenheimer correction at conical intersections", J. Chem. Phys. **144**, 184109 (2016).

[168]G. A. Meek and B. G. Levine, "The best of both reps—diabatized Gaussians on adiabatic surfaces", J. Chem. Phys. **145**, 184103 (2016).

[169]B. F. E. Curchod, W. J. Glover, and T. J. Martínez, "SSAIMS—stochastic-selection ab initio multiple spawning for efficient nonadiabatic molecular dynamics", J. Phys. Chem. A **124**, 6133–6143 (2020).

[170]J. C. Tully, "Nonadiabatic dynamics", in Modern methods for multidimensional dynamics computations in chemistry, edited by D. L. Thompson (1998).

[171]J. C. Tully, "Mixed quantum classical dynamics", Faraday Discuss. **110**, 407 (1998).

[172]R Crespo-Otero and M Barbatti, "Recent advances and perspectives on nonadiabatic mixed quantum–classical dynamics", Chem. Rev. **118**, 7026–7068 (2018).

[173]J. B. Delos, W. R. Thorson, and S. K. Knudson, "Semiclassical theory of inelastic collisions. I. classical picture and semiclassical formulation", Physical Review A **6**, 709 (1972).

[174]X Li, J. C. Tully, H. B Schlegel, and M. J. Frisch, "Ab initio Ehrenfest dynamics", J. Chem. Phys. **123**, 084106 (2005).

[175]J. C. Tully and R. K. Preston, "Trajectory surface hopping approach to nonadiabatic molecular collisions: the reaction of H^+ with D_2", J. Chem. Phys. **55**, 562–572 (1971).

[176]R. K. Preston and J. C. Tully, "Effects of surface crossing in chemical reactions: the H_3^+ system", J. Chem. Phys. **54**, 4297 (1971).

[177]S. Hammes-Schiffer and J. C. Tully, "Proton transfer in solution: molecular dynamics with quantum transitions", J. Chem. Phys. **101**, 4657 (1994).

[178]P. Vindel-Zandbergen, L. M. Ibele, J.-K. Ha, S. K. Min, B. F. E. Curchod, and N. T. Maitra, "Study of the decoherence correction derived from the exact factorization approach for nonadiabatic dynamics", J. Chem. Theory Comput. **17**, 3852–3862 (2021).

[179]A. Carof, S. Giannini, and J. Blumberger, "Detailed balance, internal consistency, and energy conservation in fragment orbital-based surface hopping", J. Chem. Phys. **147**, 214113 (2017).

[180]M. Barbatti, "Velocity adjustment in surface hopping: ethylene as a case study of the maximum error caused by direction choice", J. Chem. Theory Comput. **17**, 3010–3018 (2021).

[181]Y. Shu, L. Zhang, Z. Varga, K. A. Parker, S. Kanchanakungwankul, S. Sun, and D. G. Truhlar, "Conservation of angular momentum in direct nonadiabatic dynamics", J. Phys. Chem. Lett. **11**, 1135–1140 (2020).

[182]F. Plasser, S. Mai, M. Fumanal, E. Gindensperger, C. Daniel, and L. González, "Strong influence of decoherence corrections and momentum rescaling in surface hopping dynamics of transition metal complexes", J. Chem. Theory Comput. **15**, 5031–5045 (2019).

[183]A. W. Jasper and D. G. Truhlar, "Improved treatment of momentum at classically forbidden electronic transitions in trajectory surface hopping calculations", Chem. Phys. Lett. **369**, 60–67 (2003).

[184]G. Granucci and M. Persico, "Critical appraisal of the fewest switches algorithm for surface hopping", J. Chem. Phys. **126**, 134114–11 (2007).

[185]C. Zhu, S. Nangia, A. W. Jasper, and D. G. Truhlar, "Coherent switching with decay of mixing: an improved treatment of electronic coherence for non-Born-Oppenheimer trajectories.", J. Chem. Phys. **121**, 7658–7670 (2004).

[186]C. Zhu, A. W. Jasper, and D. G. Truhlar, "Non–Born–Oppenheimer Liouville–von Neumann dynamics. Evolution of a subsystem controlled by linear and population-driven decay of mixing with decoherent and coherent switching", J. Chem. Theory Comput. **1**, 527–540 (2005).

[187]G. Granucci, M. Persico, and A. Zoccante, "Including quantum decoherence in surface hopping", J. Chem. Phys. **133**, 134111 (2010).

[188]A. Jain, E. Alguire, and J. E. Subotnik, "An efficient, augmented surface hopping algorithm that includes decoherence for use in large-scale simulations", J. Chem. Theory Comput. **12**, 5256–5268 (2016).

[189]J.-K. Ha, I. S. Lee, and S. K. Min, "Surface hopping dynamics beyond nonadiabatic couplings for quantum coherence", J. Phys. Chem. Lett. **9**, 1097–1104 (2018).

[190]B. J. Schwartz, E. R. Bittner, O. V. Prezhdo, and P. J. Rossky, "Quantum decoherence and the isotope effect in condensed phase nonadiabatic molecular dynamics simulations", J. Chem. Phys. **104**, 5942–5955 (1996).

[191]J. Subotnik and N. Shenvi, "Decoherence and surface hopping: when can averaging over initial conditions help capture the effects of wave packet separation?", J. Chem. Phys. **134**, 244114 (2011).

[192]H. M. Jaeger, S. Fischer, and O. V. Prezhdo, "Decoherence-induced surface hopping", J. Chem. Phys. **137**, 22A545 (2012).

[193]R. Grunwald, H. Kim, and R. Kapral, "Surface-hopping dynamics and decoherence with quantum equilibrium structure", J. Chem. Phys. **128**, 164110 (2008).

[194]J. C. Tully, "Perspective on "Zur Quantentheorie der Molekeln"", Theor. Chem. Acc. **103**, 173–176 (2000).

[195]Y. Kobayashi, K. F. Chang, T. Zeng, D. M. Neumark, and S. R. Leone, "Direct mapping of curve-crossing dynamics in IBr by attosecond transient absorption spectroscopy", Science **365**, 79–83 (2019).

[196]T. S. Rose, M. J. Rosker, and A. H. Zewail, "Femtosecond real-time probing of reactions. IV. The reactions of alkali halides", J. Chem. Phys. **91**, 7415–7436 (1989).

[197]S. Hahn and G. Stock, "Quantum-mechanical modeling of the femtosecond isomerization in rhodopsin", J. Phys. Chem. B **104**, 1146–1149 (2000).

[198]M. Böckmann, N. L. Doltsinis, and D. Marx, "Unraveling a chemically enhanced photoswitch: Bridged azobenzene", Angew. Chem. Int. Ed. **49**, 3382–3384 (2010).

[199]W. Domcke and D. R. Yarkony, "Role of conical intersections in molecular spectroscopy and photoinduced chemical dynamics", Annu. Rev. Phys. Chem. **63**, 325–352 (2012).

[200]M. V. Berry and M. Wilkinson, "Diabolical points in the spectra of triangles", Proc. R. Soc. A. **392**, 15–43 (1984).

[201]F. Agostini and B. F. E. Curchod, "When the exact factorization meets conical intersections...", Eur. Phys. J. B **91**, 1–11 (2018).

[202]A. Ferretti, G. Granucci, A. Lami, M. Persico, and G. Villani, "Quantum mechanical and semiclassical dynamics at a conical intersection", J. Chem. Phys. **104**, 5517 (1996).

[203]M. D. Feit, J. A. Fleck, and A. Steiger, "Solution of the schrödinger equation by a spectral method", J. Comp. Phys. **47**, 412 –433 (1982).

[204]F. Agostini, I. Tavernelli, and G. Ciccotti, "Nuclear quantum effects in electronic (non) adiabatic dynamics", Eur. Phys. J. B **91**, 1–12 (2018).

[205]R. E. Wyatt, *Quantum dynamics with trajectories: introduction to quantum hydrodynamics* (Interdisciplinary applied mathematics, Springer, 2005).

[206]B. F. E. Curchod, F. Agostini, and E. K. U. Gross, "An exact factorization perspective on quantum interferences in nonadiabatic dynamics", J. Chem. Phys. **145**, 034103 (2016).

[207]F. Talotta, F. Agostini, and G. Ciccotti, "Quantum trajectories for the dynamics in the exact factorization framework: A proof-of-principle test", J. Phys. Chem. A **124**, 6764–6777 (2020).

[208]P. R. Holland, *The quantum theory of motion - an account of the de broglie-bohm causal interpretation of quantum mechanics* (Cambridge University Press, 1993).

[209]F. Agostini, A. Abedi, and E. K. U. Gross, "Classical nuclear motion coupled to electronic non-adiabatic transitions", J. Chem. Phys. **141**, 214101 (2014).

[210]X. Oriols, F. Martín, and J. Suñé, "Implications of noncrossing properties of bohm trajectories in one-dimensional tunneling configurations", Phys. Rev. A **54**, 2594–2604 (1996).

[211]M. Ben-Nun and T. J. Martínez, "A continuous spawning method for nonadiabatic dynamics and validation for the zero-temperature spin-boson problem", Isr. J. Chem. **47**, 75–88 (2007).

[212]B. Mignolet and B. F. E. Curchod, "A walk through the approximations of ab initio multiple spawning", J. Chem. Phys. **148**, 134110 (2018).

[213]S. C. Althorpe, T. Stecher, and F. Bouakline, "Effect of the geometric phase on nuclear dynamics at a conical intersection: extension of a recent topological approach from one to two coupled surfaces", J. Chem. Phys. **129**, 214117 (2008).

[214]L. Joubert-Doriol and A. F. Izmaylov, "Nonadiabatic quantum dynamics with frozen-width Gaussians", J. Phys. Chem. A **122**, 6031–6042 (2018).

[215]X. Bian, Y. Wu, H.-H. Teh, Z. Zhou, H.-T. Chen, and J. E. Subotnik, "Modeling nonadiabatic dynamics with degenerate electronic states, intersystem crossing, and spin separation: a key goal for chemical physics", J. Chem. Phys. **154**, 110901 (2021).

[216]D. R. Yarkony, "On the consequences of nonremovable derivative couplings. i. the geometric phase and quasidiabatic states: a numerical study", J. Chem. Phys. **105**, 10456–10461 (1996).

[217]S. Mai, P. Marquetand, and L. González, "Nonadiabatic dynamics: the sharc approach", WIREs Comput. Mol. Sci. **8**, e1370 (2018).

[218]S. Mai, M. Richter, M. Heindl, M. F. S. J. Menger, A. Atkins, M. Ruckenbauer, F. Plasser, L. M. Ibele, S. Kropf, M. Oppel, P. Marquetand, and L. González, *SHARC2.1: surface hopping including arbitrary couplings — program package for non-adiabatic dynamics*, sharc-md.org, 2019.

[219]R. Gherib, I. G. Ryabinkin, and A. F. Izmaylov, "Why do mixed quantum-classical methods describe short-time dynamics through conical intersections so well? Analysis of geometric phase effects", J. Chem. Theory Comput. **11**, 1375–1382 (2015).

[220]R. Gherib, L. Ye, I. G. Ryabinkin, and A. F. Izmaylov, "On the inclusion of the diagonal Born–Oppenheimer correction in surface hopping methods", J. Chem. Phys. **144**, 154103 (2016).

[221]B. Mignolet and B. F. E. Curchod, "Excited-state molecular dynamics triggered by light pulses—ab initio multiple spawning vs trajectory surface hopping", J. Phys. Chem. A **123**, 3582–3591 (2019).

[222]J. R. Reimers, L. K. McKemmish, R. H. McKenzie, and N. S. Hush, "Non-adiabatic effects in thermochemistry, spectroscopy and kinetics: the general importance of all three Born–Oppenheimer breakdown corrections", Phys. Chem. Chem. Phys. **17**, 24641–24665 (2015).

[223]L. K. McKemmish, R. H. McKenzie, N. S. Hush, and J. R. Reimers, "Electron–vibration entanglement in the Born–Oppenheimer description of chemical reactions and spectroscopy", Phys. Chem. Chem. Phys. **17**, 24666–24682 (2015).

[224]J. R. Reimers and N. S. Hush, "The critical role of the transition-state cusp diameter in understanding adiabatic and non-adiabatic electron transfer", Russ. J. Electrochem. **53**, 1042–1053 (2017).

[225]S. Fernandez-Alberti, D. V. Makhov, S. Tretiak, and D. V. Shalashilin, "Non-adiabatic excited state molecular dynamics of phenylene ethynylene dendrimer using a multiconfigurational Ehrenfest approach", Phys. Chem. Chem. Phys. **18**, 10028–10040 (2016).

[226]L. Joubert-Doriol, J. Sivasubramanium, I. G. Ryabinkin, and A. F. Izmaylov, "Topologically correct quantum nonadiabatic formalism for on-the-fly dynamics", J. Phys. Chem. Lett. **8**, 452–456 (2017).

[227]L Joubert-Doriol and A. F. Izmaylov, "Variational nonadiabatic dynamics in the moving crude adiabatic representation: further merging of nuclear dynamics and electronic structure", J. Chem. Phys. **148**, 114102 (2018).

[228]S Shin and H Metiu, "Nonadiabatic effects on the charge transfer rate constant: a numerical study of a simple model system", J. Chem. Phys. **102**, 9285–9295 (1995).

[229]M. Barbatti, A. J. A. Aquino, and H. Lischka, "Ultrafast two-step process in the non-adiabatic relaxation of the $CH_2NH_2^+$ molecule", Mol. Phys. **104**, 1053–1060 (2006).

[230]D. Polli, P. Altoè, O. Weingart, K. M. Spillane, C. Manzoni, D. Brida, G. Tomasello, G. Orlandi, P. Kukura, R. A. Mathies, et al., "Conical intersection dynamics of the primary photoisomerization event in vision", Nature **467**, 440 (2010).

[231]C. D. Rankine, J. P. F. Nunes, M. S. Robinson, P. D. Lane, and D. A. Wann, "A theoretical investigation of internal conversion in 1, 2-dithiane using non-adiabatic multiconfigurational molecular dynamics", Phys. Chem. Chem. Phys. **18**, 27170–27174 (2016).

[232]D. R. Yarkony, "Nuclear dynamics near conical intersections in the adiabatic representation: I. the effects of local topography on interstate transitions", J. Chem. Phys. **114**, 2601–2613 (2001).

[233]T. J. Martínez, "Ab initio molecular dynamics around a conical intersection: Li(2p)+ h_2", Chem. Phys. Lett. **272**, 139–147 (1997).

[234]D. Mendive-Tapia, B. Lasorne, G. A. Worth, M. J. Bearpark, and M. A. Robb, "Controlling the mechanism of fulvene S_1/S_0 decay: switching off the stepwise population transfer", Phys. Chem. Chem. Phys. **12**, 15725–15733 (2010).

[235]L. Blancafort, P. Hunt, and M. A. Robb, "Intramolecular electron transfer in bis (methylene) adamantyl radical cation: a case study of diabatic trapping", J. Am. Chem. Soc. **127**, 3391–3399 (2005).

[236]H.-J. Werner, "Matrix-formulated direct multiconfiguration self-consistent field and multiconfiguration reference configuration-interaction methods", Advances in Chemical Physics: Ab Initio Methods in Quantum Chemistry Part 2 **69**, 1–62 (1987).

[237]B. O. Roos, "The complete active space self-consistent field method and its applications in electronic structure calculations", Advances in Chemical Physics: Ab Initio Methods in Quantum Chemistry Part 2 **69**, 399–445 (1987).

[238]R. H. Ditchfield, W. J. Hehre, and J. A. Pople, "Self-consistent molecular-orbital methods. IX. An extended Gaussian-type basis for molecular-orbital studies of organic molecules", J. Chem. Phys. **54**, 724–728 (1971).

[239]P. C. Hariharan and J. A. Pople, "The influence of polarization functions on molecular orbital hydrogenation energies", Theor. Chem. Acc. **28**, 213–222 (1973).

[240]W. Zhou, A. Mandal, and P. Huo, "Quasi-diabatic scheme for nonadiabatic on-the-fly simulations", J. Phys. Chem. Lett. **10**, PMID: 31665889, 7062–7070 (2019).

[241]E. Runge and E. K. U. Gross, "Density-functional theory for time-dependent systems", Phys. Rev. Lett. **52**, 997–1000 (1984).

[242]M. E. Casida, "Time-dependent density-functional response theory for molecules", in Recent advances in density functional methods, edited by D. P. Chong (1995), p. 155.

[243]M. Petersilka, U. J. Gossmann, and E. K. U. Gross, "Excitation energies from time-dependent density-functional theory", Phys. Rev. Lett. **76**, 1212–1215 (1996).

[244]J. P. Perdew, K. Burke, and M. Ernzerhof, "Generalized gradient approximation made simple", Phys. Rev. Lett. **77**, 3865–3868 (1996).

[245]H. Iikura, T. Tsuneda, T. Yanai, and K. Hirao, "A long-range correction scheme for generalized-gradient-approximation exchange functionals", J. Chem. Phys. **115**, 3540 (2001).

[246]M. J. Frisch, G. W. Trucks, H. B. Schlegel, et al., *Gaussian09 Revision A.1*, Gaussian Inc. Wallingford CT 2009.

[247]H.-J. Werner, P. J. Knowles, G. Knizia, et al., *Molpro, version 2012.1, a package of ab initio programs*, 2012.

[248]B. F. E. Curchod, *Molecular tully models [dataset]*, 2020.

[249]M. Richter, P. Marquetand, J. González-Vázquez, I. Sola, and L. González, "SHARC: ab initio molecular dynamics with surface hopping in the adiabatic representation including arbitrary couplings", J. Chem. Theory Comput. **7**, 1253–1258 (2011).

[250]S. Mai, M. Richter, M. Heindl, M. F. S. J. Menger, A. Atkins, M. Ruckenbauer, F. Plasser, M. Oppel, P. Marquetand, and L. González, *SHARC2.0: surface hopping including arbitrary couplings — program package for non-adiabatic dynamics*, sharc-md.org, 2018.

[251]F. Plasser, M. Ruckenbauer, S. Mai, M. Oppel, P. Marquetand, and L. González, "Efficient and flexible computation of many-electron wave function overlaps", J. Chem. Theory Comput. **12**, 1207–1219 (2016).

[252]M. Barbatti, M. Ruckenbauer, F. Plasser, J. Pittner, G. Granucci, M. Persico, and H. Lischka, "Newton-x: a surface-hopping program for nonadiabatic molecular dynamics", WIREs Comput. Mol. Sci. **4**, 26–33 (2014).

[253]A. Prlj, NEWTON-X forum: Implementation of decoherence correction (2019).

[254]A. Toniolo, C. Ciminelli, M. Persico, and T. J. Martínez, "Simulation of the photodynamics of azobenzene on its first excited state: comparison of full multiple spawning and surface hopping treatments.", J. Chem. Phys. **123**, 234308 (2005).

[255]A. Viel, R. P. Krawczyk, U. Manthe, and W. Domcke, "The sudden-polarization effect and its role in the ultrafast photochemistry of ethene", Angew. Chem. Int. Ed. **42**, 3434–3436 (2003).

[256]G Granucci, M Persico, and A Toniolo, "Direct semiclassical simulation of photochemical processes with semiempirical wave functions", J. Chem. Phys. **114**, 10608 (2001).

[257]M. Barbatti, M. Ruckenbauer, and H. Lischka, "The photodynamics of ethylene: a surface-hopping study on structural aspects.", eng, J. Chem. Phys. **122**, 174307 (2005).

[258]M. Barbatti, J. Paier, and H. Lischka, "Photochemistry of ethylene: a multireference configuration interaction investigation of the excited-state energy surfaces", J. Chem. Phys. **121**, 11614–11624 (2004).

[259]M. Barbatti, G. Granucci, M. Persico, and H. Lischka, "Semiempirical molecular dynamics investigation of the excited state lifetime of ethylene", Chem. Phys. Lett. **401**, 276–281 (2005).

[260]E. Fabiano, T. Keal, and W. Thiel, "Implementation of surface hopping molecular dynamics using semiempirical methods", Chem. Phys. **349**, 334–347 (2008).

[261]B. Sellner, M. Barbatti, T. Müller, W. Domcke, and H. Lischka, "Ultrafast non-adiabatic dynamics of ethylene including rydberg states", Mol. Phys. **111**, 2439–2450 (2013).

[262]M. Ben-Nun and T. J. Martínez, "Ab initio molecular dynamics study of cis–trans photoisomerization in ethylene", Chem. Phys. Lett. **298**, 57 –65 (1998).

[263]M. Ben-Nun, J. Quenneville, and T. J. Martínez, "Ab initio multiple spawning: Photochemistry from first principles quantum molecular dynamics", J. Phys. Chem. A **104**, 5161–5175 (2000).

[264]J. Quenneville and T. J. Martínez, "Ab initio study of cistrans photoisomerization in stilbene and ethylene", J. Phys. Chem. A **107**, 829–837 (2003).

[265]H. Tao, B. G. Levine, and T. J. Martínez, "Ab initio multiple spawning dynamics using multi-state second-order perturbation theory", J. Chem. Phys. A **113**, 13656–13662 (2009).

[266]H Tao, T. Allison, T. Wright, A. Stooke, C Khurmi, J Van Tilborg, Y Liu, R. Falcone, A Belkacem, and T. Martinez, "Ultrafast internal conversion in ethylene. i. the excited state lifetime", J. Chem. Phys. **134**, 244306 (2011).

[267]T Mori, W. J. Glover, M. S. Schuurman, and T. J. Martinez, "Role of rydberg states in the photochemical dynamics of ethylene", J. Phys. Chem. A **116**, 2808–2818 (2012).

[268]A. Viel, R. P. Krawczyk, U. Manthe, and W. Domcke, "Photoinduced dynamics of ethene in the n, v, and z valence states: a six-dimensional nonadiabatic quantum dynamics investigation", J. Chem. Phys. **120**, 11000–11010 (2004).

[269]L. Du and Z. Lan, "An on-the-fly surface-hopping program jade for nonadiabatic molecular dynamics of polyatomic systems: implementation and applications", J. Chem. Theory Comput. **11**, 1360–1374 (2015).

[270]M. A. Kochman, A. Tajti, C. A. Morrison, and R. J. D. Miller, "Early events in the nonadiabatic relaxation dynamics of 4-(N,N-Dimethylamino)benzonitrile", J. Chem. Theory Comput. **11**, 1118–1128 (2015).

[271]G. R. Medders, E. C. Alguire, A. Jain, and J. E. Subotnik, "Ultrafast electronic relaxation through a conical intersection: nonadiabatic dynamics disentangled through an oscillator strength-based diabatization framework", J. Phys. Chem. A **121**, 1425–1434 (2017).

[272]P. J. Castro, A. Perveaux, D. Lauvergnat, M. Reguero, and B. Lasorne, "Ultrafast internal conversion in 4-aminobenzonitrile occurs sequentially along the seam", Chem. Phys. **509**, 30–36 (2018).

[273]G. Miao and J. Subotnik, "Revisiting the recoherence problem in the fewest switches surface hopping algorithm", J. Phys. Chem. A **123**, 5428–5435 (2019).

[274]M. J. Bearpark, F. Bernardi, M. Olivucci, M. A. Robb, and B. R. Smith, "Can fulvene S_1 decay be controlled? A CASSCF study with MMVB dynamics", J. Am. Chem. Soc. **118**, 5254–5260 (1996).

[275]S Alfalah, S Belz, O Deeb, M Leibscher, J Manz, and S Zilberg, "Photoinduced quantum dynamics of ortho-and para-fulvene: hindered photoisomerization due to mode selective fast radiationless decay via a conical intersection", J. Chem. Phys. **130**, 124318 (2009).

[276]D. Mendive-Tapia, B. Lasorne, G. A. Worth, M. A. Robb, and M. J. Bearpark, "Towards converging non-adiabatic direct dynamics calculations using frozen-width variational Gaussian product basis functions", J. Chem. Phys. **137**, 22A548 (2012).

[277]M. Araújo, B. Lasorne, A. L. Magalhaes, M. J. Bearpark, and M. A. Robb, "Controlling product selection in the photodissociation of formaldehyde: direct quantum dynamics from the s1 barrier", J. Phys. Chem. A **114**, 12016–12020 (2010).

[278]M. T. Do Casal, J. Toldo, M. Pinheiro Jr, and M. Barbatti, "Fewest switches surface hopping with baeck-an couplings", Open Research Europe **1** (2021).

[279]B. M. Weight, A. Mandal, and P. Huo, "Ab initio symmetric quasi-classical approach to investigate molecular tully models", J. Chem. Phys. **155**, 084106 (2021).

[280]L. M. Ibele, Y. Lassmann, T. J. Martínez, and B. F. E. Curchod, "Comparing (stochastic-selection) ab initio multiple spawning with trajectory surface hopping for the photodynamics of cyclopropanone, fulvene, and dithiane", J. Chem. Phys. **154**, 104110 (2021).

[281]Y. Lassmann and B. F. Curchod, "AIMSWISS—ab initio multiple spawning with informed stochastic selections", J. Chem. Phys. **154**, 211106 (2021).

[282]S. K. Min, I. S. Lee, J.-K. Ha, D. Han, K. Kim, T. I. Kim, and S. W. Moon, *PyUNIxMD: Python-based UNIversal eXcited state Molecular Dynamics*, https://github.com/skmin-lab/unixmd, 2021.

[283]S. M. Parker and C. J. Schiltz, "Surface hopping with cumulative probabilities: even sampling and improved reproducibility", J. Chem. Phys. **153**, 174109 (2020).

[284]G. Cui, Y. Ai, and W. Fang, "Conical intersection is responsible for the fluorescence disappearance below 365 nm in cyclopropanone", J. Phys. Chem. A **114**, 730–734 (2010).

[285]G. Cui and W. Fang, "Ab initio based surface-hopping dynamics study on ultrafast internal conversion in cyclopropanone", J. Phys. Chem. A **115**, 1547–1555 (2011).

[286]M. Filatov, S. K. Min, and C. H. Choi, "Theoretical modelling of the dynamics of primary photoprocess of cyclopropanone", Phys. Chem. Chem. Phys. **21**, 2489–2498 (2019).

[287]J. Suchan, J. Janoš, and P. Slavíček, "Pragmatic approach to photodynamics: Mixed Landau–Zener surface hopping with intersystem crossing", J. Chem. Theory Comput. **16**, 5809–5820 (2020).

[288]I. S. Ufimtsev and T. J. Martínez, "Quantum chemistry on graphical processing units. 1. strategies for two-electron integral evaluation", J. Chem. Theory Comput. **4**, 222–231 (2008).

[289]I. S. Ufimtsev and T. J. Martinez, "Quantum chemistry on graphical processing units. 2. direct self-consistent-field (scf) implementation", J. Chem. Theory Comput. **5**, 3138–3138 (2009).

[290]I. S. Ufimtsev and T. J. Martinez, "Quantum chemistry on graphical processing units. 3. analytical energy gradients, geometry optimization, and first principles molecular dynamics", J. Chem. Theory Comput. **5**, 2619–2628 (2009).

[291]S. Seritan, C. Bannwarth, B. S. Fales, E. G. Hohenstein, S. I. Kokkila-Schumacher, N. Luehr, J. W. Snyder Jr, C. Song, A. V. Titov, I. S. Ufimtsev, et al., "Terachem: accelerating electronic structure and ab initio molecular dynamics with graphical processing units", J. Chem. Phys. **152**, 224110 (2020).

[292]S. Seritan, C. Bannwarth, B. S. Fales, E. G. Hohenstein, C. M. Isborn, S. I. Kokkila-Schumacher, X. Li, F. Liu, N. Luehr, J. W. Snyder Jr, et al., "Terachem: a graphical processing unit-accelerated electronic structure package for large-scale ab initio molecular dynamics", WIREs Comput. Mol. Sci., e1494 (2020).

[293]J. W. Snyder Jr, E. G. Hohenstein, N. Luehr, and T. J. Martínez, "An atomic orbital-based formulation of analytical gradients and nonadiabatic coupling vector elements for the state-averaged complete active space self-consistent field method on graphical processing units", J. Chem. Phys. **143**, 154107 (2015).

[294]A. B. Stephansen, R. Y. Brogaard, T. S. Kuhlman, L. B. Klein, J. B. Christensen, and T. I. Sølling, "Surprising intrinsic photostability of the disulfide bridge common in proteins", J. Am. Chem. Soc. **134**, 20279–20281 (2012).

[295]M. Minitti, J. Budarz, A. Kirrander, J. Robinson, D. Ratner, T. Lane, D Zhu, J. Glownia, M Kozina, H. Lemke, et al., "Imaging molecular motion: femtosecond x-ray scattering of an electrocyclic chemical reaction", Phys. Rev. Lett. **114**, 255501 (2015).

[296]M. G. Pullen, B. Wolter, A.-T. Le, M. Baudisch, M. Hemmer, A. Senftleben, C. D. Schröter, J. Ullrich, R. Moshammer, C.-D. Lin, et al., "Imaging an aligned polyatomic molecule with laser-induced electron diffraction", Nat. Commun. **6**, 1–6 (2015).

[297]B. Wolter, M. G. Pullen, A.-T. Le, M. Baudisch, K Doblhoff-Dier, A. Senftleben, M. Hemmer, C. D. Schröter, J. Ullrich, T. Pfeifer, et al., "Ultrafast electron diffraction imaging of bond breaking in di-ionized acetylene", Science **354**, 308–312 (2016).

[298]A. R. Attar, A. Bhattacherjee, C. Pemmaraju, K. Schnorr, K. D. Closser, D. Prendergast, and S. R. Leone, "Femtosecond x-ray spectroscopy of an electrocyclic ring-opening reaction", Science **356**, 54–59 (2017).

[299]M. S. Schuurman and A. Stolow, "Dynamics at conical intersections", Ann. Rev. Phys. Chem. **69**, 427–450 (2018).

[300]T. J. Wolf, D. M. Sanchez, J Yang, R. Parrish, J. Nunes, M Centurion, R Coffee, J. Cryan, M. Gühr, K. Hegazy, et al., "The photochemical ring-opening of 1, 3-cyclohexadiene imaged by ultrafast electron diffraction", Nat. Chem. **11**, 504–509 (2019).

[301]J. M. Ruddock, H. Yong, B. Stankus, W. Du, N. Goff, Y. Chang, A. Odate, A. M. Carrascosa, D. Bellshaw, N. Zotev, et al., "A deep UV trigger for ground-state ring-opening dynamics of 1, 3-cyclohexadiene", Sci. Adv. **5**, eaax6625 (2019).

[302]B. Stankus, H. Yong, N. Zotev, J. M. Ruddock, D. Bellshaw, T. J. Lane, M. Liang, S. Boutet, S. Carbajo, J. S. Robinson, et al., "Ultrafast x-ray scattering reveals vibrational coherence following rydberg excitation", Nat. Chem. **11**, 716–721 (2019).

[303]B. C. Arruda and R. J. Sension, "Ultrafast polyene dynamics: the ring opening of 1, 3-cyclohexadiene derivatives", Phys. Chem. Chem. Phys. **16**, 4439–4455 (2014).

[304]V. S. Petrović, M. Siano, J. L. White, N. Berrah, C. Bostedt, J. D. Bozek, D. Broege, M. Chalfin, R. N. Coffee, J. Cryan, et al., "Transient x-ray fragmentation: probing a prototypical photoinduced ring opening", Phys. Rev. Lett. **108**, 253006 (2012).

[305]F. Rudakov and P. M. Weber, "Ground state recovery and molecular structure upon ultrafast transition through conical intersections in cyclic dienes", Chem. Phys. Lett. **470**, 187–190 (2009).

[306]S. Adachi, M. Sato, and T. Suzuki, "Direct observation of ground-state product formation in a 1, 3-cyclohexadiene ring-opening reaction", J. Phys. Chem. Lett. **6**, 343–346 (2015).

[307]S Breda, I Reva, and R Fausto, "UV-induced unimolecular photochemistry of 2(5H)-furanone and 2(5H)-thiophenone isolated in low temperature inert matrices", Vib. Spectrosc. **50**, 57–67 (2009).

[308]D. Murdock, S. J. Harris, J. Luke, M. P. Grubb, A. J. Orr-Ewing, and M. N. Ashfold, "Transient UV pump–IR probe investigation of heterocyclic ring-opening dynamics in the solution phase: the role played by nσ^* states in the photoinduced reactions of thiophenone and furanone", Phys. Chem. Chem. Phys. **16**, 21271–21279 (2014).

[309]E Allaria, R. Appio, L Badano, W. Barletta, S Bassanese, S. Biedron, A Borga, E Busetto, D Castronovo, P Cinquegrana, et al., "Highly coherent and stable pulses from the FERMI seeded free-electron laser in the extreme ultraviolet", Nat. Photonics **6**, 699–704 (2012).

[310]A. Stolow, A. E. Bragg, and D. M. Neumark, "Femtosecond time-resolved photoelectron spectroscopy", Chem. Rev. **104**, 1719–1758 (2004).

[311]T. Suzuki, "Time-resolved photoelectron spectroscopy of non-adiabatic electronic dynamics in gas and liquid phases", Int. Rev. Phys. Chem. **31**, 265–318 (2012).

[312]W. S. Chin, Z. P. Xu, C. Y. Mok, H. H. Huang, H. Mutoh, and S. Masuda, "He I and He II photoelectron spectra of thiophenones", J. Electron Spectrosc. Relat. Phenomena **88**, 97–101 (1998).

[313]H. R. Hudock, B. G. Levine, A. L. Thompson, H. Satzger, D. Townsend, N Gador, S. Ullrich, A. Stolow, and T. J. Martinez, "Ab initio molecular dynamics and time-resolved photoelectron spectroscopy of electronically excited uracil and thymine", J. Phys. Chem. A **111**, 8500–8508 (2007).

[314]T. Shiozaki, W. Győrffy, P. Celani, and H.-J. Werner, "Communication: extended multi-state complete active space second-order perturbation theory: energy and nuclear gradients", J. Chem. Phys. **135**, 081106 (2011).

[315]A. A. Granovsky, "Extended multi-configuration quasi-degenerate perturbation theory: the new approach to multi-state multi-reference perturbation theory", J. Chem. Phys. **134**, 214113 (2011).

[316]T. Shiozaki, "BAGEL: brilliantly advanced general electronic-structure library", Wiley Interdiscip. Rev. Comput. Mol. Sci. **8**, e1331 (2018).

[317]G. Ghigo, B. O. Roos, and P.-Å. Malmqvist, "A modified definition of the zeroth-order hamiltonian in multiconfigurational perturbation theory (CASPT2)", Chem. Phys. Lett. **396**, 142–149 (2004).

[318]B.-B. Xie and W.-H. Fang, "Combined quantum trajectory mean-field and molecular mechanical (QTMF/MM) nonadiabatic dynamics simulations on the photoinduced ring-opening reaction of 2(5H)-thiophenone", ChemPhotoChem **3**, 897–906 (2019).

[319]W. Arbelo-González, R. Crespo-Otero, and M. Barbatti, "Steady and time-resolved photoelectron spectra based on nuclear ensembles", J. Chem. Theory Comput. **12**, 5037–5049 (2016).

[320]C. Adamo and V. Barone, "Toward reliable density functional methods without adjustable parameters: the PBE0 model", J. Chem. Phys. **110**, 6158 (1999).

[321]B. Mignolet, B. F. E. Curchod, and T. J. Martínez, "Rich athermal ground-state chemistry triggered by dynamics through a conical intersection", Angew. Chem. Int. Ed. **128**, 15217–15220 (2016).

[322]H. Bock, S. Mohmand, T. Hirabayashi, and A. Semkow, “Gas-phase reactions. 29. thioacrolein”, J. Am. Chem. Soc. **104**, 312–313 (1982).

[323]C.-H. Yang, S. Bhattacharyya, L. Liu, W.-h. Fang, and K. Liu, “Real-time tracking of the entangled pathways in the multichannel photodissociation of acetaldehyde”, Chem. Sci. **11**, 6423–6430 (2020).

[324]J. Tully, private communication, Oct. 22, 2020.